Self-Replenishing, Wear-Resistant and Anti-Sticking Surfaces Based on Liquid Impregnation of Microstructured Mesoporous α-Al_2O_3 Matrices

THÈSE N^{O} 7024 (2016)

PRÉSENTÉE LE 28 JUIN 2016

À LA FACULTÉ DES SCIENCES ET TECHNIQUES DE L'INGÉNIEUR
LABORATOIRE DES MATÉRIAUX PHOTONIQUES ET CARACTÉRISATION
PROGRAMME DOCTORAL EN SCIENCE ET GÉNIE DES MATÉRIAUX

ÉCOLE POLYTECHNIQUE FÉDÉRALE DE LAUSANNE

POUR L'OBTENTION DU GRADE DE DOCTEUR ÈS SCIENCES

PAR

Sriharitha ROWTHU

acceptée sur proposition du jury:

Prof. H. Hofmann, président du jury
Prof. P. Hoffmann, directeur de thèse
Dr P. Levkin, rapporteur
Dr M. Ferrari, rapporteur
Prof. P. Bowen, rapporteur

ÉCOLE POLYTECHNIQUE
FÉDÉRALE DE LAUSANNE
Suisse
2016

The doubter is a true man of science; he doubts only himself
and his interpretations, but believes in science.
–Claude Bernard

Acknowledgements

I owe my deepest gratitude to my PhD supervisor Prof. Dr. Patrik Hoffmann for giving me an opportunity to pursue my doctoral studies in his laboratory that is quite diverse and application oriented. I thank him for all the scientific freedom he has given me on the project. I find his knowledge immense and must say that my scientific discussions with him throughout the project helped me to broaden my knowledge. I acknowledge Competence Centre for Materials Science and Technology (CCMX), Switzerland for mainly funding the project under the contract 5211.00093.100.01. I acknowledge our industrial partner BOBST Mex SA, Switzerland and Roger Roch, Guy Delaloye, BOBST Mex SA for their inputs. I also thank Dr. Edin Balic for writing the funding proposal, guiding the project in the early stages and for participating in the CCMX meetings.

My special thanks to Prof. Dr. Paul Bowen, EPFL for collaborating and guidance in the slip casting process and his laboratory for providing the alumina particle size distributions. I thank Dr. Karl Böhlen, Erdem Siringil for providing laser ablated polycarbonate sheets. I thank Dr. Michler Johann, Empa Thun for providing me the accessibility to Philips S4800 HRSEM throughout my PhD project. I thank Prof. Dr. Per Magnus Kristiansen, FHNW, Brugg for providing Moldflon™ and Zonyl™ materials and collaborating on the corresponding hot embossing experiments.

I thank Durif Carolina, Empa Dübendorf for obtaining Hg intrusion porosimetry data of mesoporous alumina samples. I thank Dr. Arie Bruinink, Empa St. Gallen for designing micron sized tear drop structures. I thank Muriel Blum, Empa Thun for providing the AFM measurements. I would like to thank Anton Böll, Peter Ramseier, Damian Frey and Gerhard Bürki for their technical help. I would like to sincerely thank Yang Fei, Dr. Rolf Kaufmann, Empa Dübendorf for the collaborations on dark field X–Ray imaging of capillary uptake experiments.

I would like to thank Prof. Dr. Heinrich Hofmann (president), Prof. Dr. Paul Bowen (internal expert), Dr. Pavel Levkin (external expert), KIT, Germany, Dr. Michele Ferrari (external expert), CNR, Italy for their kind acceptance as the jury members of my PhD defense.

I would like to acknowledge Dr. Fatemeh Saeidi for the immense moral strength and being always available to listen to my technical and scientific problems in my project. I am highly indebted to my two friends Ahmad Omar, A.B. Kousalya who have been extremely supportive and had motivating discussions that helped me to move forward in my project. I once again thank all three of them for being my friends and pillars of strength for my PhD project.

My sincere thanks to my friends and colleagues: Vikrant Karra, Dr. Kilian Wasmer, Dr. Matthias Leistner, Marie Le Dantec, Dr. Muralikrishna Dibbanti, Dr. Bastian Meylan, Dr. Kishore Babu Nagumothu, Dr. Vipin Chawla, Dr. Aravind Kumar Chandiran, Sirisha Deepthi, Dr. Dinca Valentina, Kaspar Kallip, Dr. Sébastien Vaucher, Dr. Farzad Vakili Farahani, Dr. Gaurav Mohanty and Dr. Lex Pillatsch for their friendship and the help. I specially thank Marie Le Dantec and also Dr. Kilian Wasmer and Dr. Briac Lanfant for the French translation to my PhD thesis abstract. I would like to acknowledge all other members of the Advanced Materials Processing Laboratory, Empa Thun for being the part of life at Empa and for their friendliness.

I am thankful to my parents Rowthu Appanna and Rowthu Parvathi Devi, who taught me to handle difficult and complicated situations in life and for their moral support and blessings. I also thank my little brothers Rowthu Sriram and Rowthu Srikrishna for believing in me that *I can* and has helped me to face the challenges with more confidence. I would like to finally acknowledge everyone throughout my life who has indirectly or directly inspired me and provoked my curiosity in science.

Sriharitha Rowthu, 2016

Abstract

Fabrication of wear–resistant omniphobic surfaces is a persistent scientific challenge and essential for various applications such as in paint industries, fluid transport, antifouling, reduction of friction drag on ship hulls, and stain resistant textiles. However, there are very limited efforts to address this problem, especially because the conventional omniphobic surfaces are intrinsically wear–sensitive, due to the loss of either non polar coating materials or surface roughness elements during wear. Consequently, there is a need to employ novel approaches to fabricate such surfaces.

The present research work mainly focuses on fabricating anti–sticking and wear–resistant materials using liquid impregnation of mesoporous alumina (MPA) matrices. Secondly, and equally important is to study their wetting properties post wear. To achieve the outlined objectives, different impregnating liquids such as water, Hexadecane, Dodecane, Fomblin® oil and 3M™ HFE 7200 were employed in conjunction with various alumina matrix densities ranging from 70 to 99.5 %. Fomblin® oil was found to be the most efficient impregnating liquid. Indeed, anti–sticking and pinning free sliding behaviors were observed for water, Hexadecane, Dodecane, water based and oil based paints atop Fomblin® oil impregnated/lubricated composites.

Subsequently, the friction coefficient (FC) and the wear–resistance of Fomblin® impregnated MPA composites were evaluated by varying the normal load and alumina matrix density. The optimum alumina density of ~90 %, leading to a low FC and high wear–resistance was determined. Ultra–low FC values of 0.025 and small wear coefficients of 10^{-8} mm^3 N^{-1} m^{-1} were measured. The wear mechanism is mild abrasion majorly by intergranular fracture and/or third body abrasion.

Finally, the wetting characterizations of Fomblin® impregnated MPA composites post wear were evaluated using Hexadecane and water. The worn composite surfaces lost anti–sticking properties to water and Hexadecane immediately after wear, exhibiting superhydrophilicity and oleophilicity. Nevertheless, given a sufficient self–replenishing/healing time, they exhibited enhanced omniphobicity. The contributing factors towards self–replenishment are the strong capillary forces of the impregnating liquid, coupled with its surface diffusivity on the polar alumina matrix. Further, the replenishing efficiency may be improved by providing surface microstructuring to MPA samples.

Consequently, a fabrication process of large area surface microstructuring the bulk MPA samples was developed using replication and slip casting techniques. The microstructures are first rep-

licated into polydimethylsiloxane (PDMS) membranes using excimer laser (λ=248 nm) ablated polycarbonate sheets and are subsequently employed as molds in the alumina slip casting process. The developed process can produce microstructured areas up to 120 cm^2, but can be further extended to 3 m^2 and on samples as thick as 10 mm. The drying of the ceramic slurry occurs as a one dimensional process and a linear mass diffusion model developed predicts that the drying times are linearly proportional to the slurry height, PDMS membrane thickness and independent of the microstructured areas. The 3D geometries include tear cavities, micro bowls, conical micro pillars, bone pits and are not limiting. Such microstructured liquid impregnated MPA composite surfaces may also lead to anisotropic wetting and tribological properties if desired.

Keywords : Mesoporous Alumina, Liquid Impregnation, Wetting, Self–Replenishing, Wear–Resistance, Friction, Slip casting, Microstructuring.

Résumé

La fabrication de surfaces omniphobes et résistantes à l'usure est essentielle dans beaucoup de domaines d'applications tels que l'industrie de la peinture, le transport des fluides, les surfaces autonettoyantes, la réduction du frottement sur les coques des bateaux ou encore les textiles anti-taches. Cependant, leur réalisation reste un défi, et pourtant, peu d'efforts sont investis pour résoudre ces problèmes. En effet, les surfaces omniphobes classiques sont intrinsèquement sensibles à l'usure, soit à cause de la perte du matériau non polaire constituant le revêtement, soit à cause de la dégradation de la rugosité de surface pendant l'usure. Ainsi, une approche innovante est nécessaire pour fabriquer de telles surfaces.

Ce travail de recherche se concentre principalement sur la production d'un nouveau composite anti-adhérent et résistant à l'usure, en alumine mésoporeux à liquide d'imprégnation (AMP). Ensuite, une attention toute aussi particulière est portée sur la caractérisation des propriétés de mouillage de tels systèmes après usure. Pour ce faire, différents matériaux d'imprégnation tels que l'eau, l'hexadécane, le dodécane, l'huile Fomblin® et le 3M™ HFE 7200 ont été utilisés sur des matrices d'alumine de densités comprises entre 70 et 99,5%. L'huile Fomblin® a été identifié comme le plus efficace des liquides d'imprégnation. En effet, des comportements anti-adhérents du glissement ont été observés pour l'eau, l'hexadécane, le dodécane, et des peintures à l'eau et à l'huile sur des AMP lubrifiés/imprégnés d'huile Fomblin®.

Par la suite, le coefficient de frottement (CF) et la résistance à l'usure des composites AMP imprégnés d'huile Fomblin® ont été mesurés en fonction de la charge normale appliquée et de la densité de la matrice d'alumine. Une densité optimale d'alumine d'environ 90% a été identifiée comme celle conduisant à un faible CF et une forte résistance à l'usure. Des CF ultra-faibles de 0,025 et de faibles coefficients d'usure de l'ordre de 10^{-8} $mm^3N^{-1}m^{-1}$ ont été mesurés. Le mécanisme d'usure, par abrasion légère, est majoritairement dû aux fractures intergranulaires et/ou à l'abrasion à trois corps.

Enfin, les caractéristiques du mouillage des composites AMP imprégnés d'huile Fomblin® ont été évaluées après usure en utilisant de l'eau et de l'hexadécane. La surface usée des composites perd ses propriétés de non adhésion à l'eau et à l'hexadécane immédiatement après l'usure, et présentent un comportement super hydrophile et partiellement oléophile. Cependant, après un certain temps d'auto-réapprovisionnement/réparation, elles deviennent fortement omniphobes. Les grandes forces capillaires du liquide d'imprégnation avec la matrice polaire d'alumine et sa diffusivité sur la surface de cette dernière sont responsables de cet auto-réapprovisionnement continuel.

Par ailleurs, une forte amélioration de l'efficacité du réapprovisionnement est obtenue lorsque la surface du composite AMP est microstructurée.

Ainsi, un procédé de microstructuration de larges surfaces d'AMP par une technique de réplication et de coulée en barbotine a été développé. Les microstructures sont d'abord répliquées sur des membranes de polydiméthylsiloxane (PDMS) après fabrication de moules en polycarbonate par ablation par laser à excimère (λ=248 nm). Cette membrane de PDMS est ensuite utilisée comme moule lors de la coulée en barbotine de l'alumine. Ce procédé peut produire jusqu'à 120 cm^2 de surfaces microstructurées, et même atteindre 3 m^2, sur des échantillons ayant une épaisseur maximale de 10 mm. Le séchage de la suspension de particules de céramique est un procédé unidimensionnel. Un modèle basé sur la diffusion de masse linéaire prédit que les temps de séchage sont linéairement proportionnels à la hauteur de la suspension des particules et à l'épaisseur de la membrane de PDMS, mais indépendants de l'aire de la surface microstructurée. Les géométries 3D utilisées incluent des cavités en forme de larmes, de micro-sphères, de micro-piliers coniques, de structures osseuses, et d'autres peuvent être imaginées. De telles surfaces microstructurées de composites AMP peuvent permettre un mouillage et des propriétés tribologiques anisotropes, si désiré.

Mots-clefs : Alumine mésoporeux, Liquides d'Imprégnation, Mouillage, Auto-Réapprovisionnement, Résistance à l'Usure, Frottement, Coulée en Barbotine, Microstructuration.

Table of Contents

Acknowledgements ..... **i**

Abstract ..... **iii**

Résumé ..... **v**

Table of Contents ..... **vii**

List of Figures ..... **xi**

List of Tables ..... **xvii**

Nomenclature ..... **xix**

Chapter 1 Introduction **1**

1.1. Problem statement 1

1.2. Idea and hypothesis 2

1.3. Thesis outline 3

Chapter 2 State of the art review **5**

2.1. Classical wetting 5

2.1.1. Anti–sticking behavior 8

2.2. Fundamentals of wetting phenomena 8

2.2.1. Van der Waals forces of attraction 9

2.3. Wetting of porous materials 10

2.4. Mechanical durability studies 11

2.5. Friction and wear 14

2.5.1. Lubricated sliding 15

2.6. Tribological characterizations in alumina 15

Chapter 3 Materials and methods **17**

3.1. Materials used 17

3.2. Processes, experimental procedures 18
3.2.1. PDMS replication 18
3.2.2. Perfluorosilanization 19
3.2.3. Slip casting 19
3.3. Pre–sintering, sintering and densification 20
3.4. Polishing and parallelism procedure 21
3.5. Oxygen plasma treatment 21
3.6. Liquid impregnation 22
3.7. Solid impregnation and hot embossing 24
3.8. Characterizations 26
3.8.1. Centrifugal sedimentation 26
3.8.2. Rheological studies 26
3.8.3. Archimedes principle and density measurements 26
3.8.4. Scanning electron microscopy 27
3.8.5. Digital holographic microscopy 27
3.8.6. Mercury intrusion porosimetry 27
3.8.7. X–Ray diffraction 28
3.8.8. Vickers hardness 28
3.8.9. Laser confocal microscopy 29
3.8.10. Optical profilometry 29
3.8.11. Roughness using Atomic force microscopy 30
3.9. Wetting characterizations 31
3.9.1. Contact angle measurements 31
3.9.2. Liquid menisci in 3 phase systems 32
3.10. Tribological characterizations 32
3.11. Dark field X–Ray imaging 33

Chapter 4 Wetting properties of liquid impregnated mesoporous α–Al_2O_3 composites 35

4.1. Wetting properties of solid impregnated mesoporous α–Al_2O_3 composites 35
4.2. Wetting properties of liquid impregnated mesoporous α–Al_2O_3 composites 36
4.2.1. About the manuscript 36
4.3. Menisci in three phase systems 50
4.3.1. Equilibrium static contact angle measurements 50
4.4. Summary 52

Chapter 5 Tribological characterizations of Fomblin® oil impregnated mesoporous α–Al_2O_3 composites 53

5.1. As–sintered alumina matrices 54
5.1.1. Microstructural characterizations 54
5.1.2. Frictional behavior 56
5.1.3. Wear rate diagram as a function of alumina density 59
5.1.4. Characterization of samples post wear 60
5.2. Polished alumina matrices 62
5.2.1. Microstructural characterizations 62
5.2.2. Frictional behavior 63
5.2.3. Self–mating of Fomblin® lubricated alumina 64
5.2.4. Wear rate diagram versus Vickers hardness 64
5.2.5. Characterization of samples post wear 65
5.2.6. Roughness measurements post wear 66
5.3. Effect of sliding frequency 67
5.4. Effect of Fomblin® oil viscosity 68
5.5. Summary 69

Chapter 6 Self–replenishing and wetting properties post wear tests 71

6.1. Self–replenishing properties 71
6.2. Wetting properties post wear tests 75
6.2.1. About the manuscript 75
6.3. Theoretical prediction of self–healing times 88
6.4. Optimum alumina density 93
6.5. Summary 94

Chapter 7 Fabrication of bulk microstructured mesoporous α–Al_2O_3 samples 95

7.1. Effect of Surface Microstructuring 95
7.2. Preparation of microstructured MPA surfaces 95
7.2.1. About the manuscript 96
7.3. Summary 109

Chapter 8 Conclusions and outlook 111

8.1. Recommendations and outlook 113

Appendix A Wetting and tribological properties of solid impregnated MPA composites 115

A. 1. Eicosane impregnated composites 115
A. 2. Moldflon™ and Zonyl® impregnated composites 116
A. 3. Tribological characterizations of solid impregnated MPA composites 116

Appendix B Supporting information 119

B. 1.Equilibrium SCAs of liquids with flat sapphire with and without employing O_2 plasma treatment 120

B. 2.Open and closed porosity measurements 120

B. 3.Physical properties of materials used for the study 121

B. 4.Optimal parameters for Fomblin® oil infiltration into MPA 121

B. 5.Infiltration, spreading, infiltration+spreading, No infiltration+ no spreading 121

B. 6.Infiltration behavior: Change in width, height and volume of water drop atop non–infiltrated dry MPA sample 122

B. 7.Wetting dynamics of water drop atop O_2 plasma treated Fomblin® impregnated MPA sample 123

B. 8.Fomblin® oil drop atop water impregnated MPA samples 123

B. 9.Infiltration and Spreading behaviors: Change in width, height and volume of water drop atop Fomblin® impregnated and unflooded MPA 124

B. 10. Effect of viscosity on impregnation dynamics 124

B. 11. Surface energies, surface tensions of solids and liquids respectively, and their apolar and polar components 125

Appendix C Supporting Information 127

C.1. As received granulated/agglomerated alumina powder morphology 128

C.2. Particle size distribution and slurry viscosity measurements 128

C.3. Pore size distribution 129

C.4. Laser ablation of polycarbonate sheet and AFM image of DOE structures 130

C.5. Characterization of Sylgard PDMS showing several locations of set of concentric circles 131

C.6. Ceramic and Sylgard PDMS sample pictures showing macro cavity defect and defect free samples 131

C.7. Reynolds number (R_e) calculations 132

C.8. Low magnification image of Switzerland topography on alumina ceramic 133

References 135

Curriculum vitae 145

List of Figures

Figure 1.1. (a) Schematic diagrams showing the loss of low surface energy coating and deformation of microstructures present atop high surface energy material due to wear, (b) schematic diagram showing the deformation of low surface energy microstructures, (c) example of Eicosane coated microstructured alumina exhibiting superhydrophobic behavior prior to wear which lost completely the microstructures due to the wear and hence the superhydrophocity as well..... 2

Figure 1.2. Schematic diagram (not to scale) showing a liquid impregnated bulk mesoporous $\alpha-Al_2O_3$ composite with a stable test liquid droplet atop and a cylindrical counter body to be slid to study the tribological behavior. A zoomed in picture (right) of the composite showing that the impregnating liquid has strong capillary forces due to the mesopores and the surface diffusivity that cause the continuous replenishment of it on the alumina surface. This continuous replenishment causes the anti−sticking behavior towards another class of liquids and good wear−resistance. Also, this continuous replenishment is hypothesized to cause self−healing behavior of these kind of composites..... 3

Figure 2.1. Schematic diagram of the effect of curvature on the energy of the bulk and the surface atoms in a 8−coordinated material. The atoms at different curvatures lead to different number of bonds associated with them and hence leads to the differences in surface energy. The image is adapted from [14]..... 6

Figure 2.2. The advancing and receding contact angles of liquid drop (blue colored) measured are at the front and rear sides of the liquid drop respectively when it starts to slide on a tilted sample. 7

Figure 2.3. (a) Wenzel and (b) Cassie states are schematically presented. In the Wenzel case, the liquid drop completely penetrated the surface protruding cylindrical features while in the Cassie state, the liquid drop is suspended on the asperities provided by the surface protruding cylindrical features. 7

Figure 2.4. (a) Friction coefficient data obtained as number of cycles in a ball−on−flat tribometer, and (b) showing the surface microstructures before and after the corresponding wear tests. The images are reprinted with permission from [63]. Copyright © (2009), American Chemical Society..... 12

Figure 2.5. (a) SEM images of Polypropylene micro−micro hierarchical structures after wear test using 310 kPa normal pressures, (b) SCA and (c) CAH measurements of polypropylene surfaces comprising of different kinds of hierarchical structures reported post wear tests

as a function of normal pressure (kPa). The images are reprinted with permission from [15]. Copyright © (2012), American Chemical Society. 12

Figure 2.6. Compacted discs of Cu metal powders, covered with electolessly deposited (< 5 μm thick) Ag layer and further coated with monolayer of alkanethiol showing the retention of superhydrophobicity after abrasion test with a metal file. The image is reprinted with permission from [71]. Copyright © (2010), American Chemical Society.....13

Figure 2.7. (a) NaOH–PP–PDMS modified PET based textile showing superhydrophobic behavior for dyed water drop which also slides for small sample tilt (inset in a) and (b) the retention of superhydrophobicity after 3000 washing cycles. The image is reprinted with permission from [72]. Copyright © (2014), American Chemical Society.....13

Figure 2.8. Schematic representation of a typical Stribeck curve illustrating the main three regimes in a lubricated sliding contact (adapted from [99,100]).....15

Figure 3.1. (a) Schematic diagram (not to scale) of a conventional slip casting process that can form a variety of shapes resulting in bulk samples. The ceramic alumina slurry (white in color) is poured into open Elastosil silicone molds (red in color) below which contains a filter paper (white in color) atop porous plaster of Paris mold (yellow in color). The plaster of Paris mold sucks the water from the slurry and aids the drying process. The filter paper has 0.2 μm pores and prevents sticking of the slurry and later green body upon drying to the plaster of Paris mold. Macroscopic bending visible in a sintered alumina sample, (b) dominant in bigger sample, (c) relatively less bending in smaller sample. 20

Figure 3.2. (a) Densification plot showing the relative density (%) of 70–99.5 % dense alumina samples as a function of sintering temperature for one step sintering process, and (b) open and closed porosity data in the respective 70, 80, 90, 95, 99.5 % dense samples..21

Figure 3.3. (a) The occurrence of ~70° static contact angle of water atop sapphire sample surface as a function of time prior to employing oxygen plasma treatment.....22

Figure 3.4. (a) High temperature compression setup installed under a hood using hydraulic press and heating systems consisting of heaters entering into blind holes drilled into steel blocks, (b) schematic diagram showing hot embossing of Zonyl® powders (top diagram) and Moldflon® sheet (bottom diagram) into mesoporous alumina sample placed in between two heating steel blocks.....25

Figure 3.5. (a) XRD data of 70, 80 and 90 % dense as–sintered unpolished alumina samples as a function of 2θ(°), (b) average crystallite size (black squares) of 70, 80 and 90 % dense alumina samples calculated using Scherrer equation of full width half maxima of XRD peaks. The average grain size (red dots) obtained from HRSEM images is also plotted for a comparison. 28

Figure 3.6. Laser confocal microscopic images of alumina sample surfaces (a) when de–agglomeration in the slurry is not complete leading to microscopic holes and (b) micro hole free sample surface due to improved de–agglomeration in the slurry.....29

Figure 3.7. (a) A typical convoluted surface profile of a 80 % dense polished MPA sample is presented along with a (b) de–convoluted surface roughness profile.....30

Figure 3.8. (a–b) Typical AFM images of 70 % and 95 % dense, polished MPA samples are presented along with their roughness values. 31

Figure 3.9. (a) Special holder for the counter body to compensate for small flatness issues and showing the normal load and frequency of sliding, (b) schematic diagram representing the geometry and materials for carrying out wear experiments in flat–on–flat condition and (c) picture showing cuboidal and cylindrical shaped α–Al_2O_3 samples sintered to 95 % relative density used for reciprocating sliding tribological characterization studies. 32

Figure 3.10. (a) Dark Field X–Ray Imaging apparatus showing X–Ray source, three gratings, sample transparent to X–Rays covered with Polyimide Kapton tape to prevent evaporation which is also transparent to X–Rays, (b) zoom in of the sample location showing a 70 % dense mesoporous alumina sample dipped into plastic container with water, (c) top view of the plastic container showing that the liquid surfaces are covered with Polyimide tape to also prevent evaporation. 33

Figure 4.1. The wetting behavior of water drops atop (a) Zonyl® impregnated 70 % dense MPA composite surface, (b–c) Moldflon™ impregnated 70 and 90 % dense MPA composite surfaces respectively. All the samples possess ~5–6 mm thickness. 35

Figure 4.2. Equilibrium liquid menisci at convex and concave curvatures of sapphire capillary for (a) Fomblin® oil–Hexadecane liquids, (b) Hexadecane–water liquids, (c) Fomblin® oil–water liquids. 51

Figure 5.1. HRSEM images of as–sintered (a) 70 % dense, (b) 90 % dense, (c) 94 % dense and (d) 99.5 % dense samples, respectively. The microstructure of 80 % dense sample is similar to 70 % dense sample. The variable T_s is the sintering temperature. 55

Figure 5.2. Average grain sizes of as–sintered alumina samples obtained from statistical treatment of SE–SEM images presented as a function of alumina density. 55

Figure 5.3. Friction coefficient data presented for two different Fomblin® impregnated 90 % dense as–sintered MPA composites plotted as the apparent normal load increased from 10 to 100 N (see right axis). The black curve presents the FC data measured for an increase in the normal load while the red curve presents the data obtained for another sample measured with a decrease in the normal load in steps of 10 N. 57

Figure 5.4. Measured friction coefficient data plotted for Fomblin® impregnated/lubricated 80, 90, 95, 99.5 % dense alumina composites along with that of commercially obtained monocrystalline (1211 plane) sapphire as a function of sliding time (min) for a change in the apparent normal loads from 10 N to 220 N (corresponding pressures of 0.2–6 MPa). 58

Figure 5.5. The measured roughness (S_a) values obtained by laser confocal microscopy in the as–sintered alumina samples before and after the wear experiments. 58

Figure 5.6. Necking density of grains for 70 and 90 % dense as–sintered alumina samples. 58

Figure 5.7. The $\log\text{arithm}_{10}$ of the estimated wear coeffcients in Fomblin® impregnated/lubricated as–sintered alumina samples plotted as a function of alumina matrix density. 60

Figure 5.8. SEM images of 70 % and 90 % dense MPA samples and their corresponding counter bodies post wear tests. 61

Figure 5.9. Representative HRSEM images of polished alumina samples having (a) 70–90 % density, (b–c) 94 % density showing non porous surfaces, (d) 99.5 % density sample showing non porous but scratches due to polishing respectively. 62

Figure 5.10. Measured average roughness (R_a) values using white light profilometer of polished alumina samples plotted as a function of alumina density. The roughness of commercially obtained sapphire is also presented for comparison.....63

Figure 5.11. Measured friction coefficient data plotted for Fomblin® impregnated/lubricated 70, 80, 90, 95 % dense polished alumina composites along with that of commercially obtained monocrystalline (1211 plane) sapphire as a function of sliding time (min) for a change in apparent normal load from 10 to 220 N (0.2–6 MPa). 63

Figure 5.12. Measured friction coefficient data plotted as a function of sliding time (min) when the normal apparent load changes from 10 to 220 N (0.2 to 6 MPa) for 99.5 % dry self–mating pair, 99. 5 % Fomblin® lubricated with dry counter body, 95 % and 99. 5 % dense Fomblin® lubricated self–mating pairs. 64

Figure 5.13. The logarithm_{10} of estimated wear coefficients in Fomblin® impregnated/lubricated alumina composites plotted as a function of alumina matrix density along with their corresponding Vickers hardness ($HV_{0.1}$) values. 65

Figure 5.14. HRSEM images post step load friction experiments of Fomblin® impregnated MPA samples for (a) 95 % alumina density, (b) 99.5 % alumina density.....66

Figure 5.15. The measured average roughness (R_a) values of (a) 70–99.5 % dense alumina samples and sapphire before and after wear experiments (step load experiments, Figure 5.11), (b) corresponding dry non impregnated alumina and diamond counter bodies are presented as a function of alumina density. 67

Figure 5.16. Friction coefficient variation of Fomblin® lubricated 95 % dense polished alumina slid against 95 % dense dry non–impregnated sample by changing the sliding frequency and apparent normal loads. The applied sliding frequencies used are 1, 6, 12, 18, 24 Hz (correspond to 0.008, 0.048, 0.096, 0.144, 0.192 m s^{-1} average sliding speeds) and the normal laods are 50, 100 and 200 N. 68

Figure 5.17. Friction coefficient data of Fomblin® impregnated 90 % dense as–sintered alumina slid against 90 % dense dry non–impregnated sample for sliding frequencies of 6 Hz and 24 Hz. The normal load continuously increased from 10 N to 200 N in the steps of 10 N. 68

Figure 5.18. Friction coefficient values plotted for Fomblin® impregnated 90 % dense as–sintered alumina samples by varying the normal load for two different viscosities of the Fomblin® oil. The temperature of the block holding the alumina composite were held at constant temperatures of 30 °C and 100 °C respectively thereby influencing the viscosity of Fomblin® oil. The viscosity of Fomblin® oil at 30 °C and 100 °C are 152 cSt and 10 cSt respectively. 69

Figure 6.1. The temporal dark field images of the capillary uptake of (a) water and (b) Fomblin® oil by 70 % dense mesoporous alumina samples covered by all the four lateral surfaces with a Polyimide Kapton tape to prevent evaporation. Both the samples in (a) and (b) have same dimensions of 20×10×2.78 (in mm). 72

Figure 6.2. The experimentally observed capillary height rise (in mm) of (a) water and (b) Fomblin® oil liquids in 70 % dense MPA sample obtained from statistical treatment of X–Ray dark field images are plotted as a function of time. The theoretically predicted curves employing Washburn equation are superimposed in both the cases for comparison with the experimental values. 75

Figure 6.3. A schematic diagram presenting the different stages of self–replenishment process in a LIMPA composite is shown here. In stage 1, the capillarity of impregnating liquid (blue colored) occurs until all the pore network is filled up with the impregnating liquid. At the end of stage 1, stage 2 begins due to the initiation of the surface diffusivity process. In stage 3, heterogeneous LIMPA surfaces may exist, containing both completely replenished regions and dry alumina regions. In stage 4, the process is complete and there is no dry alumina surface. The evaporation process occurs during all the stages, in parallel and counteracting the other two processes. 88

Figure 6.4. (a) The surface diffusivity of the Fomblin® oil from mesoporous reservoirs onto less permeable debris compacted regions is shown by the yellow colored arrows in 80 % dense polished MPA surface. (b) The largest diffusion length (x) that the Fomblin® oil may have to travel to replenish dry alumina surfaces is shown and is ~2 μm. 90

Figure 6.5. HRSEM pictures of the worn surface of 70 % dense Fomblin® impregnated MPA composite sample (a) showing the maximum diffusion length x of ~ 5 μm and (b) comprising debris particles that have relatively bigger diffusion lengths due to the three dimensional distances to be travelled. 91

Figure 6.6. (a–b) The mass flux ($m^3.m^{-2}.s^{-1}$) of capillarity and surface diffusivity process are plotted as a function of time (in h). 92

Figure 6.7. The dimensionless concentration (c/c_o) profiles plotted as a function of time for different values of x = 500 nm, 1 μm, 2μm, 5 μm and 20 μm respectively. 93

Figure 8.1.(a–b) Low and high magnification SE–SEM images of 80 % dense MPA sample that was milled with Ar ions, enabling debris compacted regions free surfaces. 113

List of Tables

Table 2.1. The contributions of Van der Waals forces in the materials systems used for the current study. 10

Table 3.1. Physical properties of the liquids used for impregnation process 22

Table 3.2. Measured equilibrium static contact angles of liquids with flat sapphire 23

Table 3.3. Optimization of Fomblin® oil high temperature impregnation for MPA samples 23

Table 3.4. Physical properties of Zonyl® and Moldflon™ materials 24

Table 3.5. Summary of parameters, their definitions and the values in the Equation (3.1) 25

Table 4.1. Molecular diameter, calculated number of molecules in 30, 50 nm pores respectively . 50

Table 4.2. Equilibrium static contact angle (SCA), advancing contact angle (ACA) and receding contact angle (RCA) in three phase systems 51

Table 6.1. List of parameters in Equation (6.3) by performing regression analysis of experimental data 73

Table 6.2. Estimate fraction of coverage of Fomblin® oil in 70–90 % dense MPA polished matrices 93

Nomenclature

A_s	Specific surface area of alumina particles (m^2 kg^{-1})
D_p	Diameter of alumina particle in the slurry (nm)
DS	Product of diffusivity of water in PDMS and solubility of water vapor in PDMS ($cm^3_{water}(STP)cm^{-3}_{PDMS}(cmHg)^{-1}m^2s^{-1}$)
D_S	Surface diffusivity coefficient (m^2 s^{-1})
d_{v50}	Diameter of 50 vol % of particles (nm)
ΔE_{imp}	Impregnation free energy (kJ m^{-2})
f_i	Area solid fraction of i with liquid drop base
F_f	Frictional force (N)
F_N	Normal load (N)
h_{slurry}	Height of alumina slurry (mm)
ΔH_{vap}	Enthalpy of vaporization (kJ kg^{-1})
H or $HV_{0.1}$	Vickers hardness at 0.1 kgf normal load
K	Permeability (m^2)
K´	Wear coefficient (mm^3 m^{-1} N^{-1})
L	Impregnation depth (mm)
L_{cap}	Capillary length of water in slurry (m)
LW	Lifshitz–Van der Waals
P_w	Saturation pressure of liquid at drying temperature (Pa)
P_a	Vapor pressure of liquid for environment temperature and humidity (Pa) or applied normal pressure (Pa)
ΔP_c	Capillary pressure at embossing temperature
ΔP_{atm}	Atmospheric pressure
Q	Total wear (mm^3 m^{-1})
r_o	Effective pore radius (nm)
r or r_w	Wenzel roughness parameter
R_a	Average profile roughness (nm)
R_e	Reynolds number
R_1	Capillary rate in the alumina slurry (m^3 m^{-2} s^{-1})
R_2	Evaporation rate (m^3 m^{-2} s^{-1})
R_3	Permeation rate of water through PDMS membrane (m^3 m^{-2} s^{-1})
r_p/r_h	Pore/hydraulic radius (nm)
S	Spreading parameter of liquid
S_a	Average area roughness (nm or μm)
S_{dr}	Increment of 3D surface area relative to 2D projected area
SSA_{pore}	Specific surface area of pores (m^2 g^{-1})

t	Time (s)
T_m	Melting point (°C)
u	Air velocity (m s^{-1})
$\dot{V}_1$	Capillary rate of liquid in porous media (m^3 m^2 s^{-1})
$\dot{V}_2$	Flux rate due to surface diffusivity (m^3 m^2 s^{-1})
$\dot{V}_3$	Evaporation rate (m^3 m^2 s^{-1})
V_{pore}	Porosity fraction
ΔV_{water}	Volume loss of water (m^3)
W_a	Average profile waviness (nm)
w	PDMS membrane thickness (mm)
w_f	Fomblin® oil film thickness (μm)

Greek Symbols

θ_{eq}, θ_{SCA}	Equilibrium static contact angle (°)
θ_{CAH}	Contact angle hysteresis (°)
θ_w	Equilibrium static contact angle in Wenzel configuration (°)
θ_{CB}	Equilibrium static contact angle in Cassie configuration (°)
θ_{ACA}	Advancing contact angle (°)
θ_{RCA}	Receding contact angle (°)
θ_{flat}	Equilibrium static contact angle of flat surface (°)
$\theta_{is}(a)$	Equilibrium static contact angle of impregnating liquid (i) with solid (s) in air (a) media (°)
$\theta_{is}(t)$	Equilibrium static contact angle of impregnating liquid (i) with solid (s) in test (t) liquid media (°)
α	Sample tilt (°)
ϕ	Solid fraction
ρ_p	Density of alumina particle (kg m^{-3})
ρ_l	Density of liquid (kg m^{-3})
ρ_{ps}	Density of porous solid (kg m^{-3})
ρ_{slurry}	Density of alumina slurry (kg m^{-3})
η_l	Viscosity of liquid (kg m^{-1} s^{-1})
μ	Water permeability in alumina slurry or Friction coefficient
γ_{la}	Surface tension of liquid (l) at air (a) interface (mN m^{-1})
γ_{sl}	Interfacial surface tension of solid (s) and liquid (l) (mN m^{-1})
γ_{12}	Interfacial surface tension of two components 1 and 2 (mN m^{-1})
γ_{sa} or γ_s	Surface energy of solid (mJ m^{-2})
γ^+	Electron acceptor component of surface tension
γ^-	Electron donor component of surface tension
γ^{LW}	Lifshitz–Van der Waals component of surface tension
λ	Wavelength of krF nanosecond laser (nm)
τ	Tortuosity of porous media

Acronyms

ACA	Advancing Contact Angle
AFM	Atomic Force Microscopy
BET	Brunauer, Emmet and Teller
BP	Boiling Point
CA	Contact Angle
CAH	Contact Angle Hysteresis
CP	Closed Porosity
CPS	Centrifugal Particle Size
CVD	Chemical Vapor Deposition
CNT	Carbon Nano Tubes
DOE	Diffractive Optical Elements
DHM	Digital Holographic Microscope
EBSD	Electron Back Scattered Diffraction
FC	Friction coefficient
FWHM	Full width at half maxima
HRSEM	High Resolution Scanning Electron Microscopy
MPA	Mesoporous Alumina
MP	Melting point
MW	Molecular weight
OP	Open Porosity
PAA	Polyacrylic Acid
PC	Polycarbonate
PDMS	Polydimethylsiloxane
PET	Polyethylene terephthalate
PTFE	Polytetrafluoroethylene
PVC	Polyvinylchloride
RCA	Receding Contact Angle
RH	Relative Humidity
SCA	Static Contact Angle
SE	Secondary Electron
TP	Total Porosity
XRD	X–Ray Diffraction

Chapter 1
Introduction

The ´wetting of surfaces´ is an ancient field, the first report dates back to 1800´s [1]. Since then, this field has attracted attention by the scientific and technical audience. In particular, this field has become a hot field in the last few decades after the discovery of the famous ´Lotus effect´ [2,3]. The ´Lotus effect´ or commonly referred to as self–cleaning effect, describes the water repellency of the Lotuf leaf due to the presence of surface waxy layer and hierarchical micro–nano surface structures. The dirt particles are picked up by the rolling water drop over the Lotus leaf, thus leading to cleaning of the surfaces. The two parameters: surface chemistry and surface roughness play a key role in determining the wetting response of a material surface [1,4,5]. There has been a large number of scientific articles produced in this field, mimicking natural plant leaf, bird´s feather, flower petal surfaces etc.[6–11] to be able to fabricate omniphobic surfaces, by employing the principle of ´Lotus effect´. Understanding the wetting phenomena plays a crucial role in several real life applications. For example, ice–repellent surfaces, oil– repellent surfaces, water–repellent surfaces are used in everyday applications such as in skiing jackets, cooking pans, cell phone protective cases and others.

The main idea to produce omniphobic surfaces is to choose the appropriate surface roughness (micro, nano, hierarchical) and the surface chemistry (low surface energy/apolar materials). Conventionally, there are two ways of achieving omniphobic surfaces: (a) coating of low surface energy material atop surface roughened high surface energy material and (b) tuning the surface topography of low surface energy material.

1.1. Problem statement

It was demonstrated that very small differences in the geometrical parameters of the roughness elements change the wetting response of the material. For example, it was shown in perfluorosilanized Si substrates, containing flat top cylindrical micropillars (diameter = 20 μm, height = 40 μm), that a change in the ratio of pitch to diameter of micropillars from 7 to 9 changes the static contact angle from 168° to 100° [12]. Also, the perimeter of the pillar top has been shown to have

a strong influence on the static contact angles [12]. Thus, it is very clear from the literature studies that the accurate shape, curvature and geometrical dimensions of the roughness elements can significantly alter the wetting response. Hence, any kind of deformation in the surface micro features may totally alter the wetting behavior.

When a surface roughened high energy material, coated with a low energy material undergoes mechanical deformation, scratch or wear tests, the roughness elements are deformed, damaged or even partially or completely removed in addition to the loss of coating material (Figure 1.1a). Also, the normal load bearing capacity of these kind of surface microstructured samples is relatively low due to the low asperity contact area. Similarly, when the surface roughened low energy material is worn, the roughness elements loose their shape and size (Figure 1.1b) and cannot withstand high normal pressure thus limiting the wear resistance in highly loaded applications. As an example, Eicosane coated 70 % dense mesoporous alumina sample surface containing protruding conical microfeatures exhibited superhydrophobic behavior and the water drops rolled off at very small sample tilts (<5°) (Figure 1.1c). However, those conical structures were completely broken due to wear and micro debris was formed. Some regions do not have any traces of microfeatures post wear thus almost turning into flat regions (Figure 1.1c). The worn region lost Eicosane coating in addition to the loss of surface microfeatures and hence lost the superhydrophobic effect.

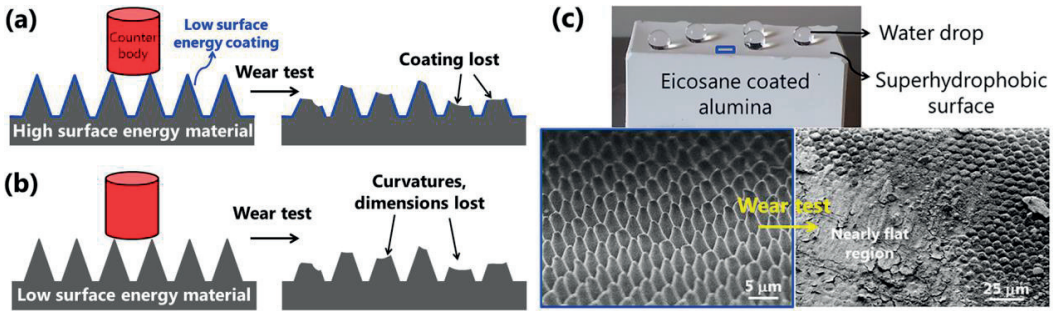

Figure 1.1. (a) Schematic diagrams showing the loss of low surface energy coating and deformation of microstructures present atop high surface energy material due to wear, (b) schematic diagram showing the deformation of low surface energy microstructures, (c) example of Eicosane coated microstructured alumina exhibiting superhydrophobic behavior prior to wear which lost completely the microstructures due to the wear and hence the superhydrophocity as well.

1.2. Idea and hypothesis

The protruding surface roughness elements were shown to be detrimental to the wear–resistance and retention of wetting characteristics post wear (Section 1.1). Hence, the conventional approach of preparing superhydrophobic surfaces containing surface roughness is intrinsically not preferred to exhibit mechanical durability or the wear/scratch resistance. Here, we propose to use liquid impregnated α–alumina matrix composites for obtaining high wear–resistance, low friction coefficient and anti–sticking behavior towards other immiscible liquids (referred to as test liquids). It is also hypothesized to have self–replenishing of the impregnating liquid due to the strong capillarity (pore sizes ~30–50 nm) and the surface diffusivity of the liquid with the solid

substrate, counteracted or aided by the evaporation process. Such continuous replenishment aids in a continuous supply of the lubricant during tribological studies and to further retain the wetting characteristics post wear. Figure 1.2 shows a schematic diagram representing the liquid impregnated mesoporous alumina composite, a test liquid drop (blue in color), immiscible with the impregnating liquid (green in color) and a cylindrical counter body (red in color). The alumina matrix is characterized by connected open porosity as the matrix density ranged from 70 to 90 % relative densities.

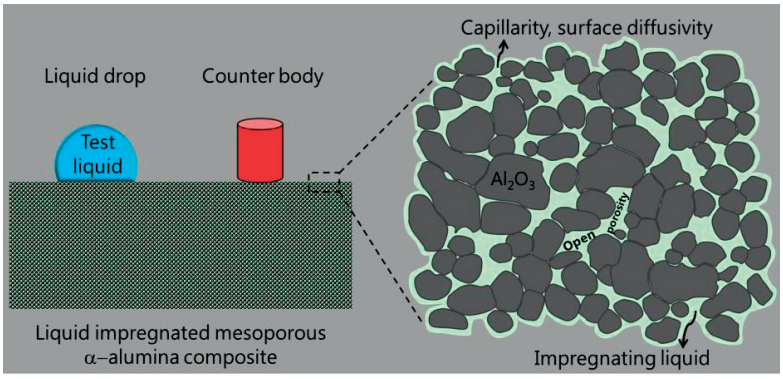

Figure 1.2. Schematic diagram (not to scale) showing a liquid impregnated bulk mesoporous α–Al_2O_3 composite with a stable test liquid droplet atop and a cylindrical counter body to be slid to study the tribological behavior. A zoomed in picture (right) of the composite showing that the impregnating liquid has strong capillary forces due to the mesopores and the surface diffusivity that cause the continuous replenishment of it on the alumina surface. This continuous replenishment causes the anti–sticking behavior towards another class of liquids and good wear–resistance. Also, this continuous replenishment is hypothesized to cause self–healing behavior of these kind of composites.

The wear resistant, anti–sticking surfaces may find an application in the paint industries. The excess oil based and water based paints flowing out of the roller periphery during the printing is usually drained through the metallic/polymer drain channels. After the completion of one printing cycle with one type of paint (water based or oil based), the other type needs to be used in the printing units (die, rollers etc.). Often, the dried paints sticking to the metallic/polymer drain channels are removed by scratching with a screw driver, thereby increasing the roughness of the metallic/polymer drain channels, which in turn increases the sticking efficiency of the paints to channel surfaces and is undesirable. Such drain channels need to have a coating which is oil and water repellent and is also wear–resistant. It is much more desirable if the surfaces can self–replenish the anti–sticking properties after wear. Such coatings will enable easy cleaning after usage of water/oil based paints. Other applications may be in cooking non–sticky pans or in organic electronics.

1.3. Thesis outline

The current dissertation started with Chapter 1 which explains briefly the pertinent scientific problem, the objectives of this PhD and the approach adopted to achieve the objectives. Further, this chapter briefly describes the thesis outline.

Chapter 2 describes the history and the background works relevant to the current study.

Chapter 3 describes in detail, the materials and experimental procedures used in the current study. The procedures include reproducible sample preparation through conventional slip casting, sintering followed by polishing the samples and liquid impregnation. All the microstructural characterizations, wetting and tribological characterization details are also described.

In Chapter 4, the wetting behaviors of solid and liquid impregnated mesoporous alpha–alumina (later referred to as LIMPA) composites are presented and discussed. The three main behaviors spreading, infiltration and anti–sticking sliding behaviors, respectively, were observed in LIMPA composites for different combinations of test and impregnating liquids. Also, the influence of oxygen plasma treatment on the wetting dynamics in LIMPA composites is presented and discussed. The relative order of Van der Waals forces of attraction between the liquid (test or impregnating) and alumina matrix can be obtained by the aforementioned wetting observations. Such observations are further supported by the liquid contact angles in three phase systems consisting of sapphire capillary which forms an interesting section of this chapter. These experimental observations are in good agreement with the van Oss–Choudary–Good equation. From this study, an optimum impregnating liquid: Fomblin® oil was picked up for carrying out further tribological and wetting characterizations.

In Chapter 5, the tribological studies of 70–99.5 % dense Fomblin® impregnated mesoporous alumina composites are presented and discussed.

Chapter 6 presents the sliding behaviors of water and oil based acrylic based paints, water, Hexadecane drops atop Fomblin® oil impregnated mesoporous alumina (referred to as MPA). Further and more importantly, the wetting characterizations post wear studies are presented. Additionally, the self–replenishing/healing characteristics of these composites post wear tests are demonstrated. A theoretical model was developed to estimate the self–replenishing time to achieve sufficient impregnating liquid coverage atop dry alumina surfaces, which further aids in retaining the wetting characteristics post wear. It was then suggested the use of surface microstructuring the MPA surfaces to enhance the self–replenishing efficiency and improve the tribological properties.

In Chapter 7, large area, ceramic surface microstructuring through replication techniques during the slip casting process using microstructured Polydimethylsiloxane (PDMS) membranes is presented. The developed process has the ability to produce microstructured mesoporous alumina bulk samples, with defect free and a simple theoretical model was developed to predict the drying behavior of the ceramic slurry.

In Chapter 8, conclusions are presented and recommendations of the future work are suggested.

The appendix section comprises of three sections: (A) preliminary wetting and tribological characterization of solid impregnated MPA composites, (B–C) the supporting information of the respective peer reviewed/to be submitted journal articles from Chapters 4 and 7 respectively.

Chapter 2
State of the art review

2.1. Classical wetting

The wetting behavior of surfaces is determined just by the surface chemistry and independent of the bulk material properties. Zisman et al., [13] demonstrated that only a few surface monolayers (~20 Å thick) are sufficient to change the wetting response of a material. The wetting behavior is surface–liquid pair dependent and hence is not an intrinsic property of a material.

The wetting behavior of surfaces is characterized by an equilibrium static contact angle (SCA or θ_{eq}), dynamic contact angles, contact angle hysteresis (CAH or $\Delta\theta_{CAH}$) and roll off angles (α), all of which will be defined as follows. In general, bigger SCAs, smaller CAH and smaller roll off angles indicate low wettability and vice versa. A surface is usually termed as superhydrophilic if SCA of water is 0^o, hydrophilic or partially wetting if 0^o<SCA<90^o, hydrophobic when SCA>90^o, and superhydrophobic when SCA>150^o with low CAH (typically ≤ 10°) respectively. The surface which is both hydrophobic and oleophobic is referred to as omniphobic surface.

Mathematically, SCA of a liquid (l) on an atomically flat, homogeneous and rigid surface (s) was described by famous Thomas Young's Equation (2.1) as reported in 1805 [1].

$$cos\theta_{eq} = \frac{\gamma_{sa} - \gamma_{sl}}{\gamma_{la}} \tag{2.1}$$

where γ_{sa}, γ_{sl}, γ_{la} are the surface energy of solid in air (a) medium, interfacial surface tension of solid–liquid and interfacial surface tension of liquid–air respectively, the latter is commonly referred to as the surface tension of a liquid. On a fundamental level, solid surface energy depends on the molecular bond strength and molecular co–ordination number of molecules or atoms present on the surface, while liquid surface tension represents cohesive forces within the liquid such as Van der Waals forces, hydrogen bonding or electrostatic forces. Finally, the interfacial surface tension (γ_{sl}) depends on the interactions between the solid surface and the liquid which can again be strong electrostatic forces such as ion–ion interactions, but also weak electrodynamic forces such as Van der Waals forces and hydrogen bonding.

It is evident from the Equation (2.1) that higher contact angles (θ_{eq}) are obtained for surfaces comprising smaller surface energies and vice versa. Secondly, higher liquid surface tension results in higher contact angles for a same solid and comparable interfacial tension and vice versa. Finally, higher positive interfacial tension (γ_{sl}) values (corresponding to weak solid–liquid interactions) results in higher contact angles and vice versa. Furthermore, the surface energy of a material strongly depends on its curvature. Figure 2.1 shows a schematic diagram of atoms in a 8–coordinated material possessing a different number of bonds that are located at different curvatures (positive, flat and negative) thus leading to different surface energies. For example, the atom A at positive curvature has only 3 out of 8 bonds while atom B at flat region have 5 out of 8 bonds and atom C has 7 out of 8 bonds respectively. Thus, the order of the surface energies is atom A > atom B > atom C.

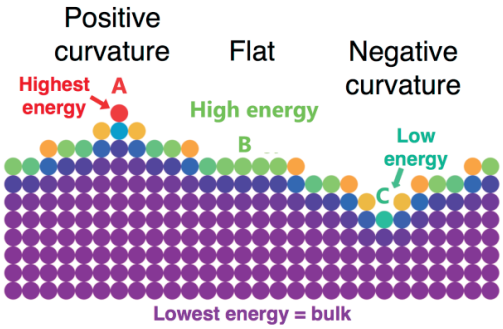

Figure 2.1. Schematic diagram of the effect of curvature on the energy of the bulk and the surface atoms in a 8–coordinated material. The atoms at different curvatures lead to different number of bonds associated with them and hence leads to the differences in surface energy. The image is adapted from [14].

The aforementioned curvature effect on the solid surface energy is a fundamental reason for the changes in the wetting behaviors of surfaces associated with change in surface roughness. For example, in Figure 2.1, the region close to atom A can be viewed as a protruding conical surface micropillar while region near the atom C can be viewed as a microhole.

There are numerous articles in the wetting field reporting the usage of protruding (positive curvature) surface micro or nano features responsible for suspending the liquid drops atop [2,12,15–23]. On the contrary, macro/micro/nano holes in the material was demonstrated to enhance the wettability of surfaces [19]. Such behaviors can be ascribed to minimization of total free energy of the solid–liquid system, thus, the wetting of highest energy regions (pillars) occurs first, followed by high energy regions (flat) and followed by low energy regions (holes). This can also explain the relative dynamics of infiltration and spreading of liquids in porous materials.

The dynamic contact angles: advancing (ACA or θ_{ACA}) and receding (RCA or θ_{RCA}) contact angles can be measured by tilting the solid substrate to an angle (α) where the liquid drop starts sliding, with the front and rear sides of the liquid drop exhibiting the advancing and receding contact angles and was proposed by McDougall and Ockrent [24] respectively (see Figure 2.2). The difference between the advancing and receding contact angles is called contact angle hysteresis ($\Delta\theta_{CAH} = \theta_{adv} - \theta_{rec}$).

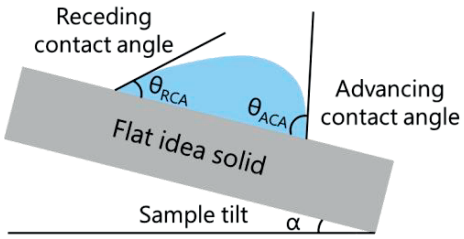

Figure 2.2. The advancing and receding contact angles of liquid drop (blue colored) measured are at the front and rear sides of the liquid drop respectively when it starts to slide on a tilted sample.

The liquid drop takes two configurations atop a roughened solid substrate. They are described as Wenzel and Cassie states and are depicted in Figure 2.3. Wenzel and Cassie theories were proposed by Robert Wenzel and Cassie–Baxter in 1936 and 1944, respectively [25,26]. When the liquid drop completely wets the underlying roughness elements forming a two phase solid–liquid interface, it is referred to as Wenzel state (Figure 2.3a) and the equilibrium SCA (θ_w) is mathematically described by the Equation (2.2) [25].

When the liquid drop lies on a heterogeneous surface, comprising of two different surface chemistries (1 and 2) and surface roughness factors, generalized Cassie–Baxter Equation (2.3) [26] describes the contact angle (θ_{CB}) adapted. If one of the two regions is air, then the liquid drop is suspended on the roughness elements forming a composite interface which consists of liquid–air interface and liquid–solid interface (Figure 2.3b). In such a case, Equation (2.3) is adapted to Equation (2.4) to mathematically describe the Cassie SCA (θ_{CB}).

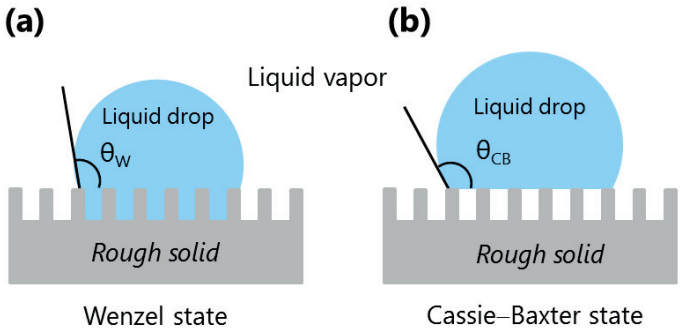

Figure 2.3. (a) Wenzel and (b) Cassie states are schematically presented. In the Wenzel case, the liquid drop completely penetrated the surface protruding cylindrical features while in the Cassie state, the liquid drop is suspended on the asperities provided by the surface protruding cylindrical features.

$$cos\theta_w = rcos\theta_{flat} \tag{2.2}$$

$$cos\theta_{CB} = f_1 cos\theta_1 + f_2 cos\theta_2 \tag{2.3}$$

$$cos\theta_{CB} = r_f f cos\theta_{flat} + f - 1 \tag{2.4}$$

where θ_{flat}, r, f_i are contact angle on a idealized flat surface, Wenzel roughness and solid–liquid area fraction, respectively, and θ_1, θ_2 represent the SCAs on regions 1 and 2. The Wenzel

roughness (r or r_w) is defined as the ratio of the real area of solid in contact with the liquid to the solid–liquid projected area [27].

The liquid drops in Cassie state can easily roll off the surface while in the Wenzel state, they experience pinning forces from the solid due to the penetration of liquid into the asperities thus preventing the liquid drops to easily roll off. In the latter case (Figure 2.3b), the pinning forces are due to structural heterogeneity, however, they can also result from chemical heterogeneity [26,28]. During rolling, the liquid drops can take away the dust particles that are physically attached to the surfaces, this effect is termed as "self–cleaning effect". Such phenomenon is commonly known as Lotus effect [2,3].

There have been various types of surface topographies that were investigated to achieve superhydrophobicity: fractal surfaces [18,29,30], microstructured pillars [12,19], nanostructured pillars [27], nanofibers [31], nanotubes [21] etc. either randomly [31] or regularly distributed [27]. The surface micro or nanofeatures are majorly obtained by conventional photolithography [12,19], chemical etching techniques [32,33] and recently by laser ablation [34–39] etc. However, these techniques are limited in fabrication areas, shapes and curvatures and are often expensive. Replication and molding techniques might be a promising solution.

2.1.1. Anti–sticking behavior

It was a common notion until almost a decade ago to believe that self–cleaning effect can only be achieved with superhydrophobicity [2,20,40–46]. However, in the recent past, another type of self–cleaning effect was demonstrated with superhydrophilic substrates based on photocatalytically active oxidizing TiO_2 [47,48]. If the liquid drops, irrespective of their SCAs can slide on the tilted surfaces without being pinned, then the liquid drops have the ability to self–clean the surfaces and exhibit anti–sticking behavior. In the current study, it will be shown that the liquid drops (water, Hexadecane) and acrylic based paint drops exhibit SCAs < 90° atop Fomblin® impregnated mesoporous alumina composite surfaces (Chapter 4 and Chapter 6), but exhibit anti–sticking and even sliding behaviors for small sample tilts.

2.2. Fundamentals of wetting phenomena

In general, most commercial polymers possess lower polar components of surface energy as compared to ceramics [49] (refer Section B. 11, Appendix B). For example, α–Al_2O_3 ceramic having a surface energy of 44.8 mJ m^{-2} with polar and apolar components of $\gamma^+ = 0.004$ mJ m^{-2}, $\gamma^- = 80.5$ mJ m^{-2} and $\gamma^{LW} = 43.7$ mJ m^{-2} respectively [49]. However, polyvinylchloride (PVC) possessing a similar total surface energy of 43.8 mJ m^{-2} has polar and apolar components of $\gamma^+ = 0.04$ mJ m^{-2}, $\gamma^- = 3.5$ mJ m^{-2} and $\gamma^{LW} = 43$ mJ m^{-2} (LW refers to Lifshitz–Van der Waals component) respectively [49], indicating that the polar contribution to the Van der Waals forces in alumina are significantly higher than that of PVC. Such higher polar contributions to the Van der Waals attrac-

tive forces can cause omniphilicity of ceramic surfaces, which is also the reason for relatively higher surface contamination of ceramics as compared to polymers. Thus, it is important to employ very careful cleaning procedures to obtain the desired surface chemistry. Often, chemical and plasma treatments such as chromic acid exposure [49], Ar plasma [50] and O_2 plasma [51] are employed to remove hydrocarbon contamination, obtained from the environment. The O_2 plasma cleaning was employed to clean α–Al_2O_3 ceramic surfaces in the current study and is presented in Section 3.5, Chapter 3. The fundamental physics underlying the Van der Waals attractive forces is the presence of molecular dipole moments and polarizability and are briefly explained in Section 2.2.1.

2.2.1. Van der Waals forces of attraction

The Van der Waals forces of attraction between two molecules or surfaces can be of three types: (a) Dispersion or London forces, (b) Debye forces and (c) Keesom forces [52]. London forces arise from the transient dipoles that all molecules possess as a result of fluctuations in the instantaneous positions of electrons. These forces are also termed as induced dipole–induced dipole interactions. Debye forces referred to as dipole–induced dipole interactions and arise from a permanent dipole and an induced dipole in a partner molecule or object. The polarizability of the induced dipole strongly influences the strength of the Debye forces. Keesom forces are a result of a permanent dipole interacting with another permanent dipole. In addition to weak Van der Waals forces, hydrogen bonding can also exist for hydrogen atom associated with one of the following highly electronegative atoms: N, O and F. It was proposed that the total Van der Waals attractive forces between two molecules (1 & 2) are additive in nature as described by Equation (2.5) [49]. Hence, van Oss–Choudary–Good developed Equations (2.6)–(2.7) [49] to predict the apolar or Lifshitz–Van der Waals (LW) and polar components (AB) of interfacial interactions. The polar component comprises of all electron donor components (γ^-), electron acceptor components (γ^+) and Lewis acid–base interaction component and designated by superscript AB.

$$\gamma_{12} = \gamma_{12}^{LW} + \gamma_{12}^{AB} \tag{2.5}$$

$$\gamma_{12}^{LW} = \left(\sqrt{\gamma_1^{LW}} - \sqrt{\gamma_2^{LW}}\right)^2 \tag{2.6}$$

$$\gamma_{12}^{AB} = 2\left(\sqrt{\gamma_1^+\gamma_1^-} + \sqrt{\gamma_2^+\gamma_2^-} - \sqrt{\gamma_1^+\gamma_2^-} - \sqrt{\gamma_1^-\gamma_2^+}\right) \tag{2.7}$$

In Equation (2.7), if $\sqrt{\gamma_1^+\gamma_1^-} + \sqrt{\gamma_2^+\gamma_2^-} < \sqrt{\gamma_1^+\gamma_2^-} + \sqrt{\gamma_1^-\gamma_2^+}$, then $\gamma_{12}^{AB} < 0$. Further, if γ_{12}^{AB} is more negative than γ_{12}^{LW} in Equation (2.5), then γ_{12} can be negative. Similarly, γ_{12} can be also positive or zero. Negative values of γ_{12} imply that the adhesive electrostatic forces between the components 1 and 2 ($\sqrt{\gamma_1^+\gamma_2^-} + \sqrt{\gamma_1^-\gamma_2^+}$) are bigger than the cohesive electrostatic forces in each of the components ($\sqrt{\gamma_1^+\gamma_1^-} + \sqrt{\gamma_2^+\gamma_2^-}$). A zero value of γ_{12} is also possible and demonstrates that

the electrostatic forces of attraction (γ_{12}^{AB}) between the components 1 and 2 are counteracted by apolar (γ_{12}^{LW}) Van der Waals forces.

The decreasing order of molecular dipole moments in materials of the current study are 3M™ HFE 7200 (2.5 Debye [53] or 3.56 Debye [54]) > water (1.85 Debye) [52] > Fomblin® oil (–NA–) > Hexadecane (0.06 Debye) (data sheet of company). The decreasing order of polarizability in the aforementioned materials is alumina > Hexadecane > Dodecane > water > 3M™ HFE 7200 > Fomblin® oil. Based on the aforementioned dipole moment and polarizability values, one can realize the contributing Van der Waals forces between different kinds of materials as listed in Table 2.1.

Table 2.1. The contributions of Van der Waals forces in the materials systems used for the current study.

Interacting materials	**London forces**	**Debye forces**	**Keesom forces**	**Hydrogen bonding**
Al_2O_3–Water	✓	✓	✓	✓
Al_2O_3–Hexadecane	✓	✓ (very weak)	✓	×
Al_2O_3–Fomblin® oil	✓	✓ (very weak)	✓ (weak)	✓ (very weak)
Al_2O_3–3M™ HFE 7200	✓	✓	✓	✓ (very weak)
Water–Hexadecane	✓	✓	✓	×
Water– Fomblin® oil	✓	✓	✓	✓
Water–3M™ HFE 7200	✓	✓	✓	✓
Hexadecane– Fomblin® oil	✓	✓	✓	×
Hexadecane–3M™ HFE 7200	✓	✓	✓	×
Fomblin® oil–3M™ HFE 7200	✓	✓	✓	✓

Table 2.1 only gives qualitative information about the type of Van der Waals forces between the interacting materials in the study. The quantification of these forces in alumina–liquid systems will be presented in Chapter 4 using Equation (2.5) along with experimental evidences.

2.3. Wetting of porous materials

The wetting behavior of porous and rough structures is complex and significantly vary for omniphobic and omniphilic surfaces. The quantity of liquid in a droplet placed atop porous omniphilic material is not constant because of infiltration of the liquid into the porous structure. Therefore, three typical cases are reported to exist [55] as follows.

a. The infiltration of the liquid is much slower than the spreading: pores have a negligible influence on wetting behavior.

b. The infiltration is much faster than the spreading: wetting is not a relevant property.

c. Infiltration and spreading have similar time constants:wetting will be strongly influenced by the infiltration process.

In the latter case, spreading is thus interrupted prior to completion by the infiltration of the liquid into the porous structure, and the relative rates of spreading and infiltration will determine the ultimate diameter achieved by the spreading droplet [55]. The surface chemistry of the porous medium plays a paramount role in the dynamics of the wetting. The spreading, infiltration behaviors in non–impregnated dry mesoporous alumina samples and liquid impregnated mesoporous alumina samples were studied and are presented in Chapter 4.

2.4. Mechanical durability studies

There have been quite a few literature reports on the abrasion/wear resistance studies of superhydrophobic sufaces. Most studies utilized the custom built in–house experiments such as rubbing the sample surfaces against some kind of cloth [56–58], abrasive sandpaper [57,59,60], synthetic leather [61] or cotton swab [62]. Other procedures include ball–on–disk [63], pin–on–disc [15], sand abrasion or scouring with high–speed water jet [63–67] and scotch peel tests [68]. All the aforementioned reported studies employed very small normal pressures of a maximum of 310 kPa. Additionally, very limited studies exist on the effect of wear on the wetting behavior. Different criteria used in the literature include the change in SCA [58], CAH [57,59], water sliding angle [61] or roll–off behavior [56]. Few specific interesting examples from literature are categorized based on different approaches and briefly discussed as follows.

Hierarchical structured surfaces

Nanostructured and hierarchical (micro–nano) structured surfaces fabricated in carbon nanotube (CNT) based materials was shown to have retention of superhydrophobiciy post water jet experiments with pressurized droplets using pressures up to 45 kPa [63]. Also, tribological characterizations were carried out on such surfaces using the ball–on–flat configuration (normal loads up to 10 mN) reporting friction coefficient values of ~0.4 (Figure 2.4). However, these surfaces are limited in load bearing capacity and wetting studies post wear tests are not reported.

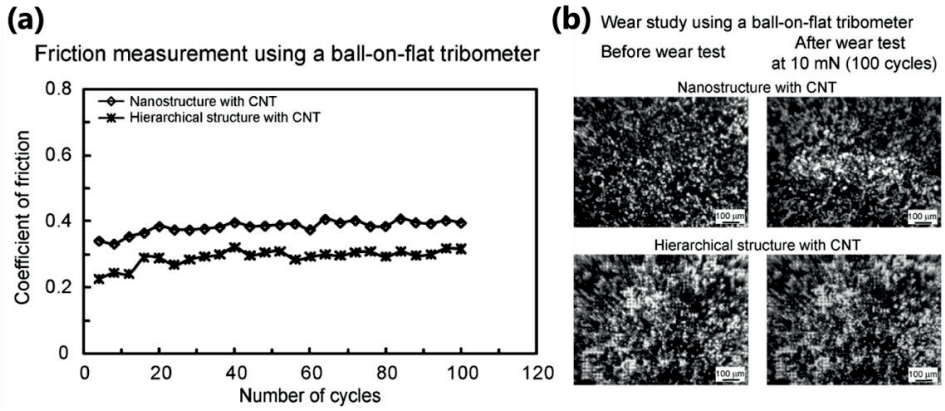

Figure 2.4. (a) Friction coefficient data obtained as number of cycles in a ball–on–flat tribometer, and (b) showing the surface microstructures before and after the corresponding wear tests. The images are reprinted with permission from [63]. Copyright © (2009), American Chemical Society.

Another interesting report is on the abrasion resistance of superhydrophobic surfaces containing hierarchical structures (micro–nano and micro–micro) of Polypropylene using pin–on–disk experiments [15]. It was observed that micro–micro (Figure 2.5a) showed better performance than micro–nano [15]. However, micro–micro hierarchical structures also lost superhydrophobicity when the normal pressures exceeded 310 kPa (see Figure 2.5b–c).

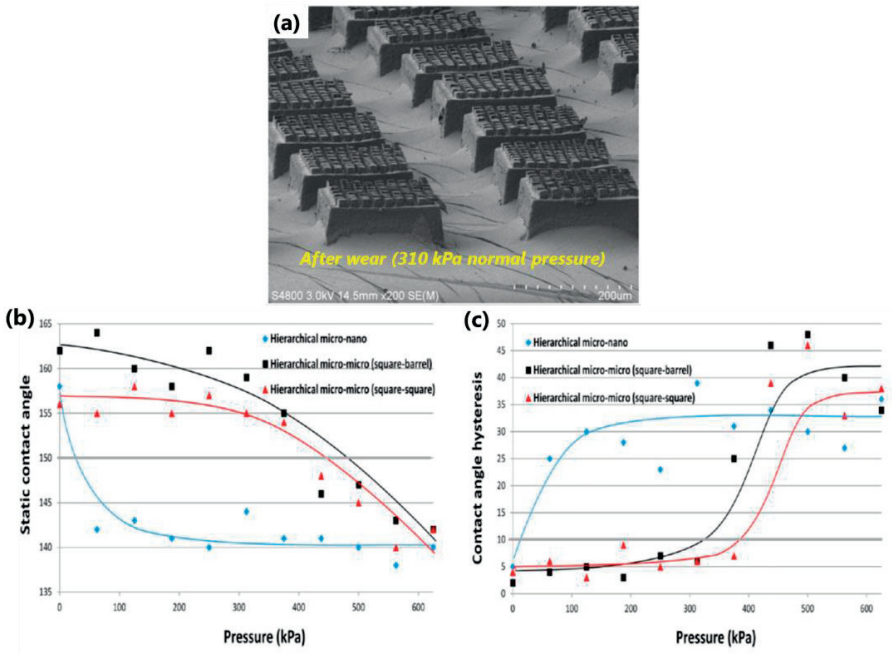

Figure 2.5. (a) SEM images of Polypropylene micro–micro hierarchical structures after wear test using 310 kPa normal pressures, (b) SCA and (c) CAH measurements of polypropylene surfaces comprising of different kinds of hierarchical structures reported post wear tests as a function of normal pressure (kPa). The images are reprinted with permission from [15]. Copyright © (2012), American Chemical Society.

Complex chemical treatment

Al sheets coated with a composite alumina/chitosan/poly[octadecene–alt–(maleic anhydride)] exhibited superhydrophobicity prior and post abrasion test but the abrasion resistance was not so high because it is equivalent to testing with velvet–covered roller (normal pressure of only 750 Pa) [56]. The chitosan composite material, however, lost its superhydrophobicity when applied normal pressures are ≥ 1.5 kPa. Similarly, there are reports on the retention of superhydrophobicity in highly porous gels [69] and solid foams [70] when cut by a razor blade. Further, compacted discs of decanethiol hydrophobisized, electrolessly Ag coated, Cu metal powders (~15 µm avg. diameter) showed superhydrophobic nature after abrasion with metal file or 100 grit, 150 um grain size abrasive paper, removing ~0.5 mm depth of the material [71] (Figure 2.6). However, the latter materials possess a very low tensile strength of only 2 MPa and extremely wear sensitive.

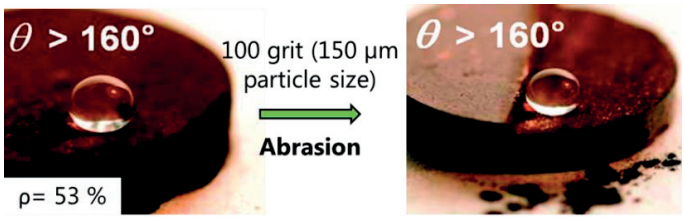

Figure 2.6. Compacted discs of Cu metal powders, covered with electolessly deposited (< 5 µm thick) Ag layer and further coated with monolayer of alkanethiol showing the retention of superhydrophobicity after abrasion test with a metal file. The image is reprinted with permission from [71]. Copyright © (2010), American Chemical Society.

Chemically and thermally treated PET–PDMS based textiles showed the retention of superhydrophobicity after 3000 washing cycles (Figure 2.7). However, the chemical treatment involved the usage of NaOH followed by coating with PE film further followed by PDMS and three thermal treatment steps [72]. Also, the textile underwent only very less normal pressures (up to 45 kPa) and is not wear–resistant.

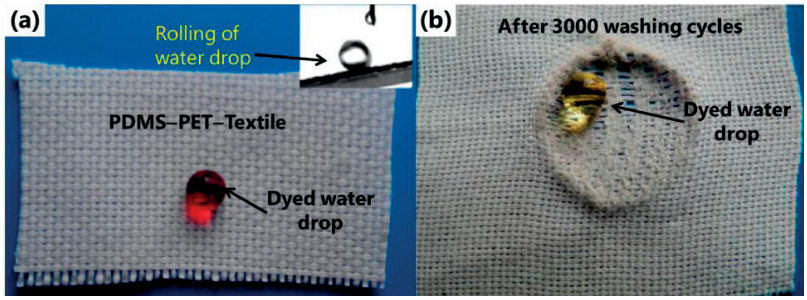

Figure 2.7. (a) NaOH–PP–PDMS modified PET based textile showing superhydrophobic behavior for dyed water drop which also slides for small sample tilt (inset in a) and (b) the retention of superhydrophobicity after 3000 washing cycles. The image is reprinted with permission from [72]. Copyright © (2014), American Chemical Society.

Liquid impregnated composites

Recently, Wong et. al.,[73] showed that perfluorinated oil infused bulk nanoporous PTFE surfaces showed anti–sticking behavior towards alkanes, blood, crude oil and water thus exhibiting

omniphobic character. However, PTFE substrate is not highly wear–resistant and limited in tensile (43 MPa) and compressive (15 MPa) strengths* respectively. Such liquid impregnation approach was adapted by other researchers [64,74–92], and mostly applied on functionalized and textured surfaces. There are recent reports that the liquid impregnated microstructured polymeric composites exhibited anti–biofouling and anti–bacterial [93–96], enhanced droplet condensation [76], anti–icing and anti–frosting properties [84,90]. There is no single study reporting the wear resistance of such surfaces. Presumably, such composites will be wear sensitive because of the protruding surface micro/nano features and functional groups which will be lost after harsh wearing exposures/tests.

Therefore, a polished non–functionalized α–Al_2O_3 ceramic matrix for employing the liquid impregnation approach was used in the current study. Alumina (94 % dense) samples possess high, room temperature flexural and compressive strengths of 330 MPa and 2100 MPa[#] and therefore were hypothesized to be potential candidates to withstand high mechanical damage during harsh wear experiments. The fundamentals of friction, wear and the state of the art literature on the tribological characterizations of alumina are briefly discussed in the following Sections 2.5 and 2.6 respectively.

2.5. Friction and wear

The friction between two contacting surfaces in motion is referred to as kinetic friction and mathematically expressed using the friction coefficient (μ) given by Equation (2.8). In this current dissertation, all the friction coefficient data are kinetic friction coefficient values.

$$\mu = \frac{F_f}{F_N} \tag{2.8}$$

where F_f is the frictional force exerted by each surface on the other. It is parallel to the surface, in a direction opposite to the net applied force and F_N is the apparent normal load applied to the surfaces. In sliding contacts, wear may occur on one or both the surfaces. Among all quantitative models for sliding wear, the Archard wear equation is one of the simplest and most applied theoretical models to quantify wear of sliding surfaces and given by Equation (2.9) [97].

$$Q = \frac{K\,F_N}{H} \tag{2.9}$$

where Q is the total wear rate (volume removed per sliding distance, mm^3/m), which was reported to be proportional to sliding distance [98], H is the hardness of the softer contacting surface and K is a dimensionless constant called the wear coefficient, and is always less than one [99]. The Archard wear equation is also valid for abrasive type of wear, which is the dominant wear mechanism in alumina samples.

*reference for PTFE–http://www.bearingworks.com/content_files/pdf/retainers/PTFE%20datasheet.pdf,
#reference for alumina–http://accuratus.com/alumox.html

2.5.1. Lubricated sliding

The most common way to reduce friction and wear rate between two sliding surfaces is by employing a lubricant. A lubricant can be a gas, liquid or solid introduced between two sliding solid bodies that possess lower shear strength than that resulting from the contact between the dry sliding surfaces. For a conformal contact (a flat on flat configuration in the current study is conformal) and in the presence of a lubricant, three main lubrication regimes can occur: hydrodynamic lubrication, boundary lubrication and mixed lubrication (an intermediate regime between the first two regimes).

Depending on the load, sliding speed, lubricant viscosity, the geometry of the contact and surface roughness, one of these three aforementioned lubrication regimes can occur. These regimes are summarized in a curve known as Stribeck curve (Figure 2.8). The Stribeck curve shows the dependence of friction coefficient on the load, sliding speed and lubricant viscosity [99,100]. In the boundary lubrication, the lubricant film is very thin and asperity contacts are present. In the mixed lubrication regime, the lubricant film can carry part of the applied load, whereas the remaining load is supported by the contacting asperities of the two surfaces. And finally, in the hydrodynamic regime, the thickness of the lubricant, in comparison with the height of the asperities, is large enough to prevent any contact between the asperities, and hence the sliding surfaces are assumed to be completely separated.

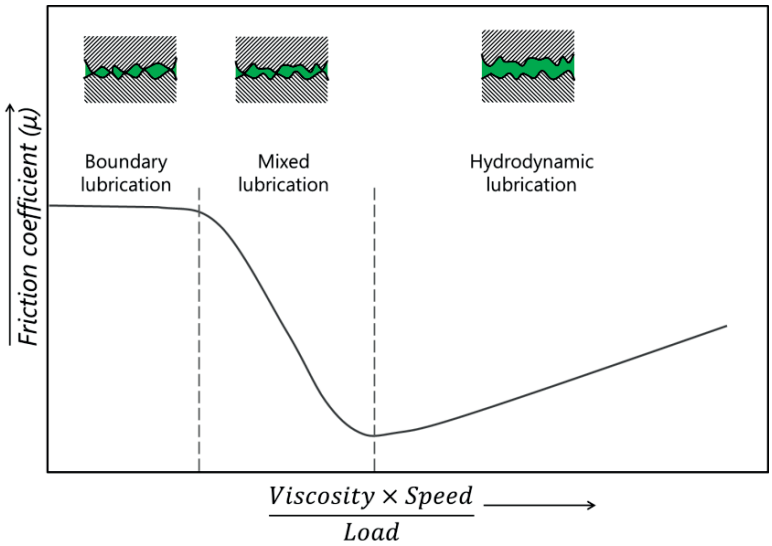

Figure 2.8. Schematic representation of a typical Stribeck curve illustrating the main three regimes in a lubricated sliding contact (adapted from [99,100]).

2.6. Tribological characterizations in alumina

Alumina, in particular self–mated alumina is a well studied system in understanding it´s tribological behavior. The literature reports on wear of self–mated alumina reveal that the wear parameters such as normal load, sliding speed, relative humidity strongly influence the wear mechanism.

The frictional and wear properties of ceramics strongly depend on the surrounding atmosphere [101]. Alumina can react with moisture forming a hydroxide layer which is beneficial to reduce friction [102]. On the contrary, the ability to form a tribo–film on an alumina surface decreases with increasing humidity. In case of a self–mating ceramic in unlubricated condition, the wear debris formed may fill up the cavities and create agglomerates on the surfaces. The local pressures and temperatures in a sliding contact are high enough to sinter the agglomerated particles of debris to a solid *tribo–film*. This phenomenon is called tribo–sintering. This type of tribo–film has been shown to smoothen the surface topography and may have a thickness up to 6 μm [103].

The common wear mechanisms in ceramics are abrasive, adhesive, corrosive and fatigue wear [104]. In general, the wear of ceramics is dominated by cracking [104]. There are typically two wear regimes for ceramics, mild and severe wear. In sliding under low contact pressures, the wear is mild, the surfaces become polished, the roughness decreases and the wear rates are low [105,106]. Smooth surfaces and low pressures give lower coefficients of friction [107,108]. Conversely, severe wear takes place under high contact pressures where stresses exceed the *tensile strength* of the material and grain fracture leads to formation of wear debris and an increased wear rate [105,106]. At very high pressures, whole grains will chip out from the ceramic matrix and the surface roughness increases drastically [109]. The size of wear debris typically increases with contact pressure. Further, the sliding speed has an influence on the wear of ceramics. The wear normally increases with increasing sliding velocity [107,108]. It has also been demonstrated that increase in grain size increases the wear rate in sliding contacts [110].

Specifically, there is no literature available for wear of liquid impregnated alumina against non–impregnated alumina or self–mating liquid impregnated alumina. It is of high input to study the effect of tribological parameters on friction and wear behavior and further the wetting behavior post wear tests. Chapter 5 will present results on the tribological behavior of Fomblin® impregnated/lubricated alumina samples as a function of alumina matrix density and apparent normal load.

Chapter 3
Materials and methods

The materials used, processes adapted, all the characterization techniques used along with experimental parameters for the whole thesis are presented in this chapter in the following subsections.

3.1. Materials used

99.9 % purity α–Al_2O_3 powders were obtained from BMA 15, Baikowski, France. The specific surface area of the powders was obtained from BET measurements taken from the technical data sheet of Biakowski, France and is 14900 m^2 kg^{-1}. 65 wt. % polyacrylic acid (PAA, MW = 2000) obtained from Sigma–Aldrich, Switzerland was used as a dispersant in the ceramic slurry preparation. 1–Octanol, Sigma–Aldrich, Switzerland was used as a surfactant for ceramic slurry. 30 wt. % NH_4OH obtained from Sigma–Aldrich, Switzerland was used to maintain pH at 10 for the 2 wt. % aqueous PAA solution, the latter used for preparing Al_2O_3 slurry/suspension. Commercially obtained 99.9 % dense ~1 mm diameter α–Al_2O_3 beads, TOSOH Europe B.V, Netherlands were used for low energy milling of alumina slurry. Whatman® nitrocellulose membrane filters with a pore size of 0.2 μm and 142 mm diameter, Sigma–Aldrich, Switzerland obtained were used in the slip casting process.

Dodecane ($C_{12}H_{26}$), Hexadecane ($C_{16}H_{34}$), Fomblin® Y25 oil, Eicosane ($C_{20}H_{42}$), Sigma–Aldrich, Switzerland, HFE–7200 3M™ Novec™ ($C_4F_9OC_2H_5$), 3M Belgium S.A./N.V and Millipore de–ionised water (12 MΩ–cm) were used for wetting studies. 40 μm, 20 μm diamond blades and 15, 6, 3, 1, 0.25 μm diameter particles containing diamond slurries obtained from Struers MD Dur™, Switzerland were used for polishing sintered mesoporous and fully dense alumina samples. Plastic syringes, Teflon® and alkylsilane coated needles, Krüss GmbH, Germany obtained were used for wetting studies to obtain spherical droplets of liquids. Commercially obtained 1 mm thick CVD diamond disk samples atop 4 mm WC cylinder substrates, Diamond Materials, Germany were used as counter bodies in tribological characterizations of alumina/single crystal sapphire samples. Commercially ob-

tained flat single crystal sapphire discs (20 mm diameter), Stettler Sapphire SA, Lyss, Switzerland were used as reference materials for evaluating tribological behaviors of liquid impregnated polycrystalline mesoporous alumina samples.

Elastosil 622 RT A/B, Ameba AB, Switzerland is commercially obtained two component silicone mixture and was used to prepare silicone open molds required in the slip casting process. Sylgard 184, PDMS was commercially obtained from VWR International GmbH, Switzerland and was used for replication purposes. Repliset–F5, Struers, Switzerland is a silicone paste and also used for replication. 1H, 1H, 2H, 2H–Perfluorodecyltrichlorosilane (97 %) was obtained from ABCR GmbH & Co. KG, Germany and used as a releasing agent at the PDMS–ceramic green body interface.

Zonyl® MP 1100, Moldflon™ were obtained from Du Pont, USA and were used as a second phase, impregnated into open mesoporous networks of alumina samples to obtain alumina matrix composites, the impregnated composites were used to study the wetting and tribological behaviors. Technovit 5071, a two–component resin, Naas Werkstoffprüfung, Switzerland was used to embed alumina samples for carrying out polishing with diamond blades and diamond slurries respectively. Transparent polycarbonate (PC) sheets were obtained from Sabic Lexan™, Switzerland and were used to obtain surface microstructural features using excimer laser ablation. 150 μm thick Ni sheets were commercially obtained after carrying out electrodeposition of corresponding laser ablated PC sheets from 3DAG, Switzerland.

3.2. Processes, experimental procedures

3.2.1. PDMS replication

Elastosil 622 RT A/B two component silicone mixture, red in color mixed in 9:1 curing ratio was poured out into respective machined Al molds and cured at 100 °C for 30 min to obtain cuboidal ($24\times12\times17$ mm^3) and disc shaped (40, 120 mm diameters and 20 mm high) cavity containing silicone molds respectively. These silicone molds were used in the slip casting process (Section 3.2.3) as open silicone molds to obtain cuboidal and cylindrical shaped alumina green compacts. Sylgard 184 is a two component mixture and mixed in 1:10 curing agent ratio and degassed in vacuum (200 mbar) for 30 min to minimize air bubbles and was then cast on a laser ablated PC sheet and cured for 48 h at 25 °C to obtain negative replication of structures. Repliset–F5 silicone has the ability to replicate structures with precision down to 100 nm, and was used to replicate structures from alumina ceramics since it has a shorter curing time of 18 min at 25 °C.

3.2.2. Perfluorosilanization

To help easy, de–molding of the ceramic green bodies that can prevent deformation of the microstructural features on the ceramic surface, a thin perfluoro–terminated siloxane coating was applied on a structured Sylgard. The coating was obtained from 1H, 1H, 2H, 2H–Perfluorodecyltrichlorosilane (97 %) and was applied to the structured Sylgard in a vacuum desiccator for 12 h which acts as a releasing agent. The coating process was carried out without applying any hydration process to the Sylgard samples and is similar to that proposed in the literature [111].

3.2.3. Slip casting

α–Al_2O_3 powders with average mean particle diameter, d_{v50} =135–150 nm were used to prepare ceramic slurries and slip cast similar to that proposed in the literature [112] with slight modifications. 2 wt. % polyacrylic acid was obtained by mixing commercially obtained 154 g of 65 wt. % polyacrylic acid with 118 g of 30 wt. % NH_4OH and 728 g of de–ionized water to obtain 1000 g of 10 wt. % PAA solution which is diluted to 2 wt. % for further use in the slip casting process. As–received aggregated Al_2O_3 powders (refer to Section C.1, Appendix C for the SEM image) were mixed with PAA (2 wt. %) aqueous solution having pH 10 to form ceramic slurry containing 25 vol. % solid fraction. The slurry was then ultrasonicated with a probe for 15 min followed by the addition of 3–5 drops (5–10 µl) of Octanol to disperse the possible agglomerates. Further de–agglomeration was carried out by milling with ~1 mm Al_2O_3 balls for 24 h which was slip cast in a porous silicone mold to form cuboidal and disc shaped green compacts. The slurry was dried in 2 stages: first at 90 % relative humidity (RH) for 24 h and then at 45% for the next 24 h, which finally produced ~60 % dense microstructured mesoporous α–Al_2O_3 samples. Additionally, the alumina slurry can be cast onto a microstructured Sylgard membrane to achieve microstructured mesoporous alumina samples, the development of the complete process can be found in Chapter 7; the exact duration depends on the Sylgard membrane thickness and the height of the ceramic slurry. The schematic diagram of the conventional slip casting process is presented in Figure 3.1.

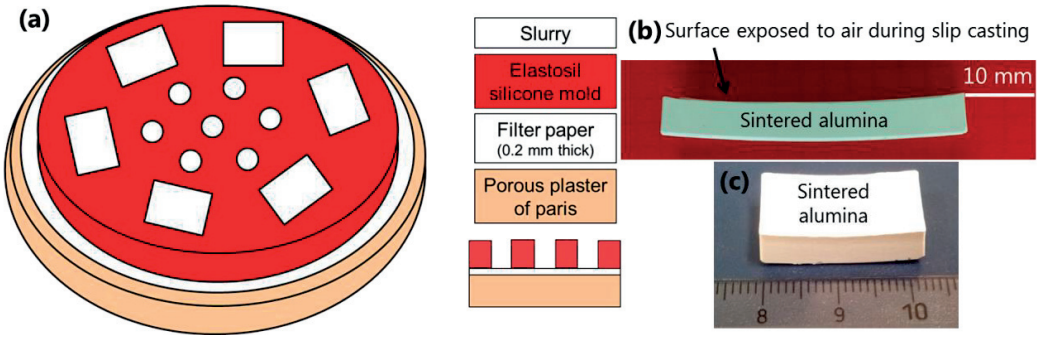

Figure 3.1. (a) Schematic diagram (not to scale) of a conventional slip casting process that can form a variety of shapes resulting in bulk samples. The ceramic alumina slurry (white in color) is poured into open Elastosil silicone molds (red in color) below which contains a filter paper (white in color) atop porous plaster of Paris mold (yellow in color). The plaster of Paris mold sucks the water from the slurry and aids the drying process. The filter paper has 0.2 µm pores and prevents sticking of the slurry and later green body upon drying to the plaster of Paris mold. Macroscopic bending visible in a sintered alumina sample, (b) dominant in bigger sample, (c) relatively less bending in smaller sample.

It is noteworthy that the produced alumina green compacts can have microscale defects throughout the sample if the slurry is not well dispersed to break all the aggregates into primary particles. The defects are usually microscopic holes which will be shown in Section 3.8.9. Additionally, there will be some unavoidable macroscopic bending of the samples (see Figure 3.1b) which probably arise due to density and packing gradients across the height of the sample due to sedimentation effect. Hence, it is advisable to remove off 1–2 mm of alumina green body surfaces prior to carrying out further sintering. A set of sintering experiments carried out on alumina green compacts comprising of different dimensions (24×12×10 in mm, 56×9×7 in mm, 7.5 mm diameter and 15 mm height cylindrical) revealed that always bending takes place in one direction (see Figure 3.1b). However, strong bending effect is not visible in smaller samples (Figure 3.1 c), which were the ones used for evaluating wetting and tribological properties.

3.3. Pre–sintering, sintering and densification

The green compacts were pre–sintered to 600 °C at a heating rate of 1 K min^{-1}, 1 h isothermal holding at 600 °C to remove the dispersant and the surfactant. The pre–sintered samples were sintered in air at 1150, 1205, 1250, 1325, 1500 °C in a tubular furnace at 10 K min^{-1} heating rate, 1 h isothermal holding at the corresponding highest temperature, to achieve 70±3, 80±3, 90±3, 95±, 99.5±0.5 % theoretical densities respectively. In 70, 80 and 90 % dense samples, ultrafine grains and mesoporosity are retained. For samples having relative densities greater than 90 %, pronounced grain growth was observed which can be avoided by a two–step sintering process.

The 2–step sintering process includes sintering to 1350, 1450 °C at 10 K min^{-1} heating rate and 15 min isothermal holding at the corresponding highest temperature and sudden cooling to 1000 °C followed by further holding time of 24 h to obtain 95, 99.5 % dense alumina samples respectively. The open porosity, closed porosity and total porosity of at least 10 sintered samples for each of 70, 80, 90, 95, 99.5 % densifications were measured by Archimedes principle with water as the suspending medium. The densification plot for one step sintering process is presented in Figure 3.2a and the corresponding open and closed porosity data are presented in Figure 3.2b.

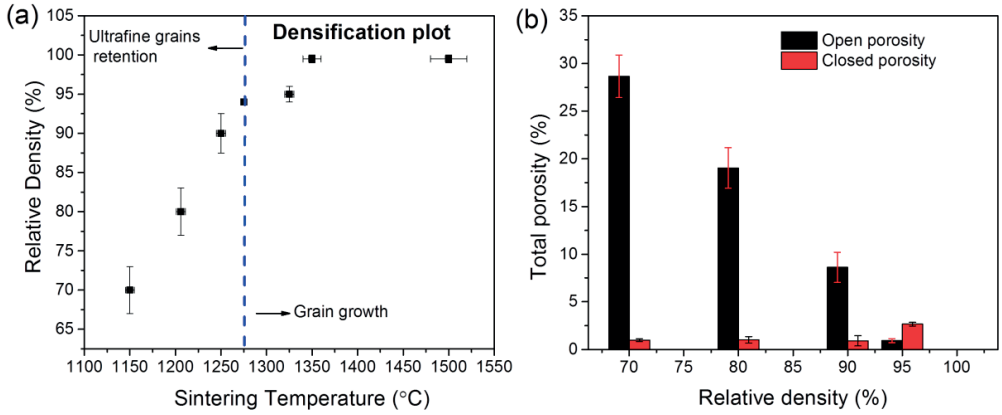

Figure 3.2. (a) Densification plot showing the relative density (%) of 70–99.5 % dense alumina samples as a function of sintering temperature for one step sintering process, and (b) open and closed porosity data in the respective 70, 80, 90, 95, 99.5 % dense samples.

3.4. Polishing and parallelism procedure

The further bending of the sintered alumina samples needs to be removed as it is very crucial to tribological and wetting studies. The flatness can be achieved by parallel diamond blade machining both sides of the sample. Subsequently, the sintered samples were embedded in Technovit 5071 epoxy, a 2–component resin and further polished with 40, 20 µm diamond blades followed by 15 min polishing with each of diamond slurries containing 15, 6, 3, 1 and 0.25 µm sized particles respectively at 150 rpm and 215–280 N normal pressure. The polished samples at every stage were checked with an optical microscope to check the crack formation. The polished samples were heated to 600 °C at ~3 °C/min and holding time of 2–5 h at the highest temperature to evaporate the resin completely and burn the carbon contamination obtained from polishing.

3.5. Oxygen plasma treatment

The hydrocarbon accumulation on the surfaces exposed to normal/lab environment is a common phenomenon that significantly affects their wetting response [50,113,114], especially for polar or high

energy substrates such as ceramics, metals etc. Hence, mesoporous alumina (MPA) and sapphire samples can be anticipated to have hydrocarbon accumulation. It is known that alumina surfaces are highly polar in nature and are superhydrophilic i.e. attract water strongly. The presence of open meso-porosity further enhances the attraction due to capillary forces. Hence, a water drop should ideally completely wet alumina surfaces i.e. form 0° static contact angle (SCA). However, Figure 3.3 shows that ~67° SCA was formed atop sapphire sample surface at time t = 0 min, eventually decreasing to 18° in 8 min.

Hence, the polished mesoporous 70, 80 and 90 % dense alumina sample surfaces and sapphire sample surfaces were cleaned with oxygen plasma, Plasma PreP_2, GaLa Instrumente, Germany for 15 min zsing 50 Hz frequency, 0.1–0.3 mbar pressure, 100 Watt and 400 cm^3 min^{-1} flow rate prior to the wetting studies or liquid impregnation. When the sapphire surface underwent oxygen treatment, it showed superhydrophilic behavior as observed by the 0° static contact angle of the water drop (not shown here) that spreads on the surface in just ~2 s.

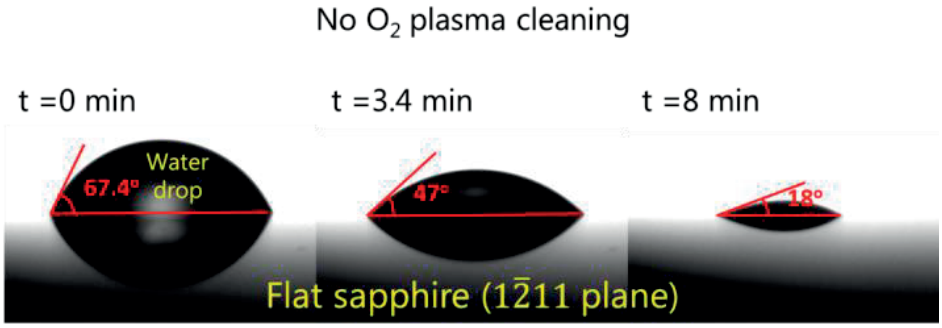

Figure 3.3. (a) The occurrence of ~70° static contact angle of water atop sapphire sample surface as a function of time prior to employing oxygen plasma treatment.

3.6. Liquid impregnation

The physical properties of the liquids used for carrying out the impregnation process are tabulated in Table 3.1 and the measured equilibrium static contact angles of those liquids with flat sapphire with and without employing oxygen plasma treatment are tabulated in Table 3.2.

Table 3.1. Physical properties of the liquids used for impregnation process

Liquid (Molecular Formula)	**Dynamic Viscosity (η) at 20 °C (mPa s)**	**BP (°C)**	**Density (g cm^{-3})**	**Surface Tension at 20 °C (mN m^{-1})**
Water (H_2O)	1.002	100	1	72
Dodecane ($C_{12}H_{26}$)	1.786	214–218	0.75	25

Hexadecane ($C_{16}H_{34}$)	3.89	271–291	0.773	27.47
Fomblin® Y25 ($CF_3O[-CF(CF_3)CF_2O-]_x(-CF_2O-)_yCF_3$)	475	>270	1.9	22
HFE–7200 3M™ Novec™ ($C_4F_9OC_2H_5$)	0.43	76	1.43	13.6

Table 3.2. Measured equilibrium static contact angles of liquids with flat sapphire

Liquid	**Contact angle (θ°) with flat sapphire**	
	Employing O_2 plasma treatment	**Without O_2 plasma treatment**
Water	0	18
Fomblin® Y25	0	20
Dodecane	0	0
Hexadecane	0	0
HFE–7200	0	0

Water, Dodecane, Hexadecane and HFE–7200 liquids are low viscous liquids (Table 3.1). Alumina is hydrophilic and oleophilic as observed by 0° static contact angles (Table 3.2) and hence complete infiltration of the alumina mesopores with aforementioned low viscosity liquids was carried out at room temperature for 2 h by simply dipping the samples in the respective liquid. However, Fomblin® oil is a very high viscosity liquid (2 orders of magnitude higher than aforementioned liquids) and hence need high temperature impregnation. The Fomblin® oil should be pre–heated to 150 °C followed by impregnation of MPA samples for 2 h. These impregnation conditions are determined by measuring the fraction of open porosity filling tests summarized in Table 3.3 using the Archimedes principle (see Section 3.8.3 for details on Archimedes principle for measuring the filling fraction of open porosity).

Table 3.3. Optimization of Fomblin® oil high temperature impregnation for MPA samples

Infusion T (°C)	**Infusion Time (h)**	**% Open Porosity Filled**
20	2	40
150	1	96
150	2	99.5

The completely infiltrated samples can have two configurations for an impregnating liquid atop a liquid impregnated alumina composite surface: (a) case of complete flooding the solid surface roughness features referred to as *flooded* configuration, (b) infiltrated liquid follows the roughness

elements forming a very thin film (few monolayers thick). The excess liquid on the surface can be removed by either blowing away with compressed N_2 gas or using a non–linting optical paper and referred to as *unflooded* configuration.

3.7. Solid impregnation and hot embossing

Eicosane is a solid at room temperature (MP = 36.5 °C). Hence, the mesoporous alumina samples are impregnated with Eicosane by heating the latter to 60 °C, followed by dipping the sample into liquid Eicosane for 2 h. However, hot embossing experiments were carried out to impregnate solid flourinated materials into mesopores of alumina to evaluate their wetting properties (Chapter 4). Zonyl® MP 1100 powders (PTFE powders) having an average particle size of 4 µm and moldflon™ sheet respectively, were hot embossed into mesopores of 70, 80 and 90 % dense alumina samples. The physical properties of Zonyl® and Moldflon™ materials are tabulated in Table 3.4.

Table 3.4. Physical properties of Zonyl® and Moldflon™ materials

Material	Particle Size (µm)	Surface Energy (mJ m^{-2})	Melting Point (°C)	Service Temperature Range (°C)
Zonyl® MP1100	4	18	325	-190 to 250
Moldflon™ Modified PTFE (C, F, O elements form the structure)	-[a]NA- (Sheet)	18	315–324	-260 to 260

[a]NA–Not Applicable

To carry out hot embossing experiments, a home–made, small high temperature compression machine (Figure 3.4) was set up under a hood. This setup comprises of a hydraulic press and a heating system. The heating system is a pair of steel blocks with blind holes filled with 4 cartridge heaters to heat the blocks symmetrically to reach the required high temperatures up to 400 °C. A `k´ type thermocouple was inserted into the bottom steel block close enough to the sample surface to measure the service temperatures.

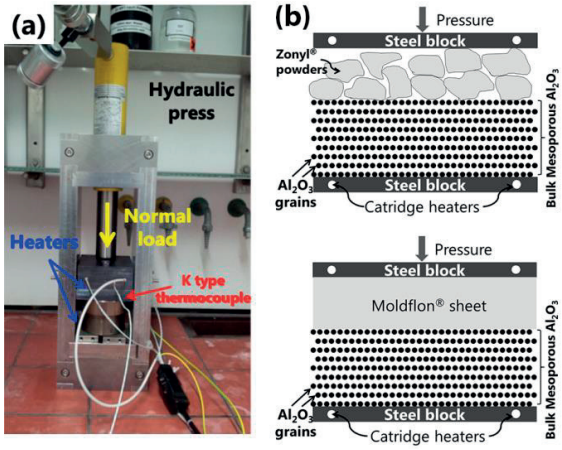

Figure 3.4. (a) High temperature compression setup installed under a hood using hydraulic press and heating systems consisting of heaters entering into blind holes drilled into steel blocks, (b) schematic diagram showing hot embossing of Zonyl® powders (top diagram) and Moldflon® sheet (bottom diagram) into mesoporous alumina sample placed in between two heating steel blocks.

The impregnation time (t) of the hot embossing process can be determined by using Equation (3.1), where the parameters in the equation are tabulated in Table 3.5.

$$t = \frac{\eta v_{pore} L^2}{2k(P_a - \Delta P_c - \Delta P_{atm})} \tag{3.1}$$

Table 3.5. Summary of parameters, their definitions and the values in the Equation (3.1)

Parameter	Parameter definition	Values
η	Viscosity at embossing temperature	1000–3000 Pa.s at 250 °C
V_{pore}	Porosity fraction	0.3, 0.2, 0.1
L	Impregnation depth	5–10 mm
k	Permeability	~10^{-15} m^2 at 250 °C
P_a	Applied normal pressure (Pa)	30–100 MPa
ΔP_c	Capillary pressure at embossing temperature (T) given by: $\Delta P_c = \frac{2(0.018 - 0.058(T-20))cos\theta}{r_{pore}}$ where θ is CA with the alumina	393923 Pa for 50 nm pore diameter θ = 10°
ΔP_{atm}	Atmospheric pressure	101325 Pa

The impregnation temperature of 250 °C for 6 h impregnation time was used to impregnate the Zonyl® and Moldflon™ materials into open porosity of 70, 80 and 90 % dense samples respectively. Following the impregnation, it was quite tedious to demold the alumina composites from steel press and most often resulted in the breaking of the samples. However, with small applied normal pressures

(P_a), it was feasible to demold alumina composites. The cross–section lamella was analyzed to study the depth of impregnation in these composites.

3.8. Characterizations

3.8.1. Centrifugal sedimentation

The particle/grain size and specific surface area of completely de–agglomerated Al_2O_3 powders have been measured using a disc centrifuge (CPS disc centrifuge, CPS Instruments, Europe, The Netherlands) and a median particle diameter, d_{v50} between 130–150 nm (d_{v50} means 50 vol. % of particles have diameters smaller than 150 nm) was measured. The majority of the particles have sizes between 90 and 220 nm (refer Section C.2, Appendix C).

3.8.2. Rheological studies

The completely de–agglomerated alumina slurries were characterized to obtain rheological properties as a function of slurry solid fraction (vol. %). Shear stress versus shear strain data was obtained for 20, 25, 30, 37 vol. % solid containing slurries for at least 3 samples for each solid fraction slurry respectively using Thermo/HAAKE RheoStress RS100 Rheometer, USA. Please refer to Section C.2, Appendix C for the viscosity measurements.

3.8.3. Archimedes principle and density measurements

The open porosity and total porosity of at least 10 sintered samples for each of 70, 80, 90, 95, 99.5 % densifications were measured by Archimedes principle with de–ionised (12 M Ω–cm) water as the suspending medium using Mettler–Toledo GmbH XP 205 excellence plus XP analytical balance, Switzerland. The open, total and closed porosity of at least 5 green bodies/compacts fabricated by slip–casing were estimated by Archimedes principle using isopropanol as the suspending medium using Equations (3.2), (3.3) and (3.4) respectively. The balance has a precision of 10^{-4} g thus obtaining very accurate density measurements. All the density measurements were carried out at 23±2 °C and 35±10 % RH.

$$Open\ porosity\ (OP) = \frac{wet\ weight - dry\ weight}{wet\ weight - immersed} \tag{3.2}$$

$$Total\ porosity\ (TP) = 1 - \frac{dry\ weight \times \rho_l}{(wet\ weight - immersed\ weight) \times \rho_s} \tag{3.3}$$

$$Closed\ porosity\ (CP) = Total\ porosity\ (TP) - Open\ porosity\ (OP) \quad (3.4)$$

where ρ_l and ρ_s are suspending liquid density (1000 kg m^{-3} for water and 786 kg m^{-3} for isopropanol respectively) and theoretical solid full density (3987 kg m^{-3} for $\alpha-Al_2O_3$) respectively.

3.8.4. Scanning electron microscopy

As–received Al_2O_3 powders from the supplier, Al_2O_3 green compacts, sintered Al_2O_3 bulk samples prior and post wear tests, microstructured Al_2O_3 samples, laser ablated PC sheets, Ni sheets and microstructured PDMS samples were characterized with a Philips S4800 high resolution scanning electron microscope (HRSEM) in secondary electron mode (SE) using 1.5–5 keV acceleration voltage and 10 μA beam current from top view and at 45–70° sample tilt. PC sheets, Ni sheets, PDMS samples were coated with Au prior to HRSEM studies. The grain sizes, micro homogeneity of the sample surfaces and the wear track of the alumina samples can be obtained using electron microscopy.

3.8.5. Digital holographic microscopy

Very shallow structures like diffractive optical elements (DOE) on a PC sheet have been characterized with digital holographic microscope (DHM). CVD diamond samples have been characterized with DHM to measure the mean roughness (R_a) prior and post wear tests.

3.8.6. Mercury intrusion porosimetry

The pore size distribution data for 70, 80 and 90 % dense bulk alumina samples have been obtained by using a Hg intrusion porosimeter, Pascal 440, Germany. The samples used for the measurements have weight of ~ 3g and around 4–5 mm diameter cylinders. The technique is based on the principle of measuring the pressure (P) required for Hg (surface tension of Hg (γ_1) is 468.5 mN m^{-1}) to be penetrated into a pore of the material. Knowing the equilibrium contact angle (θ = 140°) that Hg makes with Alumina, Washburn Equation (3.5) allows to calculate the pore radius (r) and hence the pore diameter. The cumulative number of pores versus pore diameter was obtained for a minimum of three samples for each densification for reproducibility. The average pore sizes are 47±12, 34±10 and 25±7 nm for 70, 80 and 90 % dense MPA samples, respectively (refer Section C.3, Appendix C for pore size distributions).

$$P = -\frac{2\gamma_1 cos\theta}{r} \quad (3.5)$$

3.8.7. X–Ray diffraction

The crystallite sizes of the sintered alumina samples were characterized with Bruker AXS D8 Discover, Germany, X–Ray diffractometer (XRD) with Cu K_α (λ = 0.154 nm) radiation for 2θ scan from 20° to 140°, with excitation voltage of 40 keV and current of 40 mA and step size of 0.02° in theta 2 theta mode. Since alumina samples have approximately spherical grains and strain free, Scherrer Equation (3.6) was employed to obtain crystallite sizes for 70, 80 and 90 % dense alumina samples from their Full Width at Half Maxima (FWHM) of XRD patterns (Figure 3.5a). The estimated average crystallite size in 70, 80 and 90 % dense samples are 125, 160 and 280 nm respectively, and plotted along with grain size measurements from HRSEM for a comparison (Figure 3.5b) indicating that the samples have ultrafine grains.

$$d_{crystallite} = \frac{0.9\lambda_{Cu}}{\beta cos\theta} \tag{3.6}$$

where β can be described by equations β =b–s, $\beta=b^2-s^2$ assuming Cauchy and Gaussian fitting of the profiles respectively, where b=full width at half maxima (FWHM) and s is instrumental broadening (obtained from standard corundum sample).

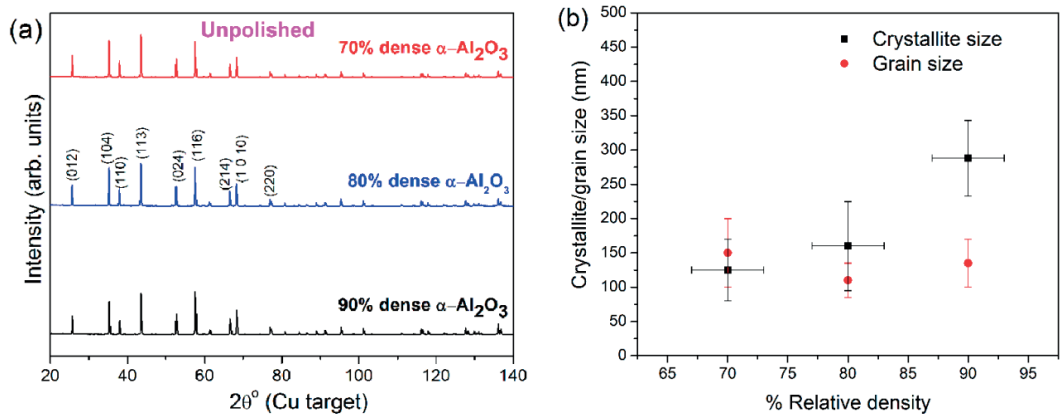

Figure 3.5. (a) XRD data of 70, 80 and 90 % dense as–sintered unpolished alumina samples as a function of 2θ(°), (b) average crystallite size (black squares) of 70, 80 and 90 % dense alumina samples calculated using Scherrer equation of full width half maxima of XRD peaks. The average grain size (red dots) obtained from HRSEM images is also plotted for a comparison.

3.8.8. Vickers hardness

The Vickers hardness ($HV_{0.1}$) measurements were carried out on three samples for each densification; 5 measurements on each side, and on both the sides of the sample. The hardness measurements were also carried out on a commercially obtained flat single crystal sapphire disc for a comparison.

The hardness values are useful for calculating the wear coefficients using Archard wear Equation (2.9). The load of 0.1 kgf (0.98 N) and 15 s dwell time were used for the measurements.

3.8.9. Laser confocal microscopy

Micro homogeneity of the alumina samples were tested with VK–8700, laser confocal microscope, using 658 nm wavelength light at 10–50 X magnifications. As mentioned in Section 3.2.3, micro defects of ~10–100 μm diameter holes can be present as shown in Figure 3.6a. They arise due to incomplete de–agglomeration of alumina slurry which contained air bubbles, the latter appear as holes post sintering. However, careful de–agglomeration of alumina slurry leads to defect free alumina samples as shown in Figure 3.6b. Such defect free samples were used in this present study.

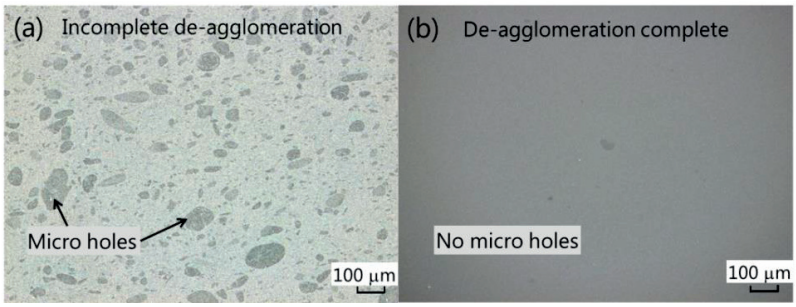

Figure 3.6. Laser confocal microscopic images of alumina sample surfaces (a) when de–agglomeration in the slurry is not complete leading to microscopic holes and (b) micro hole free sample surface due to improved de–agglomeration in the slurry

3.8.10. Optical profilometry

The flatness, waviness (W_a) and roughness (R_a, r_w) measurements of polished alumina and monocrystalline sapphire samples were carried out using white light AltiProbe Optic® profilometer according to the standard DIE EN ISO 4288, ASME B46.1. At least 10 measurements were taken for each sample and 3 samples for each of 70, 80, 90, 95, 99.5 % densifications thus resulting in a total of 30 measurements for each densification. The theoretical lateral and depth resolutions are 500 nm and 20 nm respectively. A typical convoluted surface profile of 80 % dense, polished MPA is shown in Figure 3.7 along with the respective de–convoluted roughness (R_a) profile.

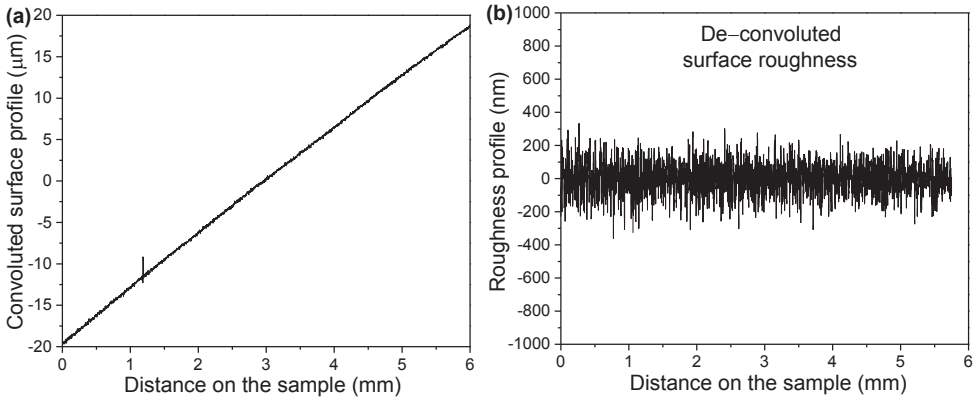

Figure 3.7. (a) A typical convoluted surface profile of a 80 % dense polished MPA sample is presented along with a (b) de–convoluted surface roughness profile.

An experimentally obtained parameter (S_{dr}) using optical profilometer is a ratio of the increment of the interfacial surface area relative to the 2D projected area. The wetting roughness parameter (r or r_w), expressed by Equation (3.7) can be co–related to S_{dr} parameter using Equation (3.8).

$$r_w = \frac{True\ area}{Apparent\ area} \tag{3.7}$$

$$r_w = \frac{S_{dr}}{100} + 1 \tag{3.8}$$

For a totally flat surface, the surface area and the area of the xy plane are the same and hene S_{dr} = 0 % which leads to r_w = 1. As the lateral resolution in this technique is much bigger than the pore sizes (50 nm pore diameters) in MPA samples, the pores cannot be revealed by this technique. The underlying physics of the optical profilometry is the formation of interference fringes due to variation in the path lengths travelled by the light in the sample as compared to a reference material. In the case of MPA samples, it is a composite of air and alumina whose refractive indices are 1 and 1.7 respectively. Therefore, the optical path lengths in air and alumina vary significantly and may influence the roughness values. Hence, a complimentary technique is necessary to ensure the accuracy of the roughness values. Atomic Force Microscopy (AFM) was employed to obtain the roughness values and will be described in the following section.

3.8.11. Roughness using Atomic force microscopy

The roughness measurements were obtained using ScanAsyst–Air–HR probe (silicon nitride tip with 2 nm radius) in tapping mode using Bruker AFM, USA with 2 Hz scan rate. The typical AFM 2D profiles of the polished 70 % and 95 % dense, polished MPA sample surfaces are presented in Figure

3.8. The typical scan areas are 35×35 μm^2 and the measurements were repeated on three places of each densification.

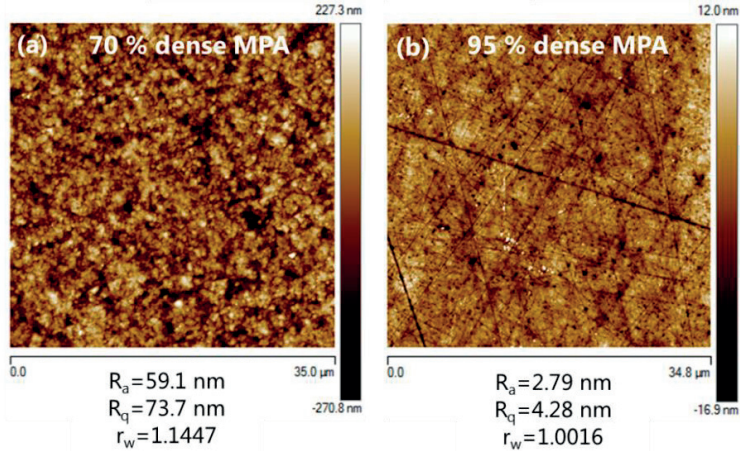

Figure 3.8. (a–b) Typical AFM images of 70 % and 95 % dense, polished MPA samples are presented along with their roughness values.

The R_a values of 70 % and 95 % densifications obtained from AFM measurements are 60±5 nm and 3±0.5 nm while that obtained from optical profilometer are 88±14 nm and 38±14 nm respectively. A comparison of the values suggests that the order of magnitude of the roughness values are similar while using the two approaches. Due to the feasibility to scan large areas (up to several mm^2) and easy access, further roughness measurements were carried out using an optical profilometer in the present study.

3.9. Wetting characterizations

3.9.1. Contact angle measurements

The non–impregnated dry MPA samples and liquid impregnated polished MPA samples with and without employing oxygen plasma treatment were characterized with a contact angle goniometer, GBX Digidrop, France to obtain static contact angle measurements and study the sliding behaviors of different liquids atop liquid impregnated MPA (will be referred to as LIMPA) samples. To study the wetting behavior of dual scale micro and nano rough MPA surfaces, the samples were coated with a thin layer of Eicosane solution obtained by dissolving Eicosane (0.5 g) in Hexane (50 ml). The volume of the liquid droplets is ~2–3 μl and plastic syringes and Teflon®/alkysilane coated needles were used to form the spherical droplets. All the contact angle measurements were carried out at 23±2 °C and 35±10 % RH environment.

3.9.2. Liquid menisci in 3 phase systems

The liquid menisci shapes in three phase systems were carried out using sapphire capillary with the following combinations of liquids: (a) Fomblin® oil–Hexadecane, (b) Hexadecane–water, (c) Fomblin®–water. The sapphire capillary has 1.5 mm outer diameter and 1 mm internal diameter and the static and dynamic wetting studies were observed with high speed camera (frame rates of 32, 63) attached to an optical microscope. Typically, a sapphire capillary cleaned with HNO_3, ultrasonicated in de–ionised Millipore water (12 MΩ–cm) followed by a rinse or ultrasonication in ethanol and dried in an oven was suspended into two immiscible liquids. One side of the tubular sapphire capillary is in the air while the other end in the denser liquid.

3.10. Tribological characterizations

Fully polished alumina samples which have parallel surfaces (<30 μm flatness over areas of 22×11 mm^2) were impregnated/lubricated with different materials: Eicosane, Moldflon™, Zonyl® and Fomblin® oil respectively, and the counter body was slid dry in reciprocating sliding contact in flat–on–flat configuration with SRV® III, Optimol Instruments Prüftechnik GmbH tribometer, Germany to obtain friction coefficient data. The set–up of flat–on–flat configuration is known to be problematic. Consequently, a special holder was used to prevent the inclination of the counter–body and to ensure flat–on–flat conditions (see Figure 3.9a). The tribological studies of monocrystalline sapphire were conducted using diamond as the counter body using the same tribological conditions. The samples were weighed with a high precision balance (precision of 10^{-4} g) before and after the sliding tests to calculate the wear rates. Figure 3.9 shows the sample holder, tribological flat–on–flat configuration, sample and the counter body.

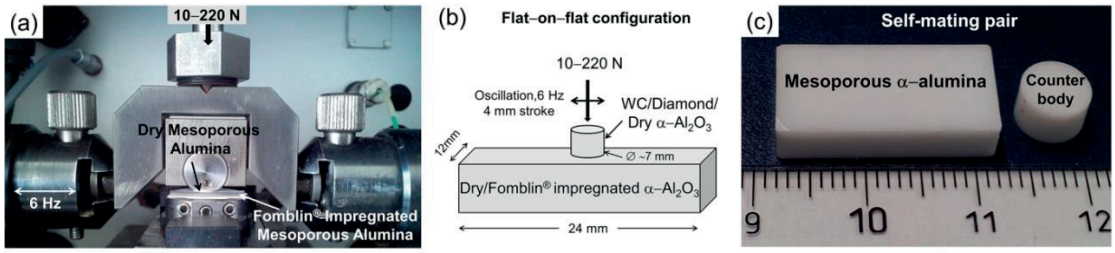

Figure 3.9. (a) Special holder for the counter body to compensate for small flatness issues and showing the normal load and frequency of sliding, (b) schematic diagram representing the geometry and materials for carrying out wear experiments in flat–on–flat condition and (c) picture showing cuboidal and cylindrical shaped α–Al_2O_3 samples sintered to 95 % relative density used for reciprocating sliding tribological characterization studies.

The maximum flatness of the samples is only 10 μm for a stroke length of 4 mm, which can be compensated by the specially designed counter body holder. The normal load varied from 10 to 220 N

for flat on flat contact type with 36–42 mm^2 contact areas for 70–90 % dense samples. Hence the normal pressures range from 0.24–5.24 MPa, 0.27–5.87 MPa, and 0.28–6.11 MPa for 70, 80 and 90 % dense samples respectively. The frequency and stroke are 6 or 13 Hz and 4 mm respectively. The sliding tests were carried out in a controlled environment where the chamber RH was maintained at 30±5 % and the temperature is 30±3 °C for all the tests.

3.11. Dark field X–Ray imaging

As–sintered 70 % dense MPA samples were cut with parallel diamond blades on 4 sides to obtain cuboidal shapes possessing dimensions of 20×10×2.78 (length×width×thickness, in mm). The dark field X–Ray imaging apparatus is shown in Figure 3.10a indicating the location of the X–Ray source, gratings and sample location. Four sides of the sample were covered with Polyimide Kapton tape, which is sufficiently transparent to X–Rays to prevent the evaporation of the liquid from the lateral surfaces as shown in Figure 3.10 (b–c). The description of the experiment and underlying physics can be found in the literature [115]. The dark field images were obtained for water and Fomblin® oil uptake by open pore network of the MPA samples. The total measurement time for water uptake lasted for 30 min while for Fomblin® oil, it lasted for 12 h. The dark field radiographs were captured every 46 s in each of these measurements.

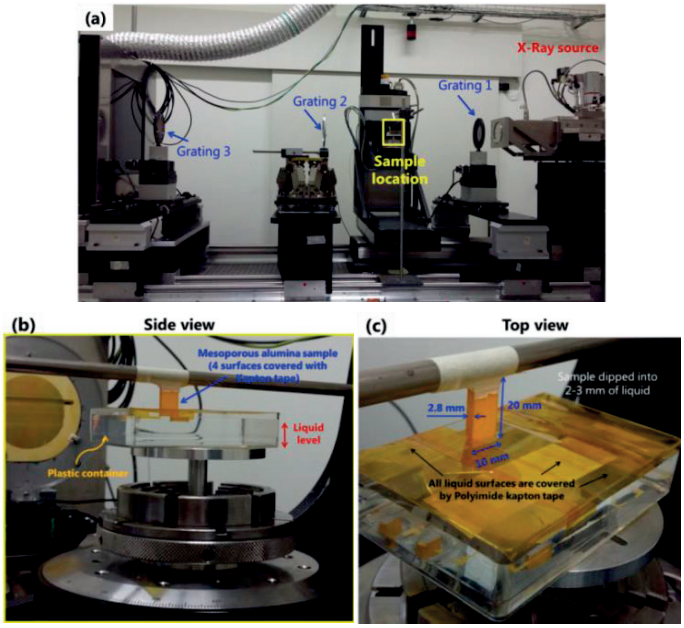

Figure 3.10. (a) Dark Field X–Ray Imaging apparatus showing X–Ray source, three gratings, sample transparent to X–Rays covered with Polyimide Kapton tape to prevent evaporation which is also transparent to X–Rays, (b) zoom in of the sample location showing a 70 % dense mesoporous alumina sample dipped into plastic container with water, (c) top view of the plastic container showing that the liquid surfaces are covered with Polyimide tape to also prevent evaporation.

Chapter 4

Wetting properties of liquid impregnated mesoporous α–Al_2O_3 composites

Mesoporous alumina matrices can be impregnated with either solids or liquids and the obtained composite materials can be evaluated for wetting and tribological performances. In this chapter, the wetting and tribological studies of a few solid impregnated alumina composites are briefly presented showing that they are not promising in terms of retention of wetting characteristics post wear. Liquid impregnation approach therefore is the main content of the thesis and further sections will focus on the wetting and tribological characterizations of liquid impregnated alumina composites.

4.1. Wetting properties of solid impregnated mesoporous α–Al_2O_3 composites

Three different solid impregnated alumina composites were prepared using (a) Hydrocarbon (Eicosane) impregnation and (b) fluorocarbon impregnation (Moldflon™ and Zonyl®). The experimental details of the impregnation processes and the physical properties of the impregnating materials can be found in Section 3.7, Chapter 3. Here, the wetting behaviors of Zonyl® impregnated 70 % dense MPA composite, Moldflon™ impregnated 70 and 90 % dense MPA composites are presented in Figure 4.1. The water drops exhibited high SCAs and rolling/sliding for sample tilts of ~<30°.

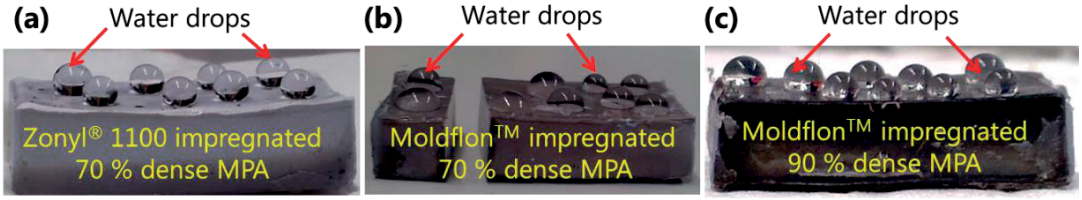

Figure 4.1. The wetting behavior of water drops atop (a) Zonyl® impregnated 70 % dense MPA composite surface, (b–c) Moldflon™ impregnated 70 and 90 % dense MPA composite surfaces respectively. All the samples possess ~5–6 mm thickness.

However, the samples exhibited complete hydrophilicity (SCA of <5°) post wear experiments [refer Appendix A, for complete details]. The solid impregnated alumina composites lost superhydrophobicity post wear due to the inability to self–replenish the dry alumina regions. Additionally, the roughness and thickness of second phase material atop the composite surfaces could not be precisely controlled. Hence, deeper studies were not carried out with these material systems. However, one cannot strongly eliminate the use of solid impregnated alumina composites and may become a part of another scientific study.

The self–replenishment capability in liquid impregnated alumina composites will be greater than solid impregnated alumina composites due to strong capillary forces and enhanced surface diffusivity. Hence, the thesis will be focused on the wetting and tribological behaviors of liquid impregnated alumina composites.

4.2. Wetting properties of liquid impregnated mesoporous α–Al_2O_3 composites

The wetting behaviors of liquid impregnated mesoporous alumina composites were studied and a manuscript to be communicated, 2016. The following section briefly describes the content of the attached manuscript.

4.2.1. About the manuscript

The following manuscript will discuss the wetting behaviors in three different types of liquid impregnated alumina composites namely hydrocarbon impregnated composites, water impregnated composites and perfluoropolyether impregnated composites. It was observed that spreading, infiltration behaviors were observed in water and Hexadecane impregnated composites with the corresponding immiscible liquid drops atop. However, for Fomblin® impregnated composites, water and Hexadecane were shown to form stable interfaces, which is considered as the desired configuration to be able to achieve anti–sticking behaviors. Such variation in wetting behaviors is explained based on the Van der Waals forces of attraction employing van Oss–Choudary–Good theory. There are two important variations of this work compared to that of literature, namely the unemployment of any surface functional coating materials atop an omniphilic alumina substrate and the absence of protruding surface microstructural features atop alumina. Finally, the relative thermodynamic stability of the liquid impregnated alumina composites is discussed in comparison with that of liquid impregnated polymeric composites often used in literature. The supporting information document of this manuscript is attached as an Appendix B at the end of the thesis.

To be communicated, 2016

Sliding Behavior and Stability of Liquid–Liquid Impregnated Mesoporous Alumina Composite Interfaces

Sriharitha Rowthu*, Edin E. Balic, Patrik Hoffmann*

Advanced Materials Processing Laboratory, Empa, Swiss Federal Laboratories for Materials Science and Technology, Feuerwerkerstrasse 39, 3602 Thun, Switzerland

E–Mail*: haritha.iitm@gmail.com; patrik.hoffmann@empa.ch

Abstract

Mechanically durable, anti–liquid sticking surfaces are of high technological and scientific importance and needs to be researched. Hence, surfaces possessing both high wear resistance and liquid repellency need to be developed. To this effect, we propose to study the wetting behavior of liquid impregnated polished, polycrystalline, mesoporous α–Al_2O_3 (referred to as MPA) composites without employing any surface hydrophobization. Slip–casting and subsequent sintering of ultrafine α–Al_2O_3 powders lead to connected porous alumina matrices containing 10–30 % open porosity. The open porosity was impregnated with liquids (surface tension values at 20 °C) such as: HFE–7200 3M^{TM} (13.6 mN m^{-1}), Fomblin® oil (22 mN m^{-1}), *n*–Dodecane (25 mN m^{-1}), *n*–Hexadecane (27.5 mN m^{-1}) and water (72.8 mN m^{-1}) that exhibited three different kinds of interfaces/configurations with liquid impregnated MPA (referred to as LIMPA) composite surfaces. They are (a) Spreading+Infiltration of (i) water drop on Hexadecane/Fomblin® impregnated MPA, (ii) Hexadecane drop atop water impregnated MPA; (b) Heterogeneuous two phase interfaces of (i) Hexadecane drop atop Fomblin® impregnated MPA, (ii) Fomblin® drop atop Hexadecane/water impregnated MPA; (c) Homogeneous two phase interface of water/Hexadecane drops atop Fomblin® impregnated MPA surfaces. The observed relative decreasing order of Van der Waals forces with alumina is water > Hexadecane/Dodecane > Fomblin® oil > HFE–7200 3M^{TM} also supported by the static contact angle (SCA) measurements of the liquids in three phase systems consisting of sapphire and two immiscible liquids. However, the observed decreasing order of efficient impregnating liquid is Fomblin® oil > water > Hexadecane/Dodecane. It was observed that the wetting dynamics were significantly enhanced when O_2 plasma treatment was employed to alumina surface prior to wetting studies. Further, the free energy calculations predict that the relative stability of liquid impregnated composites is linearly proportional to the spreading parameter (S) of the impregnating liquid.

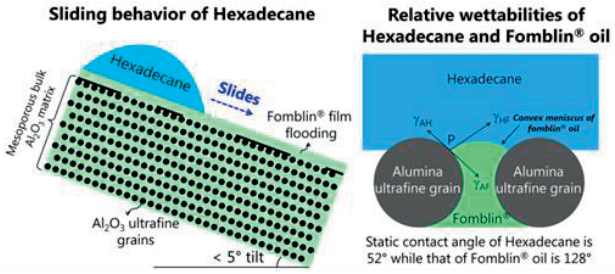

The sliding behavior of Hexadecane drop atop Fomblin® oil (perfluoroether) impregnated mesoporous alumina (left in Figure), in spite of the former liquid strongly wetting the alumina (right in Figure).

1. Introduction

The scientific treatment of "wetting of surfaces" is at least two centuries old, the famous scientific report dates back to early 1800´s and was submitted by Thomas Young.[1] Since then, this field has attracted deeper attention two times: firstly in 1930–1960´s by Wenzel et al.[2], Cassie[3], Zisman[4] and several others; and secondly end of last century by Barthlott et al.[5,6]. The rediscovery of the Lotus effect[5,6] reveals that both the surface chemistry and the surface roughness affect the wetting behavior of surfaces. There are numerous articles in this field reporting the production of artificial surfaces with micro and nano structures as well as mimicking the nature in an attempt to produce omniphobicity. However, fabrication of mechanically durable omniphobic surfaces is still an open scientific challenge in the wetting community, which could potentially find its applications in tribology, bioengineering, photovoltaics etc. To this effect, we fabricated liquid impregnated mesopo-

rous α–Al_2O_3 composites, novel material systems and investigated their wetting behavior and stability of *liquid–LIMPA composite* interfaces. The tribological results of these LIMPA composites will be presented in another report.

The liquid impregnation approach has already been employed for surface microstructured polymeric matrices and surface hydrophobisized non–polymeric matrices to achieve anti–liquid sticking behavior and is a very recent development reported in the literature as slippery liquid infused porous surfaces (SLIPS).[7] Such SLIPS have been reported to exhibit enhanced condensation[8], anti–liquid sticking behavior of optically transparent materials[9] anti–ice and anti–frost performance[10] and pressure stable omniphobicity[7]. Almost all the aforementioned liquid impregnated composite surfaces used in the literature consisted of low surface/apolar energy substrates or coatings such as PTFE,[7,11] perfluoroalkylphosphonic acid modified alumina gel,[12] PDMS based organogels,[13] partially fluorinated ionic liquid infused microtextured silica–siloxane systems,[14] fluorinated textured polypyrrole coated Al matrix,[10] fluorinated acrylate[15] etc. that are by themselves intrinsically hydrophobic or oleophobic.[7–28] However, we have explored the feasibility of using a polycrystalline MPA ceramic matrix which is intrinsically omniphilic in nature. We hypothesized and show here theoretically that the relatively higher interfacial surface tension between alumina and the employed impregnating liquids compared to aforementioned substrate materials lead to relatively stable LIMPA composites.

Additionally, we keep the MPA surfaces un–textured, without any micro features and have not carried out any surface hydrophobization on alumina surfaces. Furthermore, the MPA surfaces are polished, unlike the other literary reports to study their wetting behavior. Such polished LIMPA surfaces can be of further interest in the field of tribology.

2. Experimental Details

2.1. Alumina Samples Preparation

Commercially available ultrafine 99.5 % pure α–Al_2O_3 powders (BMA 15, Baikowski, France) with average particle diameter, d_{v50} =135–150 nm (d_{v50} means 50 vol. % of the particles have diameters smaller than 150 nm) were used to prepare ceramic slurries similar to that proposed in literature[29,30] for slip–casting. Briefly, the slurry was dried in 2 stages: first at 90 % relative humidity (RH) for 24 h and then at 45 % RH for another 24 h which finally produced mesoporous α–Al_2O_3 cuboidal and disc shaped green compacts. The green compacts were pre–sintered similar to that reported earlier[30] to produce ~60 % relative dense samples. The pre–sintered samples were sintered in air at 1150±5, 1205±5, 1250±5 °C in a tubular furnace at 10 °C min^{-1} heating rate, 1 h isothermal holding at the corresponding highest temperature to achieve 70±3, 80±3, 90±3 % theoretical densities, respectively. The open porosity and total porosity of at least 10 samples for each densification were measured using the Archimedes principle with water as the liquid medium.

2.2. Polishing Procedure

Technovit 5071, a two–component methacrylate based epoxy, Naas Werkstoffprüfung, Switzerland was used to embed sintered alumina samples for polishing the latter with diamond blades and diamond slurries obtained from Struers MD Dur™, Switzerland. Briefly, the polishing was carried out with 40 μm, 20 μm diamond blades followed by 15 min polishing with each of diamond slurries containing 15, 6, 3, 1 and 0.25 μm sized particles respectively at 150 rpm and 215–280 N normal load (0.173 to 0.226 MPa). The fully polished samples were heated to 900 °C at ~3 °C min^{-1} and holding time of 2–5 h at the highest temperature to evaporate the resin completely and burn the carbon contamination obtained from polishing. The polished samples were subsequently ultrasonicated for 20 min in ethanol bath and dried in an oven prior to carrying out wetting tests or O_2 plasma treatment or liquid impregnation.

2.3. O_2 Plasma Treatment and Liquid Impregnation

The polished 70, 80 and 90 % dense MPA sample surfaces and commercially obtained flat single crystal sapphire discs, 20 mm in diameter, (Stettler Sapphire SA, Lyss, Switzerland) were cleaned with O_2 plasma in a Plasma $PreP_2$, (GaLa Instrumente, Germany) for 15 min at 50 Hz frequency, 0.1–0.3 mbar pressure, 100 Watt and 400 cm^3 min^{-1} flow rate prior to the wetting studies or liquid impregnation so as to remove the surface hydrocarbon contamination deposits obtained from the environment.

Dodecane ($C_{12}H_{26}$), Hexadecane ($C_{16}H_{34}$), Fomblin® Y25 oil obtained from Sigma–Aldrich, Switzerland;

HFE–7200 3M™ Novec™ ($C_4F_9OC_2H_5$), 3M Belgium S.A./N.V and de–ionised water (resistivity of 12 MΩ–cm) were used as impregnating liquids. All the aforementioned liquids with respective surface tensions at 20 °C: 3M–HFE (13.6 mN m^{-1}), Fomblin® oil Y25 (22 mN m^{-1}), *n*–Dodecane (25 mN m^{-1}), *n*–Hexadecane (27.5 mN m^{-1}) and water (72.8 mN m^{-1}) wets the alumina surfaces [see Table S1, Supporting Information for SCAs]. The dynamics of impregnation, however, depend on surface contamination and liquid viscosities (will be discussed in Section 3.1).

As–sintered 70 to 90 % dense MPA samples are characterized with a higher fraction of open porosity and minor fraction of closed porosity (closed porosity is ~1 % for 70 to 90 % dense samples and the rest is open porosity) [refer to Section S2, Supporting Information for open and closed porosity data]. The average pore sizes of 70, 80 and 90 % dense samples are 47±12, 34±10 and 25±7 nm respectively and reported in our earlier article.[30]

Liquid impregnations were carried out at 23±2 °C for low viscous liquids (Dodecane, Hexadecane, HFE–7200 3M™, and water) and at 150 °C for the high viscous Fomblin® oil [refer Table S3, Supporting Information for physical properties of liquids] by completely submerging the samples for 2 h to be sure to infiltrate all the open porosity [see Table S4, Supporting Information for optimum impregnation parameters for Fomblin® oil]. Following the complete liquid impregnation, the excess impregnated viscous liquid on LIMPA composite surfaces was removed by blowing with compressed N_2 and absorbing with fiber free optical paper, referred to as *unflooded configuration*. Alternatively, a thin pure liquid film is retained atop LIMPA sample substrate completely submerging the surface roughness elements, referred to as *flooded configuration*. The thickness of the flooded film is about ~ > 500 μm as determined by weight measurements.

2.4. Samples Characterization

The microstructures of the as–sintered and surface–polished 70, 80, 90 % dense MPA samples were studied using Philips S4800 high resolution scanning electron microscope (HRSEM) in secondary electron (SE) mode at 1.5 keV acceleration voltage and 10 μA beam current without any conductive coating. As–sintered samples (70–90 % dense) do not possess surface microfeatures but possess nano roughness remaining after partial necking of ultrafine grains as shown for one representative sample of 80 % dense MPA sample (Figure 1a). The grain size distribution (Figure 1b) obtained from at least three micrographs for each densification reveals that the grain sizes after sintering are in between 50 to 300 nm. Thus, the maximum surface roughness R_z (peak to valley distance) is ~ grain size/2 = 150 nm. As–polished, 70–90 % dense MPA samples do not possess any micro features and contain heterogeneous surface microstructure as shown for one representative sample of 80 % dense MPA sample after sintering and polishing (Figure 1c). The representative surface microstructure consists of flattened debris compacted regions and porous regions nearby. The area fractions of these two regions were obtained by analyzing an equivalent 2D binary color image (Figure 1d) with Image J software. After polishing the debris compacted regions occupy about 70–75 % of the surface area indicating that a very small fraction of the surfaces remains porous (with several tens of nanometers opening wall distances) to access to the open pore network. The debris compacted regions resist harsh cleaning conditions such as 20 minutes ultrasonication in ethanol. The debris compacted regions possess much smaller pore sizes as evidenced by the HRSEM images.

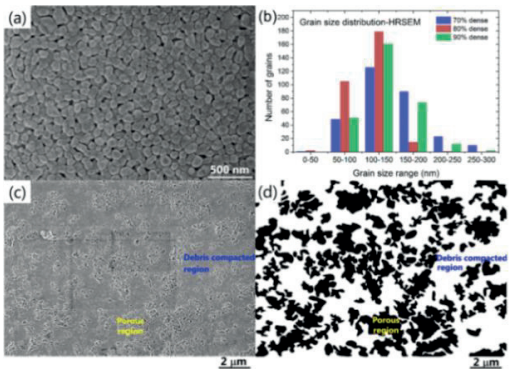

Figure 1. (a) SEM image of a 80 % dense as–sintered sample showcasing ultrafine grains and open connected porosity, (b) Grain size distribution of 70, 80 and 90 % dense alumina samples obtained from statistical treatment of measured grains imaged by SEM, (c) SEM image of an as–polished 80 % dense alumina sample and (d) equivalent binary color image of (c) representing the areas of flattened debris compacted regions (in white) and porous regions (in black).

The crystal orientation of sapphire samples was obtained using Electron Back Scattered Diffraction. The optical roughness measurements of the polished alumina samples and industrially obtained flat sapphire samples were carried out with AltiProbe Optic® Profilometer according to

the standard DIE EN ISO 4288, ASME B46.1. At least 5 measurements were taken for each sample and 3 samples for each of 70, 80, 90 % densifications, sapphire samples thus resulting in a total of 15 measurements for each densification/sample. All MPA samples possess optically non detectable sub 100 nm diameter pores within the porous regions. The optically detectable roughness (R_a) for all the samples range between 10 and 90 nm.

2.5. Wetting Characterizations

Plastic syringes, Teflon® and alkylsilane coated needles, Krüss GmbH, Germany were used for wetting studies to obtain ~2–3 µl spherical droplets of liquids. The equilibrium static contact angles (SCAs) of water, Dodecane, Hexadecane, Fomblin® oil and HFE–7200 3M™ atop non–infiltrated dry MPA, LIMPA composites and flat sapphire were characterized with a contact angle (CA) goniometer, Digidrop, France at ambient temperature (23±2 °C) and 35±10 % RH. At least 3 samples for each densification and 3 measurements of each sample were carried out for reproducibility. The temporal behaviors of drop dimensions (width, height and volume) were analyzed leading to 8 possible wetting cases, categorized as infiltration, spreading and spreading+infiltration and finally neither spreading nor infiltration (see Table S5, Supporting Information for the arrival of these 8 wetting cases).

3. Results

3.1. Wetting Behaviors and Influence of O_2 Plasma Treatment

The temporal evolution of a water drop atop single crystal ($1\bar{2}11$ plane), flat sapphire (R_a = 10±5 nm) and non–impregnated dry MPA exposed to the laboratory environment is presented in Figure 2. After a high initial CA of 67° at time t = 0 min atop sapphire surface, it continuously decreased with an average rate of 6.125°/min to an equilibrium SCA of 18° in 8 minutes (Figure 2) until complete evaporation. However, for non-impregnated dry MPA, water drop continuously infiltrates (Figure 2b and also Figure S2, Supporting Information).

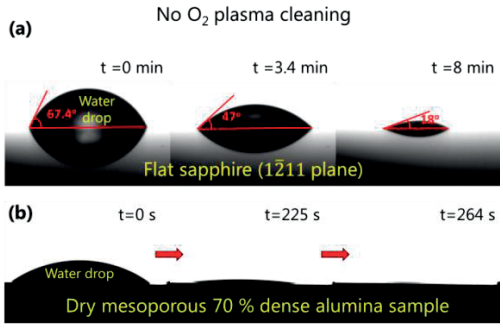

Figure 2. Optical side view pictures from a contact angle goniometer of the evolution of a water drop atop (a) flat sapphire sample ($1\bar{2}11$ plane) and (b) non–impregnated dry MPA sample exposed to the laboratory environment. It takes ~8 mins for a water drop to reach a stable SCA of 18° on a sapphire sample and takes 300 s for a water drop to completely impregnate into 70 % dense polished dry MPA sample.

The O_2 plasma treatment applied to the MPA samples modified the 2 µl water drop infiltration dynamics from 300 seconds to less than 2 seconds. A strong enhancement in infiltration dynamics was also observed for Hexadecane, much less, but still almost twice as fast for Fomblin® oil. These results are graphically summarized under dry MPA in Figure 3 on the left side of the graph.

The wetting behaviors of the polished, nanoroughened alumina based LIMPA composites were studied as a function of alumina matrix density and a variety of impregnating liquids possessing a wide range of surface tensions and viscosities. The 3 chemically different types of LIMPA composites are produced by (a) hydrocarbon impregnation: (Dodecane, Hexadecane) (b) water impregnation, and (c) long chain perfluoroether or short chain perfluoroalkyl–alkylether impregnation (Fomblin® oil (high viscous liquid), HFE–7200 3M™ (low viscous liquid)) as the second phase into the mesopores of the alumina samples. The wetting behaviors of the deposited liquid droplets (referred to as test liquids) revealed to be the same for 70, 80 and 90 % densifications, however, significant changes in the wetting dynamics were observed, which become more pronounced if the samples were treated with O_2 plasma.

The temporal evolution of the measured SCAs of the immiscible test liquid drops atop 70, 80, and 90 % dense LIMPA sample composite surfaces were obtained. The stable test liquid–LIMPA kind of interfaces (refer Sections 3.2 and 3.3 for stable interfaces) were unaltered by employing O_2 plasma treatment. However, O_2 plasma treatment influenced the wetting dynamics for infiltration and spread-

ing cases in LIMPA samples as shown in Figure 3 on the right side of the graph. A water drop atop unflooded Fomblin® impregnated MPA surface takes only ~ 57.4 s to completely infiltrate+spread (Figure 3 and Figure S3, Supporting Information) after the plasma cleaning whereas it took ~300 s without plasma treatment (Figure 2b, Figure 3). The enhancement in the wetting dynamics was also observed with a water drop atop Hexadecane impregnated MPA surface (Figure 3). The organic, oily liquid Hexadecane drop infiltrates and replaces water from the water impregnated 90 % dense MPA both with and without employing O_2 plasma treatment to the MPA samples in ~ 100 s and ~20 s respectively (Figure 3). However, for 70 and 80 % dense water impregnated MPA composites, Hexadecane drops formed a stable interface.

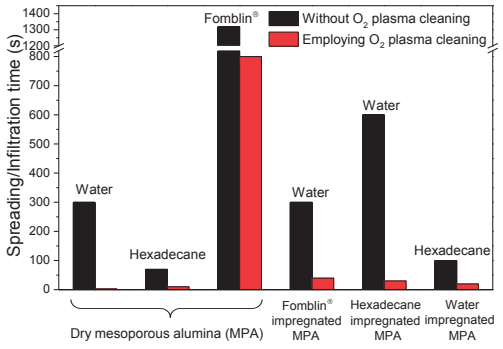

Figure 3. The spreading and infiltration dynamics of various test liquids: water, Hexadecane and Fomblin® oil atop non–infiltrated dry and LIMPA samples with and without employing O_2 plasma treatment to the alumina samples prior to impregnation and wetting tests.

In order to avoid confusion, we present the resume of the results ordered schematically in Figure 4, with detailed description of the cases afterwards. The respective changes in the width, height and volume of the test liquid drop as a function of time resulted in the distinction of the following cases presented schematically in Figure 4a, where the test liquid forms a homogeneous two phase interface with impregnating liquid alone and exhibiting sliding behavior for sample tilt < 5°. However, when water was used as the impregnating liquid, Fomblin® test liquid formed a stable interface as shown in Figure 4b, but exhibiting no sliding. Also Fomblin® oil forms a stable interface atop Hexadecane/water impregnated MPA samples and Hexadecane forms a stable interface atop Fomblin® impregnated MPA composite surfaces. However, the water drop spreads and infiltrates (Figure 4c) into Fomblin® impregnated unflooded MPA samples. Similar behavior was observed for water drop atop Hexadecane/Dodecane impregnated MPA samples. The test liquid in such a case replaces the impregnating liquid.

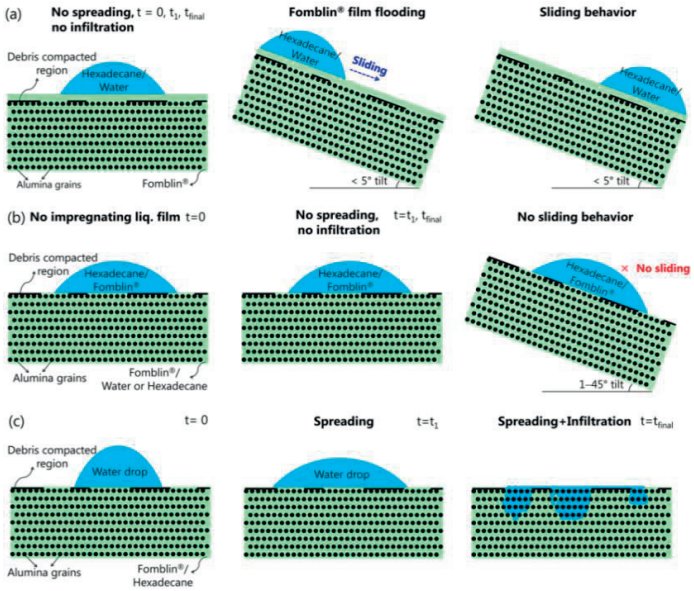

Figure 4. Schematic diagrams (not to scale) showcasing a variety of test liquid (blue color)–LIMPA composite interfaces as a function of time from left to right and sample tilt. The cases of (a) Stable interface with sliding behavior, (b) Stable interface, but no sliding behavior and (c) Spreading+Infiltration are shown.

3.2. Stable Interfaces With Sliding Behavior

When the impregnating Fomblin® oil floods the MPA surface, Hexadecane and water drops form a stable two phase interface with stable SCAs as shown schematically in Figure 4a and presented in Figure 5. Since, the interface is a liquid–liquid interface, the test liquid drops slide on such flooded surfaces with a slight inclination of ≤ 5° of sample tilt. A water drop makes a stable SCA of 70° atop Fomblin® impregnated *flooded* 70 % dense polished MPA sample surface (3° tilt) and slides 2 mm distance in 29.4 s as shown in Figure 5b [see also Video S1, Supporting Information]. Similar sliding behaviors were also observed in 80 and 90 % dense Fomblin® impregnated MPA samples.

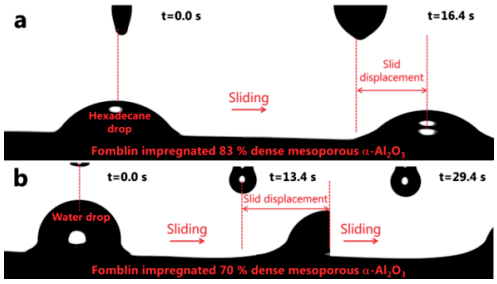

Figure 5. Selected optical pictures of a high speed camera video sequence demonstrating the sliding behavior of (a) a Hexadecane drop atop 3° tilted Fomblin® impregnated (flooded configuration), polished 83 % dense MPA sample as a function of time, (b) a water drop atop 3° tilted Fomblin® impregnated (flooded configuration), polished 70 % dense MPA sample as a function of time.

3.3. Stable Interfaces, But No Sliding Behavior

For Fomblin® impregnated unflooded MPA samples, a Hexadecane drop forms a stable interface, with a stable SCA of 53° which does not change as a function of time (Figure 6a). The Hexadecane drop does not slide when the sample surface is tilted to 45°. A similar behavior is observed when the test liquid and the impregnating liquid are reversed, i.e. Fomblin® oil forms a stable SCA of 22° (Figure 6b) atop a Hexadecane impregnated MPA surface. The Fomblin® drops do not slide on the inclined Hexadecane impregnated MPA surfaces neither. Also, Fomblin® drops formed a stable interface atop water impregnated MPA samples with an equilibrium SCA of ~ 18° (see Figure S4, Supporting Information).

3.4. Infiltration + Spreading in LIMPA Composites

A water drop decreases its contact angle from 34° to 0° atop Fomblin® impregnated unflooded surface as a function of time (Figure 6c). The water drop spreads and infiltrates parallel to evaporation [see Figure S5, Supporting Information for individual spreading and infiltration temporal evolutions] atop both the Fomblin® impregnated unflooded and Hexadecane impregnated MPA composite surfaces as also schematically expressed in Figure 4c.

Briefly, the order of efficient impregnating liquid into MPA samples to have a stable test liquid–LIMPA composite interface and have sliding behavior of the test liquids is Fomblin® oil > water > Hexadecane/Dodecane.

4. Discussion

From Figure 3, we can observe that the viscosity of a liquid plays a major role in the observed wetting dynamic differences, comparing the infiltration times of Fomblin® oil [see also Figure S6, Supporting Information] and water. Another contribution to the wetting dynamics comes from the cleaniness of the MPA samples. It is well known that hydrocarbon contamination[31–33] of surfaces, especially that of high surface energy/polar materials can significantly alter the wetting response.

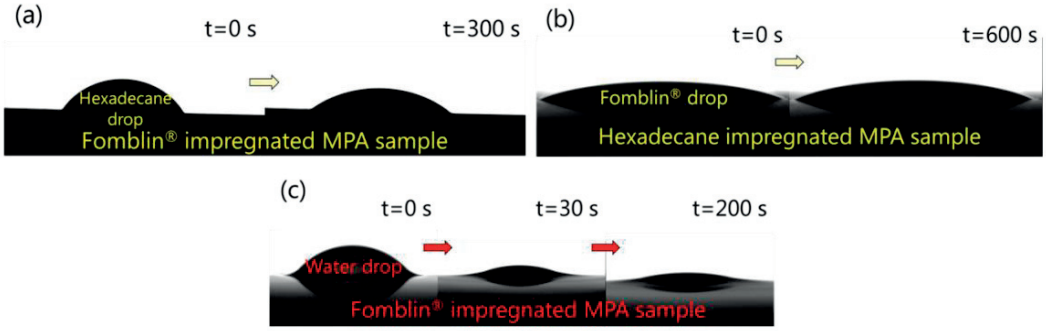

Figure 6. Side view video pictures at indicated times t in seconds of (a) a Hexadecane drop atop a Fomblin® impregnated MPA surface, (b) a Fomblin® drop atop Hexadecane impregnated MPA surface, (c) a water drop atop Fomblin® impregnated unflooded MPA surface.

Sapphire has a low surface energy of ~ 53 mJ m^{-2},[34] but has high polar contributions ($\gamma^- = \gamma^+ = 25.5$ mN m^{-1})[35] and hence could also have surface hydrocarbon contamination. Similarly, the surface energy of polycrystalline $\alpha-Al_2O_3$ is 44.8 mJ m^{-2} with $\gamma^{LW} = 43.7$ mJ m^{-2}, $\gamma^+ = 0.004$ mJ m^{-2} and $\gamma^- = 80.4$ mJ m^{-2}, respectively which could thus have surface hydrocarbon contamination. The high water SCA at t = 0 min atop sapphire surface and a non zero equilibrium SCA as shown in Figure 2a, are indications of surface hydrocarbon contamination.

4.1. Stability of *Test Liquid– LIMPA Composite* Interfaces

Having studied the stability of *test liquid–LIMPA composite* interfaces experimentally, it is of scientific interest to be able to predict the stability of such an interface. Wong et al.,[7] and Smith et al.,[8,16] proposed to predict the stability of surface microstructured liquid impregnated surfaces based on the minimization of Gibbs´s free energy approach. The following equations proposed by Wong et al.,[7]: $r_w(\gamma_i cos\theta_{is} - \gamma_t cos\theta_{ts}) - \gamma_{it} > 0$ and $r_w(\gamma_i cos\theta_{is} - \gamma_t cos\theta_{ts}) + \gamma_t - \gamma_i > 0$ describe the design criteria necessary to form a stable interface where r_w= Wenzel roughness factor of MPA surfaces (ratio of true to apparent surface area) and measured using an optical profilometer. The measured r_w values are 1.018±0.005 with no measurable differences among 70, 80 and 90 % dense, polished alumina samples, respectively, and γ_i, γ_t are surface tensions of the impregnating and the test liquids in air, θ_{is},θ_{ts} are equilibrium SCAs of impregnated and test liquid with the flat solid matrix material surface and γ_{it} is the interfacial surface tension between the impregnated and the test liquid respectively. Smith et al.[16], proposed that $\theta_{is(a)} = 0$ and $\theta_{is(t)} = 0$ are necessary conditions to have a stable interface and to exhibit sliding behavior by the test liquids. If $\theta_{is(a)} = 0$ and $0 < \theta_{is(t)} = cos^{-1}(\frac{1-\emptyset}{r_w-\emptyset})$, then the interface is stable, but the test drops do not slide on LIMPA surfaces; where, ϕ is debris compacted region area fraction, $\theta_{is(a)}$ and $\theta_{is(t)}$ are equilibrium SCAs of impregnating liquid with the solid in air and test liquid media, respectively. Table 1 summarizes the theoretical predictions and the experimental observations of stability of *test liquid–LIMPA composite* interfaces in 70, 80 and 90 % dense LIPMA composites. Theoretical prediction as per Wong et al.,[7] is experimentally validated for all the combinations of *test liquid–LIMPA composite interfaces* except for Hexadecane/Dodecane drop atop Fomblin®/water impregnated MPA surfaces (Table 1). However, this theory is also not capable of predicting the configuration of test liquid atop LIMPA composite surface for a stable interface. A more detailed theory was proposed by Smith et al.,[16] which not only predicts the stability, but also predicts the configurations of test liquids atop LIMPA composite surfaces. This theory predicts that the test liquid replaces impregnating liquid in all the cases of LIMPA composites except for Fomblin® drop atop Hexadecane/Dodecane impregnated MPA (Table 1). However, among 4 out of the 7 cases, this theory predicts wrongly as evidenced from the experimental observations (Sections 3.2, 3.3 and 3.4).

Table 1. Theoretical predictions and experimental observations of stability of *test liquid–LIMPA composite* interfaces

Impregnated liquid	**Test liquid**	**Theoretical prediction– by Wong et al.,[7]**	**Theoretical prediction– by Smith et al.,[16]**	**Experimental observations**
3M–7200	Water	No stable interface	Test liquid replaces impregnating liquid	Test liquid replaced impregnating liquid
Fomblin®	Water	No stable interface		Stable film when Fomblin® floods MPA surface and water replaces Fomblin® for no excess Fomblin® film
	Hexadecane/Dodecane	No stable interface		*Stable interface*
Water	Fomblin®	Stable interface		Stable interface
	Hexadecane/Dodecane	Stable interface		May or may not be unstable (drop spreads)
Hexadecane/Dodecane	Water	No stable interface		Test liquid replaced impregnating liquid
	Fomblin®	Stable interface	May or may not be stable	Stable interface

Among the 4 cases wrongly predicted, it is noteworthy that the stability of Hexadecane–Fomblin® impregnated MPA composite interface is wrongly predicted by both the theories. This could be because, the theories proposed were based on the free energy calculations and did not consider the three phase contact line and curvature effects in solid–liquid, liquid–liquid interfaces. The force balance equation based on interfacial surface tensions may lead to better prediction of the stability of such interfaces. Another reason for the failure of the predictions is the kinetics of the process until it would reach the thermodynamic equilibrium.

4.2. Proposed Mechanisms For Wetting Behavior of LIMPA Composites

The interfacial surface tension (γ_{12}) between two components 1 and 2 having surface tensions γ_1 and γ_2 can be calculated using van Oss–Choudary–Good Equation (1)[35] and are tabulated for alumina–liquid systems along with their corresponding calculated spreading coefficients, S ($S = \gamma_{sa} - \gamma_{sl} - \gamma_l$) in Table 2.

$$\gamma_{12} = (\sqrt{\gamma_1^{LW}} - \sqrt{\gamma_2^{LW}})^2 + 2(\sqrt{\gamma_1^+\gamma_1^-} + \sqrt{\gamma_2^+\gamma_2^-} - \sqrt{\gamma_1^+\gamma_2^-} - \sqrt{\gamma_1^-\gamma_2^+}) \quad (1)$$

where LW=Lifshitz–Van der Waals /apolar interactions and + indicates electron acceptor component and – indicates electron donor component of surface tension.

The direction of interfacial surface tension at the solid–liquid contact line is into the liquid drop[1]. Hence, by convention, positive interfacial tension values indicate weak Van der Waals attractive forces and the negative values indicate stronger Van der Waals attractive forces respectively. Therefore, the predicted decreasing order of Van der Waals attractive forces with alumina is Water > Hexadecane > Dodecane > 3M–HFE > Fomblin® oil.

Table 2. Calculated spreading coefficients of liquid on ideal flat alumina sample and interfacial surface tensions of alumina–liquid systems

α-Al_2O_3 (Liquid)	Spreading coefficient (S)	Interfacial surface tension (mN m^{-1})
α-Al_2O_3 – Water	7.35	-35.35
α-Al_2O_3 – Hexadecane	14.3	3.002
α-Al_2O_3 – Dodecane	15.83	3.62
α-Al_2O_3 – 3M-HFE	10.72	20.48
α-Al_2O_3 – Fomblin®	12.26	10.54

From the Results Section 3.4, it can be clearly concluded that water exhibited stronger Van der Waals attractive forces with alumina than that of Fomblin® oil based on it´s infiltration behavior in spite of its relatively lower density than Fomblin® oil. Also, Hexadecane has stronger Van der Waals attractive forces with alumina than Fomblin® oil due to the formation of stable interface between Fomblin® oil and Hexadecane impregnated MPA surface (Figure 6b), in spite of Fomblin® oil being the heavier liquid. However, sliding of Fomblin® oil atop Hexadecane impregnated MPA (Figure 6b) does not occur because Hexadecane may have formed one or few monolayers on alumina surface. However, based on the infiltration behavior of water into dry non–impregnated MPA (Figure 2b) and the infiltration of Hexadecane into water impregnated MPA only in 90 % dense MPA, one can conclude that the water and Hexadecane liquids may have comparable Van der Waals attractive forces with alumina. Hence, the experimentally observed decreasing order of Van der Waals attraction forces between alumina and the liquids is water ≈ Hexadecane > Fomblin® oil which is in very good agreement with that predicted by calculating interfacial surface tensions of alumina with the corresponding liquids.

Table 3. Equilibrium SCA measurements in three phase systems

System	**Liquid**	**SCA with sapphire (°)**	**Schematic diagram of three phase system**
Fomblin®–Hexadecane–Sapphire	Fomblin® oil	128±3	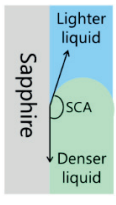
Hexadecane–Water–Sapphire	Water	88±4	
Fomblin®–Water–Sapphire	Fomblin® oil	120±4	

To further validate the Van der Waals tendencies through direct experimental evidences, equilibrium SCAs of the two immiscible liquids (test and impregnating) with the sapphire surface were measured at the interface of two liquids and are tabulated for the three 3 phase systems (Table 3). It can be concluded based on the SCA measurements that water wets sapphire slightly stronger than Hexadecane and Hexadecane wets very strongly than Fomblin® oil respectively. Therefore, the attractive tendency of liquids with sapphire is of the following order: water > Hexadecane > Fomblin® oil which is in very good agreement with the order deduced from the observed stability of test liquid–LIMPA interfaces and also the theoretical interfacial surface tension calculations. The wetting behaviors in polycrystalline α–Al_2O_3 will be similar to sapphire or even more strongly attracting the liquids due to higher polar component as mentioned in the aforementioned text.

A Hexadecane drop atop Fomblin® impregnated MPA does not replace impregnated Fomblin® oil (Figure 6a), due to its lower density (density of Hexadecane = 0.775 g cm^{-3} and Fomblin® density =1.9 g cm^{-3}), although Hexadecane has relatively stronger Van der Waals attractive forces with alumina than that of Fomblin® oil. However, local preferential wetting of alumina with Hexadecane might occur, thus leading to a heterogeneous interface between Hexadecane and Fomblin® impregnated unflooded MPA composite surface. Such heterogeneous interface comprises of Hexadecane–alumina and Hexadecane–Fomblin® oil interfaces. Thus, the pinning forces of the alumina restrict the sliding behavior of the Hexadecane drop atop such a heterogeneous interface.

Water and Hexadecane liquids have relatively competing Van der Waals attraction forces with sapphire as evidenced 88° SCA (Table 3). These competing tendencies can also explain the dual behaviors (infiltration, stable interface) of Hexadecane drop atop water impregnated MPA systems as mentioned in the Section 3.1. On the other hand, water always infiltrates into Hexadecane impregnated MPA because water is heavier in addition to the slightly stronger Van der Waals attraction forces. Similarly, in water drop atop Fomblin® impregnated MPA sample, although water is less dense than Fomblin® oil, but infiltrates into Fomblin® impregnated MPA composite because of the very strong Van der Waals attraction forces. On the contrary, for water impregnated MPA, the water viscosity is quite low, and hence there is no flooding water film remaining on the alumina surface as the water drains out through the open porosity of the alumina matrix. A very thin water layer remaining as the adsorbate in the form of hydroxyl groups on the alumina surface is inefficient in avoiding sufficiently the strong attractive interactions of Fomblin® oil–alumina, to allow sliding on the water impregnated surfaces.

In brief, we can conclude that the relative Van der Waals attraction of liquids with alumina is in the order water > Hexadecane > Dodecane > Fomblin® oil. Having studied the wetting behavior of LIMPA composites, it would be of scientific interest to find out the relative thermodynamic stability of LIMPA composites with that of conventional liquid impregnated polymeric matrices which will be discussed in the following Section 4.3.

4.3. Thermodynamic Stability of LIMPA Composites

After successfully demonstrating stable *test liquid–LIMPA composite interfaces,* especially without having needed any surface hydrophobisization which is a significant step to carry out severe mechanical durability tests, it would be of scientific interest to study the relative thermodynamic stability of liquid impregnated solid matrix composites. Although there was a recent study showing the usage of anodic alumina[36] as the matrix material, polycrystalline MPA has an added advantage of high mechanical strength. Hence, the relative thermodynamic stability of liquid impregnated solid matrices was evaluated by developing the free energy equations for the same.

The change in free energy due to the liquid impregnation into an MPA/any solid matrix is hereby termed as impregnation free energy (ΔE_{imp}). The following Equations (2)–(6) are developed to obtain ΔE_{imp}, which describes whether the liquid impregnated composite is thermodynamically stable or not. The negative values of ΔE_{imp} indicate thermodynamically stable liquid impregnated composites. The initial free energies of a cubic unit volume of porous solid matrix ($E_{i,ps}$) and unit volume of impregnating liquid (equivalent volume of spherical drop with radius r), prior to impregnation are expressed by Equations (2)–(3).

$$E_{i,\,ps} = \gamma_s \times SSA_{pores} \times \rho_{ps} \qquad (2)$$

Table 4. Parameter, parameter definition and the corresponding values at 20 °C and atmospheric pressure (101325 Pa) used in Equations 2–6.

Parameter	Parameter definition	Value (experimentally measured/ obtained from literature/calculated)
γ_s	Surface energy of solid in air	53 mJ m^{-2} for sapphire[34] 44.7 mJ m^{-2} for α–Al_2O_3 (calculated) Other solids [Table S6, Supporting Information]
γ_l	Surface tension of impregnated liquid in air	13.6 mN m^{-1} to 72 mN m^{-1} (HFE 7200 3M–water) [Table S6, Supporting Information]
γ_{sl}	Interfacial surface tension of solid and impregnated liquid	-64.08 to 51.33 mN m^{-1} [Table S7, Supporting Information] (calculated)
SSA_{pores}	Specific surface area of porous solid	70 % dense MPA – 8.98 to 11.045 m^2 g^{-1}, 80 % dense MPA – 8.362 m^2 g^{-1} 90 % dense MPA – 4.249 m^2 g^{-1} (measured)
ρ_{ps}	Density of porous solid	2.7909 g cm^{-3}, 3.1896 g cm^{-3}, 3.5883 g cm^{-3} for 70, 80 and 90 % dense MPA samples respectively (measured)
ρ_s	Density of 100 % dense solid	3.987 g cm^{-3} (α–Al_2O_3)
S	Spreading coefficient	Figure 8b, Table 2

$$E_{i,l} = \frac{3\gamma_l}{r} \quad (3)$$

where $r = \left[\frac{3(1-\rho_{ps}/\rho_s)}{4\pi}\right]^{1/3}$. The total final energy ($E_{f,LIS}$) of the unflooded LIMPA composites, post impregnation can be expressed by Equation (4).

$$E_{f,LIS} = \gamma_{s,l} \times SSA_{pores} \times \rho_{ps} + 6r\gamma_l \quad (4)$$

Hence, the impregnating free energy, ΔE_{imp} ($\Delta E_{imp} = E_{f,LIS} - E_{i,ps} - E_{i,l}$) of the unflooded LIMPA composite can be expressed by Equation (5), a further development into Equation (6) shows the linear dependency on the spreading parameter (S) of the impregnating liquid, all the parameters in Equations 2–6 are tabulated in Table 4.

$$\Delta E_{imp} = (\gamma_{s,l} - \gamma_s) SSA_{pores}\, \rho_{ps} + 6r\gamma_l - 3\gamma_l \left[\frac{4\pi}{3(1-\rho_{ps}/\rho_s)}\right]^{1/3} \quad (5)$$

$$\Delta E_{imp} = SSA_{pores}\rho_{ps} S + \gamma_l SSA_{pores}\rho_{ps} + 6r\gamma_l - 3\gamma_l \left[\frac{4\pi}{3(1-\rho_{ps}/\rho_s)}\right]^{1/3} \quad (6)$$

Free energy of impregnation (ΔE_{imp}) for 60, 70, 80 and 90 % dense MPA samples were calculated and plotted in Figure 7 with corresponding values for mesoporous PTFE, an example of low surface energy material often used in literature. It can be observed from Figure 7 that higher the open porosity, higher is the impregnation energy. It is also evident that alumina matrix has the higher driving force than PTFE matrix for liquid impregnation, based on higher negative values of impregnation energy. Thus, it is even easier for an impregnating liquid to stay stably in MPA than that of mesoporous PTFE. However, the ease of test liquids having high Van der Waals forces of attraction with alumina is relatively higher than that for PTFE ($\gamma_{Alumina-water}$ = –35.348 mN m^{-1}, while $\gamma_{PTFE-water}$ = 51.192 mN m^{-1}) and can hence might have unstable liquid interfaces with LIMPA surfaces. Hence, a careful and appropriate selection of impregnating liquids is necessary.

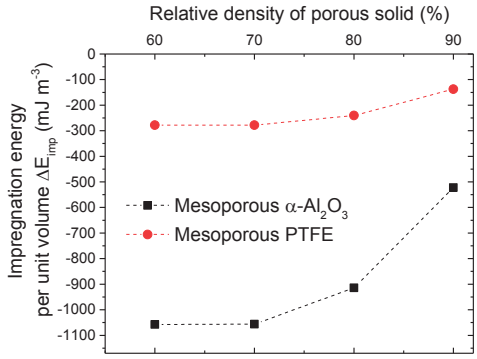

Figure 7. Specific energy (energy per unit cubic meters volume) difference calculated using Equation 5 for Fomblin® oil impregnated MPA and corresponding mesoporous PTFE as a function of matrix relative density. A very high energy difference between Fomblin® impregnated MPA and that of mesoporous PTFE clearly indicates that the Fomblin® oil impregnated MPA is thermodynamically more stable than Fomblin® oil impregnated PTFE.

Also, plotted is the impregnation energy as a function of matrix surface energy (Figure 8a) and no special trend can be observed for surface energies between 17 to 47 mJ m^{-2}. Hence, a higher surface energy matrix does not necessarily possess higher impregnation energy. However, when the impregnation energy is plotted as a

function of spreading parameter of Fomblin® oil atop different matrix flat solid surfaces, a perfectly linear behavior was observed (Figure 8b). The higher the negative spreading parameter (S), the higher negative values of impregnation energies are achieved. Thus, a higher negative spreading parameter leads to more favorable thermodynamic impregnation condition.

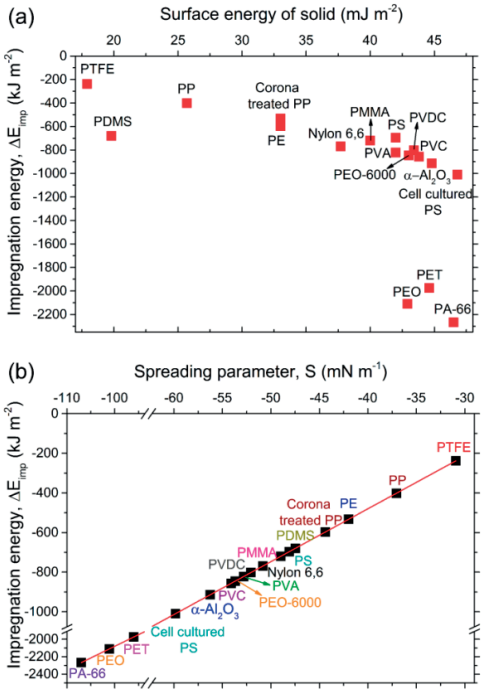

Figure 8. Impregnation energy (ΔE_{imp}) of Fomblin® oil impregnated 80 % dense matrix composite calculated using Equation 6 and plotted as a function of (a) matrix solid surface energy for different materials having surface energies from ~17 to 47 mJ m^{-2} respectively, which shows no special behavior and (b) spreading parameter (S) of Fomblin® oil on different matrix flat solid materials exhibiting a perfectly linear trend. It is observed that, a higher negative spreading parameter results in higher negative impregnation energy. Hence, impregnation of mesoporous PET is more thermodynamically favored as compared to that of MPA and that of mesoporous PTFE respectively.

Hence, the thermodynamic stability of impregnated composites is in the order Polyamide (PA–66) > Polyethyleneoxide (PEO) > Polyethyleneterephthalate (PET) > cell cultured Polystyrene (PS) > α–Al_2O_3 > Polyvinylchloride (PVC) > Polyvinylalcohol (PVA) > Polyvinylidene chloride (PVDC) > Nylon 6, 6 > Polymethylmethacrylate (PMMA) > PS > Polydimethylsiloxane (PDMS) > corona treated Polypropylene (PP) > Polyethylene (PE) > PP > PTFE (Figure 8b).

Hence, it is possible to calculate the spreading parameters and predict the relative thermodynamic stability of liquid impregnated composites. The calculated spreading parameters of various liquids with α–Al_2O_3 (Table 2) indicate that the stability of LIMPA composites is in the order α–Al_2O_3–water > α–Al_2O_3–HFE–7200 3M™ > α–Al_2O_3–Fomblin® > α–Al_2O_3–Hexadecane > α–Al_2O_3–Dodecane. This thermodynamic stability prediction is also valid in other material systems and can be useful to design novel liquid impregnated matrix composites.

Briefly, the stability of LIMPA composites depends not solely on the solid surface energy, but also on the interfacial surface tension of solid matrix–impregnating liquid.

5. Summary and Conclusions

Anti–sticking and sliding behaviors of the test liquids atop LIMPA composite surfaces have been successfully obtained without the need of carrying out any surface hydrophobization, unlike the most literature. The relative order of the Van der Waals´s attractive forces of liquids with alumina is in the order: water > Hexadecane > Dodecane > Fomblin® oil> HFE–7200 3M™ obtained by calculating the interfacial solid–liquid surface tensions, which matches perfectly well with the static CA measurements of the liquids in three phase systems. Also, the aforementioned order is in conjunction with the observed infiltration behaviors of test liquids into selected LIMPA composites replacing the respective impregnating liquids. However, the thermodynamic stability of LIMPA composites is in the order: α–Al_2O_3–water > α–Al_2O_3–HFE–7200 3M™ > α–Al_2O_3–Fomblin® > α–Al_2O_3–Hexadecane > α–Al_2O_3–Dodecane. The aforementioned order is because, the thermodynamic stability not only depends on the interfacial solid–liquid surface tension, but also depends on the solid surface energy and liquid surface tensions respectively, and mathematically, a linear function of the spreading parameter.

However, the order of efficient impregnating liquid to achieve the sliding behavior of test liquids is Fomblin® oil > water > Hexadecane/Dodecane. Although Fomblin® oil is thermodynamically not the best impregnating liquid for MPA samples, it is a better impregnating liquid for kinetic reasons due to its very high viscosity, in agreement with literature[7,12]. In case of spreading and infiltration behaviors, the wetting dynamics are significantly enhanced by employing O_2 plasma treatment to the alumina surfaces. Such plasma treatment is anticipated to

remove hydrocarbon contamination from surfaces in agreement with the literature[31–33].

The proposed theories from the literature[7,16] based on the free energy minimization could not fully predict the stability of all the *test liquid–LIMPA composite* interfaces. Therefore, we proposed to explain our experimental observations based on the force balance approach of interfacial surface tensions at the three phase contact line in the three phase systems (alumina–impregnating liquid–test liquid). The SCA measurements of the liquids in a three phase system containing sapphire and respective two liquids aided to determine the adapted liquid curvatures at the ultrafine alumina grain surface to obtain the force balance diagram.

Further, the relative stability of Fomblin® oil impregnated composites (alumina/polymer based matrices) can be theoretically predicted based on free energy calculations and indicates that the Fomblin® impregnated MPA is more stable than that of mesoporous PTFE thus allowing ceramics as future matrix materials for the liquid impregnation approach. It further predicts that the impregnation energy, which determines the stability of LIMPA composite is a linear function of spreading parameter (S) of the impregnating liquid.

Supporting Information

The supporting information contains: (i) Equilibrium static CAs of liquids with sapphire with and without employing O_2 plasma treatment of the sapphire surface, (ii) Open and closed porosity data of MPA samples, (iii) Physical properties of the materials used, (iv) Fomblin® oil impregnation parameters, (v) infiltration and spreading classifications based on change in width, height and volume of test liquid drop, (vi) Volume, height and width changes of water drop atop non–infiltrated dry MPA, (vii) Wetting dynamics of water drop atop O_2 plasma treated Fomblin® impregnated MPA sample, (viii) Equilibrium SCA of Fomblin® oil drop atop water impregnated MPA samples, (ix) Volume, height and width changes of water drop atop Fomblin® impregnated unflooded MPA, (x) Effect of viscosity on impregnation dynamics, (xi) Surface energies/tensions and their components of materials in the study and the calculated interfacial surface tension between the liquids. The supporting information is attached as Appendix B at the end of the thesis.

Author Contributions

Rowthu Sriharitha performed all the experiments, proposed and carried out all the calculations and written down the complete manuscript. Edin E. Balic wrote the funding proposal for the project, followed the project updates and reviewed the manuscript. Patrik Hoffmann supervised the project, had technical and scientific discussions throughout and strongly contributed to the revision of the manuscript.

Funding Information

The project was mainly funded by CCMX, Switzerland with project number 5211.00093.100.01. We thank Bobst, Switzerland, CCMX industrial partner for partially funding the project.

Acknowledgements

We thank Prof. Paul Bowen, LTP, EPFL for aiding in the slip casting process. We thank Dr. Kilian Wasmer, Empa Thun for providing the sapphire discs. We acknowledge Dr. Muralikrishna Dibbanti, Bridgestone for providing the feedback on the manuscript. We thank Dr. Fatemeh Saeidi, Empa Thun for few technical discussions.

References

(1) Young, T. An Essay on the Cohesion of Fluids. *Philosophical Transactions of the Royal Society of London* **1805**, 65–87.

(2) Wenzel, R. N. Resistance of Solid Surfaces to Wetting by Water. *Industrial \& Engineering Chemistry* **1936**, *28*, 988–994.

(3) Cassie, A. B. D.; Baxter, S. Wettability of Porous Surfaces. *Trans. Faraday Soc.* **1944**, *40*, 546–551.

(4) Fowkes, F. M.; Zisman, W. A.; others. Contact Angle, Wettability, and Adhesion. **1964**.

(5) Barthlott, W.; Neinhuis, C. Purity of the Sacred Lotus, or Escape from Contamination in Biological Surfaces. *Planta* **1997**, *202*, 1–8.

(6) Neinhuis, C.; Barthlott, W. Characterization and Distribution of Water-Repellent, Self-Cleaning Plant Surfaces. *Annals of Botany* **1997**, *79*, 667–677.

(7) Wong, T.-S.; Kang, S. H.; Tang, S. K.; Smythe, E. J.; Hatton, B. D.; Grinthal, A.; Aizenberg, J. Bioinspired Self-Repairing Slippery Surfaces with Pressure-Stable Omniphobicity. *Nature* **2011**, *477*, 443–447.

(8) Anand, S.; Paxson, A. T.; Dhiman, R.; Smith, J. D.; Varanasi, K. K. Enhanced Condensation on Lubricant-Impregnated Nanotextured Surfaces. *Acs Nano* **2012**, *6*, 10122–10129.

(9) Ganesh, V. A.; Safari, S.; Jayaraman, S.; Sridhar, R.; Raut, H. K.; Góra, A.; Baji, A.; Nair, S.; Ramakrishna, S. One-Step Fabrication of Robust and Optically Transparent Slippery Coatings. *RSC Adv.* **2014**, *4*, 55263.

(10) Kim, P.; Wong, T.-S.; Alvarenga, J.; Kreder, M. J.; Adorno-Martinez, W. E.; Aizenberg, J. Liquid-Infused Nanostructured Surfaces with Extreme Anti-Ice and Anti-Frost Performance. *ACS Nano* **2012**, *6*, 6569–6577.

(11) Yao, X.; Hu, Y.; Grinthal, A.; Wong, T.-S.; Mahadevan, L.; Aizenberg, J. Adaptive Fluid-Infused Porous Films with Tunable Transparency and Wettability. *Nat Mater* **2013**, *12*, 529–534.

(12) Ma, W.; Higaki, Y.; Otsuka, H.; Takahara, A. Perfluoropolyether-Infused Nano-Texture: A Versatile Approach to Omniphobic Coatings with Low Hysteresis and High Transparency. *Chemical Communications* **2013**, *49*, 597–599.

(13) Urata, C.; Dunderdale, G. J.; England, M. W.; Hozumi, A. Self-Lubricating Organogels (SLUGs) with Exceptional Syneresis-Induced Anti-Sticking Properties against Viscous Emulsions and Ices. *Journal of Materials Chemistry A* **2015**, *3*, 12626.

(14) Miranda, D. F.; Urata, C.; Masheder, B.; Dunderdale, G. J.; Yagihashi, M.; Hozumi, A. Physically and Chemically Stable Ionic Liquid-Infused Textured Surfaces Showing Excellent Dynamic Omniphobicity. *APL Materials* **2014**, *2*, 056108.

(15) Lafuma, A.; Quéré, D. Slippery Pre-Suffused Surfaces. *EPL (Europhysics Letters)* **2011**, *96*, 56001.

(16) Smith, J. D.; Dhiman, R.; Anand, S.; Reza-Garduno, E.; Cohen, R. E.; McKinley, G. H.; Varanasi, K. K. Droplet Mobility on Lubricant-Impregnated Surfaces. *Soft Matter* **2013**, *9*, 1772–1780.

(17) Tsuruki, Y.; Sakai, M.; Isobe, T.; Matsushita, S.; Nakajima, A. Static and Dynamic Hydrophobicity of Alumina-Based Porous Ceramics Impregnated with Fluorinated Oil. *Journal of Materials Research* **2014**, *29*, 1546–1555.

(18) Eifert, A.; Paulssen, D.; Varanakkottu, S. N.; Baier, T.; Hardt, S. Simple Fabrication of Robust Water-Repellent Surfaces with Low Contact-Angle Hysteresis Based on Impregnation. *Advanced Materials Interfaces* **2014**, *1*, 1300138.

(19) Grinthal, A.; Aizenberg, J. Mobile Interfaces: Liquids as a Perfect Structural Material for Multifunctional, Antifouling Surfaces. *Chemistry of Materials* **2013**, *26*, 698–708.

(20) Sunny, S.; Vogel, N.; Howell, C.; Vu, T. L.; Aizenberg, J. Lubricant-Infused Nanoparticulate Coatings Assembled by Layer-by-Layer Deposition. *Advanced Functional Materials* **2014**, *24*, 6658–6667.

(21) Urata, C.; Masheder, B.; Cheng, D. F.; Hozumi, A. Unusual Dynamic Dewetting Behavior of Smooth Perfluorinated Hybrid Films: Potential Advantages over Conventional Textured and Liquid-Infused Perfluorinated Surfaces. *Langmuir* **2013**, *29*, 12472–12482.

(22) Kim, P.; Kreder, M. J.; Alvarenga, J.; Aizenberg, J. Hierarchical or Not? Effect of the Length Scale and Hierarchy of the Surface Roughness on Omniphobicity of Lubricant-Infused Substrates. *Nano letters* **2013**, *13*, 1793–1799.

(23) Yu, R.; Jacobi, A. M. Self-Healing, Slippery Surfaces for HVAC\&R Systems. **2014**.

(24) Vogel, N.; Belisle, R. A.; Hatton, B.; Wong, T.-S.; Aizenberg, J. Transparency and Damage Tolerance of Patternable Omniphobic Lubricated Surfaces Based on Inverse Colloidal Monolayers. *Nature communications* **2013**, *4*.

(25) Liu, Q.; Wang, X.; Yu, B.; Zhou, F.; Xue, Q. Self-Healing Surface Hydrophobicity by Consecutive Release of Hydrophobic Molecules from Mesoporous Silica. *Langmuir* **2012**, *28*, 5845–5849.

(26) Manabe, K.; Nishizawa, S.; Kyung, K.-H.; Shiratori, S. Optical Phenomena and Antifrosting Property on Biomimetics Slippery Fluid-Infused Antireflective Films via Layer-by-Layer Comparison with Superhydrophobic and Antireflective Films. *ACS applied materials \& interfaces* **2014**, *6*, 13985–13993.

(27) Aizenberg, J.; Aizenberg, M.; Kang, S. H.; Wong, T. S.; KIM, P. Slippery Surfaces with High Pressure Stability, Optical Transparency, and Self-Healing Characteristics. **2014**.

(28) Cheng, D. F.; Masheder, B.; Urata, C.; Hozumi, A. Smooth Perfluorinated Surfaces with Different Chemical and Physical Natures: Their Unusual Dynamic Dewetting Behavior toward Polar and Nonpolar Liquids. *Langmuir* **2013**, *29*, 11322–11329.

(29) Bowen, P.; Carry, C.; Luxembourg, D.; Hofmann, H. Colloidal Processing and Sintering of Nanosized Transition Aluminas. *Powder Technology* **2005**, *157*, 100–107.

(30) Rowthu, S.; Böhlen, K.; Bowen, P.; Hoffmann, P. Surface 3D Micro Free Forms: Multifunctional Microstructured Mesoporous α-Alumina by In-Situ Slip Casting Using Excimer Laser Ablated Polycarbonate Molds. *ACS applied materials \& interfaces* **2015**, *7*, 22458–22469.

(31) Preston, D. J.; Miljkovic, N.; Sack, J.; Enright, R.; Queeney, J.; Wang, E. N. Effect of Hydrocarbon Adsorption on the Wettability of Rare Earth Oxide Ceramics. *Applied Physics Letters* **2014**, *105*, 011601.

(32) Golub, M. A.; Wydeven, T.; Cormia, R. D. ESCA Study of the Effect of Hydrocarbon Contamination on Poly (tetrafluoroethylene) Exposed to Atomic Oxygen Plasma. *Langmuir* **1991**, *7*, 1026–1028.

(33) Egitto, F.; Matienzo, L. Modification of Polytetrafluoroethylene and Polyethylene Surfaces Downstream from Helium Microwave Plasmas. *Polymer Degradation and Stability* **1990**, *30*, 293–308.

(34) Dobrovinskaya, E. R.; Lytvynov, L. A.; Pishchik, V. *Sapphire: Material, Manufacturing, Applications*; Springer Science \& Business Media, 2009.

(35) Van Oss, C. J. *Interfacial Forces in Aqueous Media*; CRC press, 2006.

(36) Wang, X.; Liu, X.; Zhou, F.; Liu, W. Self-Healing Superamphiphobicity. *Chemical Communications* **2011**, *47*, 2324–2326.

4.3. Menisci in three phase systems

The SCA measurements in three phase systems as reported in Table 3 of the attached manuscript (Section 4.2.1) were carried out using sapphire capillary submerged into two immiscible liquids (refer Section 3.9.2, Chapter 3 for details on experimental setup). The alumina grains used in this study are ultrafine (~150 nm avg. diameter) (refer Section C.2, Appendix C) and liquid menisci experiments were carried out with macro size (1.5 mm outer diameter, 1 mm internal diameter) sapphire capillary. However, the wetting results obtained for macro sapphire capillary and ultrafine alumina samples can be considered the same. This is because, it was reported in the literature [116–119] that the intrinsic wetting behavior does not change with change in macro to nano world.

Simple liquids such was water, Dodecane, Hexadecane can be considered as Newtonian liquids for practical purposes. The number of liquid molecules across the pore diameter can change the continuity of matter that is valid in macro and micro scales to discretization of molecules in nanoscopic scale. But, it was recently reported [120] that even with 10 liquid molecules across the pore diameter, they still obeyed macroscopic laws of capillarity and menisci behaviors for Newtonian liquids. The number of liquid molecules (calculated as the ratio of pore diameter to liquid molecule diameter) in a 30 nm diameter alumina mesopore for water, Dodecane, Hexadecane, Fomblin® oil are 120, 75, 77, 15 respectively (see Table 4.1). Hence, based on the above discussion, the static menisci shape at a 1.5 mm sapphire capillary interface can be considered the same for 150 nm diameter alumina grain interface.

Table 4.1. Molecular diameter, calculated number of molecules in 30, 50 nm pores respectively

Molecule	**Molecular diameter (Å)**	**Number of molecules in 30 nm pore**	**Number of molecules in 50 nm pore**
Water	2.5[121]	120	200
Dodecane	7.12[122], 4[123]	42, 75	70, 125
Hexadecane	3.9[124]	77	128
Fomblin® oil Y25/6	50±30[125]	4-15	6–25

However, high viscous or non–Newtonian liquids might experience non zero slip behavior at the solid interface at the nanoscopic level in contradiction to the macro world [119,120]. Therefore, the dynamic wetting behavior of high viscous Fomblin® oil may have slip relative to the sapphire capillary walls at nano scale unlike macro scale and hence, dynamic wetting behaviors at macro scale may not be precisely represented at the nanoscale.

4.3.1. Equilibrium static contact angle measurements

Figure 4.2 presents the equilibrium liquid menisci in three types of 3 phase systems at sapphire capillary such as in (a) Hexadecane and Fomblin® oil system; (b) Hexadecane and water system and (c) water and Fomblin® oil system. In Figure 4.2a, Hexadecane wets sapphire stronger than

Fomblin® oil as evidenced by the concave shape of the Fomblin® oil at the convex and concave surfaces of the sapphire capillary. However, the SCAs at the convex (outer diameter) and concave (internal diameter) sapphire surfaces differ significantly (Table 4.2) for both the liquids. Extending these observations in water–Hexadecane–sapphire three phase system, water wets sapphire stronger than Hexadecane as evidenced by the convex shape of the water meniscus at both the concave and the convex sapphire surfaces (Figure 4.2b). It is thus evident from the aforementioned observations that the water wets sapphire stronger than Fomblin® oil as also observed (Figure 4.2c) (refer Table 4.2 for precise SCAs).

Water and Hexadecane liquids have competing Van der Waals attraction forces with sapphire as evidenced by very similar SCAs at the concave sapphire surface (Figure 4.2b,Table 4.2). However, water wets stronger at the convex sapphire surface. This competing tendencies can also explain the dual behaviors (infiltration, stable interface) of Hexadecane drop atop water impregnated MPA systems as mentioned in O_2 plasma section, submitted article in this chapter (Section 4.2.1). On the other hand, water always infiltrates into Hexadecane impregnated MPA because water is heavier in addition to the stronger Van der Waals attraction forces. It is thus evident from the liquid menisci in both the aforementioned three phase systems that the water will wet sapphire stronger than Fomblin® oil and is also confirmed (Figure 4.2c, Table 4.2). Although, water is less dense than Fomblin® oil, it infiltrates into Fomblin® impregnated MPA composite because of very strong Van der Waals attraction forces.

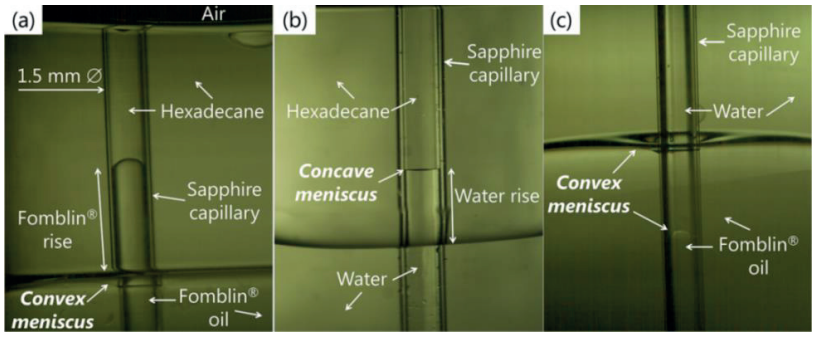

Figure 4.2. Equilibrium liquid menisci at convex and concave curvatures of sapphire capillary for (a) Fomblin® oil–Hexadecane liquids, (b) Hexadecane–water liquids, (c) Fomblin® oil–water liquids.

Table 4.2. Equilibrium static contact angle (SCA), advancing contact angle (ACA) and receding contact angle (RCA) in three phase systems

System	**Liquid**	**At sapphire outer diameter**			**At sapphire internal diameter**		
		SCA	**ACA**	**RCA**	**SCA**	**ACA**	**RCA**
Fomblin®–Hexadecane–Sapphire	Fomblin® oil	128±3	140±5	56±4	150±3	159±3	138±6
Hexadecane–Water–Sapphire	Water	88±4	148±3	90±3	80±5	85±3[a]	85±3[a]
Fomblin®–Water–Sapphire	Fomblin® oil	120±4	145±5	10±3	135±3	141±7[a]	136±5[a]

[a] Not real advancing and receding angles due to no relative motion of liquid menisci w.r.t. sapphire capillary.

The main conclusion that can be drawn from the static contact angle measurements in 3 phase systems relevant to the current study is the relative order of Van der Waals forces with alumina which is water > Hexadecane > Fomblin® oil. This order confirms with the theoretical predictions using van Oss–Choudary–Good equation and experimental investigations of spreading, infiltration and stable test liquid–LIMPA composite interfaces as presented earlier in Section 4.2.1. The capillary rise of Fomblin® oil in a sapphire capillary (Figure 4.2a) depends on the amount of Hexadecane in a sapphire capillary and is not the focus of the current study. Indeed, theoretical calculations are currently ongoing to predict this height rise and in understanding such behaviors.

4.4. Summary

In this chapter, the wetting and tribological behaviors of solid impregnated alumina composite materials, namely Eicosane impregnated alumina, Moldflon™ impregnated alumina and Zonyl® impregnated alumina were shown. The wetting properties of these composites post wear tests are not promising as they are not retained. Additionally, these composites suffer from the technical challenges of uncontrollable surface roughness and the fraction of the second phase in contact with liquid drops atop. Hence, this chapter mainly focused on the wetting behaviors of polished and non functionalized liquid impregnated alumina composite surfaces, namely, water impregnated alumina composites, hydrocarbon (Hexadecane and Dodecane) impregnated composites and perfluoropolyether (Fomblin®, 3M™ HFE–7200) impregnated composites. The wetting dynamics in oxygen plasma treated samples is strongly enhanced both for non–infiltrated dry and liquid impregnated alumina samples. It was shown that there is at least one combination of impregnating and test liquids which are Fomblin® oil and Hexadecane that showed a stable interface in LIMPA composites.

The other wetting behaviors revealed are spreading and infiltration of the test liquid drops atop MPA and LIMPA samples. Such behaviors are explained using relative Van der Waals forces of attraction between the liquid and the alumina employing van Oss–Choudary–Good equation. The relative order of Van der Waals forces obtained from the theoretical calculations is also validated by experimental observations using three phase systems comprising of sapphire capillary submerged into two immiscible liquids and measuring the equilibrium contact angles at the three phase contact line. While the theories based on free energy minimization taken from literature could not predict a few of the wetting cases in LIMPA samples, the order of Van der Waals forces explains all the observed wetting behaviors.

Chapter 5

Tribological characterizations of Fomblin® oil impregnated mesoporous α–Al_2O_3 composites

Based on the wetting results presented in Chapter 4, it is clear that the Fomblin® impregnated MPA composites exhibited promising anti–sticking properties and allowing easy sliding of the immiscible test liquid droplets atop. The test liquid droplets not only include low viscosity Hexadecane, Dodecane and water, but also include high viscous paints, the latter will be described in Section 6.2.1, Chapter 6. Fomblin® oil impregnated composites were therefore used to evaluate the tribological properties using in–house fabricated dry non–impregnated cylindrical alumina samples as the counter bodies. The fabrication of the latter samples was carried out using the same slip casting and sintering processes, adapted for the cuboidal alumina samples (refer Sections 3.2.3 and 3.3, Chapter 3 for experimental details). Further, a couple of tribological tests were also carried out in self–mating condition.

Both as–sintered and polished alumina matrices were used to evaluate the tribological properties and are presented in the following subsections. 67–92 % dense sintered alumina matrices possess connected open pore network as already described in Section 4.2.1, Chapter 4 and are hereafter referred to as "*impregnated"* composites. Contrastingly, 94–99.5 % dense alumina and fully dense monocrystalline sapphire samples do not possess an open pore network, as evidenced by the porosity measurements using the Archimedes principle (see Figure 3.2b). For consistency, they are also treated with the same procedure as the liquid impregnation approach that was used for the former samples (see Section 3.6, Chapter 3). This allows the coating of these surfaces with a liquid film and hence they are hereafter referred to as "*lubricated"*.

In this chapter, the tribological properties of Fomblin® impregnated/lubricated alumina composites are presented mainly as a function of alumina density and by varying the applied normal load. The difference in the sample preparation such as as–sintered or polished show a strong influ-

ence on their wear rates but not on the friction coefficients. The effect of other secondary parameters such as Fomblin® oil viscosity and the reciprocating sliding frequency do not strongly influence the friction coefficients. The main aim of this chapter is to only to demonstrate low friction coefficient values and high wear resistance in Fomblin® impregnated/lubricated alumina composites. Therefore, deeper scientific analysis were not carried out in this chapter.

5.1. As–sintered alumina matrices

In this section, the tribological characterizations of Fomblin® impregnated/lubricated as–sintered alumina composites are presented as a function of alumina density and by varying the normal load. MPA samples fabricated by slip casting and subsequent sintering may possess large flatness and surface roughness variations. Although, it is well established that the flatness and surface roughness play very critical roles in lowering the friction coefficients [126], the tribological evaluations were carried out using the as–sintered samples since the polishing of MPA samples drastically decreased the surface porosity (refer to Section 2.4 of attached manuscript in Chapter 4) due to the presence of less permeable debris compacted regions. Such a reduction in the surface porosity decreases the rate of lubricant supply and thus diminishes the self–replenishing efficiency, the latter plays a vital role in the retention of wetting properties post wear.

5.1.1. Microstructural characterizations

The microstructural characterization of the samples before wear treatment is very essential as it strongly influences the tribological properties. In this subsection, the variations in microstructures of as–sintered alumina samples are briefly presented as a function of alumina density from 70 % to 99.5 %. 70 %, 80 % and 90 % dense MPA samples possess similar microstructures as already presented in Section 4.2.1, Chapter 4 but are again presented here in Figure 5.1a–b for a comparison with high density (>94 %) samples. They possess open porous networks, narrow grain size distributions and ultrafine grains. On the other hand, 94–99. 5 % dense samples do not have any porous networks and a representative 2D microstructures are presented in Figure 5.1c–d. In 94.5 % dense samples, the grains remain equiaxed while in 99.5 % dense samples, the grains exhibited anisotropic growth and have a rod like structures.

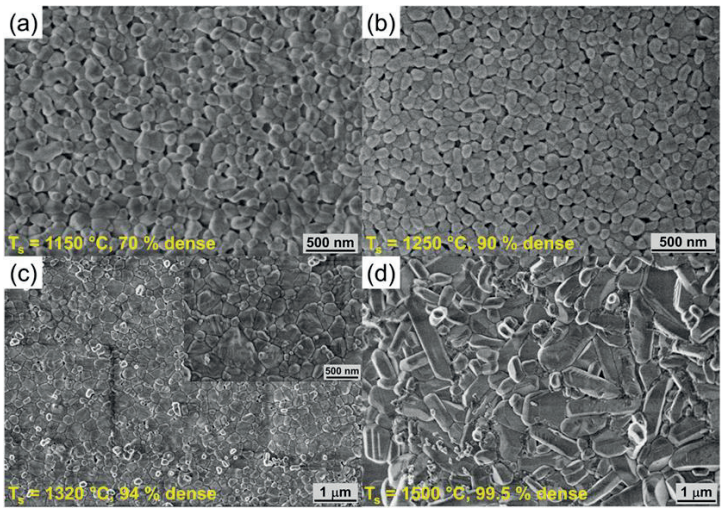

Figure 5.1. HRSEM images of as–sintered (a) 70 % dense, (b) 90 % dense, (c) 94 % dense and (d) 99.5 % dense samples, respectively. The microstructure of 80 % dense sample is similar to 70 % dense sample. The variable T_s is the sintering temperature.

The average grain sizes for 70–99.5 % dense as–sintered alumina samples obtained from the statistical treatment of SE–SEM images (measured for 1000 grains) are plotted in Figure 5.2 along with the starting primary particle size in the alumina powders. From Figure 5.2, an increase in the grain size can be observed for 94 % dense samples to 330 nm from its original primary particle size of 150 nm. The grain growth becomes much more pronounced in 99.5 % dense samples and the grains are no longer ultrafine as they exhibit a grain size of ~1–2 μm. Such grain growth is common in sintered alumina samples, sintered by one step sintering process and often reported in literature [127–129].

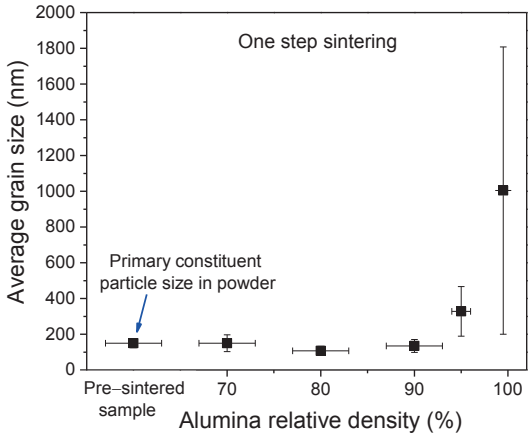

Figure 5.2. Average grain sizes of as–sintered alumina samples obtained from statistical treatment of SE–SEM images presented as a function of alumina density.

5.1.2. Frictional behavior

In this subsection, the friction coefficient (μ or referred to as FC) data of Fomblin® impregnated/lubricated as–sintered composites are presented. For a comparison and to observe the influence of Fomblin® oil lubricant, few tribological studies of dry non–impregnated alumina samples were also carried out. The FC of a self–mating dry non impregnated 90 % dense as–sintered pair was measured when the apparent load increased from 10 N to 100 N (corresponding pressures of ~0.3 to ~3 MPa) in the steps of 10 N, each for 15 min. It was observed that the FC decreased in the beginning followed by an increase as the normal load increased, but exhibited a steady state value of ~1 (not shown here). Such a high FC is caused by the lack of flatness and large roughness of the samples in contact area. The worn samples showed an increase in the roughness (S_a) from 4.5 μm to 8 μm (Figure 5.5) due to wear. Here, it is important to keep in mind only the increase in the roughness and not the absolute values. Although the normal pressures are mild, such an increase in the roughness can be mainly ascribed to the initial surface finish and lack of lubricant.

Similar to the dry samples, the FC data of Fomblin® impregnated/lubricated as–sintered alumina composites were studied as a function of apparent normal loads between 10 N and 220 N employing dry non–impregnated corresponding dense MPA as the counter body. Figure 5.3 presents the FC curves of two different Fomblin® impregnated 90 % dense as–sintered alumina composites for increasing ((10 N to 100 N) and decreasing the normal loads (100 N to 10 N) respectively. The FC lies between 0.22 and 0.35 and is almost 5 times lower than the dry non–impregnated samples. Such a strong reduction in the FC is explained by the lubrication effect of the employed Fomblin® impregnating liquid. Fomblin® oil is a high viscosity (250 cSt at 20 °C) perfluoropolyether. Fomblin® oil is a branched long chain (8 nm length) and hence the presence of even one monolayer reduces the asperity contacts. For low sliding frequencies employed in the current study, the lubrication regime is *mixed* type in the Stribeck curve (see Figure 2.8). In this regime, the shear strength of a Fomblin® impregnated composite surface is lower as compared to the dry MPA surface. It can be observed from Figure 5.3, that the FC trend and the values match very well when increasing and decreasing the apparent normal loads. Hence, the running–in time for these tests is quite small and 15 min time for every load step is supposedly sufficient to obtain the steady state FC in the samples. To further verify, constant load (at 50 N and 200 N) experiments were carried out for 3 h sliding time (not shown) and corresponding same FC values were obtained as that of the step load experiments.

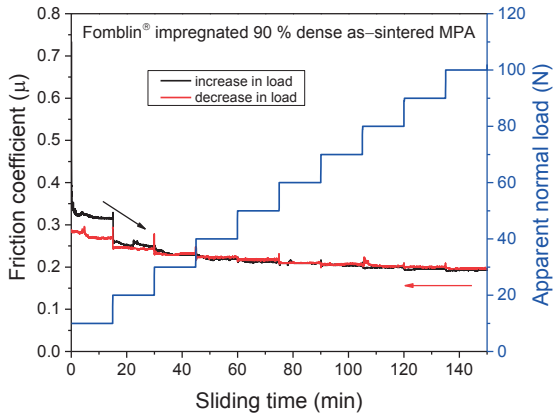

Figure 5.3. Friction coefficient data presented for two different Fomblin® impregnated 90 % dense as–sintered MPA composites plotted as the apparent normal load increased from 10 to 100 N (see right axis). The black curve presents the FC data measured for an increase in the normal load while the red curve presents the data obtained for another sample measured with a decrease in the normal load in steps of 10 N.

Further, it can be observed from Figure 5.3, that the FC decreases with an increase in the normal load, in contrary to that expected from the conventional Stribeck curve. Fomblin® oil has very high pressure–viscosity coefficient (α) of ~4.46×10^{-8} Pa^{-1} [130]. Hence, for change in normal pressures from 0.3 MPa to 3 MPa, the viscosity increase is ~13 cSt as calculated using Barus law, mathematically described by Equation (5.1) [131].

$$\eta = \eta_o e^{\alpha P} \tag{5.1}$$

where P is the pressure (in Pa) and η_o is viscosity at atmospheric pressure. Evidently, the viscosity increases and one might expect the reduction in FC with an increase in the load. Similarly, a small drop in FC values were reported for paraffin lubricated fully dense alumina samples, while constant FC values are reported when water was employed as the lubricant [132] for an increase in the applied normal load. Although, the article does not explain the differences in such behaviors, the pressure–viscosity coefficient values of water and paraffin such as 0 [133] and 1.5×10^{-8} Pa^{-1} [130] respectively may explain such behaviors. In addition to the viscosity–pressure effect in Fomblin® impregnated MPA samples, there might be capillary forces of the Fomblin® oil between the counter dry alumina and the rigid impregnated alumina samples that aid in the reduction of the asperity contacts. Alternatively, the mesopores might also increase the lubricant supply in low density samples.

The same tribological tests were carried out by varying the alumina matrix density and are presented in Figure 5.4. As a reference, the FC of monocrystalline ($1\bar{2}11$ plane) Fomblin® impregnated sapphire employing diamond as the counter body is plotted.

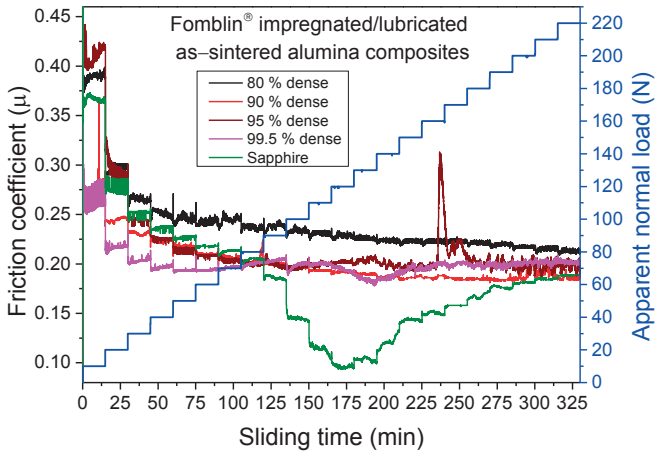

Figure 5.4. Measured friction coefficient data plotted for Fomblin® impregnated/lubricated 80, 90, 95, 99.5 % dense alumina composites along with that of commercially obtained monocrystalline ($1\bar{2}11$ plane) sapphire as a function of sliding time (min) for a change in the apparent normal loads from 10 N to 220 N (corresponding pressures of 0.2–6 MPa).

It can be observed that the FC decreases with an increase in alumina matrix density from 80 % to the higher densifications. This could be because, the samples possessing higher densities have lower roughness values (Figure 5.5) as a result of the increased grain necking formation as shown in Figure 5.6. The higher roughness in the samples may lead to higher solid–solid contacts thus exhibiting slightly higher FC values while employing low density matrices.

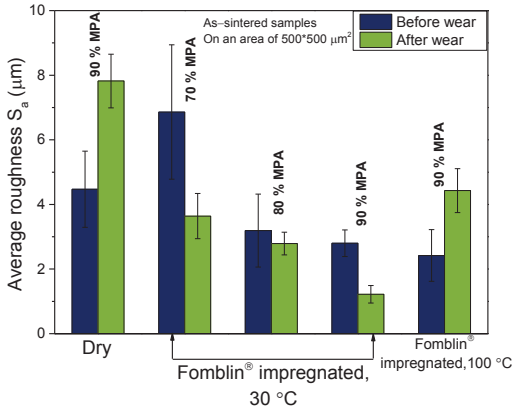

Figure 5.5. The measured roughness (S_a) values obtained by laser confocal microscopy in the as–sintered alumina samples before and after the wear experiments.

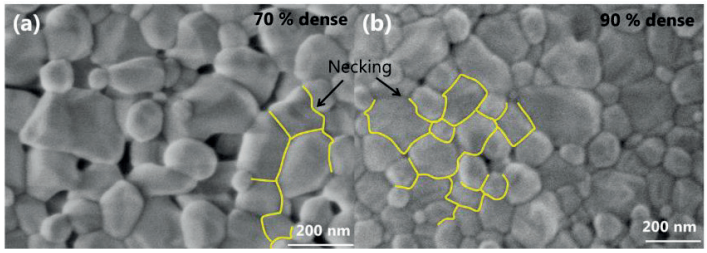

Figure 5.6. Necking density of grains for 70 and 90 % dense as–sintered alumina samples.

One can observe from the Figure 5.4 that for normal loads ≤ 80 N (< 1 MPa), the trend for FC is 70* % > 80 % > sapphire > 90 % ≈ 95 % > 99.5 % dense samples. It is promising that the Fomblin® impregnated/lubricated ultrafine as–sintered 90–99.5 % dense MPA composites have slightly lower FC values than Fomblin® lubricated polished commercially obtained sapphire samples. However, for the normal loads between 140 N and 220 N (1.5 to 2 MPa), the trend for the FC is 80 % > 95 % ≈ 99.5 % > 90 % > sapphire. Although, commercially available sapphire based samples exhibited the lowest FC, 90 % dense alumina matrix shows optimum among the polycrystalline as–sintered alumina samples, which is very interesting. The reasons are briefly discussed as follows. In 70% and 80 % dense samples, the microstructures are similar to 90 % density but, (a) the roughness is relatively higher, as already shown in Figure 5.5 (compare before wear values), (b) relatively low hardness values (refer Figure 5.13) and (c) weak grain to grain necking as already shown in Figure 5.6. Hence, it is intuitive in abrasive type of wear, the FC should be lowest for 90 % density as compared to 70 % and 80 % densifications. On the other hand, for samples with a density > 90 %, the open pore network no longer exists, which diminishes the continuous lubricant supply by capillarity. Additionally, the grain sizes are much larger than for the 90 % dense samples as already mentioned in the Section 5.1.1, Figure 5.2 which may also have a slight influence and more studies are needed to characterize this difference.

5.1.3. Wear rate diagram as a function of alumina density

Besides low FC values, the wear of the samples is of paramount importance in tribological systems. Typically, the tribological studies reported in literature [101,102,134–138] often used high density (≥ 94 %) alumina samples in dry or in lubricated conditions. Unlike the literature, this section will briefly summarize the wear rates in MPA based composites containing porosity as big as 30 %.

The wear coefficients (K´) of Fomblin® impregnated/lubricated MPA samples in this current study were estimated using the Archard wear Equation (2.9) and presented in Figure 5.7 as a function of alumina matrix density. The wear coefficients of 70, 80 and 90 % dense MPA samples lie in–between 10^{-2} and 10^{-5} $mm^3.N^{-1}.m^{-1}$, indicating that the samples underwent severe wear. A weak neck formation between the grains could lead to removal of big particles from the sample surfaces causing such high wear coefficients. While for samples possessing 95 % and 99.5 % densities, the wear is mild as the wear coefficients are ~10^{-8} $mm^3.N^{-1}.m^{-1}$ due to the nearly completion of necking of the grains in three dimensions.

*FC studies of 70 % dense sample were only carried out until 100 N and hence are not presented in Figure 5.6. The FC decreases from 0.7 to 0.32 when the load increased from 10 N to 100 N.

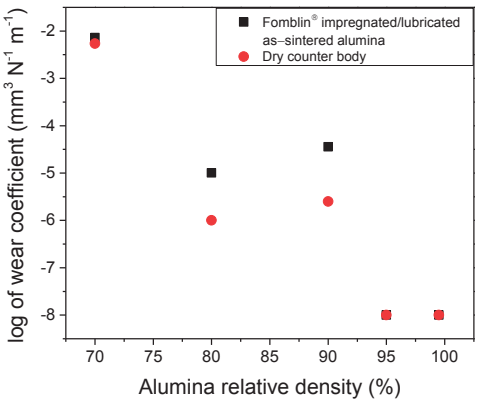

Figure 5.7. The logarithm$_{10}$ of the estimated wear coeffcients in Fomblin® impregnated/lubricated as–sintered alumina samples plotted as a function of alumina matrix density.

5.1.4. Characterization of samples post wear

The microstructural and the roughness characterizations of the worn samples are necessary to understand the type of wear and their effect on the wetting properties post wear treatment. Since 70–90 % dense MPA samples containing open pore network are interesting for wetting behaviors, the microstructural evolutions of only 70–90 % dense as–sintered samples are presented in this section. Figure 5.8 presents the SE–SEM images of 70 % and 90 % dense samples post wear tests (step load friction experiments corresponding to Figure 5.4). In 70 % dense sample, it is clearly observed that the grains became smaller due to the wear, arising from the grain fracture commonly known as transgranular/intragranular fracture [99]. In addition to transgranular grain fracture, particles comprising several grains were removed as wear debris and this type of removal is referred to as intergranular fracture. Further, a minor fraction of the worn regions became slightly polished and the dry counter body acquired large cracks due to wear. On the contrast, in 90 % dense sample, a major fraction of the worn region is highly polished in addition to the presence of numerous micro cracks.

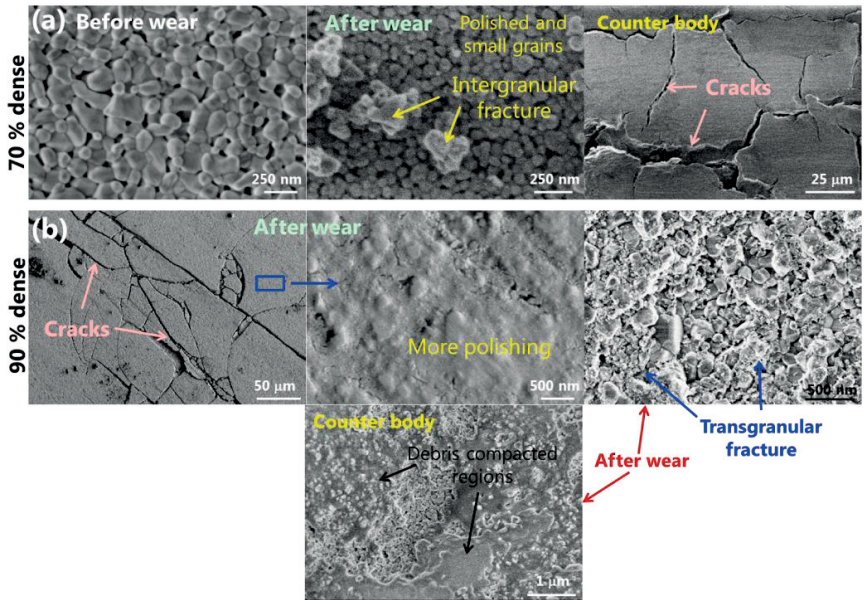

Figure 5.8. SEM images of 70 % and 90 % dense MPA samples and their corresponding counter bodies post wear tests.

The decrease in the roughness in both 70 % and 90 % dense MPA samples due to the wear is also supported by roughness measurements as shown in Figure 5.5 (see before and after wear). Additionally, in certain regions of 90 % dense MPA sample, sub 10 nm debris were observed suggesting a contribution of transgranular fracture. Interestingly, the debris compacted regions are vsisible on counter body, as if the surfaces underwent high temperature plastic deformation. The microstructural features observed in the current study due to wear were already reported in the literature for self–mating 95±1 % dense alumina samples in unlubricated condition [137,139].

Based on the above microstructural analysis, the wear mechanism in these composites is abrasive type, showing the transition from severe wear in 70 % dense samples to mild in 90 % dense samples. Precisely, it is principally intergranular fracture in 70 % dense samples, while it is principally transgranular type in 90 % dense samples. Such transition from intergranular to transgranular fracture type was usually observed in ceramics and often reported in self–mating fully dense unlubricated alumina [99]. The weak grain to grain necking in 70 % dense samples lead to bigger debris particles, which causes high wear rates and typically intergranular fracture type. While in 90 % dense samples, higher grain to grain necking retains the bonding of the grain with others but fractures a part of it and hence causes lower wear rates.

Since the wear rates in as–sintered samples are quite high, especially, for lower densifications, and it is well known that the surface roughness and flatness play critical roles in determining the friction coefficients and wear coefficients, the tribological experiments were also carried out using polished and flat alumina matrices which will be presented in the following sections.

5.2. Polished alumina matrices

In this section, the tribological characterizations of Fomblin® impregnated/lubricated polished alumina composites are presented as a function of alumina density and by varying the normal load, exactly same as that of as–sintered matrices, while employing polished counter bodies.

5.2.1. Microstructural characterizations

The microstructures of 70–99.5 % dense polished alumina samples are presented in Figure 5.9. As already discussed in the attached manuscript of Chapter 4, 70–90 % dense polished sample surfaces contain debris compacted regions and porous regions. But, for 94 % and 99.5 % densifications, the surfaces are polished as shown in Figure 5.9b and very rarely, having polishing scratches and closed pores visible in SE–SEM (Figure 5.9c–d). The debris compacted regions in the former samples may have sub nanometer pores, which could not be revealed using SEM. So, these regions are less permeable to Fomblin® oil as compared to meso porous regions.

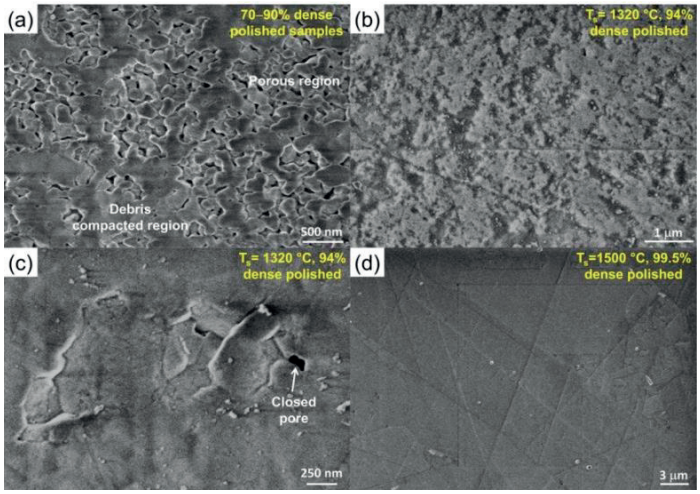

Figure 5.9. Representative HRSEM images of polished alumina samples having (a) 70–90 % density, (b–c) 94 % density showing non porous surfaces, (d) 99.5 % density sample showing non porous but scratches due to polishing respectively.

The average roughness (R_a) of all the 70–99.5 % dense samples lie in between 20 and 90 nm, and that of sapphire is 10 nm as presented in Figure 5.10.

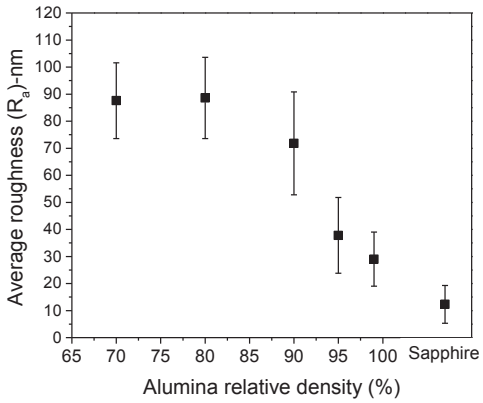

Figure 5.10. Measured average roughness (R_a) values using white light profilometer of polished alumina samples plotted as a function of alumina density. The roughness of commercially obtained sapphire is also presented for comparison.

5.2.2. Frictional behavior

In this study, the polished 99.5 % dense alumina (sintered at 1350 °C), having an average grain size of 1.2 μm exhibited a FC of 0.185 in self–mating condition. A comparison with literature reveals higher FC values of 0.4 [140], 0.9 and even higher values [110] were reported for fully dense self–mating unlubricated α–Al_2O_3 pair consisting of bigger grains (5 μm–10 μm). Evidently, the large difference in the measured and literature values is due to difference in the grain sizes.

In the following, the FC results of Fomblin® impregnated/lubricated polished alumina composites are presented. Figure 5.11 presents the FC data of the such composites by varying the apparent normal loads from 10 N to 220 N (corresponding 0.2 to 6 MPa normal pressures).

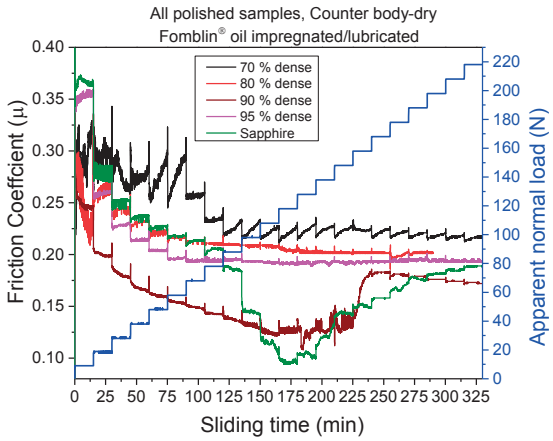

Figure 5.11. Measured friction coefficient data plotted for Fomblin® impregnated/lubricated 70, 80, 90, 95 % dense polished alumina composites along with that of commercially obtained monocrystalline ($1\bar{2}11$ plane) sapphire as a function of sliding time (min) for a change in apparent normal load from 10 to 220 N (0.2–6 MPa).

The FC decreases with an increase in the normal load. An optimum density of 90 %, similar to that of as–sintered samples was also observed to achieve lowest FC, even smaller than sapphire

depending on the normal pressures. These results can be explained similar to that of as–sintered samples and the reader may refer Section 5.1.2 for the discussion. However, 90 % dense samples showed a different behavior, as minimum FC was observed at ~120 N normal loads. Similar trend was observed in a sapphire sample, but the measurement was not repeated the second time. It is just shown here for a comparison and more measurements would be needed to understand the occurrence of minimum FC value. A comparison of FC values of as–sintered (Figure 5.4) and polished samples (Figure 5.11), indicate the absolute minima differ only by 0.06. Hence, to achieve comparable FC values, one can directly use the as–sintered samples by avoiding the tedious polishing procedure.

5.2.3. Self–mating of Fomblin® lubricated alumina

If both the fixed bottom alumina sample and the counter body are lubricated, for instance in 95 % and 99. 5 % dense samples, the FC further decreases as compared to that of dry non–impregnated self–mating samples or when a dry counter body is used. The FC data of such pairs are presented in Figure 5.12. A lowest FC of 0.025 is achieved by Fomblin® lubricated 95 % dense self–mating pair and is promising for further exploring. This is because the lubricant film thickness between the contacting surfaces could be higher as compared to the dry self–mating pair or when the counter body is held dry. On the other hand, a difference for 95 % and 99. 5 % dense self–mating pairs may be associated to difference in grain sizes, and need deeper studies for the confirmation.

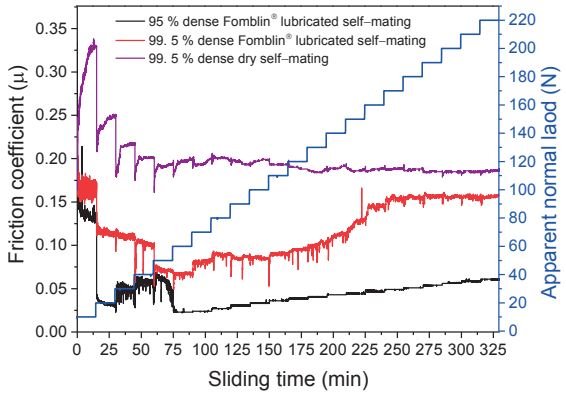

Figure 5.12. Measured friction coefficient data plotted as a function of sliding time (min) when the normal apparent load changes from 10 to 220 N (0.2 to 6 MPa) for 99.5 % dry self–mating pair, 99. 5 % Fomblin® lubricated with dry counter body, 95 % and 99. 5 % dense Fomblin® lubricated self–mating pairs.

5.2.4. Wear rate diagram versus Vickers hardness

The wear coefficients (K´) estimated using the Archard wear Equation (2.9) for step load experiments are presented in Figure 5.13, along with their Vickers hardness as a function of alumina matrix density. The wear coefficients in polished 70, 80 and 90 % dense samples are $\leq 10^{-5}$ $mm^3.N^{-1}.m^{-1}$, exhibiting 3 orders of magnitude reduction compared to as–sintered samples (Figure 5.7).

Although, it was suggested earlier in the Section 5.2.2, to directly use as–sintered samples instead of polished samples to achieve comparable FC values, the latter are preferred due to enhanced wear resistance. The wear coefficients reveal that the former samples underwent mild wear. However, for 95 % and 99.5 % dense alumina samples, the wear is negligible ($<10^{-8}$ mm^3 N^{-1} m^{-1}). For abrasive type of wear, the wear rate was reported to be linearly proportional to the soft material´s hardness [139], which is also valid in the Fomblin® impregnated/lubricated alumina composites in the present study. It was reported that a reduced grain size and a narrow grain size distribution often promotes the abrasive wear resistance of unlubricated material systems in sliding contacts in [141–143]. Especially, when the grain size is in sub micron range, the wear resistance was reported to have been strongly enhanced as compared to micron grain size [144]. However, there is no single study on the tribological properties of Fomblin® impregnated self–mating alumina composites or while employing dry alumina counter body. Hence, a direct comparison of our measurements with that of literature may not be appropriate.

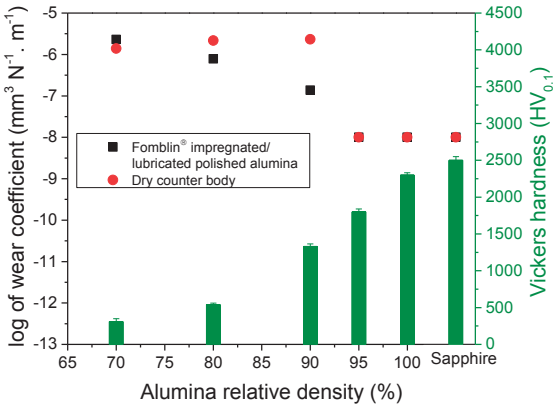

Figure 5.13. The $logarithm_{10}$ of estimated wear coefficients in Fomblin® impregnated/lubricated alumina composites plotted as a function of alumina matrix density along with their corresponding Vickers hardness ($HV_{0.1}$) values.

To study the influence of higher sliding distances and normal pressures, constant load experiments using ball on disc were carried out for 99. 5 % dense polished alumina and sapphire samples in unidirectional sliding. The apparent contact pressures of 350 MPa, 2 km sliding distance and 0.1 m s^{-1} sliding speed were used. The measured FC values of 99.5 % dense alumina and sapphire samples are 0.15±0.01 and 0.13±0.01 respectively, which matches well with that reported in the literature [139]. These values are in the same order of magnitude as that obtained using the oscillating tribometer as reported in the Section 5.2.2, although the latter were carried out at small contact pressures.

5.2.5. Characterization of samples post wear

The polished alumina matrices were used to evaluate the wetting properties post wear treatment. Therefore, it is essential to study the microstructural evolutions of these composites due to wear and are presented in this section. Only the wear track of 70 % dense MPA sample can be seen

with naked eyes, while for 80–99.5 % dense samples, the wear track is not visible. Even optical microscopy could only reveal few scratches but not a distinct wear track. The microstructures post wear tests of 70 %, 80 % and 90 % dense samples are similar, as studied using electron microscopy (will be shown in Section 6.2.1, Chapter 6). The wear mechanism is majorly by intergranular fracture. In 95 % and 99.5 % dense alumina samples, although the wear tracks are not optically visible, scratches and cracks were observed in HRSEM in addition to the formation of micro/nano debris. The HRSEM images of 95 % and 99.5 % dense samples and their corresponding counter bodies post wear (step load experiments presented in Figure 5.11) are presented in Figure 5.14. The cracks in 99. 5 % dense sample as well as its counter body along with micro debris reveal an intergranular fracture and probably third body abrasion caused by the formed debris.

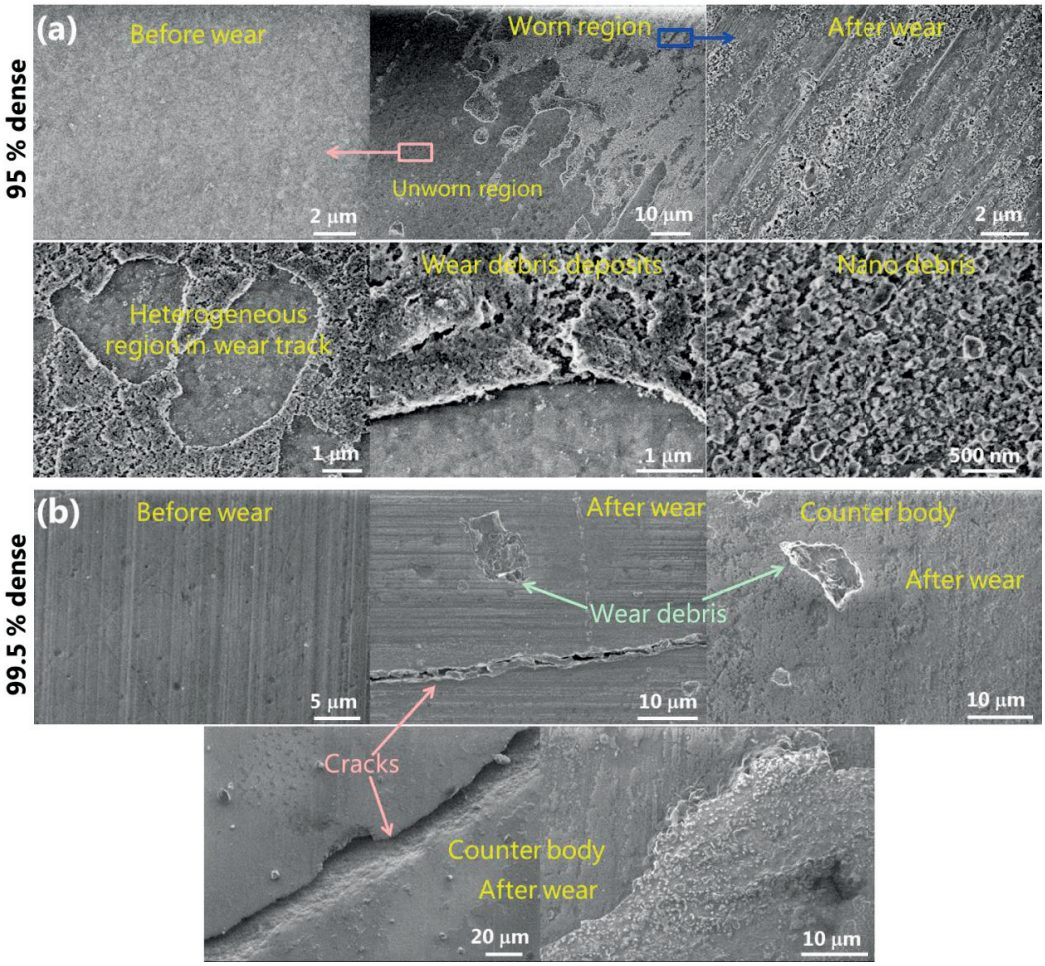

Figure 5.14. HRSEM images post step load friction experiments of Fomblin® impregnated MPA samples for (a) 95 % alumina density, (b) 99.5 % alumina density.

5.2.6. Roughness measurements post wear

The average roughness (R_a) measurements of alumina samples and their corresponding counter bodies before and after wear experiments (step load, Figure 5.11) are presented in Figure 5.15.

In general, the counter bodies possessed slightly higher roughness than the lubricated bottom samples even before wear treatment. In 70–90 % dense samples, the wear treatment did not strongly influence the roughness. However, there is a pronounced increase in the roughness of 94–99.5% dense alumina and the sapphire samples and their respective counter bodies except for diamond. The large error bars associated in the R_a values are due to strong inhomogeneity in the worn regions as also confirmed with electron microscopy investigations. Interestingly, inspite of higher hardness, high density alumina samples exhibited an increase in the roughness due to wear. Such contradictory behavior as compared to lower density samples may be due to the absence of continuous replenishment of Fomblin® oil in the former samples. The continuous replenishment may keep certain thickness of lubricant film thus reducing the asperity contacts. However, when there is no replenishment, the lubricant would have been pushed away due to reciprocal movement of the counter body and hence could cause more asperity contacts which could also be a reason to observe 3rd particle abrasion in 99.5 % dense samples.

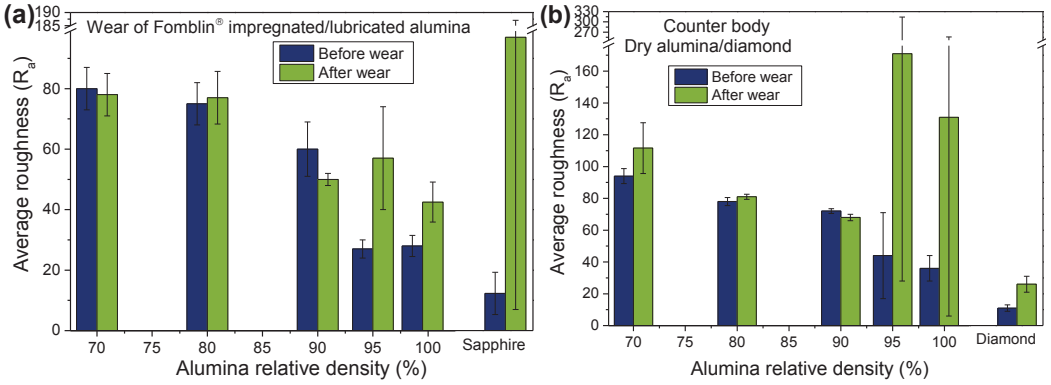

Figure 5.15. The measured average roughness (R_a) values of (a) 70–99.5 % dense alumina samples and sapphire before and after wear experiments (step load experiments, Figure 5.11), (b) corresponding dry non impregnated alumina and diamond counter bodies are presented as a function of alumina density.

5.3. Effect of sliding frequency

The effect of sliding frequency on the frictional behavior of 95 % dense Fomblin® lubricated polished alumina against corresponding dense dry counter body was investigated and presented in Figure 5.16. The FC data corresponding to 6 Hz frequency for 50 N, 100 N and 200 N normal loads match very closely with that reported in Figure 5.11, showing a very high reproducibility. There is a significant decrease in the FC when the frequency increased from 1 Hz to 6 Hz for 50 N, 100 N and 200 N apparent normal loads. However, for further increase in frequency from 6 Hz to higher values, there is no significant difference in the FC for 50 N and 100 N apparent normal loads but a significant lowering for 200 N. To confirm the latter decrease, step load experiments were carried out for the same tribological as–sintered pair with sliding frequencies of 6 Hz and 24 Hz and are presented in Figure 5.17. It can be observed that changes in sliding frequency from 6 Hz to 24 Hz do not have any distinct influence on the frictional behavior.

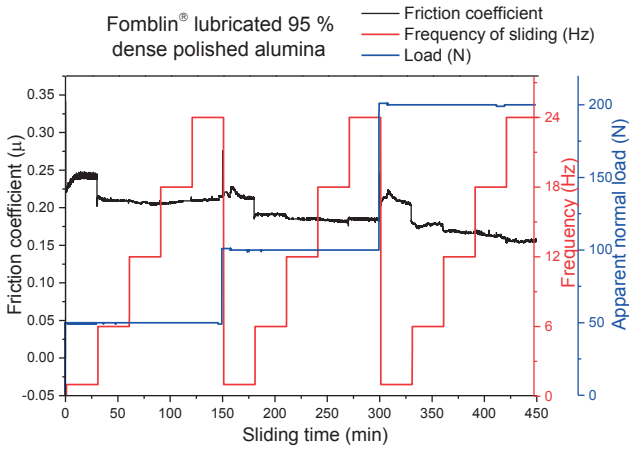

Figure 5.16. Friction coefficient variation of Fomblin® lubricated 95 % dense polished alumina slid against 95 % dense dry non–impregnated sample by changing the sliding frequency and apparent normal loads. The applied sliding frequencies used are 1, 6, 12, 18, 24 Hz (correspond to 0.008, 0.048, 0.096, 0.144, 0.192 m s^{-1} average sliding speeds) and the normal laods are 50, 100 and 200 N.

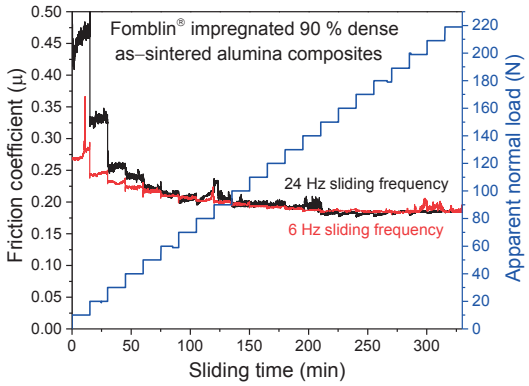

Figure 5.17. Friction coefficient data of Fomblin® impregnated 90 % dense as–sintered alumina slid against 90 % dense dry non–impregnated sample for sliding frequencies of 6 Hz and 24 Hz. The normal load continuously increased from 10 N to 200 N in the steps of 10 N.

5.4. Effect of Fomblin® oil viscosity

Fomblin® oil is a high viscous fluid at room temperature and possess a viscosity of 250 cSt (475 mPa.s) at 20 °C. However, a considerable decrease in the viscosity to 10 cSt by continuously heating the sample to 100 °C throughout the tribological test resulted in a small but significant increase in the FC as shown in Figure 5.18. Such a small rise is due to decrease in the film thickness at the contacting surfaces which can increase the asperity contacts, counteracted by the lubricant supply by the mesopores. In the mixed lubrication of the Stribeck curve (Figure 2.8), such an increase in the FC is observed with a decrease in the lubricant viscosity. Unlike the corresponding room temperature measurements, the post wear tests resulted in an increase in the roughness (Figure 5.5).

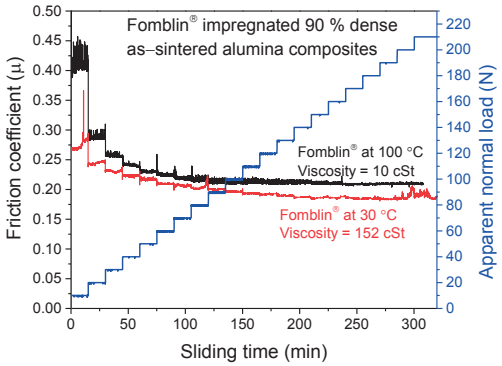

Figure 5.18. Friction coefficient values plotted for Fomblin® impregnated 90 % dense as–sintered alumina samples by varying the normal load for two different viscosities of the Fomblin® oil. The temperature of the block holding the alumina composite were held at constant temperatures of 30 °C and 100 °C respectively thereby influencing the viscosity of Fomblin® oil. The viscosity of Fomblin® oil at 30 °C and 100 °C are 152 cSt and 10 cSt respectively.

5.5. Summary

The tribological properties of novel composite material systems: Fomblin® impregnated/lubricated alumina against dry counter body or in self–mating condition were investigated using mild apparent normal pressures, majorly by increasing the normal load from 10 N to 220 N (corresponding 0.2 to 6 MPa) for different alumina matrix densities. It was observed that the FC decreases with an increase in the normal load for most cases. The general trend for the friction coefficient values in alumina samples (as–sintered and polished) is 70 % dense > 80 % dense > 95 % > 99.5 % dense> sapphire ≈90 % dense samples. Further, a very low friction coefficient of 0.025 can be obtained for self–mating Fomblin® lubricated 95 % dense alumina pair. The variation of sliding frequency from 6 Hz to 24 Hz do not have a distinct influence on the friction coefficient, while the decrease in the viscosity of Fomblin® slightly increased the friction coefficient. The friction coefficient of polished samples are only lesser by 0.06 compared to as–sintered samples.

The estimated wear coefficients in these composites continuously decreased with an increase in the alumina matrix density and were directly proportional to the hardness of the alumina matrix. The wear coefficients in polished alumina samples are 10^{-5} to $<10^{-8}$ and almost 3 orders of magnitude lower than the as–sintered samples. Based on the friction coefficient and wear coefficients results, it was found that 90 % alumina density is an optimum to achieve the best tribological performance. The wear mechanisms in the as–sintered samples transit from severe to mild abrasive wear as the alumina density increased. For 70 % dense based alumina composites, intergranular fracture is the major dominant mechanism while for 90 % dense samples, polishing and transgranular fracture are the dominant wear mechanisms. The roughness measurements and the electron microscopy investigations indicate that the as–sintered samples experience polishing during the wear. On the other hand, polished samples exhibited only mild intergranular fracture and third particle abrasion. Since the polished samples exhibit much higher resistance, they are further used to evaluate the wetting characterizations post wear tests and will be presented in the Chapter 6.

Chapter 6

Self–replenishing and wetting properties post wear tests

In this chapter, the wetting properties of Fomblin® impregnated MPA composites immediately after wear treatment and after providing sufficient self–replenishing or self–healing times are presented. For a comparison, the wetting properties of unworn regions after self–replenishing process and before wear without self–replenishing process are also presented. Water and Hexadecane were employed as the test liquids to evaluate the wetting properties post wear treatment. Further, a simple model was developed to predict the self–replenishing times to be able to achieve few monolayers coverage of the impregnating liquid film atop dry alumina surfaces. A sufficient coverage enables to retain the anti–sticking properties of Fomblin® impregnated MPA surfaces.

6.1. Self–replenishing properties

The technical challenge of this work is to obtain a wear–resistant and non–sticking material. As wear cannot be completely avoided, a mechanism of keeping or regaining the wetting properties is of paramount importance. Self–replenishing of a wetting determining impregnating liquid is one elegant approach to meet this goal. In order to understand the limitations of this self–replenishing or self–healing process, the capillarity uptake of the impregnating liquid is estimated using an available simple theoretical approach from the literature [145], followed by an experimental verification of the model and both are presented in this section.

In theoretical approach, the capillary height rise, h(t) of a no–slip liquid in the porous samples as a function of time may be estimated by employing a modified Washburn Equation (6.1) [145]. Briefly, if the liquid does not interact with the solid substrate and experience neither pinning nor strong attractive forces, then the liquid is referred to as no–slip liquid [145].

$$h(t) = \sqrt{\frac{r_o \gamma_{LV} cos\theta t}{2\tau\eta}} \tag{6.1}$$

where the symbols r_0–effective pore radius, γ_{LV}–liquid–vapor surface tension, θ–contact angle of liquid with substrate material, t–time, τ–tortuosity, η–dynamic viscosity of liquid. The tortuosity quantifies the connectivity and the meanderness of the pores. Straight capillaries parallel to the flow of the liquid gives τ=1. The meanderness of the pores increases the flow path, leading to an increased τ value. For isotropically distributed pores, a value of τ=3 can be used [146]. For a straight capillary having 50 nm diameter, the maximum height rise (h_{max}) can be estimated as ~75 m employing the Equation (6.2) [147]. It is important to note that the Equation (6.1) is valid for height $h(t) \leq h_{max}$. The heights we are interested are only maximum of few millimeters and eventually employing Equation (6.1) is logical.

$$h_{max} = \frac{2\gamma cos\theta}{\rho g r} \tag{6.2}$$

The capillary uptake observations were carried out by the experts at X–Ray center at Empa in Dübendorf using dark field X–Ray imaging, the experimental procedure is similar to as reported in the literature [115] and the method is briefly described in the Section 3.11, Chapter 3. The temporal X–Ray dark field images of capillary uptake of water and Fomblin® oil measurements in 70 % dense dry MPA are presented in Figure 6.1. It can be observed that the water already has an initial capillary height at time t= 0 min due to the dead time between placing the sample and starting the measurement (Figure 6.1a). The water takes ~11 min to rise by 6.5 mm in height while Fomblin® oil takes 684 min (~11 h 24 min) to rise by 3.4 mm in height. Such a strong difference in the time scales is due to the high viscosity and lower surface tension values of Fomblin® oil as compared to water. These direct experimental evidences show that the liquids exhibit strong capillary forces in MPA samples. The strong capillarity aids in self–replenishing process, required for the retention of wetting properties post wear experiments.

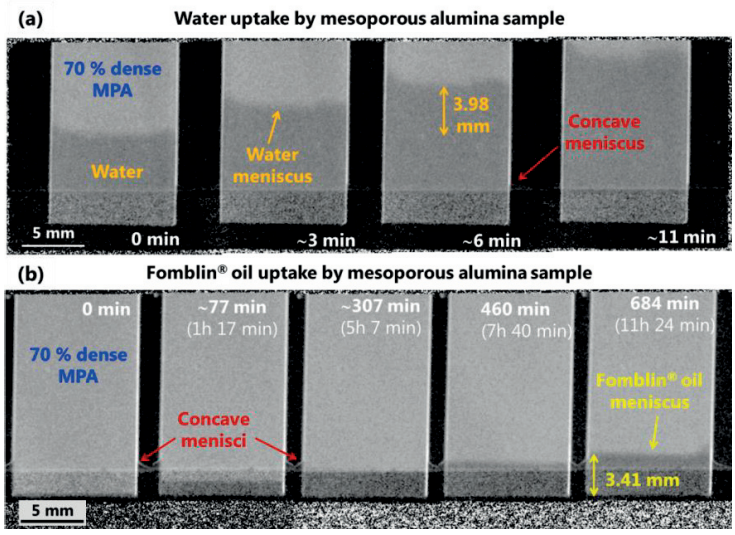

Figure 6.1. The temporal dark field images of the capillary uptake of (a) water and (b) Fomblin® oil by 70 % dense mesoporous alumina samples covered by all the four lateral surfaces with a Polyimide Kapton tape to prevent evaporation. Both the samples in (a) and (b) have same dimensions of 20×10×2.78 (in mm).

It is not only of scientific interest to observe the capillary uptake of different liquids in MPA samples, but also to quantify the liquid supply for lubrication and wetting purposes. By further treatment of the dark field images, the experimentally observed capillary height rise of water and Fomblin® oil in 70 % dry MPA can be presented as a function of time, see Figure 6.2.

The experimental height $h(t_n)$ of the liquid rise at a time t_n in an MPA matrix can be written in the form of Equation (6.3), similar o Washburn Equation (6.1).

$$h(t_n) = \sqrt{\frac{r_o \gamma_{LV} cos\theta}{2\tau\eta}} (t_o + \Delta t_n)^a \tag{6.3}$$

where t_o is the dead time between placing the sample and starting of the measurement, as already explained before, Δt_n is time difference between each measurement point and $\Delta t_n = t_n - t_{n-1}$, a is a constant that needs to be determined.

The tortuosity value (τ) of 70 % dense MPA sample is unknown. Although, the average diameter of the pores and the pore size distribution are known, the appropriate value of radius (r_o) that determines the capillarity in MPA network is unknown and hence $\frac{r_o}{\tau}$ needs to be determined. The treatment of dark field images in both water and Fomblin® oil uptake experiments can lead to n number of equations of type (6.3), where n = 16 for water and n = 800 for Fomblin® oil. Regression analysis was carried out to obtain the values of a, t_o and $\frac{r_o}{\tau}$ and tabulated as Table 6.1.

Table 6.1. List of parameters in Equation (6.3) by performing regression analysis of experimental data

Liquid employed	**By regression analysis of experimental data**			**By regression analysis of experimental data, taking a = 0.5**	
	a	t_o (min)	$\frac{r_o}{\tau}$ (nm)	t_o (min)	$\frac{r_o}{\tau}$ (nm)
Water	0.56618	5.2	2.16	4.1	5.72
Fomblin® oil	0.49775	3.2	15.06	3.2	7.54

By considering that all the three parameters: a, t_o and $\frac{r_o}{\tau}$ are unknown, the regression analysis gives values of a = 0.49775 and 0.56618 for Fomblin® oil and water respectively. These values are close to 0.5 and indicate the validity of classical Washburn´s equation in MPA matrices, which was reported to be valid at microscopic scale.The deviation of a value from expected value of 0.5, especially in the case of water could be explained by the errors associated with Image J treatment of the dark field images to obtain the height $h(t_n)$ values. For instance, solving the three equations (6.3) analytically for n= 0, 3, 12 in water system, the values of a = 0.4864 and $\frac{r_o}{\tau}$ = 6.53 nm are obtained. Similarly, solving in the Fomblin® oil system, the values of a = 0.52603 and $\frac{r_o}{\tau}$ = 8.06 nm are obtained. It is thus clear that the values of the aforementioned three parameters show a strong sensitivity to the height $h(t_n)$ values obtained. Nevertheless, it is noteworthy that in both the analysis, values for both water and Fomblin® oil are ~ 0.5 and therefore follows the Washburn equation.

There is an ongoing debate on the applicability of the Washburn´s equation to nano and mesoscopic systems. It is important to keep in mind that several factors such as fluid–wall interactions, liquid slip, surface roughness, dissolved gases and the shape of fluid molecules were reported to influence the validity of Washburn´s equation [145].

The values of $\frac{r_o}{\tau}$ in water and Fomblin® oil systems, obtained by regression analysis are 2.16 nm and 15.06 nm respectively (Table 6.1). They strongly differ from one another. In the first approximation, assuming no slip boundaries at water–alumina and Fomblin® oil–alumina interfaces, such strongly differing values cannot be explained. Since water has strong Van der Waals forces of attraction with alumina, a negative slip length of water may be possible with alumina. A negative slip length refers to sticking of water molecules at the alumina interface [145]. A negative slip length leads to smaller $\frac{r_o}{\tau}$ values. However, slip length of 12.9 nm (difference of 15.06 nm and 2.16 nm) means sticking of 51 water molecules (diameter of water molecule is 2.5 Å [121]) to alumina surface before the liquid front and seems improbable. Therefore, the errors in height data could be strongly contributing to the errors in both *a* and $\frac{r_o}{\tau}$ values.

In the next approach, the value of a is fixed at 0.5 for both water and Fomblin® oil and the regression analysis was again carried out to obtain values of t_o and $\frac{r_o}{\tau}$ and are presented in Table 6.1. The value of $\frac{r_o}{\tau}$ in water and Fomblin® oil cases still differ by 1.82 nm that represents sticking of 7 water molecules at alumina interface and seems more logical. Assuming that the correct value of $\frac{r_o}{\tau}$ is obtained from the Fomblin® oil system and equal to 7.54 nm, the values or r_o range from 7.54 nm to 35 nm for corresponding tortuosity values between 1 and 4.6. The limit of 35 nm is considered because the pore size distribution (refer Section C.3, Appendix C for pore size distributions) in 70 % dense MPA reveals that the majority of the pore radii lie below 35 nm. If we assume that the tortuosity is ~3, a commonly used value for open porous network [146], then the radius r_o is 22.6 nm. This indicates that the capillary transport of Fomblin® oil and water occur by the biggest pores and the smaller pores are not the flux limiting ones. This means that the liquid transport is not obstructed if a small pore is encountered in the path and the liquid takes a different route for the upward transportation and the route is 3 times longer. The alternative explanation is that, the liquid transport occurs as in straight cylindrical columns with equivalent pore radius of 7.54 nm.

The experimental data of the capillary height uptake as a function of time are plotted for water and Fomblin® oil in 70 % dense MPA samples and shown in Figure 6.2. A theoretical fitted curves are also superimposed on the experimental data points in both the graphs to show the validity of the Washburn equation in the mesoporous alumina matrices.

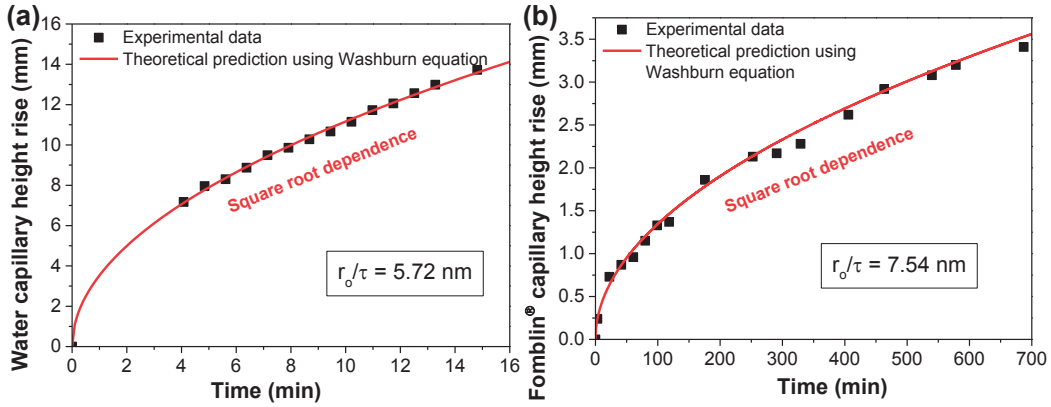

Figure 6.2. The experimentally observed capillary height rise (in mm) of (a) water and (b) Fomblin® oil liquids in 70 % dense MPA sample obtained from statistical treatment of X–Ray dark field images are plotted as a function of time. The theoretically predicted curves employing Washburn equation are superimposed in both the cases for comparison with the experimental values.

Briefly, it was shown that the capillary uptake of the liquids contributes to the self replenishment process in the LIMPA samples. Hence, the evaluation of wetting properties after wear treatment is meaningful and will be presented in the following section.

6.2. Wetting properties post wear tests

The wetting properties of Fomblin® oil impregnated MPA composites post wear treatment were studied and a manuscript will have to be communicated in 2016. The following section briefly describes the content of the attached manuscript.

6.2.1. About the manuscript

The wetting properties of Hexadecane atop Fomblin® impregnated MPA composite surfaces in 4 cases are presented such as in: (a) before wear, unflooding Fomblin® film configuration, (b) before wear, flooding Fomblin® film configuration, (c) unworn regions after a 20 h self–replenishing time and (d) worn regions after 15 h self–replenishing times. Further, the wetting properties of water immediately after wear and providing sufficient self–replenishing times respectively are presented. They reveal that the worn surfaces are superhydrophilic and oleophilic immediately after the wear. However, the self–healing process retained the anti–sticking properties and enables easy sliding of both water and Hexadecane liquid drops atop. The influence of wear debris on the wettability is also briefly discussed. Additionally, the wetting properties of water based and oil based viscous paints atop Fomblin® impregnated MPA composites and dry MPA surfaces are shown.

To be communicated, 2016

Retention of Anti–Sticking and Sliding Behaviors in Perfluoropolyether Impregnated Mesoporous Alumina Composites Post Wear

Sriharitha Rowthu, Patrik Hoffmann**

Advanced Materials Processing Laboratory, Empa, Swiss Federal Laboratories for Materials Science and Technology, Feuerwerkerstrasse 39, 3602 Thun, Switzerland

E–Mail*: haritha.iitm@gmail.com; patrik.hoffmann@empa.ch

Abstract

Preparation of wear–resistant omniphobic surfaces is a fundamental challenge in the wetting community. The conventional omniphobic surfaces are vulnerable to wear either due to the loss of surface roughness elements or the loss of functional coatings or both. Therefore, the present work aims at demonstrating the post wear anti–sticking properties of perfluoropolyether (Fomblin® oil) impregnated mesoporous alumina (referred to as MPA). Low viscosity liquids such as water and Hexadecane, and even high viscosity water based and oil based paints exhibit anti–sticking behaviors and pinning free sliding atop Fomblin® oil impregnated/lubricated alumina composites. The tribological evaluations were carried out using reciprocating sliding in flat–on–flat configuration, with normal pressures up to 10 MPa. The worn samples exhibited superhydrophilicity immediately after the wear. Nevertheless, given a self–healing/self–replenishing time of 15 h, they showed retention of anti–sticking properties and allowed pinning free sliding for water and Hexadecane drops. The composite materials exhibited very small wear coefficients of ~10^{-5}–10^{-7} $mm^3\ N^{-1}\ m^{-1}$ and possessed micro debris particles as evidenced from electron microscopy. The presence of micro debris in conjunction with a self–healing process led to a strong increase in the static contact angle measurements in the worn samples as compared to unworn regions.

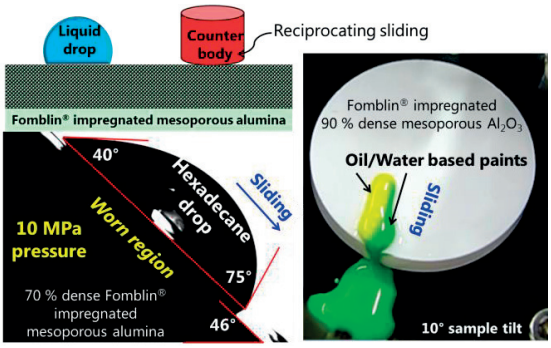

Keywords: wear–resistant, mesoporous alumina, liquid impregnation, anti–sticking, wetting retention, acrylic paints, Fomblin® oil

1. Introduction

It is well known that the liquid repellency of a surface depends on the surface chemistry and the surface roughness.[1,2,3] Apolar surfaces coupled with high surface roughness favor liquid repellency. On the contrary, the wear resistance of a material is inversely related to the surface roughness and linearly proportional to Vickers hardness, especially for abrasive type of wear[4]. Therefore, often liquid repellent surfaces are usually not wear–resistant and vice versa. However, one can imagine a wide variety of applications that require surfaces to have combination of functions such as in anti–fouling materials in extreme environments, fluid transportation, self–cleaning, paint industries and others. Evidently, there is a thrust to obtain anti–sticking surfaces which are wear–resistant and importantly retain the wetting characteristics post wear.

There have been limited scientific studies carried out to produce a liquid–repellent and wear–resistant material, few examples include decanethiol hydrophobized compacted Cu metal powders,[5] a composite of alumina/chitosan/poly[octadecene–alt–(maleic anhydride)],[6] highly porous gels,[7] solid foams,[8] liquid impregnated anodized alumina[9], PDMS coated alkali treated PET textiles[10], Ethoxysilane coated interconnected and attached to perfluorosilanized silica microspheres[11], micro–micro hierarchical textured PP surfaces[12] and others[13,14]. All the aforementioned reported studies employed very small normal

pressures of a maximum of 310 kPa. In all the studies, the surfaces either lacked high wear–resistance or mechanical strength or led to the loss of liquid repellency properties after very mild abrasion or possess complex chemical treatment.

The recently proposed liquid impregnation approach in literature[15] popular as SLIPS has been applied to a variety of surface functionalized materials that have surface protruding microstructural features. However, presumably, such surface protruding features are vulnerable to wear, may lead to large friction coefficients, with the functional coatings worn off during the wear process, and leading to the loss of the desired wetting properties. Hence, we propose to use liquid impregnated mesoporous α–Al_2O_3 composites without carrying out any surface functionalization of alumina nor having surface protruding micro features to evaluate the wetting response post severe wear tests. We have already demonstrated earlier[16], the anti–sticking and sliding behaviors of alkanes and water drops atop Fomblin® impregnated MPA composite surfaces. In this report, we will show the retention of anti–sticking and sliding behaviors post harsh wear treatments.

2. Materials and Methods

Mesoporous alumina samples were prepared as reported in our earlier articles[16,17] and sintered in air at 1150, 1205, 1250, 1325, 1500 °C to achieve 70±3, 80±3, 90±3, 95±1, 99±0.5 % theoretical densities respectively. 70 % to 90 % dense samples contain open porosity as the major fraction and closed porosity as the minor fraction (closed porosity is ~1 % for 70–90 % dense samples and the rest is open porosity)[16] while for 95 % dense samples, the closed porosity is the majority (~2.5 %)[18]. The area fractions of debris compacted regions in 95 % and 99.5 % dense samples are ~98 % and 100 % respectively. The complete sample preparation, polishing procedure, liquid impregnation, flatness, waviness, roughness and microstructural characterizations are reported in our other articles[16,18].

The static contact angles of water and Hexadecane drops atop Fomblin® oil impregnated/lubricated mesoporous alumina composites were characterized with a contact angle goniometer, Digidrop, France. The volume of aforementioned test liquids is ~2–3 μl and the measurements were carried out at ambient temperature (25 °C) and 35±10 % RH. The wetting behavior of water based and oil based acrylic paints atop Fomblin® oil impregnated/lubricated MPA samples have also been studied.

The cuboidal Fomblin® impregnated MPA samples and dry alumina samples were slid in reciprocating sliding contact in flat–on–flat configuration with SRV® III, Optimol Instruments Prüftechnik GmbH, Germany tribometer to obtain friction coefficient data. The counter body material is cylindrically shaped dry porous alumina/WC/diamond and held in a special holder which can compensate for small sample tilts or flatness issues between the two sliding surfaces. The normal load varied from 10 N to 220 N for all the oscillating tribological tests. The contact areas for 70–90 % dense samples are between 36–42 mm^2 respectively. Hence the normal pressures range from 0.24–5.24 MPa, 0.27–5.87 MPa, and 0.28–6.11 MPa for 70 %, 80 % and 90 % dense samples respectively. The frequency and the stroke are 6/13 Hz and 4 mm respectively. Also, the friction measurements were carried out with a unidirectional sphere on disc tribometer using normal pressures between ~300–350 MPa and 0.1 m s^{-1} speed and 2 km sliding distance for Fomblin® lubricated 99.5 % dense alumina and monocrystalline sapphire samples respectively. The friction tests were carried out in a controlled chamber environment where the chamber RH is maintained at 30 % and the temperature is 30 °C for all the tests. All the tribological tests were repeated at least twice unless otherwise stated. The samples were weighed with a high precision (10^{-4} g) weighing balance before and post wear tests to calculate the wear rates.

3. Results

The wetting behaviors of 70–99.5 % dense Fomblin® impregnated, flooded polished MPA composites prior and post wear experiments are presented in the following. The self–healing of these composites will be demonstrated by evaluating the wetting properties of water drops atop worn regions immediately after wear experiments and providing sufficient healing time.

3.1. Wetting Behavior Prior to Wear

We demonstrated earlier[16] that low viscous liquids such as water and alkanes (Hexadecane and Dodecane) exhibited anti–sticking and sliding behaviors atop Fomblin® impregnated, polished, *flooded* (refer Section 4.2.1, Chapter

4, for flooded and unflooded configurations) MPA composites. The details of sample preparation, liquid impregnation, microstructural characterizations, and wetting behaviors can be found in our other articles[16,18]. Here, we will show anti–sticking and sliding behaviors of water and oil based, high viscous paints. The wetting behaviors of such paints atop dry, non–impregnated, fully dense (99.5 % dense) alumina samples are presented in Figure 1a after a certain time t. It can be observed that both types of paint leave a trace behind on the alumina surfaces. However, for 70–90 % dense alumina based Fomblin® impregnated flooded samples, water and oil based paint drops (≤15 µl in volume) exhibited anti–sticking and sliding behaviors. The typical sliding behaviors of water and oil based paints are shown for 80 % and 90 % dense Fomblin® impregnated MPA samples in Figure 1b–d.

3.2. Wear Characterizations

The friction and wear behaviors of Fomblin® impregnated/lubricated (refer Chapter 5 for explanation on impregnated and lubricated terms) flooded α–Al_2O_3 composites have been extensively studied as a function of alumina matrix density, sliding frequency, apparent normal pressures, and the Fomblin® oil viscosity and will be presented as a separate report.[18] Here, we present a typical friction coefficient curve of 80 % dense Fomblin® impregnated MPA composite in Figure 2 when the apparent normal load increase from 10 N to 220 N (corresponding pressures of 270 kPa to 6 MPa). It can be observed that the friction coefficient (µ) decreases continuously with an increase in apparent normal load.

The friction coefficient values of 70–99.5 % dense based Fomblin® impregnated/ lubricated alumina composites lie in–between 0.095 and 0.37.[18] The wear coefficients (K´) of aforementioned composites were estimated using Archard wear Equation (1)[19].

$$K' = \frac{Q}{F_N S} \tag{1}$$

where Q is the total wear rate (volume removed, in mm^3), which was reported to be proportional to the sliding distance S (in m)[20] and F_N is the average normal load (in N).

The wear rates of 70–90 % dense alumina based composites lie in–between 10^{-5} and 10^{-7} mm^3 N^{-1} m^{-1}, while for samples possessing alumina density ≥ 94 %, the wear rates are ≤10^{-8} mm^3 N^{-1} m^{-1} and more details will be discussed in another report[18].

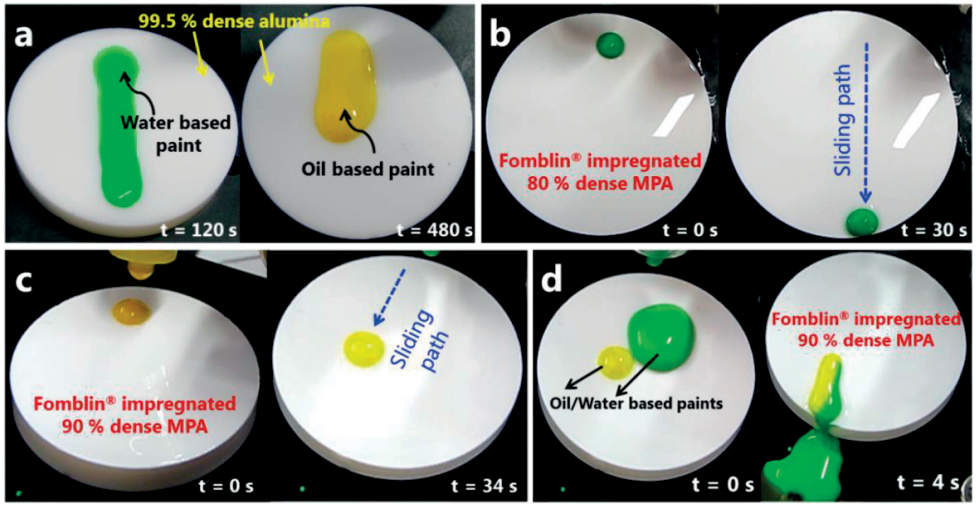

Figure 1. (a) The water (green colored) and oil (yellow colored) based viscous paints stick to full polished non–impregnated 99.5 % dense alumina sample and leave traces of paints behind. The sliding behaviors of ~2.5 µl (b) water and (c) oil based paint drops atop 80 and 90 % dense Fomblin® impregnated and *flooded* MPA samples, respectively are shown at times t =0 and t ≥ 30 s. (d) Anti–sticking and sliding behaviors of ~15 µl water and ~2.5 µl oil based paint drops atop 90 % dense Fomblin® impregnated and *flooded* MPA sample is presented at time t = 0 and t = 4 s. The sample tilt in all the experiments is 10°.

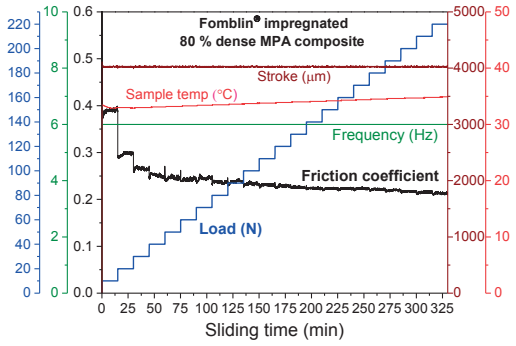

Figure 2. A typical measured friction coefficient curve for Fomblin® oil impregnated 80 % dense alumina composite sliding against dry 80 % alumina as the counter body. The apparent normal load varies from 10 N to 220 N (corresponding to 270 kPa to 6 MPa).

3.3. Wetting Characterizations Post Wear Tests

The wetting properties of water and Hexadecane liquids atop 70–90 % dense Fomblin® oil impregnated MPA composites post aforementioned wear experiments were evaluated and are presented in this section. The worn samples were left undisturbed for 15 h at 25±5 °C and 30±5 % RH to allow self–replenishing of Fomblin® oil atop dry alumina surfaces.

3.3.1. Wetting behavior of Hexadecane

We demonstrated earlier that the excess Fomblin® film (referred to as flooding film) atop MPA composite surfaces plays a crucial role in determining the sliding behaviors and even anti–sticking properties of deposited liquid droplets atop[16]. Hence, it is necessary to know whether the worn surfaces retained flooding Fomblin® oil films immediately after wear. The visible flooding Fomblin® film (thickness ~500 μm) present atop composite surfaces prior to wear experiments was absent in the worn regions immediately post wear experiments, and after 15 h of self–replenishing time as observed with naked eyes. However, in the unworn regions of the sample, such flooding films were visible after a total time of ~20 h (~5 h friction experiment+15 h self replenishing time). The equilibrium static contact angles (SCAs) of Hexadecane drops atop Fomblin® impregnated/lubricated 70–99.5 % dense alumina and sapphire composites were measured in the following 4 cases: (a) Before wear and possessing flooding Fomblin® film, (b) Before wear, without flooding Fomblin® film, (c) Unworn region, given 15 h self–healing time post wear and (d) Worn region, after 15 h self–replenishment time, and are presented in Figure 3a. It can be clearly observed that the SCAs were not altered when the alumina matrix density increased in the case (a) i.e. when the Fomblin® is flooding. However, in the case (b), the SCAs continuously decreased with an increase in alumina matrix density from 70 % to 99.5 %.

On the contrary, the SCAs exhibited a slight increase in the case (c) for an increase in alumina density from 70 % to 90 %. While in the case (d), there is no special trend exhibited for SCAs for an increase in alumina density from 70 % to 90 %, but are significantly larger as compared to all the other 3 cases. Exceptionally, in 80 % density based composites, the Hexadecane drop post wear and prior wear (unflooding) closely match with each other. The SCAs post wear experiments reveal that the composites retained or even exhibited improved wetting behaviors. Since the SCAs alone are insufficient to characterize the wetting properties of a surface, we have investigated the sliding behaviors of Hexadecane drops atop the composite surfaces by tilting the substrate to a minimum tilt angle (α), where the Hexadecane drops start sliding. The sample tilt angle (α) is presented for Hexadecane drops sliding as a function of alumina matrix density in Figure 3b.

For the samples prior to wear and possessing flooding Fomblin® film, a very small sample tilt of <5° was sufficient to allow sliding of Hexadecane drops, for more details and proof, please refer our earlier article[16]. In the unflooding case, prior to wear, for 70–90 % and 94–99.5 % density ranges, α increased with increase in alumina density, but exhibiting an absolute minimum for 90–94 % density range. However, observations with naked eyes clearly demonstrate that the Hexadecane drops leave a trace behind as they slide, for the aforementioned samples. The values of α in the unflooding configuration are significantly higher as compared to the flooding case. The values of α in the worn regions of the samples increased with an increase in alumina density from 70 % to 90 % and are 2–4 times higher as compared to those representing prior to wear in unflooding configuration. It is interesting that the Hexadecane drops slide in the worn regions of the sample without leaving any trace behind, however possessing some local pinning regions. In the unworn regions after the wear, the Hexadecane

drops exhibited dual behaviors such as sliding with and without leaving a trace behind and hence the corresponding α values are not presented here. When there is a visible Fomblin® film remaining on the unworn regions after wear, the Hexadecane drops cold slide off for $\alpha \leq 5°$. On the other hand, when there is no Fomblin® flooding, the values of α match with that of worn regions given a 15 h self–healing time. The discussion and interpretation of these results will be presented in the Discussion section in "*wetting prior and post wear tests"* section.

3.3.2. Dynamic CA measurements and microstructural characterizations

The dynamic CA measurements and contact angle hysteresis (CAH) of Hexadecane drops atop unflooded Fomblin® impregnated/lubricated alumina composites before wear are presented in Figure 4a, when the samples are tilted by corresponding α values of each densification. As already mentioned, the Hexadecane drops in this case leave a trace behind as they slide. The advancing CAs (referred to as ACA) and receding CAs (referred to as RCA) are very small and < 20°, with an absolute minimum of contact angle hysteresis (CAH = ACA–RCA) at 94 % alumina density. The advancing and receding CAs of Hexadecane atop 70 % dense Fomblin® impregnated MPA composites prior and post wear experiments are shown in Figure 4b–c along with their corresponding SEM images in Figure 4d–f. Despite the worn regions are exhibiting higher CAH of 35°, the Hexadecane drops slide without leaving any trace as presented in Figure 5, but possessing few pinning regions. The microstructure of unworn regions (Figure 4d) represents the whole surface prior to wear possessing the debris compacted regions and the porous regions.

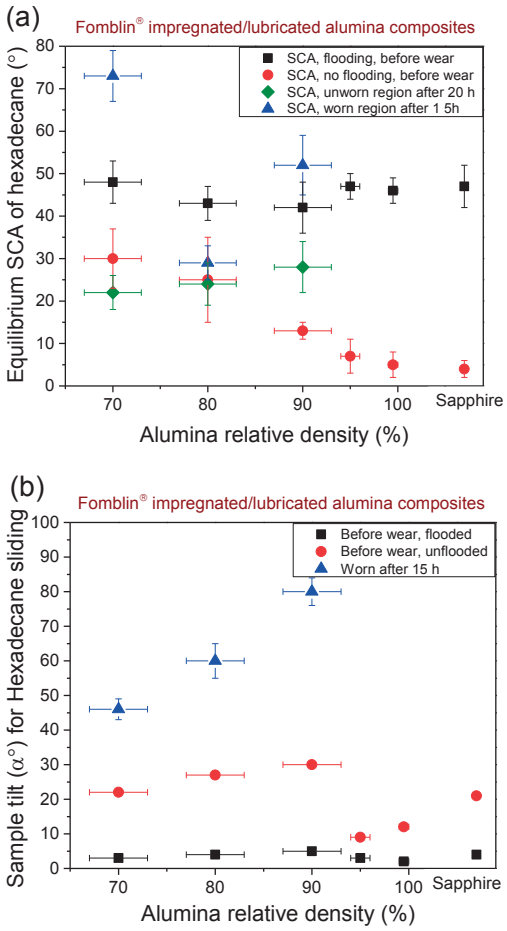

Figure 3. (a) Measured equilibrium static contact angles (SCAs) of Hexadecane drops atop 70–99.5 % dense Fomblin® impregnated/lubricated alumina composites and sapphire samples and (b) Minimum sample tilt angle (α°) of the substrate where Hexadecane drops starts sliding, presented as a function of alumina matrix density.

However, in the worn regions, there are many micro debris particles and scratches. The scratches at higher magnifications, revealed polished surfaces. The roughness (R_a) measurements of 70–90 % dense dry alumina samples before and after the wear experiments (step load experiments) lie in–between 50 and 90 nm with no significant changes due to wear.[18]

Self–replenishing and wetting behaviors post wear tests

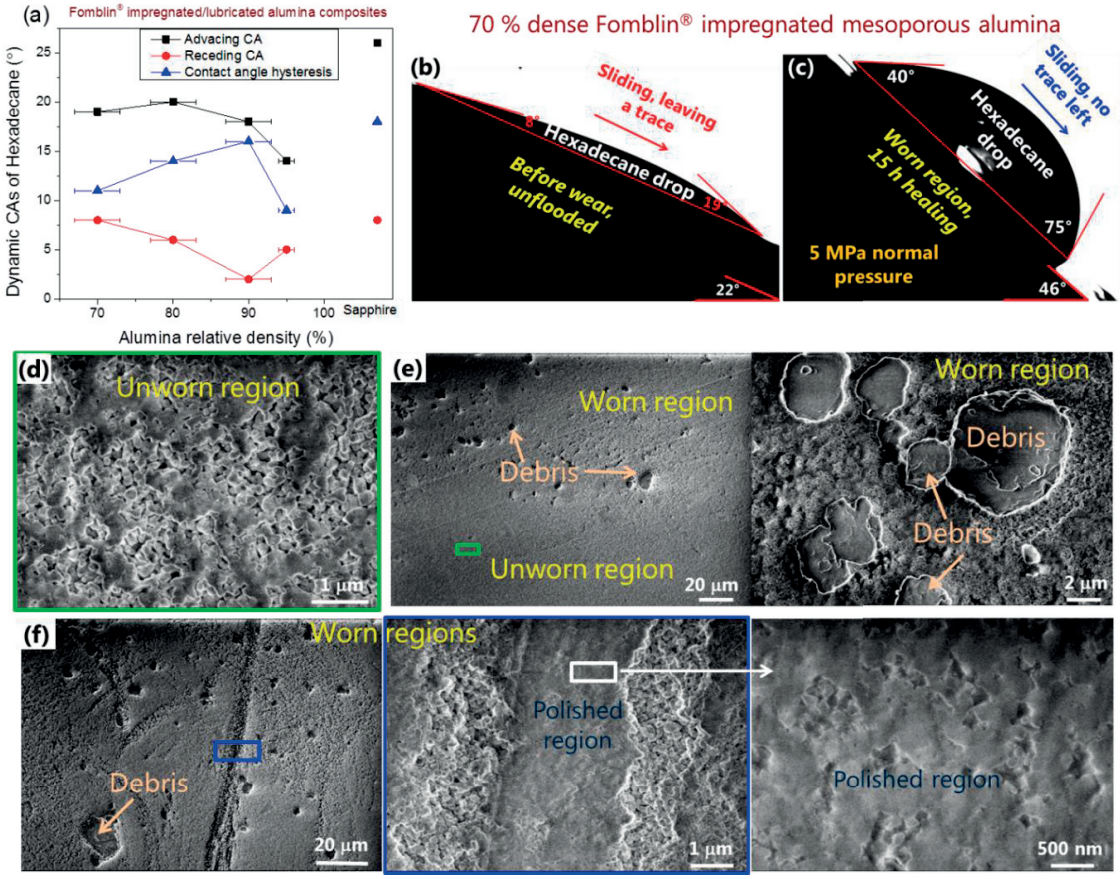

Figure 4. (a) Dynamic CAs of Hexadecane in Fomblin® impregnated/lubricated unflooded alumina composites before wear where the Hexadecane drops slide by leaving their trace, (b) a selected optical image of a Hexadecane drop atop Fomblin® impregnated 70 % dense, unflooded composite before wear and (c) a selected optical image of a 7th drop among 10 consecutive sliding drops from a video recorded using high speed camera, demonstrating the dynamic CAs of Hexadecane drop atop worn region, the latter was given a 15 h of self–healing time and (d–f) corresponding SE–SEM images of unworn and worn regions.

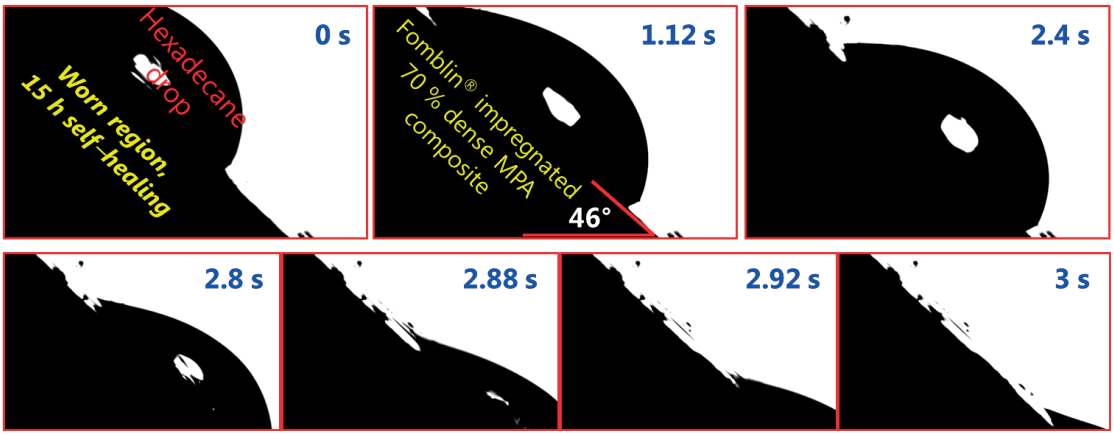

Figure 5. Selected image sequence of 5th drop (~2.5 µl volume) among 10 consecutive sliding drops captured using high speed camera, demonstrating the sliding behavior of a Hexadecane drop atop Fomblin® impregnated 70 % dense MPA sample post wear given a self–healing time of 15 h, as a function of time from 0 to 3 s.

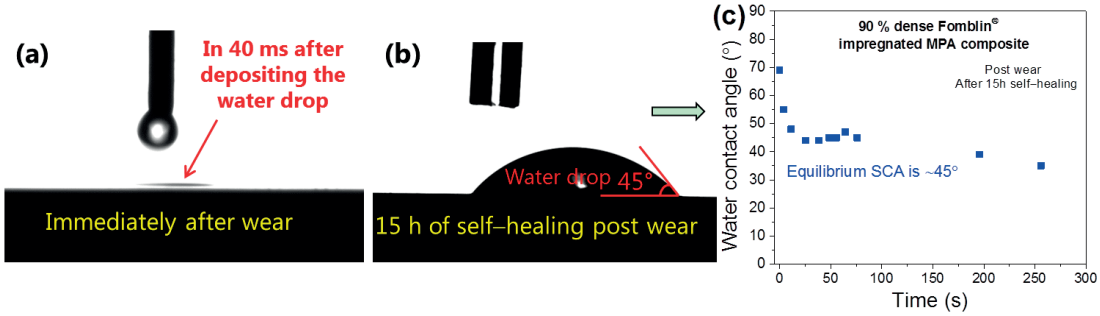

Figure 6. Optical images as recorded with a high speed camera of water drops atop 90 % dense Fomblin® impregnated MPA composite presenting for (a) immediately after the wear and (b) given a 15 h self–healing time. The corresponding CA sequence of (b) as a function of time after the deposition of the water drop is presented in (c).

3.4. Wetting behaviors of Water

The wetting behaviors of water drops atop the worn composites based on 70–90 % alumina density, were evaluated and are presented in this section. Immediately after the wear, the composite surfaces showed superhydrophilicity, a typical optical image of water drop atop 90 % dense based Fomblin® impregnated composite is shown in Figure 6a. There is no water drop visible on the surface due to its spreading and infiltration behaviors. However, a different sample having undergone the same treatment and given a 15 h self healing time, showed an initial SCA of 69° at time of 0 ms which reached to its equilibrium SCA of 45° after 12 s and remained constant for next 2 mins as presented in Figure 6b–c. Further, a slight decrease in the SCA after 3 mins after deposition of the drop was observed. The water drop in Figure 6b also exhibited sliding behavior for a sample tilt of ~5°.

In addition to the aforementioned wear experiments

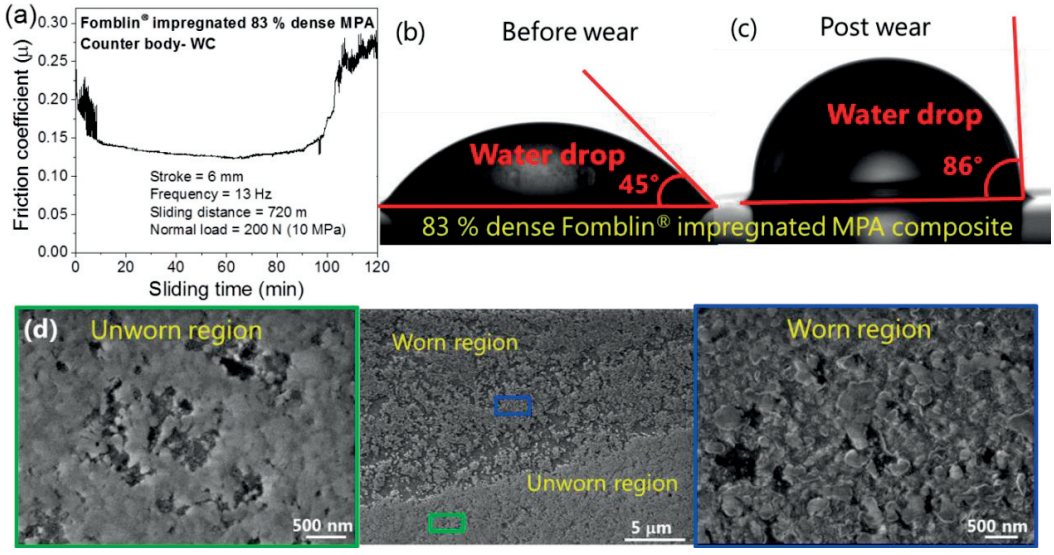

Figure 7. (a) Friction coefficient (μ) curve of 83 % dense Fomblin® impregnated MPA composite as a function of time. The sample was slid against WC with 10 MPa normal pressures, 4 mm stroke, 13 Hz frequency and for 720 m sliding distance. (b) Equilibrium static contact angle of a water drop atop 83 % dense Fomblin® impregnated MPA composite before and immediately post wear test and (d) their corresponding SE–SEM images of unworn and worn regions of the sample.

and wetting experiments post wear, a constant load experiment was carried out using 83 % dense Fomblin® impregnated alumina composite in the unflooding configuration, with WC as the counter body to study the wetting behavior of water before and post wear test. The tribological parameters are: sliding frequency of 13 Hz, stroke of 4 mm and 10 MPa normal pressure. A steady state friction coefficient of 0.15 was obtained and presented in Figure 7a. The roughness (R_a) increased from 30±4 to 100±25 nm due to wear and a significant wear rate of ~10^{-5} mm^3 N^{-1} m^{-1} was estimated using Archard wear equation. It was observed that the worn regions did not have any flooding film post wear tests. A deliberate addition of 2 µl Fomblin® oil to the worn region exhibited hydrophobicity immediately after wear without providing any self–replenishing time. The equilibrium SCA increased from 45° to 86° due to wear as shown in Figure 7b–c. The corresponding SE–SEM images of the unworn and the worn regions are presented in Figure 7d.

4. Discussion

In this section, the most important results will be discussed and the versatility of these composites is highlighted in comparison with literature. Considering Figure 1, water and oil based acrylic paints stick to dry alumina surfaces since alumina is omniphilic in nature. Whilst, water based and oil based paints exhibited anti–sticking and sliding behaviors atop *flooded* polished Fomblin® impregnated polished MPA (67–93 % dense) composites as shown in Figure 1b–d. Such observations are because the interface of water and oil based paints and the substrate is a liquid–liquid type and immiscible. The paint drops are ~2–3 orders of magnitude more viscous than water and therefore slide more slowly as compared to water. Hence, any sort of pinning forces can obstruct the motion of the paint which can eventually get stuck to the sample surface. As–sintered dry alumina samples possess large roughness in the order of ~3–5 µm[18] and hence the paint drops were observed to be strongly pinned during sliding. However, the polished surfaces have mean roughness R_a of 10–100 nm and Wenzel roughness of ~1.001±0.0005[16] and hence, the pinning forces for the paint drops are very small and easily slide off. Hence, very fine polishing of the sample surface may be necessary to observe sliding behaviors of high viscous liquids or emulsions or paints.

4.1. Wear tests in comparison with literature

There have been quite a few literature reports on the abrasion/wear resistance studies of superhydrophobic surfaces. Most studies utilized the custom built in–house experiments such as rubbing the sample surfaces against some kind of cloth[6,21,22], abrasive sandpaper[21,23,24], synthetic leather[25] or cotton swab[26]. Other procedures include ball–on–disk[27], pin–on–disc[12], sand abrasion or scouring with high–speed water jet[11,14,27–29] and scotch peel tests[30]. The maximum normal pressures employed in the literature are only until 310 kPa. All the superhydrophobic or oleophobic material systems involved in the aforementioned wear resistance studies in the literature can be majorly classified into two types: (a) a solid composite, obtained with complex chemical treatment involving silanes or perfluorinated coatings and (b) apolar surface consisting of surface hierarchical structures. In the former case, the materials lack chemical resistance, ease in handling, limited in tensile strength and are wear sensitive. Presumably, the latter material surfaces cannot withstand high normal pressures and will lose the wetting properties while employing harsh wear treatment.

In the current study, we report the retention and in many cases the improved wetting properties whilst using the normal pressures at least 2 orders of magnitude higher (up to 10 MPa) than the literature. Also, the normal pressures for the materials in the current study are not limited and can be even higher by an additional factor of 35, i.e. tested up to 350 MPa normal pressures[18]. Although the wetting characterizations were not evaluated in this high pressure wear studies, it can be presumed to have retained wetting behaviors given a sufficient self–healing time. Further, the sliding distances in our study are 4 orders of magnitude higher than in literature[27]. A more relevant and interesting report from the literature showed superamniphobic properties of 40 % dense nanoporous anodic alumina impregnated with perfluorooctyl acid[9], however this matrix material has limited tensile strength as compared to the crystalline α–Al_2O_3 used in the current study. Additionally, there is no report of the effect of wear on the wetting properties in this acid impregnated anodic alumina[9].

In addition to the wetting properties retention post wear, the tribological properties of Fomblin® impregnated MPA composites are very promising (refer to our another report for extensive studies[18]), as compared to that of surface silanized silica[11], anodic alumina[31], CNT[27], micro–micro hierarchical surface structures of PP[12] since perfluoroethers are considered as good lubricants due to their low shear strength[32]. Additionally, perfluorinated impregnated composites have been reported to have other properties such as good transparency and anti–ice frosting properties.[31,33–35] Perfluoropolyether impregnated MPA composites are thus promising novel material systems to achieve multi–functionalities.

4.2. Wetting prior and post wear tests

In this subsection, the interpretations of the wetting results prior and post wear treatment (referring to Figures 3–7) will be described. Referring to the wetting behaviors of Hexadecane drops before wear in flooding configuration (Figure 3a), the SCAs exhibited no significant difference for an increase in the alumina matrix density because the Fomblin® film is quite thick (300–500 μm)[16] and hence the substrate roughness elements are completely submerged. However, when this flooding film was removed by blowing with compressed N_2 gas and lint free optical paper as described in our earlier article[16], the alumina roughness and alumina solid fraction in contact with the Hexadecane drop affect the SCAs. The SCA of Hexadecane on a flat Fomblin® oil can be considered the same as that for the flooding case which is ~45°. Assuming that the alumina roughness elements are completely covered by a few monolayers of Fomblin® oil, then Wenzel equation[36] can be used to estimate the SCAs. The SCAs of Hexadecane drops atop such a surface should decrease with a decrease in roughness for a given flat SCA of 45°.

Therefore, we expect that the SCAs to decrease for a decrease in alumina density for unflooding configuration before wear, as the lower densities constitute higher roughness. However, the experimentally observed values show a contradictory trend compared to that predicted using Wenzel equation. This could be because of chemical heterogeneity arising from partially exposed dry alumina surfaces to the Hexadecane drop, thus exhibiting a composite Cassie state. Hence the SCAs in unflooding case continuously decreased with an increase in alumina matrix density from 70 % to 99.5 %. On the contrary, in the case of unworn regions after wear, i.e. given a 20 h self–healing time, the Fomblin® oil may have covered all the dry alumina surfaces but unflooding the roughness elements. Hence, the roughness decrease causes an increase in SCAs in the measured values, as predicted earlier using the Wenzel configuration.

In the case of worn samples, higher values of SCAs were observed as compared to prior wear or the unworn regions post wear experiments. Such observations can be ascribed to the presence of wear debris in the form of micro and/or nano particles, as confirmed by observed high wear rates of 10^{-5}–10^{-7} mm^3 N^{-1} m^{-1}. The distribution and the amount of wear locally cannot be controlled and hence, the strong differences in measured SCAs for 70 %, 80 % and 90 % dense dry alumina samples were observed. The R_a values of 70, 80 and 90 % samples post wear are 78±7, 77±9 and 50±5 nm respectively. However, strong differences in SCAs in the worn regions as a function of alumina density cannot be explained by R_a values alone since they are insufficient to describe the surface roughness state in the wetting field. The presence of micro or nano debris adherent to the substrate immediately after wear, any micro cavities on the surface are not considered in the R_a values.

In the case of sliding tilt angle (α) (Figure 3b), very small angles ≤ 5° were observed for flooding configuration prior to wear because the Hexadecane–substrate (Fomblin® oil impregnated MPA) interface is of liquid–liquid type. However, in unflooding configuration before wear, the angle α increases for alumina matrix density from 70 % to 90 %, which could be associated to an increase in the chemical heterogeneity at the Hexadecane–substrate interface. However, for further increase in alumina density to 94 %, the roughness of the substrate, drastically decrease, as the open pore network is no longer available, and hence, decreases the pinning forces and hence there is an absolute minimum at 94 % density. A significant and continuous increase in the α values for 70–90 % dense alumina based composites, post wear is due to strong pinning forces due to the presence of micro sized debris present on the composite surface as shown in 70 % dense sample in Figure 4e–f. Overall, the worn regions have strong heterogeneity in

microstructure as compared to unworn regions or before wear (Figure 4d–f, Figure 7d). Also, the worn samples (Figure 4e–f, Figure 6b) were provided by a 15 h self–healing time and hence all the alumina surface in the substrate and the debris would be completely covered with one or more monolayers of Fomblin® oil. This also justifies why there is no liquid trace left behind in the worn regions of the samples as the Hexadecane and water drops slide off the surfaces.

The self–replenishing behaviors are dominantly visible for a water drop top Fomblin® impregnated MPA samples as shown in Figure 6. Water drops are preferred over Hexadecane drops to show self–replenishing behaviors because, Hexadecane makes a non–zero SCA even if the replenishment is not complete[16]. In Figure 6a, a water drop immediately penetrated into the composite substrate because there are dry alumina regions exposed to the water drop. It was already shown[16] that water drop penetrates into Fomblin® impregnated composite which does not have flooding Fomblin® film even before wear for the same reason. However, when the sample was given 15 h self–healing time, the water drop exhibited an equilibrium SCA of 45°, which matches well with that of SCA in the flooding configuration before wear (see Figure 3a). Also, this indicates that complete self–replenishing occurred during this time and Fomblin® film thickness could be larger than the surface roughness elements. It also implies that very large Fomblin® film thickness of ~500 μm is not necessary to achieve anti–sticking and sliding behaviors as suggested in our earlier article[16]. The choice of self–healing time of 15 h used in this current study is based on the capillary uptake experiments, however, more accurate values can be predicted and will be presented in a separate report.

The self–replenishing time of the impregnating liquid to completely cover all the dry alumina surfaces depends on several factors such as depth at which the Fomblin® oil is present in the substrate porous matrix at a given time, viscosity of Fomblin® oil, CA of Fomblin® oil with alumina, tortuosity of the mesoporous alumina network, effective pore radius, surface diffusivity of the impregnating liquid, area of the dry alumina surfaces and the required width of lubricant film atop alumina surfaces. All the aforementioned parameters have been used to develop a simple model which will be presented elsewhere.

5. Conclusions

The anti–sticking and pinning free sliding behaviors of high viscosity water and oil based paints (≤15 μl) were observed atop Fomblin® impregnated flooded alumina composite surfaces in addition to the low viscosity liquids such as alkanes and water. The wetting properties of Hexadecane and water were evaluated in these composites immediately after wear and after 15 h self–replenishing process. The worn regions exhibited superhydrophilicty and partial oleophilicity immediately after wear. Nevertheless, they regained the anti–sticking properties and allowed easy sliding of Hexadecane and water drops after self-healing process. We showed earlier[16] that a flooding film is necessary to show anti–sticking properties for water drops. However, interestingly, the replenished unworn regions exhibited anti–sticking properties to water and Hexadecane without containing any flooding Fomblin® film.

For the employed normal pressures up to 10 MPa, non negligible wear coefficients of 10^{-5}–10^{-7} $mm^3.N.m^{-1}$ were observed in these composites with alumina matrix densities from 70 % to 90 %. The wear debris present on the worn samples were also replenished with Fomblin® oil during the healing process and led to enhanced omniphobicity as compared to unworn regions. The normal contact pressures employed in this study are two orders of magnitude bigger as compared to those reported in conventional wetting–wear studies are not limiting the performances. Indeed, these composites can withstand very high normal contact pressures easily up to 350 MPa (6 orders of magnitude higher as compared to literature studies) and even more.

A first study on the retention of the wetting properties post wear characterizations in liquid impregnated composites, is presented here. Indeed, it can be extended to study the effect of high normal pressures (>>10 MPa) on the wetting properties. Additional in–depth studies concerning the self–replenishing efficiency are needed. Briefly, the study promotes these composites versatile for liquid repellency and wear–resistance applications and serve as multi–functional advanced composite material systems.

Author contributions

Rowthu Sriharitha conceived and performed all the experiments and written down the complete manuscript. Patrik Hoffmann supervised the project, had technical and scientific discussions. Both the authors contributed to the correction of the manuscript.

Funding Information

The project was mainly funded by CCMX, Switzerland with project number 5211.00093.100.01. We thank Bobst, Switzerland, CCMX industrial partner for partially funding the project.

Acknowledgements

We thank Peter Ramseier, technician at Empa Thun for polishing few alumina samples required for the tribological tests. We thank Dr. Kilian Wasmer, Empa Thun for the help. We thank Dr. Edin Balic, Swiss−9, GmbH for participating in the CCMX project.

References

(1) Young, T. An Essay on the Cohesion of Fluids. *Philosophical Transactions of the Royal Society of London* **1805**, 65–87.

(2) Fowkes, F. M.; Zisman, W. A.; others. Contact Angle, Wettability, and Adhesion. **1964**.

(3) Barthlott, W.; Ehler, N. Raster-Elektronenmikroskopie Der Epidermis-Oberflachen von Spermatophyten. *Trop. Subtrop. Pflanzenwelt* **1977**, *19*, 367–465.

(4) Krishnamurthy, N.; Prashantharеddy, M.; Raju, H.; Manohar, H. A Study of Parameters Affecting Wear Resistance of Alumina and Yttria Stabilized Zirconia Composite Coatings on Al-6061 Substrate. *ISRN Ceramics* **2012**, *2012*.

(5) Larmour, I. A.; Saunders, G. C.; Bell, S. E. Compressed Metal Powders That Remain Superhydrophobic after Abrasion. *ACS Applied Materials \& Interfaces* **2010**, *2*, 2703–2706.

(6) Höhne, S.; Blank, C.; Mensch, A.; Thieme, M.; Frenzel, R.; Worch, H.; Müller, M.; Simon, F. Superhydrophobic Alumina Surfaces Based on Polymer-Stabilized Oxide Layers. *Macromolecular Chemistry and Physics* **2009**, *210*, 1263–1271.

(7) Hou, W.; Mu, B.; Wang, Q. Studies on Wettability of Polypropylene/methyl-Silicone Composite Film and Polypropylene Monolithic Material. *Journal of colloid and interface science* **2008**, *327*, 120–124.

(8) Shirtcliffe, N. J.; McHale, G.; Newton, M. I.; Perry, C. C. Intrinsically Superhydrophobic Organosilica Sol-Gel Foams. *Langmuir* **2003**, *19*, 5626–5631.

(9) Wang, X.; Liu, X.; Zhou, F.; Liu, W. Self-Healing Superamphiphobicity. *Chemical Communications* **2011**, *47*, 2324–2326.

(10) Xue, C.-H.; Li, Y.-R.; Zhang, P.; Ma, J.-Z.; Jia, S.-T. Washable and Wear-Resistant Superhydrophobic Surfaces with Self-Cleaning Property by Chemical Etching of Fibers and Hydrophobization. *ACS applied materials \& interfaces* **2014**, *6*, 10153–10161.

(11) Deng, X.; Mammen, L.; Zhao, Y.; Lellig, P.; Müllen, K.; Li, C.; Butt, H.-J.; Vollmer, D. Transparent, Thermally Stable and Mechanically Robust Superhydrophobic Surfaces Made from Porous Silica Capsules. *Adv. Mater. Weinheim* **2011**, *23*, 2962–2965.

(12) Huovinen, E.; Hirvi, J.; Suvanto, M.; Pakkanen, T. A. Micro-Micro Hierarchy Replacing Micro-Nano Hierarchy: A Precisely Controlled Way to Produce Wear-Resistant Superhydrophobic Polymer Surfaces. *Langmuir* **2012**, *28*, 14747–14755.

(13) Li, H.; Wang, X.; Song, Y.; Liu, Y.; Li, Q.; Jiang, L.; Zhu, D. Super-"Amphiphobic" Aligned Carbon Nanotube Films. *Angewandte Chemie International Edition* **2001**, *40*, 1743–1746.

(14) Deng, X.; Mammen, L.; Butt, H.-J.; Vollmer, D. Candle Soot as a Template for a Transparent Robust Superamphiphobic Coating. *Science* **2012**, *335*, 67–70.

(15) Wong, T.-S.; Kang, S. H.; Tang, S. K.; Smythe, E. J.; Hatton, B. D.; Grinthal, A.; Aizenberg, J. Bioinspired Self-Repairing Slippery Surfaces with Pressure-Stable Omniphobicity. *Nature* **2011**, *477*, 443–447.

(16) Rowthu, S.; Balic, E. E.; Hoffmann, P. Sliding Behavior and Stability of Liquid-Liquid Impregnated Mesoporous Alumina Composite Interfaces. To be c*ommunicated,* **2016**.

(17) Rowthu, S.; Böhlen, K.; Bowen, P.; Hoffmann, P. Surface 3D Micro Free Forms: Multifunctional Microstructured Mesoporous α-Alumina by In-Situ Slip Casting Using Excimer Laser Ablated Polycarbonate Molds. *ACS applied materials \& interfaces* **2015**, *7*, 22458–22469.

(18) Rowthu, S.; Balic, E. E.; Hoffmann, P. Tribological Evaluations of Fomblin Impregnated Mesoporous Alumina Composites. *To be communicated, Wear* **2016**.

(19) Hutchings, I. M. *Tribology: Friction and Wear of Engineering Materials*; London: Edward Arnold, 1992; p. 280.

(20) Williams, J. *Engineering Tribology*; New York Cambridge University Press, 2005.

(21) Xiu, Y.; Liu, Y.; Hess, D. W.; Wong, C. Mechanically Robust Superhydrophobicity on Hierarchically Structured Si Surfaces. *Nanotechnology* **2010**, *21*, 155705.

(22) Yanagisawa, T.; Nakajima, A.; Sakai, M.; Kameshima, Y.; Okada, K. Preparation and Abrasion Resistance of Transparent Super-Hydrophobic Coating by Combining Crater-like Silica Films with Acicular Boehmite Powder. *Materials Science and Engineering: B* **2009**, *161*, 36–39.

(23) Bayer, I. S.; Brown, A.; Steele, A.; Loth, E. Transforming Anaerobic Adhesives into Highly Durable and Abrasion Resistant Superhydrophobic Organoclay Nanocomposite Films: A New Hybrid Spray Adhesive for Tough Superhydrophobicity. *Applied physics express* **2009**, *2*, 125003.

(24) Li, Y.; Li, L.; Sun, J. Bioinspired Self-Healing Superhydrophobic Coatings. *Angewandte Chemie* **2010**, *122*, 6265–6269.

(25) Zimmermann, J.; Reifler, F. A.; Fortunato, G.; Gerhardt, L.-C.; Seeger, S. A Simple, One-Step Approach to Durable and Robust

Superhydrophobic Textiles. *Advanced Functional Materials* **2008**, *18*, 3662–3669.

(26) Xiong, M.; Stein, J.; Zheng, L.; Lei, H.; Xiao, J.; Deng, T.; Zhu, Y. Superhydrophobic Coating Composition and Coated Articles Obtained Therefrom. **2006**.

(27) Jung, Y. C.; Bhushan, B. Mechanically Durable Carbon Nanotube-Composite Hierarchical Structures with Superhydrophobicity, Self-Cleaning, and Low-Drag. *ACS Nano* **2009**, *3*, 4155–4163.

(28) Xue, C.-H.; Ma, J.-Z. Long-Lived Superhydrophobic Surfaces. *Journal of Materials Chemistry A* **2013**, *1*, 4146–4161.

(29) Cui, Z.; Wang, Q.; Xiao, Y.; Su, C.; Chen, Q. The Stability of Superhydrophobic Surfaces Tested by High Speed Current Scouring. *Applied Surface Science* **2008**, *254*, 2911–2916.

(30) Xu, L.; Karunakaran, R. G.; Guo, J.; Yang, S. Transparent, Superhydrophobic Surfaces from One-Step Spin Coating of Hydrophobic Nanoparticles. *ACS applied materials \& interfaces* **2012**, *4*, 1118–1125.

(31) Aizenberg, J.; Aizenberg, M.; Kang, S. H.; Wong, T. S.; KIM, P. Slippery Surfaces with High Pressure Stability, Optical Transparency, and Self-Healing Characteristics. **2014**.

(32) Tao, Z.; Bhushan, B. Bonding, Degradation, and Environmental Effects on Novel Perfluoropolyether Lubricants. *Wear* **2005**, *259*, 1352–1361.

(33) Yao, X.; Hu, Y.; Grinthal, A.; Wong, T.-S.; Mahadevan, L.; Aizenberg, J. Adaptive Fluid-Infused Porous Films with Tunable Transparency and Wettability. *Nat Mater* **2013**, *12*, 529–534.

(34) Cheng, D. F.; Masheder, B.; Urata, C.; Hozumi, A. Smooth Perfluorinated Surfaces with Different Chemical and Physical Natures: Their Unusual Dynamic Dewetting Behavior toward Polar and Nonpolar Liquids. *Langmuir* **2013**, *29*, 11322–11329.

(35) Urata, C.; Masheder, B.; Cheng, D. F.; Hozumi, A. Unusual Dynamic Dewetting Behavior of Smooth Perfluorinated Hybrid Films: Potential Advantages over Conventional Textured and Liquid-Infused Perfluorinated Surfaces. *Langmuir* **2013**, *29*, 12472–12482.

(36) Wenzel, R. N. Resistance of Solid Surfaces to Wetting by Water. *Industrial \& Engineering Chemistry* **1936**, *28*, 988–994.

It was demonstrated that the wetting properties were recovered in the worn samples by a self–healing process. To understand this, a theoretical approach is presented in the next section describing the different stages of the self–replenishment process.

6.3. Theoretical prediction of self–healing times

The self–replenishing property of a LIMPA composite depends on three factors, namely capillarity, surface diffusivity and vapor phase transport including the evaporation rate of the impregnating liquid. Capillarity and surface diffusivity phenomena occur while the evaporation occurs in parallel and either contributing or counteracting both the former processes. A schematic diagram presenting the different stages of the self–replenishment process in LIMPA composite is shown in Figure 6.3. In case of a dry, non–impregnated mesoporous alumina sample suspended into a liquid reservoir bath, stage 1 (Figure 6.3) represents a dynamic step during the occurrence of capillarity process. In this stage 1 process, there will be an additional time t_o, associated for a rise in the fluid level by height h_o. The value of t_o depends only on the height h_o and can be calculated using Equation (6.1) by substituting h_o as the thickness of the sample. The stage 1 exists only when there is no liquid at the alumina top surface. Therefore, this stage 1 may not exist in LIMPA composites immediately after impregnation. Nevertheless, if the liquid exhibits a higher evaporation rate as compared to capillary rate, for example in high temperature friction experiments, then stage 1 may be present in LIMPA composites too. However, in low temperature friction experiments of Fomblin® impregnated MPA composites, stage 1 may not exist.

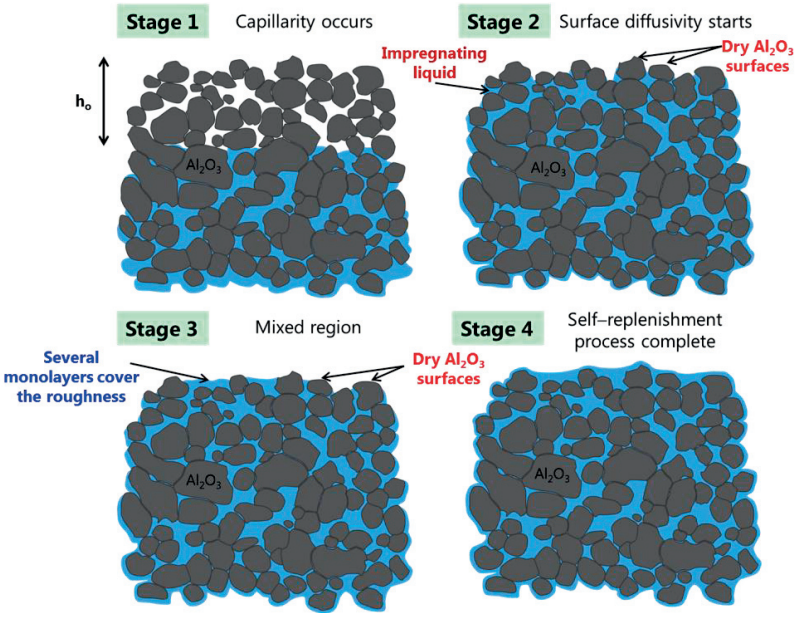

Figure 6.3. A schematic diagram presenting the different stages of self–replenishment process in a LIMPA composite is shown here. In stage 1, the capillarity of impregnating liquid (blue colored) occurs until all the pore network is filled up with the impregnating liquid. At the end of stage 1, stage 2 begins due to the initiation of the surface diffusivity process. In stage 3, heterogeneous LIMPA surfaces may exist, containing both

completely replenished regions and dry alumina regions. In stage 4, the process is complete and there is no dry alumina surface. The evaporation process occurs during all the stages, in parallel and counteracting the other two processes.

The capillary flux ($\dot{V}_1$) was obtained by simply differentiating the Washburn´s equation and mathematically described by Equation (6.4).

$$\dot{V}_1\left(\frac{m^3}{m^2 s}\right) = \frac{k(1-\phi)}{2}\sqrt{\frac{r_o \gamma_{LV} cos\theta}{2\tau\eta t}} \tag{6.4}$$

where the symbols are defined as: r_0–effective pore radius, γ_{LV} (liquid (vapor surface tension, θ (contact angle of liquid with substrate material, t–time, τ–tortuosity, η–dynamic viscosity of liquid, ϕ–debris compacted/solid fraction, k is the ratio of measured to the predicted volume rates (equal to 1 for Fomblin® oil, as deduced from Section 6.1). The molecular capillary flow rate (molecules.m^{-2}.s^{-1}) can be therefore estimated using the molecular weight (3200 g.mol^{-1}) and density (1.9 g.cm^{-3}) values of Fomblin® oil. The molecular capillary flow rate is shown in Figure 6.6 as a function of time. The order of magnitude of this flux rate is ~10^{19} molecules.m^2.s^{-1}.

In the stage 2 of the self–replenishing process, the surface diffusivity process begins to occur. The surface diffusivity value (D_s) of Fomblin® Z15 oil atop a silica substrate is 2.755×10^{-11} m^2.s^{-1} at 26 °C having a viscosity of 160 cSt a molecular weight (MW) of 13800 g.mol^{-1} and obtained from literature [148]. The surface diffusivity value of a liquid depends on the substrate–liquid interactions and may influence by ~1.5–2 times, but keeping the same order of magnitude [148]. Since the Fomblin® oil has very weak interactions both with silica substrate [148] and also presently employed alumina substrate, the surface diffusivity values obtained from literature are appropriate. In the present study, Fomblin® Y 25/6 oil is used which has a viscosity of 250 cSt at 20 °C and molecular weight of 3200 g.mol^{-1}. The surface diffusivity of a liquid is inversely proportional to its viscosity (η) and directly proportional to the temperature (T) as given by Stoke–Einstein–Sutherland relation [149] and mathematically described by Equation (6.5). Eventually, the surface diffusivity of Fomblin® Y25/6 oil was estimated to be 1.728×10^{-11} m^2.s^{-1} employing the Equation (6.5).

$$\frac{D_1}{D_2} = \frac{\eta_2 T_1}{\eta_1 T_2} \tag{6.5}$$

where D_1, D_2 are surface diffusivities possessing η_1 and η_2 viscosities at temperatures T_1 and T_2 respectively.

Recalling the microstructures of as–polished MPA samples from Figure 5.9a, there are porous regions and debris compacted regions. In the porous regions, there are mesopores (30–50 nm pore diameters) and ultrafine grains (~150 nm). The estimated time $\left(\frac{grain\ radius}{\sqrt{D_s}}\right)$ to replenish such small ultrafine grains by surface diffusivity is ~18 ms and is therefore quite fast. Hence, the porous regions act as the Fomblin® oil reservoirs for fully compacted or sintered regions in the polished

surfaces as schematically shown in Figure 6.4a. The debris compacted regions are not completely impermeable as they might contain sub nanometer pores. The reduction of pore sizes by 2 orders of magnitude decreases the capillarity flux rate ($\dot{V}_1$) by only one order of magnitude as deducted from Equation (6.4). Thus, the sub nanometer pores from the debris compacted regions also contribute to the self–replenishing process. As we follow, it will become evident that the capillarity transport by meso or sub nanometer pores is not the rate determining process in Fomblin® impregnated MPA composites. The above analysis futher suggests that the replenishing efficiency is not lowered due to mechanical surface polishing treatment of MPA samples.

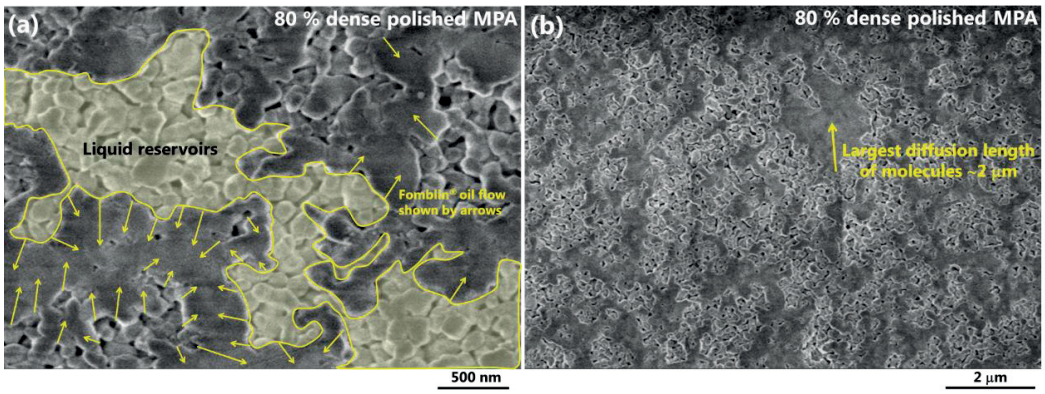

Figure 6.4. (a) The surface diffusivity of the Fomblin® oil from mesoporous reservoirs onto less permeable debris compacted regions is shown by the yellow colored arrows in 80 % dense polished MPA surface. (b) The largest diffusion length (x) that the Fomblin® oil may have to travel to replenish dry alumina surfaces is shown and is ~2 μm.

The diffusion time (t_d) of a liquid molecule traversed over diffusion distance (x) is given by Equation (6.6) [150].

$$\text{time } (t_d) = \frac{x^2}{D_s} \tag{6.6}$$

In this equation, *x* is not a constant value during the replenishing process. The maximum value of *x* can vary from as small as 75 nm (half of the average grain diameter) to as big as 2 μm in polished alumina samples prior to wear as schematically proposed in Figure 6.4. However, the worn surfaces seems to have large portions of fully dense regions as a result of tribo–sintering as shown in Figure 6.5. The debris particles could also undergo tribo–sintering when they remain as a third body during the abrasion. Such dense micron sized debris particles present on the worn composite surface (Figure 6.5b) also needs to be replenished during the healing process. The diffusion distances to be travelled by the liquid in the latter case are three dimensional accounting for the thickness of the debris particles, therefore suggest higher *x* values.

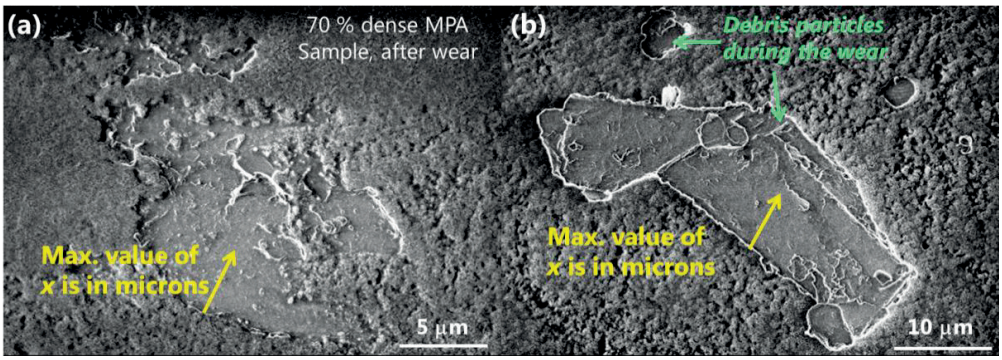

Figure 6.5. HRSEM pictures of the worn surface of 70 % dense Fomblin® impregnated MPA composite sample (a) showing the maximum diffusion length *x* of ~ 5 µm and (b) comprising debris particles that have relatively bigger diffusion lengths due to the three dimensional distances to be travelled.

During the occurrence of the surface diffusivity process, all the liquid molecules may not have to travel the maximum *x* distance. Such diffusion length values are typically the same in 70, 80 and 90 % dense, polished MPA samples as evidenced in more than 100 SE–SEM images per each densification.

The surface monolayer coverage (n_o) of a liquid can be calculated using Equation (6.7) [150].

$$n_o = \frac{1.154}{\delta^2} \tag{6.7}$$

where δ is the molecular diameter and can be estimated using the equation $\delta = 1.122\left(\frac{MW}{\rho N_A}\right)^{1/3}$. The parameters MW, ρ stands for Molecular weight, density of Fomblin® oil and N_A is the Avogradro´s number. The estimated molecular diameter of Fomblin® Y25/6 oil is 1.58 nm using MW=3200 g.mol^{-1}and ρ =1.9 g.cm^{-3}. Using this value of molecular diameter, the monolayer surface coverage (n_o) was estimated as 4.622×10^{17} molecules.m^{-2}. Alternatively, one has to realize that Fomblin® oil is a branched long chain and was reported to have a molecular coil width of 0.8 nm [151] and chain length of 5±3 nm [125]. Hence, the monolayer surface coverage (n_o) of Fomblin® oil may be therefore estimated as 1.5625×10^{15} molecules.m^{-2} and may be more appropriate.

The molecular flux ($\dot{V}_2$) due to the surface diffusion occurring in two dimensions can be given by Equation (6.8), similar to Fick´s law and first given by Taylor and Einstein [152].

$$\dot{V}_2 = -D_s \frac{\partial c}{\partial x} \tag{6.8}$$

Since the concentration of the Fomblin® oil at a certain distance (*x*) on the dry debris compacted regions is time dependent, Fick´s second law mathematically describes the concentration as a function of time and given by Equation (6.9).

$$c = c_o erfc\left(\frac{x}{2\sqrt{D_s t}}\right) \tag{6.9}$$

where erfc is a complimentary error function and $c_o \approx n_o$. If the first two terms of the Taylor series are considered, the concentration (c) can be written as Equation (6.10).

$$c = c_o\left(1 - \frac{x}{\sqrt{D_s t\pi}}\right) \tag{6.10}$$

The molecular diffusivity flux is presented in Figure 6.6 as a function of time and is ~10^7 molecules.m^2.s^{-1}. It can be observed that this surface diffusivity flux is 11 orders of magnitude smaller than the capillarity flux rate. Similarly, the third parallel process is the evaporation of the impregnating liquid. The evaporation rate may play a role in self–replenishing process if it has a high vapor pressure. In such a case, the vapor phase transport of the liquid might become an important rate determining process. However, in case of Fomblin® oil, the evaporation rates are extremely small. The saturation vapor pressure and vaporization enthalpy (ΔH_{vap}) of Fomblin® oil at 25 °C are 6×10^{-9} cmHg and 24.5 kJ.kg^{-1} respectively as taken from the technical data sheet* from the supplier. The vaporization enthalpy of Fomblin® oil is 78.4 kJ.mol^{-1}, three times bigger than that of water (40.65 kJ.mol^{-1}) and thus is a non volatile liquid. It was also reported that the evaporation loss at 120 °C for 22 h time is 0.00 wt/wt %. Moreover, it is commonly used as a vacuum pump oil at low pressures for extremely long times (several months) exhibiting very small evaporation losses. Hence, in this present study, the evaporation process has no distinct influence on the replenishing efficiency. Eventually, the surface diffusivity process is the rate determining process.

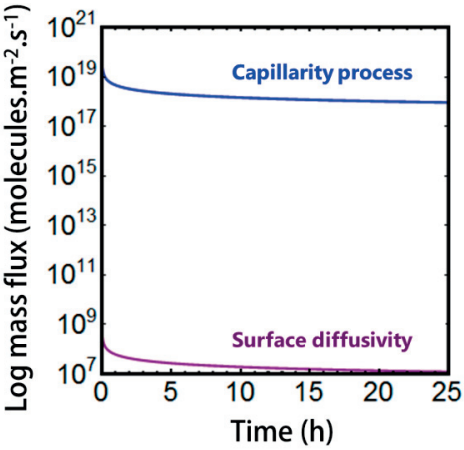

Figure 6.6. (a–b) The mass flux (m^3.m^{-2}.s^{-1}) of capillarity and surface diffusivity process are plotted as a function of time (in h).

It is evident from the Equation (6.10) that the concentration (c) at a distance x will become equal to c_o only at time t =∞. Therefore, the self–replenishing process is never 100 % complete. The completion of the process can be mathematically denoted by a ratio c/c_o profiles are plotted as a function of time for different x values in Figure 6.7. The estimated values for 50, 90, 95, 99, 99.5 and 99.95 % coverage are tabulated for x= 1 μm and 2 μm in Table 6.2. The experiments reveal that the surfaces are sufficiently self–replenished in 12–15 h to retain the omniphobicity, as already shown in Section 6.2.1. However, the theoretical estimations reveal that 99.5 % of the sur

*http://www.solvay.com/en/binaries/Fomblin-PFPE-Lubes-for-Vaccum-Applications_EN-220533.pdf

face coverage is complete in just ~50 min (for x = 2 μm). But, it is necessary to experimentally verify if this coverage is sufficient to retain the anti–sticking properties post wear tests. If the wetting properties are retained with just 50 min replenishing process, it will be a huge advantage as compared to 12–15 h time currently employed. Further experiments to verify the model were not carried out due to insufficient time, but forms an important outlook of this work.

Table 6.2. Estimate fraction of coverage of Fomblin® oil in 70–90 % dense MPA polished matrices

Coverage (%)	**Time of coverage (h)**	
	***x*=1 μm**	***x*=2 μm**
50	2.05×10^{-5}	8.18×10^{-5}
90	5.11×10^{-4}	2.05×10^{-3}
95	2.05×10^{-3}	8.18×10^{-3}
99	0.05	0.2
99.5	0.2	0.82
99.9	5.1	20.5
99.95	20.5	81.8

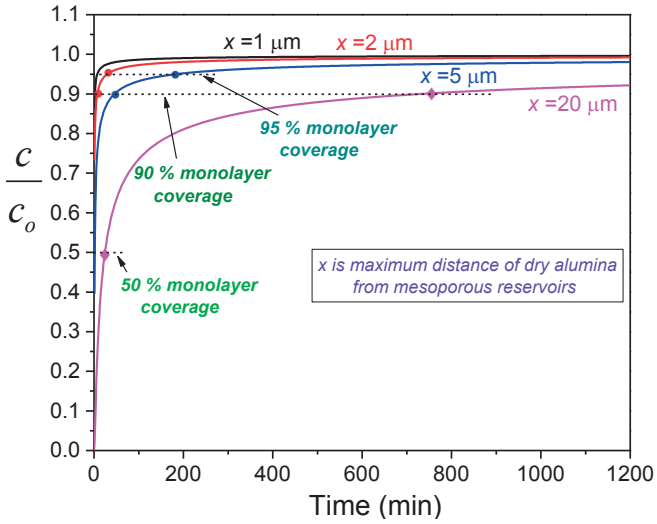

Figure 6.7. The dimensionless concentration (c/c_o) profiles plotted as a function of time for different values of x = 500 nm, 1 μm, 2μm, 5 μm and 20 μm respectively.

6.4. Optimum alumina density

The self–replenishing process as described in the previous section needs an open pore network for the capillarity process to efficiently supply the impregnating liquid. While for alumina samples having densities ~>93 %, open pore network is absent. Therefore, to efficiently retain the wetting characteristics post wear, alumina samples with ≤92 % density are favored. Furthermore, recalling

from Section 5.2.2, Chapter 5, 90 % dense alumina matrices exhibited the lowest friction coefficient (~0.12) and high wear resistance (10^{-7} $mm^3.N^{-1}.m^{-1}$) among other density matrices. Therefore, a major and an important conclusion of this present study is that, ~90 % dense mesoporous alumina matrices are optimal density materials to achieve anti–sticking and self–replenishing properties.

6.5. Summary

In this chapter, the wetting properties immediately post wear and by providing self–replenishing times of 15 h are presented for Fomblin® oil impregnated 70–90 % dense alumina based MPA composites. The worn regions showed superhydrophilicity and oleophilicty immediately after the wear. Nevertheless, given a sufficient self–healing time (15 h), the samples exhibited enhanced omniphobicity as evidenced from the non zero SCAs and sliding behaviors for the tilted sample surfaces, but having few pinning regions. It is interesting that even the micro debris particles were replenished with Fomblin® oil.

The self–replenishment process in LIMPA samples majorly occurs due to the capillarity and surface diffusivity processes. The different stages of the healing process in these composites are theoretically described and a model was developed to estimate the self–healing times. The order of magnitudes of the volume flux of capillarity and surface diffusion processes are 10^{18}, 10^7 molecules.m^{-2}.s^{-1} respectively. Evidently, the surface diffusion is the rate determining process. The capillarity uptake phenomenon was experimentally demonstrated using dark field X–Ray imaging employing Fomblin® oil in the time scales (~11 h) similar to self–replenishing process (12–15 h). Further analysis reveals that, the square root dependence of capillary height on time was observed in accordance with the Washburn equation. Indeed, the Washburn equation was employed to calculate the aforementioned capillarity volume flux in LIMPA samples.

The self–replenishment process in LIMPA samples may lead to one or very few monolayers coverage. Such small impregnating film thickness may lead to pinning regions on LIMPA surfaces, even after providing sufficient healing times (~15 h), see the attached manuscript, Section 6.2.1 . To improve the efficiency of the healing process and wetting properties post healing, providing microstructuring to the MPA surfaces may be a promising solution. Hence, microstructuring the MPA surfaces is proposed to increase the amount of impregnating liquid atop LIMPA surfaces. To this effect, as a first step, the preparation of large area and bulk microstructured MPA samples is necessary and will be presented in the next Chapter 7. Further, an important outcome of the present work is determining an optimum alumina matrix density of ~90 % to achieve multi–functional properties such as anti–sticking, lowest friction coefficient compared to other density matrices, self–replenishing capacity and low wear–resistance.

Chapter 7

Fabrication of bulk microstructured mesoporous α–Al_2O_3 samples

7.1. Effect of Surface Microstructuring

It was explained in the earlier chapter that the 90 % dense MPA matrix showed best performance in achieving multfunctionalities compared to other density samples. Nevertheless, the worn regions have few pinning regions, even after providing 15 h self–healing times. Such pinning forces might be much stronger when the normal pressures employed during the wear are >> 10 MPa. Hence, one efficient way to increase the impregnating film thickness atop LIMPA surfaces is to provide microstructuring such as microbowls, microcavities, micro tear drops etc. These micropores would serve as better reservoirs for the impregnating liquids than the mesopores, and this idea was already demonstrated in the literature to improve drug delivery in silica [153]. Also, in the recent past, there is an increased interest to improve the tribological performance by producing surface microstructures [154–156]. The reason for such an interest is due to an increase in the amount of the lubricant supply during the sliding contacts. Similarly, microstructuring the MPA surfaces may lead to further increase in the wear–resistance (currently achieved are 10^{-7} $mm^3.N^{-1}.m^{-1}$ for 90 % density, refer Figure 5.13) and decrease in the friction coefficients (currently achieved are ~0.12, refer Figure 5.11). To this effect, the first step was to fabricate microstructured MPA samples and the fabrication process is presented in this chapter.

The most commonly used microfabrication techniques are photolithography [157], laser ablation [158,159], chemical etching [160] and injection molding [161–163]. They are either limited in curvature shapes, expensive or causing surface chemical and roughness changes. Hence, a robust, economical, large area surface microstructuring of mesoporous alumina bulk samples needs to be developed which will be presented in the next section.

7.2. Preparation of microstructured MPA surfaces

The developed fabrication process to obtain microstructured MPA surfaces was published in ACS Applied Materials & Interfaces, 2015. The following section briefly describes the content of the attached manuscript.

7.2.1. About the manuscript

The following attached manuscript presents the developed process to obtain microstructured mesoporous alumina samples. Excimer laser ablation with a mask projection system has been carried out on polycarbonate (PC) sheets to obtain variety of 3D microstructural surface features. The PC master molds were used as master molds for replication of the surface 3D structures into Sylgard PDMS membranes. Such microstructured PDMS membranes were used in the alumina slip casting process to obtain one side of the sample microstructured. The drying process of the slurry is explained and a linear one dimensional model was developed to predict the drying times. The sedimentation of the alumina particles, evaporation, capillarity, diffusion of water through the PDMS membrane are the major influencing factors determining the drying process and discussed. The surface areas as large as 120 cm^2 were obtained on bulk samples as thick as 10 mm. The supporting information of this manuscript is attached as an Appendix C at the end of the thesis.

Reprinted with permission from ACS Applied Materials & Interfaces 2015, 7, 24458-24469. Copyright 2015 American Chemical Society

ACS APPLIED MATERIALS & INTERFACES

Research Article

www.acsami.org

Surface 3D Micro Free Forms: Multifunctional Microstructured Mesoporous α-Alumina by in Situ Slip Casting Using Excimer Laser Ablated Polycarbonate Molds

Sriharitha Rowthu,*[,†] Karl Böhlen,[†] Paul Bowen,[‡] and Patrik Hoffmann*[,†]

[†]Advanced Materials Processing Laboratory, Empa, Swiss Federal Laboratories for Materials Science and Technology, Feuerwerkerstrasse 39, CH-3602 Thun, Switzerland

[‡]Powder Technology Laboratory, Materials Science and Engineering, Ecole Polytechnique Fédérale de Lausanne (EPFL), Station 12, CH-1015 Lausanne, Switzerland

Supporting Information

ABSTRACT: Ceramic surface microstructuring is a rapidly growing field with a variety of applications in tribology, wetting, biology, and so on. However, there are limitations to large-area microstructuring and fabrication of three-dimensional (3D) micro free forms. Here, we present a route to obtain intricate surface structures through in situ slip casting using polydimethylsiloxane (PDMS) negative molds which are replicated from excimer laser ablated polycarbonate (PC) master molds. PC sheets are ablated with a nanosecond KrF (λ = 248 nm) excimer laser mask projection system to obtain micron-scale 3D surface features over a large area of up to 3 m^2. Complex surface structures that include 3D free forms such as 3D topography of Switzerland, shallow structures such as diffractive optical elements (60 nm step) and conical micropillars have been obtained. The samples are defect-free produced with thicknesses of up to 10 mm and 120 mm diameter. The drying process of the slip cast alumina slurry takes place as a one-dimensional process, through surface evaporation and water permeation through the PDMS membrane. This allows homogeneous one-dimensional shrinkage during the drying process, independent of the sample's lateral dimensions. A linear mass diffusion model has been proposed to predict and explain the drying process of these ceramic colloidal suspensions. The calculated drying time is linearly proportional to the height of the slurry and the thickness of the negatively structured PDMS and is validated by the experimental results. An experimentally observed optimum Sylgard PDMS thickness range of ~400 μm to 1 mm has achieved the best quality microstructured green compacts. Further, the model predicts that the drying time is independent of the microstructured areas and was validated using experimental observations carried out with microstructured areas of 300 mm^2, 1200 mm^2, and 120 cm^2. Therefore, in principle, the structures can be further replicated in areas up to 3 m^2 with the same drying time for the same slurry height. The surface-structured ceramics display interesting wetting properties, for example, eicosane-coated mesoporous microstructured alumina shows superhydrophobic behavior. Additionally, ceramic bulk samples could be further used as second-generation very hard and low-wear molds for further microfabrication.

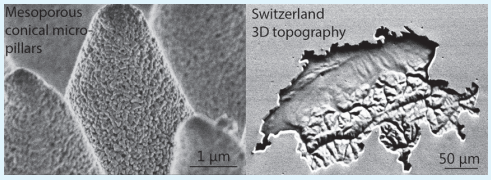

KEYWORDS: *laser ablation, dual scale micronanostructures, replication, superhydrophobicity, mesoporous alumina ceramics, slip casting, ceramic mold, drying model*

1. INTRODUCTION

Micro and nanofabrication of various types of materials is rapidly emerging as an important technological need in the fields of microfluidics, photonics, electronics, and biology.[1,2] In particular, ceramic surface microstructuring is of enormous interest due to their outstanding thermomechanical properties. Ceramic surface microstructuring has been under exploration over the past few decades and has often been carried out through replication techniques to obtain micro and nano surface features.[3−8] Alternative techniques such as laser ablation,[9−11] micro powder injection molding[12,13] and several others[14] are limited in microfeature geometries and dimensions, and are often expensive. Polydimethylsiloxane is commonly used as an elastomeric intermediate mold during slurry casting processes to obtain surface features on ceramics.[3,4,15−19] The master mold is usually obtained by cost-intensive photolithography followed by subsequent deep reactive ion etching processes,[17] thus restricting the microstructured areas to a few square centimeters commercially. Additionally, the photolithography technique cannot realize all the curvatures and wall angles for the microfeatures, for example, conical micropillars, which we will show in this article. Most studies have reported submillimeter thick ceramic tapes[6,16] with the exception of one recent study that reported thicker samples.[20]

Received: May 30, 2015
Accepted: October 19, 2015
Published: October 19, 2015

 © 2015 American Chemical Society

DOI: 10.1021/acsami.5b04748
ACS Appl. Mater. Interfaces 2015, 7, 24458−24469

Also, easy and nondestructive fabrication of three-dimensional (3D) free forms on ceramic surfaces has not been realized economically. Here, we present a fabrication technology to realize 3D surface ceramic microfeatures combining large area excimer laser PC ablation and ceramic slip casting. A key step of the process, water vapor permeation drying of the ultrafine crystalline alumina slurry through the microstructured PDMS membrane, is highlighted. The developed technology is simple, clean, robust, and very economical to achieve large-area 3D surface microstructuring of bulk ceramic samples. Here, we will show the feasibility of producing bulk samples, tested up to 10 mm thickness for cuboidal and cylindrical shaped ceramics. The master mold can be microstructured on areas up to 3 m^2 and, thus, theoretically allows the fabrication of such large areas on ceramic surfaces, too. Slip casting of ultrafine grains of α-Al_2O_3 ceramic leads to mesoporous alumina (designated as MPA). Surface microstructuring of the above-mentioned mesoporous ceramic samples using a slip casting process with microstructured PDMS molds to structure one side of the sample is referred to as "in situ slip casting" process. The presence of ultrafine grains together with surface microstructures and impregnation of mesopores can therefore lead to dual-scale roughened mesoporous microstructured alumina functional ceramics.

2. EXPERIMENTAL SECTION

Materials. Elastosil 622 RT A/B, Ameba AB, Switzerland, is a commercially obtained two-component silicone mixture and was used to prepare open silicone molds required in the slip-casting process. Sylgard 184, PDMS was commercially obtained from VWR International GmbH, Switzerland, and was used for replication purposes. 1*H*,1*H*,2*H*,2*H*-Perfluorodecyltrichlorosilane (97%) was obtained from ABCR GmbH & Co. KG, Germany and is used as a releasing agent at the PDMS—ceramic green body interface. Repliset-F5, Struers, Switzerland is a silicone paste and was used for replication. α-Al_2O_3 powders (BMA 15, 99.9% purity) were obtained from Baikowski, France. The specific surface area of the powders was obtained from nitrogen adsorption measurements given on the technical data sheet of Biakowski, France, and was found to be 14900 m^2 kg^{-1}. A poly(acrylic acid) 65 wt % solution (PAA, MW = 2000) obtained from Sigma-Aldrich, Switzerland, was used as a dispersant in the ceramic slurry preparation. 1-Octanol, from Sigma-Aldrich, Switzerland, was used as a surfactant (helps degassing) for the ceramic slurry.

PDMS Replication. Sylgard 184 is a two-component mixture and mixed in 1:10 curing agent ratio (by weight) and was degassed in vacuum (200 mbar) for 30 min to minimize air bubbles and then cast on a laser ablated PC sheet and cured for 48 h at 25 °C to obtain negative replication of structures. To help easy demolding of the ceramic green bodies that can prevent deformation of the ceramic surface microstructural features, a releasing agent was applied on the structured Sylgard surface. The releasing agent was a thin perfluoro-terminated siloxane coating obtained from 1*H*,1*H*,2*H*,2*H*-perfluorodecyltrichlorosilane (97%) that was applied to Sylgard directly after demolding from the PC mold in a vacuum desiccator for 12 h without physical or chemical treatment (such as plasma, hydration). Repliset-F5 silicone has the ability to replicate structures with a precision down to 100 nm and was used to replicate structures from alumina ceramics because it has a shorter curing time of 18 min at 25 °C. An Elastosil 622 RT A/B two-component silicone mixture, red in color and mixed in a 9:1 curing ratio (by weight), was poured into machined Al molds and cured at 100 °C for 30 min to obtain cuboidal (24 × 12 × 17 mm) and disc-shaped (40, 120 mm diameters and 20 mm high) cavities. The resulting silicone molds were used to obtain cuboidal and disc-shaped ceramic green bodies. The cross-sectional diagram for the elastosil silicone molds containing cuboidal cavities (rectangular cross section) is presented in Figure 3.

Ceramic Microstructuring. As-received alumina particles from the supplier were granulated, showing a spherical or polygonal shape and particle diameters between 10 and 100 μm, respectively (see Figure S1, Supporting Information, for characterization of as-received powders). However, they need to be dispersed or deagglomerated to primary particles for further processing. The particle size distribution of the deagglomerated α-Al_2O_3 powders was measured using disc centrifuge (CPS disc centrifuge, CPS Instruments, Europe, The Netherlands) and have median particle diameter, d_{v50}, between 130 and 150 nm (d_{v50} means 50 vol % of particles have diameters smaller than 150 nm). The majority of the particles have sizes between 90 and 220 nm (see Figure S2a, Supporting Information, for particle size distribution of deagglomerated powders). Such deagglomerated particles were used to prepare ceramic slurries and were slip cast similar to those proposed in the literature,[21] with slight modifications. Briefly, Al_2O_3 powders were mixed with a poly(acrylic acid) (2 wt. %) aqueous solution of pH 10 (adjusted with NH_4OH) to disperse the agglomerated particles and form ceramic slurries containing 25 vol % solid fraction. The volumes of slurry were typically between 44 and 56 cm^{-3} and were ultrasonicated with a UP200Ht ultrasonicator horn using 50 W, 26 kHz at 65% amplification. After intensive ultrasonication of the slurry for 15 min, 3–5 drops (5–10 μL) of octanol were added to degass the slurry and avoid air bubble voids in the slip cast ceramics. Further deagglomeration of the slurry was carried out by rolling the slurry with ∼1 mm diameter Al_2O_3 balls for 24 h. Then, the slurry was slip cast in low permeable Elastosil silicone open molds with structured Sylgard PDMS as the base to form cuboidal (24 × 12 × 10 mm) and disc (40, 120 mm diameter, 10 mm thick) shaped green compacts. The slurry viscosity has been characterized with a Thermo/HAAKE RheoStress RS100 Rheometer (Waltham, MA) as a function of solid fraction, the viscosity varied from 7 to 30 mPa·s when the solid fraction changed from 20 to 37 vol %, respectively. The optimized solid fraction is 25 vol % for this study and is based on its viscosity measurements (see section S2, Figue S2b,c, Supporting Information, for details). The viscosity of the 25 vol % slurry used in our study is 10 mPa·s. A lower viscosity slurry led to very thin green compacts and pronounced sedimentation. Higher viscosity slurries led to incomplete filling of the PDMS microstructures, and defects arose due to the difficulty in fully dispersing the alumina granules in such viscous suspensions. The density of a ceramic slurry containing 25 vol % solids was measured to be 1748.5 kg m^{-3}. The density and viscosity measurements are used for drying time calculations.

Drying Process. The specially designed Elastosil molds filled with the ceramic slurry were placed in a controlled humidity environment. Initially, the slurry was dried at 90% RH for 24 h and then at 45% RH for 3–6 days, and the exact duration depended on the Sylgard membrane thickness and the height of the ceramic slurry which finally produced ∼60% dense microstructured mesoporous α-Al_2O_3 samples referred to as green bodies or compacts.

Sintering. The green compacts were presintered to 600 °C at a heating rate of 1 K min^{-1} with a 1 h isothermal stage at 600 °C to remove the dispersant (PAA) and surfactant (Octanol). The presintered samples can be sintered in air at 1150, 1205, and 1250 °C in a tubular furnace at 10 K min^{-1} heating rate, a 1 h isothermal stage at the highest temperature to achieve 70 ± 3, 80 ± 3, and 90 ± 3% theoretical densities, respectively, retaining ultrafine grains and connected mesoporosity. For higher densities greater than 90%, a two-step sintering process should be applied to avoid pronounced grain growth.[21] For example, 99 ± 0.5% densification can be obtained by sintering to 1450 °C at a heating rate of 10 K min^{-1}, holding for 15 min, followed by sudden cooling to 1000 °C and holding for 24 h at 1000 °C with the retention of ultrafine grains. The open porosity and total porosity of at least 10 sintered samples for each of 70, 80, and 90% densifications were measured by Archimedes' principle with water as the liquid medium. The pore size distribution of 70, 80, and 90% dense bulk samples (cylindrical shaped, 3 g weight) has been characterized by using a Hg intrusion porosimeter (Pascal 440, Germany) and the respective average pore sizes are 47 ± 12, 34 ± 10, and 25 ± 7 nm,

DOI: 10.1021/acsami.5b04748
ACS Appl. Mater. Interfaces 2015, 7, 24458–24469

respectively, revealing that the samples are mesoporous (see Figure S3, Supporting Information, for pore size distributions).

Microstructural Characterization. The surface 3D microstructures on the PC sheet, the structured Sylgard PDMS, and alumina ceramic were characterized with Philips S4800 high-resolution scanning electron microscope (HRSEM) in secondary electron (SE) mode with 1.5−5 keV and 10 μA from top view and at 45−70° sample tilt after coating PC and PDMS samples with Au. Ceramic powders and bulk samples were uncoated prior to HRSEM studies. Very shallow structures such as diffractive optical elements (DOE) on a PC sheet have been characterized with digital holographic microscopy (DHM), Lyncée Tec, Switzerland.

Wetting Studies. To study the wetting behavior of dual-scale micro and nano rough MPA surface, the samples were coated with a thin layer of eicosane solution obtained by dissolving eicosane (0.5 g) in hexane (50 mL). Distilled water droplets of 2−3 μL have been used with plastic syringes and Teflon-coated needles to carry out static contact angle measurements with a contact angle goniometer, GBX Digidrop, France.

3. RESULTS AND DISCUSSION

Excimer laser ablation of PC sheets with a mask projection system to obtain 3D surface microstructural features and fabrication of the same on α-Al_2O_3 ceramic surfaces is described in detail, explaining the critical experimental parameters that affects the drying process. A variety of regular and irregular 3D shapes and sizes realized by the fabrication technology are illustrated showcasing a couple of applications. A simple theoretical model has been proposed to estimate the drying times of the ceramic slurry, which matches our experimental observations.

3.1. Laser Ablation of Polycarbonate Sheets and Their Microstructural Characterization. Laser ablation of polymers has been extensively studied for more than 3 decades.[22−28] A wide range of shapes can be obtained when optimized mask imaging techniques are used.[29] 3D microstructural features are first laser ablated into polycarbonate by direct mask projection with a KrF (λ = 248 nm) laser[30] and fluences from 100 to 600 mJ cm^{-2}. Each pulse can ablate layers between 20 and 250 nm depending on the fluence used. Feature dimensions presented in this study have depths from 50 nm to 20 μm. Standard areas of 30 × 20 mm and areas up to 300 × 300 mm have been ablated on PC sheets for the current studies; however areas up to 3 m^2 can be ablated[31] (see also section S4, Supporting Information for large area laser ablated PC sheet and further details about the ablation). Figure 1 shows representative examples of structures as SEM images of laser ablated PC sheets showing conical pillars, a relief of Switzerland and a digital holographic microscope (DHM) image of diffractive optical elements (DOE) shapes respectively. A line profile of the DOE structures (Figure 1d) obtained from AFM measurements on the same DOE sample shows shallow steps as small as 60 nm (see Figure S4b, Supporting Information, for the AFM measurement and position of the line scan). The conical micro pillars are an example of regularly shaped high aspect ratio structures (ratio of base diameter to height of pillar is 2 for these pillars); while the relief of Switzerland showcases a freeform 3D shape and DOE structures showcase quite shallow structures having depth steps of only 60 nm. Other microstructural features that have been tested are microlenses, teardrop, set of concentric circles, Siemens star, bone pits, and so on.

3.2. Fabrication Process and Surface Microstructuring. The 3D microstructures from a PC sheet are negatively replicated into a soft elastic material, Sylgard 184 PDMS which is commonly used in the literature[32] for tape casting of microstructured ceramic films. The microstructured PDMS cast layer

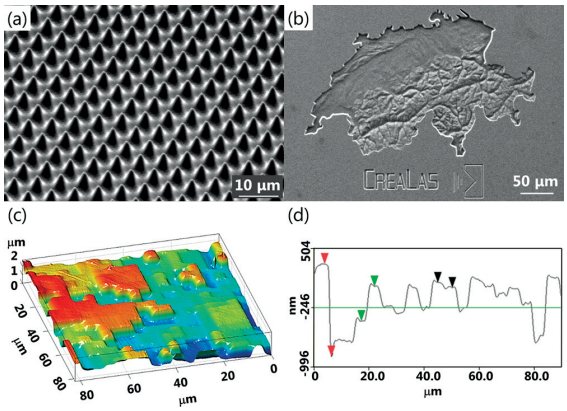

Figure 1. SEM images of laser ablated PC master molds containing surface features of (a) conical pillars with a bottom diameter of 3 μm, a height of 6 μm, and a pitch of 6 μm; (b) irregular 3D Switzerland map shape; and (c) digital holographic microscopic (DHM) image of an 8 level diffractive optical element (DOE) (units in μm); and (d) a line profile from an AFM image (Figure S4b, Supporting Information) of an earlier test sample of the same DOE with very shallow structures down to 62.6 nm (height difference of black arrows) over lateral region of 5.276 μm. The vertical separation of the red points is 1.176 μm for a horizontal distance of 2.461 μm, while for the green points, the vertical distance is 438.3 nm for a horizontal distance of 4.746 μm.

can be manually peeled off the PC sheet but can best be demolded by ultrasonication (in a bath) in ethanol for 10 min. Figure 2 shows SEM images of negatively replicated PDMS

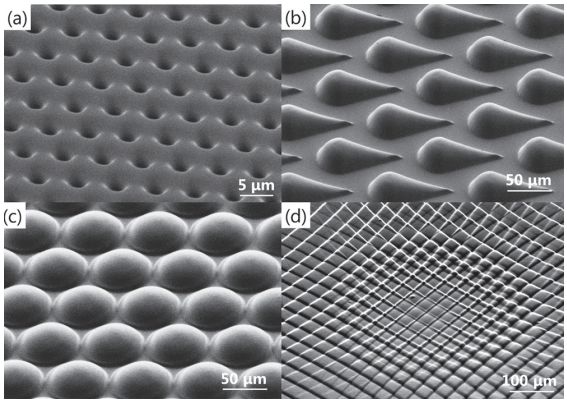

Figure 2. SEM images of negatively replicated PDMS surfaces containing (a) conical holes, (b) teardrops, (c) microlenses, and (d) crossover region of four sets of concentric circles

samples showing conical holes, replicated from corresponding PC sheets containing pillars (Figure 1a), teardrops, microlenses, and crossover region of sets of concentric circles respectively (see Figure S5, Supporting Information, for more images of concentric circles at different locations and magnifications). Micro lenses (Figure 2c) replicated into ceramics could be of interest in the optical industry as components for micro optical benches[33] due to their low thermal expansion coefficient.

The structured PDMS is used as an intermediate mold in the slip casting process to replicate 3D surface microstructural features on a mesoporous α-Al_2O_3 ceramic green body. The

DOI: 10.1021/acsami.5b04748
ACS Appl. Mater. Interfaces 2015, 7, 24458−24469

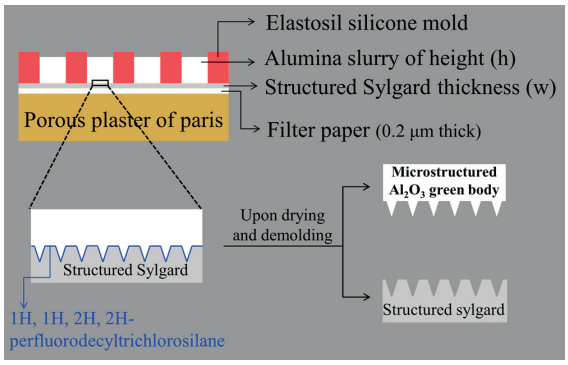

Figure 3. Cross-sectional schematic diagram (not to scale) of the in situ slip casting process using structured Sylgard silicone mold to obtain a crack-free surface microstructured α-Al_2O_3 green body upon drying. The key parameters for the process are alumina slurry height (h) and the average thickness (w) of the microstructured Sylgard PDMS membrane.

cross-sectional schematic of the fabrication process is shown in Figure 3, where the alumina slurry is cast into red Elastosil silicone molds to obtain cuboidal and cylindrically shaped samples with the structured Sylgard PDMS as the base. The structured Sylgard layer is indicated by a light gray thick line in the schematic and acts as a temporary nondestructive mold in the slip casting process and is placed above the cellulose nitrate filter paper (indicated by a thick white line), which allows one side of the ceramic green body to be microstructured upon drying the slurry. *1H,1H,2H,2H*-Perfluorodecyltrichlorosilane releasing agent, indicated by a blue line in the schematic is necessary for easy demolding of high aspect ratio ceramic body structures (more specifically conical pillars) that must be applied on the structured PDMS before casting the slurry. The macroscopic rough porous plaster of Paris molds were machined/ground using parallel steel blades and polished with SiC emery sheets on both sides of the mold prior to slip casting to make the surfaces parallel and flat. Subsequent usage of flat Sylgard PDMS during slip casting results in flat structured ceramic samples. The α-Al_2O_3 ceramic slurry prepared as described in the Experimental Section has a low dynamic viscosity of 10 mPa·s for 25 vol % solid fraction (Figure S2b,c, Supporting Information) which helps easy complete filling of the microstructural features of the structured PDMS surface.

One of the scientific interests is to achieve ceramic microstructuring on thicker alumina samples, in contrast to the submillimeter ceramic tapes commonly described in the literature, which do not require a complicated slurry drying process such as in slip-pressing.[34] In addition to the complicated drying process, slip-pressing is a mold-loss process.[34] Thick Sylgard PDMS film of about 2−3 mm has been used in the literature[32] as a secondary mold to cast small amounts of slurry on it to produce ceramic tapes. However, we discovered that using a thin Sylgard PDMS can efficiently dry the slurry faster without destroying the master and temporary molds because of a relatively high water permeation through PDMS despite having a hydrophobic character. Different PDMS thicknesses between 100 μm and 2 mm have been used to optimize the thickness range for the efficient drying of slurries. The optimum thickness range of the PDMS is ∼400 μm to 1 mm and is the most crucial parameter in this study.

PDMS membranes of 100 μm to 250 μm thickness are too thin for handling and buckle and stick to themselves; therefore, the microfeatures are not replicated correctly and homogeneously into the ceramic green body. On the other hand, for thicker PDMS membranes between 1.5 and 2 mm (see Figure S6b, Supporting Information, for images of 1.5 mm and 500 μm thick PDMS) the observed drying time is ∼14 days for a slurry height of ∼10 mm, and the samples look macroscopically inhomogeneous and have a depression cavity at the center of the sample (see Figure S6a, Supporting Information, for a sample picture of a macrocavity). Such an observation of cavity formation can be ascribed to the reduced permeation rate of water in Sylgard PDMS but maintaining the same evaporation rate. The details of permeation rates and evaporation rates will be discussed in section 3.3.

The drying for the whole process takes ∼5−8 days, the first 24 h at 90% RH and the remaining time at 30−60% RH when a ∼500−1000 μm thick PDMS layer is used for slurry heights of 10−17 mm. Precise experimental observations of drying times as a function of Sylgard PDMS membrane thickness and slurry height will be shown and discussed in section 3.3 together with theoretical quantification using a 1D mass diffusion model. The proposed stages of drying process are schematically shown in Figure 4.

The fully dried green bodies are shiny and dry on the upper (air side) surface and visibly detached from its Elastosil silicone side walls. However, with only a shiny dry top surface, the Sylgard silicone-green compact interface might still be wet, visible by the presence and transfer of wet alumina slurry to the Sylgard silicone surface upon demolding during intermediate stage of the drying process (at $t = t_3$, Figure 4). Additionally, for large slurry heights ∼≥ 15 mm, 1−2 mm of clear water has been observed (at $t = t_2$, Figure 4) at intermediate stages of the drying process. Therefore, the last stage of drying is most probably at the Sylgard−alumina green body interface and gives an indication on the completion of the drying process. Also, the mass of the samples was measured with a precise weighing balance (10^{-4} g precision) immediately after demolding and after complete drying, respectively. The measured maximum mass loss of water is ∼4% of the initial water content in the slurry and can be dried in 0.3 days when left unmolded, which is less than the standard deviation of drying times of the samples (∼0.5 day, Figure 7). Further confirmation of complete drying has been revealed by later presintering and sintering stages which leads to macro and micro crack free samples.

A couple of millimeter thick ceramic green bodies have been reported recently,[20] but in most cases, only a few hundred micrometer thick micro or nanostructured ceramic tapes have been reported.[6,16] Our study extends the possibility of surface structuring to bulk samples as thick as 10 mm on very large areas showing various microstructural features. In this study, microstructured areas of 300 mm^2, 1200 mm^2, and 120 cm^2 have been fabricated on cuboidal and cylindrical samples (see Figure S6c, Supporting Information, for proof). The latter, containing DOE structures, exhibit no visible macro cracks, and homogeneous surface structures are obtained as inspected by optical microscopy. Sintered samples with 120 cm^2 microstructured areas were cut for HRSEM analysis revealing the same degree of homogeneity as that of small samples and hence showed defect free samples and the ease of fabrication for large areas.

The completely dried green body can be easily demolded from the PDMS surface without destruction of either of them and PDMS samples can be reused after washing with water and ultrasonicating in ethanol. The green body can be polished with SiC emery sheet to take off 1−2 mm from the unreplicated side

DOI: 10.1021/acsami.5b04748
ACS Appl. Mater. Interfaces 2015, 7, 24458−24469

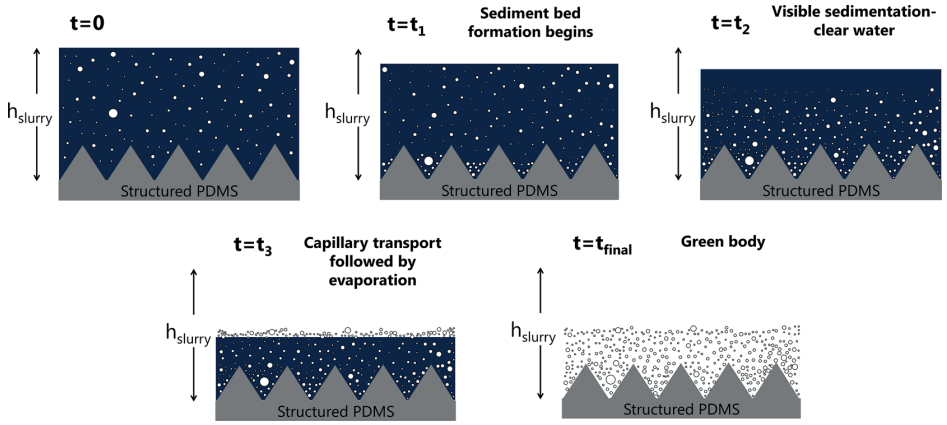

Figure 4. Schematic diagram showing the various stages of drying process. A colloidal alumina suspension at time $t = 0$ has a random distribution of the particles across the slurry height (h_{slurry}). A sediment bed begins to form accompanied by water loss from the suspension as the drying occurs both by evaporation and permeation through the PDMS membrane at time $t = t_1$. The sediment bed continues to grow with continuous removal of water from the suspension. The suspension becomes denser, and a clear water film can be observed at time $t = t_2$. Such clear water formation has been observed experimentally for large slurry heights $\geq$ 15 mm where the sedimentation rates are relatively larger than the water loss rates. Upon further loss of water, the liquid level decreases so as to form packed, dried ceramic particles at the alumina−air interface at time $t = t_3$. The water level decreases as the water is removed from the slurry, and finally, a dried green body has been obtained at time $t = t_{final}$.

of alumina prior to sintering to minimize bending and to further decrease any small inhomogeneity due to sedimentation. The ceramic green body has 60% relative theoretical density, which can be sintered to higher densities between 70 and 90%, leading to connected mesopores. The average pore diameter of 70, 80, and 90% dense samples are 47 ± 12, 34 ± 10, and 25 ± 7 nm respectively (see Figure S3, Supporting Information, for pore size distribution).

Figure 5 presents a selection of fabricated 3D shapes that are replicated on MPA surface. Every microstructural feature presented here has been successfully replicated at least 10 times, unless stated otherwise, illustrating good homogeneity and the ease of the fabrication process. Low- and high-magnification HRSEM images of tear cavities homogeneously replicated from the corresponding PDMS teardrops (Figure 2b) onto an MPA surface are presented in Figure 5a,b. These microtear cavities along with intrinsic mesoporous structures of alumina can be an interesting material for tribological applications. The mesopores can act as nanoreservoirs while tear-shape cavities can act as microreservoirs, thus providing dual scale cavities, which can help efficient lubrication. The shrinkage of the microstructural features during sintering is isotropic and, hence, predictable.

Figure 5c shows a low-magnification image of four sets of concentric circles and the zoomed in areas encircled by yellow colored boxes are shown in Figure 5d,e replicated from corresponding PDMS molds (Figure S5b−d, Supporting Information) showing the ease of replication of finest complex details. Figure 5e is the corresponding replication from its negatively structured PDMS (Figure 2d) showing the precision of ceramic replication; even a small spherical defect (Figure 2d) has been very well replicated onto the ceramic surface (Figure 5e). Hence, a perfect mold allows precise replications on ceramic surfaces. Figure 5h shows replicated DOE structures from its corresponding master PC sheet (Figure 1c). The DOE structures are quite shallow (with depth steps as small as 60 nm and up to 1.7 μm) as can be observed from the surface profile in Figure 1d, and replication into the green body and subsequent sintering can shrink these structures by 20−50%. Hence, DOE structures

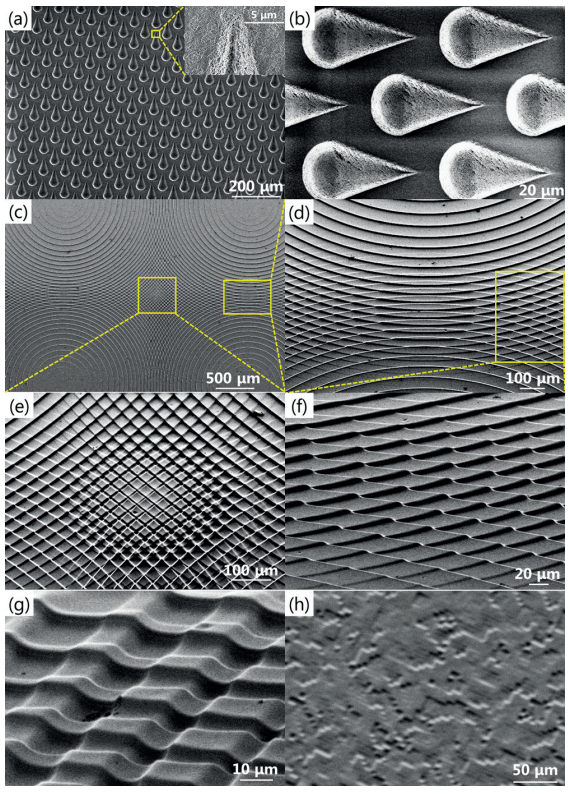

Figure 5. SEM images of MPA structures after sintering at 1150 °C showing (a and b) teardrop shapes at low and high magnifications, respectively, and (a, inset) high-magnification image of a drop corner showing the ultrafine grains of alumina; (c) set of concentric circles at low magnification and (d−g) at different locations of image c at 45° sample tilt; and (h) DOE structures replicated on mesoporous alumina surface

DOI: 10.1021/acsami.5b04748
ACS Appl. Mater. Interfaces 2015, 7, 24458−24469

showcase an example of shallow 3D surface microstructures with abrupt curvature changes.

3.3. Drying Mechanisms and 1D Mass Diffusion Drying Model. Interestingly, homogeneous drying has been observed for large and small slurry base surfaces, that is, for compartments of slurry within the low permeable red colored Elastosil silicone molds, if the Sylgard PDMS bottom membrane is between 300 and 1000 μm in thickness. This observation resulted in the development of a simple drying model, schematically presented in Figure 6.

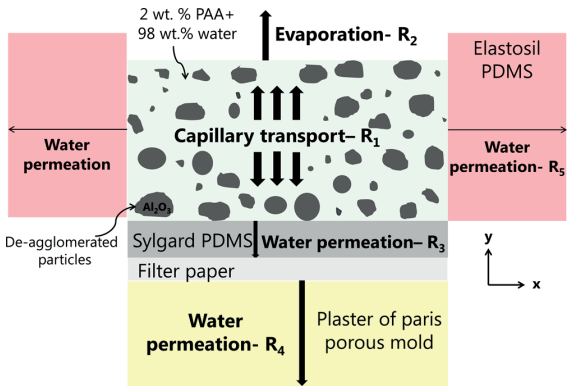

Figure 6. Schematic diagram (not to scale) of drying of the alumina slurry in the Elastosil silicone mold, especially optimized for microstructure replication at the interface of an alumina slurry and a Sylgard PDMS membrane. The qualitative water mass transport is presented with the thickness of the black arrows. Water transport mechanisms through and out of the ceramic suspension are presented as capillary transport inside the slurry (R_1), evaporation (R_2) from the top surface of the slurry, and permeation through PDMS membrane (R_3). Water permeation through plaster of Paris (R_4) is very high and not the rate determining step. Almost negligible is the water permeation through the side Elastosil PDMS walls (R_5). The water is very efficiently transported to the slurry–air and slurry–Sylgard PDMS interfaces, respectively, by capillary transport within the slurry even with advanced densification due to drying. The rate-determining mass diffusion mechanisms are evaporation and water permeation through Sylgard PDMS.

Figure 6 shows all the possible drying mechanisms (water mass transport) of a ceramic suspension: (1) mass diffusion of liquid/vapor water takes place by capillary transport inside the ceramic suspension (rate designated as R_1), (2) evaporation through the slurry surface exposed to air (rate designated as R_2), (3) permeation of water vapor through Sylgard PDMS membrane (rate designated as R_3), (4) liquid/vapor water transport through porous plaster of Paris (rate designated as R_4), and (5) permeation through elastosil PDMS side walls (rate designated as R_5).

The filter paper used in the study is a 0.2 μm thick membrane that immediately (in a fraction of a minute) allows the passage of liquid/vapor water through it to the plaster of Paris mold and is therefore not the rate determining step. Placing a 2 mm water film onto the surface of plaster of Paris molds sucks the water very fast (in less than a minute) due to capillarity caused by the pores of the plaster of Paris, and the mass diffusion though the plaster of Paris (referred to as R_5 in Figure 5) is not the rate determining step in the drying process, either.

The predominant shrinkage of the slurry occurs in the vertical direction (y direction in Figure 5) and is measured to be ~50%, at the completion of drying process, while in x–z plane (in Figure 5), the shrinkage measured is < 4%. A very small lateral shrinkage (in x–z plane) is due to negligible water permeation through Elastosil PDMS (R_5). Therefore a simple linear 1D drying model is proposed to explain the drying process of the ceramic suspension. Hence, 1D mass transfer equations in the y direction are used to quantify the drying rates and drying time, respectively. The mass diffusion rate of capillarity inside a ceramic suspension, evaporation rate and water permeation through Sylgard PDMS membrane can be calculated using Darcy's law,[35] Carrier's correlation equation,[36] and Fick's first law as given by eqs 1, 6, and 7, respectively. The variables in the eqs 1–7 are tabulated in Table 1.

$$R_1\left(\frac{m^3}{s}\right) = -\frac{\mu}{\eta}\frac{dP}{dx}A_{\text{base},m^2} \tag{1}$$

where dP, r_p, and μ are given by eqs 2–4, respectively.[35]

$$dP = P_{\text{cap}} = \frac{2\gamma\cos\theta}{r_p} \tag{2}$$

$$r_p \approx r_h = \frac{2(1-\Phi)}{A_s\Phi\rho} \tag{3}$$

$$\mu = \frac{(1-\Phi)^3}{5(A_s\Phi\rho)^2} \tag{4}$$

The parameter dx in the eq 1 is capillary length (L_{cap}) over which capillary migration occurs and can be calculated using eq 5.[35]

$$L_{\text{cap}} = \left[\frac{2h_{\text{slurry}}\Delta P(1-\Phi)^3}{5R_2\eta(A_s\phi\rho)^2}\right]^{1/2} \tag{5}$$

where ΔP in eq 5 is obtained using eq 2. The calculated values of capillary length are 62 and 26 m at 90 and 45% RH, respectively. In our experiments, the maximum slurry height is 17 mm which gives the maximum capillary length of 8.5 mm for water to be transported to the surfaces (Figure 4, at $t = t_3$). Because the experimental capillary length is smaller than the maximum calculated capillary length, the capillary transport of water will not be the rate determining step in the drying process.

$$R_2\left(\frac{kg}{h}\right) = \frac{0.76(0.089 + 0.0782u)(P_w - P_a)}{\Delta H_{\text{vap}}\left(\frac{kJ}{kg}\right)}A_{\text{base},m^2} \tag{6}$$

$$R_3\left(\frac{kg}{s}\right) = \frac{(DS)_{\text{water,PDMS}}(P_w + \rho_{\text{slurry}}gh_{\text{slurry}} - P_a)}{w} \times (RA_{\text{base},m^2}) \tag{7}$$

The area normalized rates R_1, R_2, and R_3 are calculated using eqs 1, 6, and 7 are 2.073×10^{-5}, 2.635×10^{-9}, 1.36×10^{-10} m^3 m^{-2} s^{-1}, respectively, at 90% relative humidity (RH) for 500 μm thick PDMS and 17 mm slurry. When the environment RH decreased to 45%, the calculated rates R_2 and R_3 are slightly enhanced to 1.449×10^{-8} and 6.66×10^{-10} m^3 m^{-2} s^{-1} respectively with no change in R_1 value. The enhancement in rates R_2 and R_3 is due to the increase in the water concentration gradient (P_w–P_a) in eqs 6 and 7 due to the decrease in P_a with a decrease in the environmental RH. Although the calculations show that the evaporation rate is ~19 times faster than the permeation rate (at 90% RH) and ~21 times faster at 45% RH, experimental data show a strong

DOI: 10.1021/acsami.5b04748
ACS Appl. Mater. Interfaces 2015, 7, 24458–24469

Table 1. Variables in Eqs 1−7, Their Definitions and the Values Used for the Drying Model

parameter	parameter definition	literature obtained/calculated/experimentally measured
μ	water permeability in alumina slurry	1.989×10^{-15} m^2 (calculated)
η	slurry viscosity	0.01 kg m^{-1} s^{-1} (measured)
γ	water−air surface tension	0.072 N m^{-1}
θ	contact angle of water with alumina	0° (measured)
r_p/r_h	pore/hydraulic radius	2.303×10^{-7} m (calculated)
ϕ	solid fraction of alumina slurry	25%
A_s	specific surface area of alumina particles	14900 kg m^{-2} (measured)
ρ	slurry density	1748.5 kg m^{-3} (measured)
P_w	saturation pressure of water at drying temperature (25 °C in our study)	3169 Pa/2.38 cm Hg (eqs 5/6)
P_a	vapor pressure of water at Sylgard PDMS membrane-filter paper interface at the air temperature and pressure that depends on environment relative humidity	For 90% RH, 2852 Pa/2.142 cm Hg; and for 45% RH, 1426 Pa/1.071 cm Hg (eqs 5/6)
ΔH_{vap}	water latent heat of vaporization	2272 kJ kg^{-1}
u	air velocity atop evaporating surface	0 m/s
DS	product of diffusivity of water in PDMS and solubility of water vapor in PDMS at 25 °C	3.12×10^{-9} −8.04×10^{-9} $cm^3_{water}(STP)cm^{-3}_{PDMS}$ $(cmHg)^{-1}$ m^2. s^{-1} (from literature)[37]
w	PDMS membrane thickness	0.3−1.5 mm
R	roughness factor, ratio of true area to apparent area of the microstructured PDMS	2−6 (an average of 4 has been used in the calculations)

dependence of drying time on PDMS thickness, that is, that the permeation rate through the PDMS must be equal or higher than the evaporation rate. The Carrier's correlation equation that has been used to predict the evaporation rate is an empirical equation and has been shown in the literature that this equation can estimate −14 to 44% more than the measured evaporation rates.[36] Hence, the evaporation rate has been measured for the 25 vol % solid containing slurry at 90% RH and 24 °C by measuring the mass loss using a high precision weighing balance (10^{-4} g precision). The measured evaporation rate is 2.87×10^{-10} m^3 m^{-2} s^{-1} and is ∼9 times smaller than the calculated value. Hence, the calculated evaporation rate has been overestimated by ∼9 times. The average observed water flux through 500 μm thick PDMS membrane at 90% RH is 9.82×10^{-10} m^3 m^{-2} s^{-1} and is ∼7 times larger than the calculated value, the former was calculated using a linear fit of the experimental drying times of 12 mm thick slurry while using 500 μm and 1.5 mm PDMS thicknesses respectively. Also, the average observed water flux through PDMS membrane at 45% RH is 3.28×10^{-9} m^3 m^{-2} s^{-1} and is ∼5 times the calculated value. The difference in the calculated and observed values of permeation rate through PDMS could be due to a large variation in the thickness of PDMS across the microstructured areas (by a factor of 1.5 to 2), especially for smaller PDMS thicknesses. The humidity in the process was not controlled very precisely and can have fluctuations of ± 7% RH especially at 45% RH which could also lead to the difference in the observed and calculated permeation rates. Experimental investigations to understand the role of plaster of Paris were carried out by replacing it with an impermeable glass sheet. Homogeneous and reproducible microstructured alumina green compacts have been produced with similar drying times as that of having plaster of Paris as the base. Therefore, it seems that plaster of Paris plays no significant role in the drying process. The calculated and experimental values for the evaporation rate and water permeation rate through PDMS are tabulated in Table 2.

The predicted drying times using the experimentally observed evaporation rate and water permeation rate from Table 2 are plotted by dashed lines in Figure 7. From the calculations and experimental observations, it can be concluded that both the evaporation and permeation are competing water loss mechanisms while water permeation through PDMS is ∼0.7−3.4 times higher than evaporation rate, accurate ratio depends on humidity and PDMS thickness respectively. These competing water loss mechanisms are needed to obtain macroscopic homogeneous samples.

For a total experimentally observed ∼50% volume shrinkage of the slurry and a given initial constant of t_1 = 24 h drying in a 90% humidity chamber, it is possible to calculate the further drying time (t_2) required at 45% RH to completely dry the suspension using eqs 8, 9.1, and 9.2. The mass loss of water (ΔV_{water}) can be written by eq 8, where, for first day, the evaporation and permeation through PDMS rate values are at 90% RH, and for the next t_2 days, they are at 45% RH.

$$\begin{aligned}\Delta V_{water} &= h_{slurry}(1-\Phi)\\ &= (R_{2,90\%RH} + R_{3,90\%RH})t_1\\ &\quad + (R_{2,45\%RH} + R_{3,45\%RH})t_2\end{aligned} \tag{8}$$

$$t_2 = \frac{A_{base,m^2}h_{slurry}(1-\Phi) - (R_{2,90\%RH} + R_{3,90\%RH})t_1}{R_{2,45\%RH} + R_{3,45\%RH}} \tag{9.1}$$

$$t_2 = \frac{h_{slurry}(1-\Phi) - \left(\frac{0.76\times 0.089\times (P_w - P_{w,90\%RH})}{\Delta H_{vap}\left(\frac{kJ}{kg}\right)\times 1000\times 3600} + \frac{(DS)_{water,PDMS}(P_w + \rho_{slurry}gh_{slurry} - P_{w,90\%RH})}{w\times 1000}\right)t_1}{\frac{0.76\times 0.089\times (P_w - P_{w,45\%RH})}{\Delta H_{vap}\left(\frac{kJ}{kg}\right)\times 1000\times 3600} + \frac{(DS)_{water,PDMS}(P_w + \rho_{slurry}gh_{slurry} - P_{w,45\%RH})}{w\times 1000}} \tag{9.2}$$

From eqs 9.1 and 9.2 (derived using eqs 6,−8), one can conclude that the total drying time ($t_1 + t_2$) is independent of the microstructured base area (A_{base}), parameter that appeared in eqs 1, 6, and 7. The calculations predict that the water loss

DOI: 10.1021/acsami.5b04748
ACS Appl. Mater. Interfaces 2015, 7, 24458−24469

Table 2. Evaporation Rate and Permeation Rate through PDMS for 500, 1500 μm PDMS Thicknesses at 90 and 45% RH

		calculated		experimentally observed		experimental/calculated	
RH (%)	PDMS thickness (μm)	evaporation rate – R_2 (m^3 m^{-2} s^{-1})	permeation rate through PDMS-R_3 (m^3 m^{-2} s^{-1})	evaporation rate – R_2 (m^3 m^{-2} s^{-1})	permeation rate through PDMS-R_3 (m^3 m^{-2} s^{-1})	evaporation rate	permeation rate through PDMS
90	500	2.635×10^{-9}	1.36×10^{-10}	2.87×10^{-10}	9.82×10^{-10}	0.11	7.22
90	1500		4.53×10^{-11}		3.27×10^{-10}		7.22
45	500	1.449×10^{-8}	6.66×10^{-10}	1.58×10^{-9}	3.28×10^{-9}	0.11	4.93
45	1500		2.22×10^{-10}		1.09×10^{-9}		4.91

for 17 mm slurry in first 24 h at 90% RH is only 3% of the total water in the slurry. Hence, the major drying occurred in 45% RH and hence in the eq 9.2, if the term with t_1 is neglected, t_2 is linearly proportional to PDMS thickness. Briefly, the drying time is linearly proportional to the slurry height (h_{slurry}) and a linear function of Sylgard membrane thickness (w) and independent of the microstructured base area (A_{base}). Therefore, in principle it should take the same drying time for 3 m^2 or 24 × 12 mm^2 base areas for the same slurry height and same PDMS thickness. Microstructured areas of 300 mm^2, 1200 mm^2, and 120 cm^2 areas have been fabricated to achieve 10 mm thick samples using a 500 μm thick sylgard PDMS membrane (see Figure S6c, Supporting Information to see microstructured sample pictures) and observed to have the same drying times.

The total slurry drying time ($t_1 + t_2$) can be calculated (eq 9.2) a function of the slurry height for a specific Sylgard membrane thickness and Sylgard PDMS thickness for a specific slurry height respectively. Figure 7 shows the theoretically predicted and experimentally observed total drying times as a function of slurry heights for Slygard PDMS thickness of 500 μm, Sylgard PDMS thickness for 12 mm slurry height, microstructured areas respectively.

However, it is important to consider sedimentation of particles during the drying process. When large heights of sediment beds form, the capillary transport inside the alumina slurry can be reduced drastically and vapor-phase diffusion might occur. The typical sedimentation rate referred to as free settling velocity (V_p) can be calculated using Stokes' law (eq 10) which can give an idea of its effect on the drying process. However, Stokes law can be used only for laminar flow of particles and the latter can be determined by calculating Reynolds number (R_e). The Reynolds number for 25 vol % solid containing alumina slurry is calculated as 1.68×10^{-11} and is $\ll 1$ which determines that the flow is laminar [see section S7, Supporting Information for details on Reynolds number calculations].

$$V_p = \frac{(\rho_p - \rho_l) g D_p^2 (1 - \Phi)^2 Psi}{18 \eta_l} \quad (10)$$

where ρ_p, ρ_l are density of particle and liquid respectively, g is the gravitational constant, D_p is diameter of the particle, η_l is the viscosity of the liquid in the slurry and Psi = $(1/10^{1.82\Phi})$. For ϕ = 0.25 (25 vol % solid fraction), $\eta_l \approx 0.001$ kg m^{-1} s^{-1} (98 wt % water is the surrounding liquid), D_p = 150 nm (average diameter of particles), ρ_p = 3987 kg m^{-3}, ρ_l = 1000 kg m^{-3}, terminal velocity is calculated to be 72.193×10^{-10} m s^{-1}.

For a slurry height (h_{slurry}), the particles at different locations in the well-dispersed colloidal ceramic suspension have different sedimentation distances (defined as distance of the sediment bed to the floating particle) and changes as a

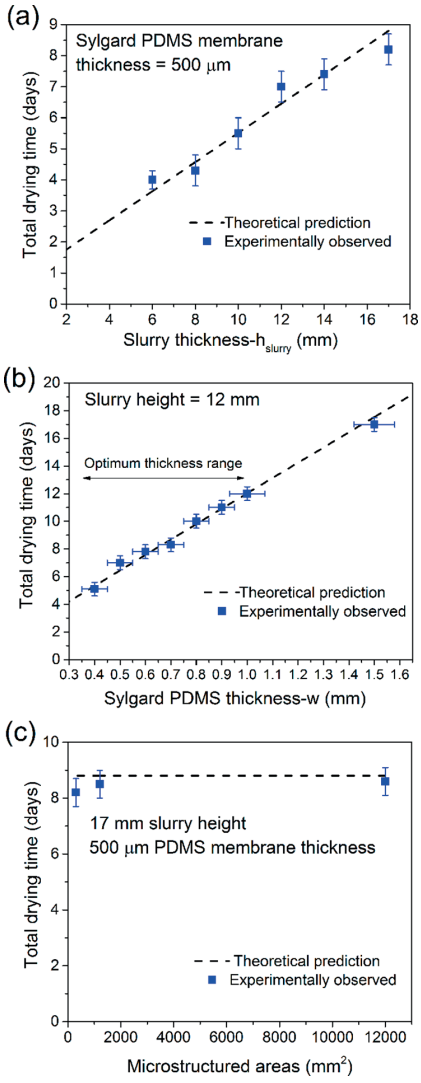

Figure 7. (a) Total theoretical and experimental drying times plotted as a function of slurry thickness for 500 μm thick Sylgard PDMS membrane, indicating a linear trend with a positive slope. (b) Total theoretical and experimental drying times plotted as a function of Sylgard PDMS thickness for a slurry height of 12 mm indicating a linear trend with a positive slope. (c) Total theoretical and experimental drying times plotted as a function of microstructured base areas indicating constant drying times. The experimental microstructured areas in panel c are 300, 1200, and 12 000 mm^2, respectively.

DOI: 10.1021/acsami.5b04748
ACS Appl. Mater. Interfaces 2015, 7, 24458–24469

function of time. Because the final dried bed (green body) has a height equal to half of the total slurry height, the maximum sedimentation distance is half of the slurry height. However, the particles close to Sylgard PDMS have smaller sedimentation distances. Hence, for an average sedimentation distance of 4 mm (taken as h/4 for 16 mm high slurry), the sedimentation time can be calculated to be ∼6.5 days. However, when the drying of slurry occurs due to evaporation and permeation of water through PDMS membrane, the solid fraction of the slurry increases from 25% to 100% leading to a decrease in the particle velocity however with a simultaneous decrease in sedimentation distances. The sedimentation times for big slurry heights is in a similar order as that of the total drying times. Experimental observations for slurry heights ≥15 mm revealed that visible sedimentation occurred leaving a one or two mm thick clear water on the sediment bed for drying times >5 days which finally dried by evaporation and water permeation across PDMS membrane. Although, the sediment bed decreases the permeation of water slightly through it to reach the Sylgard PDMS membrane, this has been neglected for simplicity to develop the drying model in section 3.3 and is valid for slurry heights up to ∼20 mm. It is to be noted, however, that the replication quality or microstructural homogeneity is not affected due to sedimentation because of the very narrow particle size distribution of the powder with the majority of the particle diameters between 90 and 220 nm (see Figure S2a, Supporting Information, for particle size distribution).

For h_{slurry} = 12 mm, t_1 = 24 h, w = 0.05 cm, t_2 can be calculated to be ∼5.5 days. Hence, the total drying time is $t_1 + t_2$= 6.5 days for 500 μm Sylgard membrane thickness, which matches well with experimental observations as shown in Figure 7. While a 100 μm slurry tape requires only ∼7 h predicted drying time at 90% RH, a 17 mm thick slurry needs ∼8.5 days of predicted drying time for 500 μm thick Sylgard membrane as shown in Figure 7a. Therefore, it is theoretically feasible to obtain 3 m^2 (area) × 8.5 mm (thickness) microstructured ceramic plates in 8.5 days economically, without the need of any complicated equipment/technology and defect free thus allowing easy upscaling of the process.

4. APPLICATIONS AND OUTLOOK

The developed fabrication process extends the ability to produce defect free samples with no changes in chemical phase, surface roughness, surface porosity, or grain size, in addition to being free from mechanical or thermal residual surface stresses during the process which cannot be realized with direct laser ablation of ceramic surfaces;[9,38] which makes it a robust technology that can easily be up scaled for commercial purposes. A few specific applications of microstructured MPA samples fabricated in this study will be illustrated in the next successive subsections.

4.1. Wetting Behavior of Dual Scale Roughened Surface. It is well-known in the literature that surface topography (micro and/or nano features) combined with appropriate surface chemistry can influence the wetting response of a surface.[39−41] A 70% dense conical micropillared MPA surface is shown in Figure 8a,b replicated from the corresponding PC sheet (Figure 1a) having the following pillar dimensions: bottom diameter (d) = 3 μm; height (h) = 6 μm and center-to-center distance between nearest pillars, referred to as pitch (p) = 6 μm. Incomplete necking of the ultrafine alumina grains exists in 70% dense sample which leads to nano

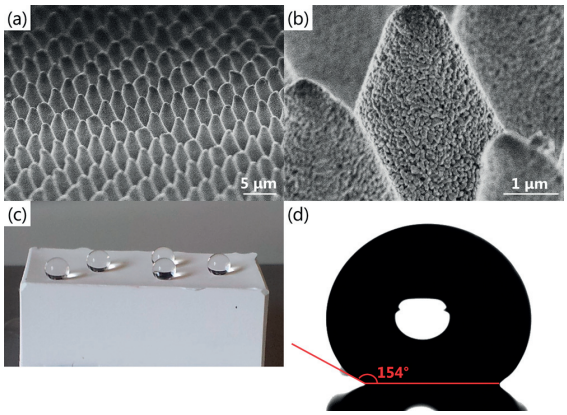

Figure 8. (a) Low- and (b) high-magnification SEM images showing conical micron pillars having dual scale micro and nano roughness on MPA surface; (c) an image showing nearly spherical 2.5 μL water droplets on eicosane coated 70% dense MPA surface; and (d) 154° static contact angle measured on eicosane sprayed micropillared MPA surface.

roughness (peak to valley distance, $R_{z,avg}$ ≈ grain size/2) and hence the MPA samples with incomplete densification have an intrinsic nano roughness throughout. The micro pillars render the micro level roughness and ultrafine grains of the partially densified ceramic render the nano roughness thus having dual scale roughness on the surface. Submicron features are fabricated as observed in Figure 8b where the top diameter of the conical pillar is ∼500 nm. Such a ceramic surface when sprayed with hydrophobic eicosane ($C_{20}H_{42}$) showed a superhydrophobic response with static contact angles of 150 ± 5° as shown in the Figure 8c,d. Figure 8c shows an ∼8 mm thick alumina sample that was fabricated to have conical pillars suspending the water drops in Cassie state supported by rolling off the water drops from the surface when it is tilted by less than 10°.

4.2. Microstructured Ceramic Surface As Second Generation Mold for Microfabrication. It is well-known that ceramic materials act as permanent molds for casting metals and obtaining requisite shapes and sizes. Similarly, one can use microstructured alumina ceramic samples obtained by the current fabrication process as second generation permanent molds[42] to obtain microstructures on different classes of materials like polymers, metals and others. The 3D surface structures shown in Figures 5 and 8 are regular, but it is also feasible to make complex irregular 3D shapes using the developed fabrication process. One such example is shown in Figure 9a, where a topographic relief of Switzerland is shown, where 1 km in reality corresponds to 1 μm on the sample (see Figure S7, Supporting Information, for low magnification image). Here, the micro Switzerland shape is embedded into a hard alumina ceramic surface from the corresponding master PC sheet (Figure 1b). The minimum feature dimension that can be fabricated was shown to be 500 nm at the tip of the micro pillar (see section 4.1, Figure 8b). However, that is not a directly controlled dimension; nevertheless, we can see clearly from Figure 9c that the features can be as small as 1 μm. The Switzerland relief is replicated into commercially available silicone polymer (repliset-F5) from the alumina ceramic surface and the HRSEM image of the repliset polymer is presented in

DOI: 10.1021/acsami.5b04748
ACS Appl. Mater. Interfaces 2015, 7, 24458−24469

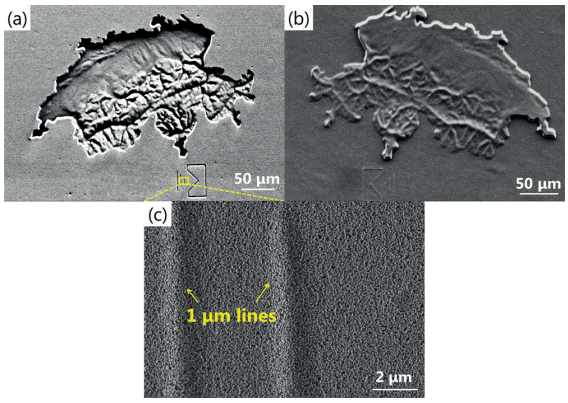

Figure 9. (a) MPA surface containing complex 3D embedded Switzerland map shape replicated in situ slip casting acting as permanent mold. (b) Replicated surface of silicone polymer (repliset-F5) from MPA permanent mold. (c) Lateral resolution of lines fabricated on MPA surface sintered at 1250 °C to obtain 90% density.

Figure 9b to show that a microstructured MPA surface can act as a permanent mold to easily replicate on flexible polymers.

The demolding of the repliset silicone can be carried out by manual peeling off or ultrasonication in an ethanol bath without leaving any traces of silicone on the ceramic surface. The repliset silicone polymer has homogeneous microstructures on large areas tested up to 24 × 12 mm^2 and replicated more than five times for repeatability. Detailed investigations in this direction are presently being carried out.

In brief, the developed fabrication process can be easily applied to a wide range of materials that can be slip cast such as ZrO_2, ITO (indium tin oxide), mullite, SiC, SiO_2, alumina +MgO, alumina+talc, AlN, YSZ (yittria-stabilized zirconia), ZnO−Al_2O_3 composites,[43,44] and several others. If the master molds have better resolution, then the replication process should in principle be able to produce the same or better resolution of the structures in the sintered ceramic surface. Tuning the grain size and grain size distribution of ceramic particles can lead to increased sharpness and the ability to replicate smaller structures on ceramic bodies with better precision as also illustrated in the literature.[16] The surface microstructures in combination with mesopores being filled up with a second phase material can lead to interesting functional ceramic matrix composites (CMC). The teardrops and bone pit structures can also be used in biology for cell growth studies. Furthermore, the microbowls and teardrop structures along with mesopores can serve as dual scale lubricant reservoirs during wear between contact surfaces leading to lower frictional forces. Also, mesoporous conical pillars may also be potentially used in photovoltaics to increase the light trapping efficiency.

5. CONCLUSIONS

A modified slip casting process using microstructured Sylgard PDMS negative molds, which are further replicated using laser ablated PC master molds, resulted in the formation of ceramic surface 3D micro free-forms. A variety of microstructural features such as complex Switzerland 3D topography maps, shallow diffractive optical elements, microconical pillars, teardrop structures with inherent nano roughness, and homogeneous porosity have been obtained. Also the reproducibility and homogeneity of the microstructures and the process has been demonstrated. Green compacts with cuboidal and disc shapes have been produced with one microstructured surface upon completion of the drying process.

The drying process has been observed to be in one direction, perpendicular to microstructured areas. Hence, a linear 1D mass diffusion drying model has been developed assuming that the mass diffusion in the slurry is mainly by capillary transport and the drying occurs by evaporation at the air−slurry interface and by water permeation across Sylgard PDMS membrane at the slurry−PDMS interface. The linear 1D model predicts that the drying time is linearly proportional to height of the slurry and a linear function of thickness of the Sylgard PDMS membrane respectively. The thickness of PDMS membrane was found to be the quality determining factor to achieve macro- and microdefect-free microstructured samples. The optimum thickness range was found to be 400 μm to 1 mm, and the best results were obtained for a thickness of ∼500 μm. Further, the model predicts that the drying time is independent of microstructured areas. The above theoretical predictions were validated by our experimental observations. Ceramic green bodies with microstructured areas of 300, 1200, 12 000 mm^2 respectively, have been fabricated with sample heights of 10 mm having the same drying times. Because the PC sheets can be ablated to achieve 3 m^2 microstructured areas and the drying time is area-independent, it is feasible to produce structured ceramics up to 3 m^2 in area and maybe even higher.

The microstructured ceramics also display remarkable properties and are also promising for various applications. Conical micropillars in combination with nanoroughness provided by ultrafine grains and mesopores provide a dual-scale roughness that cause superhydrophobic behavior for mesoporous alumina samples when coated with an eicosane waxy layer.

Furthermore, we have also demonstrated that the ceramic samples produced by this technology can be used as second-generation permanent molds for further micro- and nanofabrication. The technology and the model can be easily extended to a variety of other slip castable materials. Thus, the outlined process can be utilized to develop innovative multifunctional ceramics or ceramic matrix composites for tribology and wetting, as well as biology and photovoltaics.

■ ASSOCIATED CONTENT

Supporting Information

The Supporting Information is available free of charge on the ACS Publications website at DOI: 10.1021/acsami.5b04748.

Powder morphology of as-received from the supplier, particle size distribution and viscosity measurements that are needed for theoretical model proposed, Hg porosimeter measurements to measure pore size distribution, excimer laser ablated PC sheet showing 1300 × 800 mm^2 microstructured areas and an AFM image of DOE structures, HRSEM images of negative PDMS stamps to show the intermediate steps for more clarity and proof, real sample pictures showing macro cavity defect and defect free samples with corresponding PDMS samples, Reynolds number calculations, and low-magnification image of 3D Switzerland map shape to show homogeneous replication are available. (PDF)

DOI: 10.1021/acsami.5b04748
ACS Appl. Mater. Interfaces 2015, 7, 24458−24469

AUTHOR INFORMATION

Corresponding Authors

*E-Mail: haritha.iitm@gmail.com.
*E-mail: patrik.hoffmann@empa.ch.

Author Contributions

R.S. conceived and performed all the experiments, except the laser ablation of PC sheets, developed the calculations, and wrote the manuscript. K.B. designed and supervised the realization of the master structures in polycarbonate and wrote the part on laser ablation. P.B. contributed in the slurry preparation process, provided particle size distributions, had technical and scientific discussions about the slip casting process, and corrected the manuscript. P.H. designed the micropillar dimensions, supervised the project, had technical and scientific discussions, and corrected the manuscript.

Funding

The project is partially funded by CCMX, Switzerland under project number 5211.00093.100.01.

Notes

The authors declare no competing financial interest.

ACKNOWLEDGMENTS

We acknowledge Arie Bruinink, Empa St. Gallen for designing the teardrop structures. We acknowledge Erdem Siringil for the realization of some of the structures by laser ablation. We acknowledge Sebastien Equis for obtaining DHM image of PC sheet containing DOE structures. We thank Durif Caroline, Empa Dübendorf for carrying out Hg intrusion measurements. We thank Edin Balic, SwiSS-9, GmbH for participating in the CCMX project.

REFERENCES

(1) Heckele, M.; Schomburg, W. Review on Micro Molding of Thermoplastic Polymers. *J. Micromech. Microeng.* **2004**, *14*, R1.
(2) Quake, S. R.; Scherer, A. From Micro- to Nanofabrication with Soft Materials. *Science* **2000**, *290*, 1536−1540.
(3) Radha, B.; Kulkarni, G. U. A Modified Micromolding Method for Sub-100-Nm Direct Patterning of Pd Nanowires. *Small* **2009**, *5*, 2271−2275.
(4) Wooh, S.; Koh, J. H.; Lee, S.; Yoon, H.; Char, K. Trilevel-Structured Superhydrophobic Pillar Arrays with Tunable Optical Functions. *Adv. Funct. Mater.* **2014**, *24*, 5550−5556.
(5) Pham, T. A.; Kim, D.-P.; Lim, T.-W.; Park, S.-H.; Yang, D.-Y.; Lee, K.-S. Three-Dimensional SiCN Ceramic Microstructures via Nano-Stereolithography of Inorganic Polymer Photoresists. *Adv. Funct. Mater.* **2006**, *16*, 1235−1241.
(6) Yang, H.; Deschatelets, P.; Brittain, S.; Whitesides, G. Fabrication of High Performance Ceramic Microstructures from a Polymeric Precursor Using Soft Lithography. *Adv. Mater.* **2001**, *13*, 54−58.
(7) Vogelaar, L.; Lammertink, R. G. H.; Barsema, J. N.; Nijdam, W.; Bolhuis-Versteeg, L. A. M.; van Rijn, C. J. M.; Wessling, M. Phase Separation Micromolding: A New Generic Approach for Micro-structuring Various Materials. *Small* **2005**, *1*, 645−655.
(8) Auger, M. A.; Schilardi, P. L.; Caretti, I.; Sánchez, O.; Benítez, G.; Albella, J. M.; Gago, R.; Fonticelli, M.; Vázquez, L.; Salvarezza, R. C.; et al. Molding and Replication of Ceramic Surfaces with Nanoscale Resolution. *Small* **2005**, *1*, 300−309.
(9) Ihlemann, J.; Scholl, A.; Schmidt, H.; Wolff-Rottke, B. Nanosecond and Femtosecond Excimer-Laser Ablation of Oxide Ceramics. *Appl. Phys. A: Mater. Sci. Process.* **1995**, *60*, 411−417.
(10) Samant, A. N.; Dahotre, N. B. Laser Machining of Structural Ceramics—a Review. *J. Eur. Ceram. Soc.* **2009**, *29*, 969−993.
(11) Boehlen-Stassen, K. L.; Rumsby, P. T.; Cerezo, A.; Huang, M. Fabrication of Axisymmetric Ceramic Micro Parts Using Pulsed Laser Ablation. *Proc. SPIE* **2001**, *4557*, 130.
(12) Ruprecht, R.; Gietzelt, T.; Müller, K.; Piotter, V.; Haußelt, J. Injection Molding of Microstructured Components from Plastics, Metals and Ceramics. *Microsyst. Technol.* **2002**, *8*, 351−358.
(13) Piotter, V.; Bauer, W.; Benzler, T.; Emde, A. Injection Molding of Components for Microsystems. *Microsyst. Technol.* **2001**, *7*, 99−102.
(14) Ritzhaupt-Kleissl, H. J.; Johander, P. *Ceramics Processing in Microtechnology*; Whittles Publishing: Caithness, United Kingdom 2009.
(15) Jackman, R. J.; Duffy, D. C.; Cherniavskaya, O.; Whitesides, G. M. Using Elastomeric Membranes as Dry Resists and for Dry Lift-Off. *Langmuir* **1999**, *15*, 2973−2984.
(16) Schönholzer, U. P.; Gauckler, L. J. Ceramic Parts Patterned in the Micrometer Range. *Adv. Mater.* **1999**, *11*, 630−632.
(17) Xia, Y.; Whitesides, G. M. Soft Lithography. *Annu. Rev. Mater. Sci.* **1998**, *28*, 153−184.
(18) Zhang, Y.; Lin, C.-T.; Yang, S. Fabrication of Hierarchical Pillar Arrays from Thermoplastic and Photosensitive SU-8. *Small* **2010**, *6*, 768−775.
(19) Patil, S.; Mangal, R.; Malasi, A.; Sharma, A. Biomimetic Wet Adhesion of Viscoelastic Liquid Films Anchored on Micropatterned Elastic Substrates. *Langmuir* **2012**, *28*, 14784−14791.
(20) Holthaus, M. G.; Kropp, M.; Treccani, L.; Lang, W.; Rezwan, K. Versatile Crack-Free Ceramic Micropatterns Made by a Modified Molding Technique. *J. Am. Ceram. Soc.* **2010**, *93*, 2574−2578.
(21) Bowen, P.; Carry, C.; Luxembourg, D.; Hofmann, H. Colloidal Processing and Sintering of Nanosized Transition Aluminas. *Powder Technol.* **2005**, *157*, 100−107.
(22) Srinivasan, R.; Mayne-Banton, V. Self-Developing Photoetching of Poly (ethylene Terephthalate) Films by Far-Ultraviolet Excimer Laser Radiation. *Appl. Phys. Lett.* **1982**, *41*, 576−578.
(23) Kawamura, Y.; Toyoda, K.; Namba, S. Effective Deep Ultraviolet Photoetching of Polymethyl Methacrylate by an Excimer Laser. *Appl. Phys. Lett.* **1982**, *40*, 374−375.
(24) Srinivasan, R.; Braren, B. Ultraviolet Laser Ablation of Organic Polymers. *Chem. Rev.* **1989**, *89*, 1303−1316.
(25) Miller, J. C.; Haglund, R. F. Laser Ablation Mechanisms and Applications. In *Laser Ablation Mechanisms and Applications*; **1991**; Vol. 389.10.1007/BFb0048346
(26) Fogarassy, E.; Lazare, S., Eds. *Laser Ablation of Electronic Materials: Basic Mechanisms and Applications*, North Holland Publishing: Amsterdam, **1992**; Vol. *4*.
(27) Shao, J.; Ding, Y.; Wang, W.; Mei, X.; Zhai, H.; Tian, H.; Li, X.; Liu, B. Generation of Fully-Covering Hierarchical Micro-/Nano-Structures by Nanoimprinting and Modified Laser Swelling. *Small* **2014**, *10*, 2595−2601.
(28) Röhrig, M.; Thiel, M.; Worgull, M.; Hölscher, H. 3D Direct Laser Writing of Nano- and Microstructured Hierarchical Gecko-Mimicking Surfaces. *Small* **2012**, *8*, 3009−3015.
(29) Holmes, A. S.; Pedder, J. E.; Boehlen, K. L. Advanced Laser Micromachining Processes for MEMS and Optical Applications. *Proc. SPIE* **2006**, *2006*, 62611E−62611E.
(30) Boehlen, K. L.; Boehlen, I. B. S. Laser Micromachining of High-Density Optical Structures on Large Substrates. *Proc. SPIE* **2004**, 118−126.
(31) Boehlen, K. L.; Stassen Boehlen, I. B.; Allott, R. M. Advanced Laser Micro-Structuring of Super-Large-Area Optical Films. *Proc. SPIE* **2005**, 204−211.
(32) Qin, D.; Xia, Y.; Whitesides, G. M. Soft Lithography for Micro- and Nanoscale Patterning. *Nat. Protoc.* **2010**, *5*, 491−502.
(33) Piotter, V.; Benzler, T.; Gietzelt, T.; Ruprecht, R.; Haußelt, J. Micro Powder Injection Molding. *Adv. Eng. Mater.* **2000**, *2*, 639−642.
(34) Bauer, W.; Ritzhaupt-Kleissl, H.-J.; Hausselt, J. Micropatterning of Ceramics by Slip Pressing. *Ceram. Int.* **1999**, *25*, 201−205.
(35) Lewis, J. A. Colloidal Processing of Ceramics. *J. Am. Ceram. Soc.* **2000**, *83*, 2341−2359.
(36) Shah, M. M. Analytical Formulas for Calculating Water Evaporation from Pools. ASHRAE Annual Meeting, Salt Lake City, UT, June 22−25, 2008, ASHRAE: Atlanta, GA, 2008, vol. *114* .

DOI: 10.1021/acsami.5b04748
ACS Appl. Mater. Interfaces 2015, 7, 24458−24469

(37) Heo, Y. S.; Cabrera, L. M.; Song, J. W.; Futai, N.; Tung, Y.-C.; Smith, G. D.; Takayama, S. Characterization and Resolution of Evaporation-Mediated Osmolality Shifts That Constrain Microfluidic Cell Culture in Poly (dimethylsiloxane) Devices. *Anal. Chem.* **2007**, *79*, 1126−1134.
(38) Harimkar, S. P.; Dahotre, N. B. Rapid Surface Microstructuring of Porous Alumina Ceramic Using Continuous Wave Nd: YAG Laser. *J. Mater. Process. Technol.* **2009**, *209*, 4744−4749.
(39) Barthlott, W.; Ehler, N. Raster-Elektronenmikroskopie Der Epidermis-Oberflachen von Spermatophyten. *Trop. Subtrop. Pflanzenwelt* **1977**, *19*, 367−465.
(40) Bormashenko, E.; Stein, T.; Whyman, G.; Bormashenko, Y.; Pogreb, R. Wetting Properties of the Multiscaled Nanostructured Polymer and Metallic Superhydrophobic Surfaces. *Langmuir* **2006**, *22*, 9982−9985.
(41) Bhushan, B.; Jung, Y. C.; Koch, K. Micro-, Nano-and Hierarchical Structures for Superhydrophobicity, Self-Cleaning and Low Adhesion. *Philos. Trans. R. Soc., A* **2009**, *367*, 1631−1672.
(42) Duong, B.; Gangopadhyay, P.; Brent, J.; Seraphin, S.; Loutfy, R. O.; Peyghambarian, N.; Thomas, J. Printed Sub-100 Nm Polymer-Derived Ceramic Structures. *ACS Appl. Mater. Interfaces* **2013**, *5*, 3894−3899.
(43) Li, Y.; Lin, J.; Gao, J.; Qiao, G.; Wang, H. Fabrication of Reaction-Bonded SiC Ceramics by Slip Casting of SiC/C Suspension. *Mater. Sci. Eng., A* **2008**, *483*, 676−678.
(44) Hotza, D.; Greil, P. Review: Aqueous Tape Casting of Ceramic Powders. *Mater. Sci. Eng., A* **1995**, *202*, 206−217.

DOI: 10.1021/acsami.5b04748
ACS Appl. Mater. Interfaces 2015, 7, 24458−24469

7.3. Summary

The preparation of microstructured mesoporous alumina surfaces was shown in the attached manuscript. A variety of shapes and structures include diffractive optical elements, tear drop cavities, conical micro shaped pillars, conical holes, bone pits, Siemens stars etc. but not limiting in shapes and curvatures. Having able to obtain bulk alumina samples where one side of the samples is microstructured in addition to the presence of mesoporosity, these surfaces can be impregnated with Fomblin® oil to evaluate their wetting and tribological properties. The hierarchical porosity will enhance the lubricant supply and increase the self–replenishing efficiency, an essential property to retain wetting characterizations post wear tests especially for omniphilic materials. The latter proposed study becomes an important outlook of this dissertation.

Chapter 8
Conclusions and outlook

In this dissertation, the wetting and tribological properties of liquid impregnated mesoporous alumina composites are presented as a function of alumina matrix density. Additionally, the wetting properties post wear tests were studied and the effect of self–replenishment in these composites is demonstrated. Further, the preparation of large area, microstructured mesoporous alumina sample surfaces was carried out as a suggestion to enhance the self–replenishing efficiency in these composites. The most important outcomes of this study are summarized in this chapter as follows, and the recommendations for the future work are given.

- It was successfully shown that the polished and surface non–functionalized α–Al_2O_3 matrices can be used in the liquid impregnation approach to exhibit anti–sticking properties and allow pinning free sliding for both low viscous liquids such as Hexadecane, water and high viscous water and oil based paints for sample tilts ≤10°.
- The relative order of the Van der Waals attractive forces of liquids with alumina is in the order: water > Hexadecane > Dodecane > Fomblin® oil> HFE–7200 3M™. Nevertheless, among the employed impregnating liquids, the relative order of efficiency to achieve sliding and anti–sticking properties is Fomblin® oil > water > Hexadecane/Dodecane.
- Free energy calculations developed for the liquid impregnated composites reveal that the impregnation energy, which is related to the thermodynamic stability of the composites is directly proportional to the spreading parameter (S) of the impregnating liquid with the matrix material. It further predicts that Fomblin® impregnated MPA composites are thermodynamically more stable than the corresponding commonly employed PTFE based composites.
- The tribological characterizations of Fomblin® impregnated/lubricated alumina composites reveal that the friction coefficient (FC) decreases with an increase in the normal load from 10 N to 220 N for most of the alumina matrix densities.

- The general trend of FC in alumina samples (as–sintered and polished) is 70 % dense > 80 % dense > 95 % > 99.5 % dense> sapphire ≈90 % dense samples. Hence, 90 % alumina density was found to be an optimum for best tribological properties.
- Ultra–low FC of 0.025 can be obtained for self–mating Fomblin® lubricated 95 % dense alumina pair.
- The sliding frequencies from 6 Hz to 24 Hz does not have any influence on the FC, while the decrease in the viscosity of Fomblin® from 475 cSt to 10 cSt, slightly increased the FC by 0.05 in 90 % dense based Fomblin® impregnated MPA.
- The wear rates measured in these composites continuously decreased with an increase in the alumina matrix density, and directly proportional to the hardness of the alumina matrix. The wear rates in as–sintered samples lie in–between 10^{-2}–10^{-8} mm^3 N^{-1} m^{-1}, while that of polished samples lie in–between 10^{-5}–10^{-8} mm^3 $N^{-1}m^{-1}$ indicating a decrease of 3 orders of magnitude in the latter samples.
- The wear mechanisms in the as–sintered samples transit from severe to mild abrasive wear as the alumina density increased. For 70 % dense based alumina composites, intergranular fracture is the major dominant mechanism while for 90 % dense samples, polishing and transgranular fracture are the dominant wear mechanisms.
- The wear mechanisms in polished alumina based composites are majorly intergranular fracture type, while occasionally, third body abrasion was also observed especially while using high density alumina matrices.
- The roughness measurements and electron microscopy investigations indicate that the as–sintered samples experience polishing during the wear.
- The worn regions exhibited superhydrophilicity immediately after wear. However, anti–sticking and sliding behaviors were observed given a sufficient self–healing time of 15 h.
- It was observed to have a strong enhancement in the SCAs of water due to the presence of micro sized wear debris, as compared to unworn samples.
- The self–replenishing process can be classified into 4 stages: (I) occurrence of capillarity process, (II) beginning of surface diffusivity process, (III) mixed regime comprising of both the replenished and dry regions, (IV) completion of replenishment process to retain the wetting properties, with the evaporation process occurring throughout. A simple model was developed to predict the self–replenishing times, in which surface diffusivity is the rate determining process. To further enhance the self–replenishing efficiency, fabrication of hierarchical porous surfaces comprising micro and meso porosity was proposed.

- A large area fabrication process to obtain microstructured MPA surfaces was developed using slip casting and replications techniques.
- The drying of the slurry occurs as a one dimensional process, along the slurry height. A simple mass diffusion model developed predicts that the drying time is a linear function of slurry height, PDMS membrane thickness and independent of the microstructured areas.
- The surface microstructuring can be achieved on areas as big as 120 cm^2 and bulk samples as thick as 10 mm by this technology.
- It was demonstrated that this technology can produce with same ease different curvatures, 3D free forms, micro cavities and protruding structures, thus allowing to obtain liquid impregnated microstructured mesoporous alumina composites.

8.1. Recommendations and outlook

There are still a number of additional works that could/should be carried out to arrive at a better fundamental understanding. To extend and complete this work, the recommended future works are:

- The first interesting study would be to evaluate the wetting properties post wear tests for different self–replenishment times such as 30 min, 1 h, 2 h and so on. These experimental data can be verified with the theoretically predicted self–replenishing times.
- The self–replenishment efficiency can be improved by healing at elevated temperatures. Alternatively, the healing efficiency can be improved by preventing the formation of surface debris compacted regions. The debris compacted regions reduced the surface porosity, thus decreasing the self–replenishing times. However, Ar ion milling enables to keep the surface porosity same as the bulk and shown in the Figure 8.1. Such milling can be feasible and tested up to areas of 4 mm^2 using a standard process. However, bigger areas may be milled which enables to use the surfaces for evaluating the self–replenishing properties necessary for achieving optimum wetting and tribological properties.

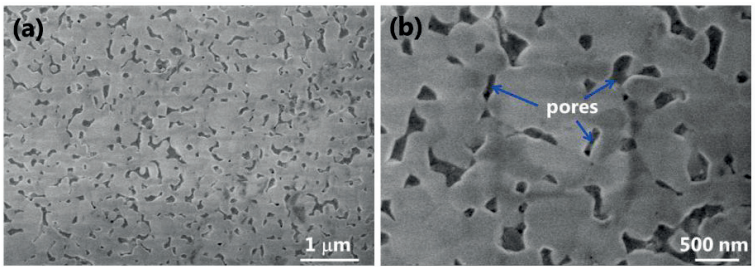

Figure 8.1.(a–b) Low and high magnification SE–SEM images of 80 % dense MPA sample that was milled with Ar ions, enabling debris compacted regions free surfaces.

- The effect of the normal pressures of only up to 10 MPa on the tribological properties of Fomblin® impregnated MPA composites were systematically studied in this dissertation. However, these studies can be extended for normal pressures > 10 MPa. Also, the wetting properties post harsh wear tests (for pressures >> 10 MPa) can be of interest to obtain the influence of a large amount of wear debris.
- An important recommendation is to carry out wetting and tribological characterizations of liquid impregnated microstructured MPA composites. Especially, the micro tear cavities may lead to anisotropic wetting and tribological properties that may be desired in specialized applications.
- The impregnating materials are not limiting and one could explore the use of silicone oils or high viscous emulsions.
- The replication of microstructures onto metal, rigid polymers and other ceramics using microstructured mesoporous alumina samples as the permanent master molds can be of technological interest. Hot embossing or melting techniques may be explored as viable techniques.

Appendix A

Wetting and tribological properties of solid impregnated MPA composites

A. 1. Eicosane impregnated composites

The wetting behaviors of water and Hexadecane drops atop Eicosane impregnated MPA composites were investigated and presented in this section. Figure A.1 presents the equilibrium SCAs of water drops atop polished and unpolished 70 % dense Eicosane impregnated MPA composites. The polished alumina sample consists of flattned regions and porous regions as shown in Figure A.1b while in unpolished as–sintered alumina, the microstructure is homogeneous as shown in Figure A.1d. In a polished case, the water drops exhibited a very large difference (~30°) in SCAs of water drops atop the sample surface. In the case of unpolished surface, a maximum SCA of 110° (large error bars are associated with SCA measurements) was obtained for 70 % dense Eicosane impregnated MPA sample surface. It was observed that the water drops did neither slide off nor roll down in both the cases even when the sample is turned upside down, similar to that demonstrated by rose petal effect [8]. These observations indicate that the water drops are in Wenzel configuration and experience high pinning forces at the composite surface.

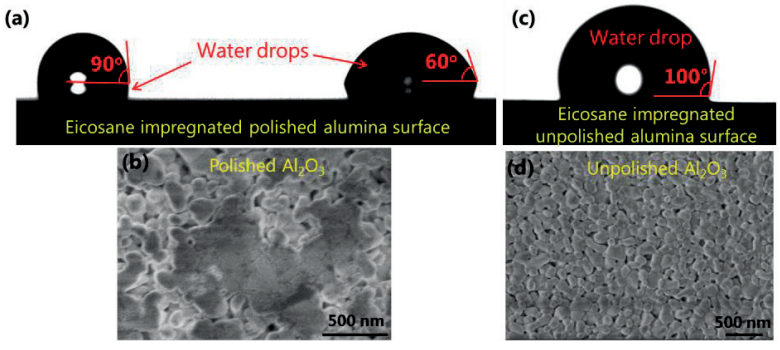

Figure A.1. Equilibrium SCAs of two water drops atop 70 % dense Eicosane impregnated mesoporous alumina surfaces such as: (a) polished surface, whose microstructure is shown in (b), (c) unpolished as–sintered surface whose microstructure is shown in (d). A large difference in SCAs in the former case indicates that the surfaces comprise of heterogeneity either in terms of roughness or chemistry.

The measured equilibrium SCA of water atop flat Eicosane is ~108°. If Eicosane is present as 10, 20, 30 % solid fraction and the rest is occupied by alumina, Cassie Equation (2.3) predicts static contact angles of 30°, 43° and 53° for 90, 80 and 70 % dense samples respectively, assuming both alumina and Eicosane are perfectly flat. However, alumina and solidified Eicosane will not be flat. Also, some liquid Eicosane would have covered part of alumina surfaces during solidification and thereby increasing the Eicosane solid fraction with water which explains such a strong difference in observed SCAs atop polished surfaces. The equilibrium SCAs of water, Hexadecane and Fomblin® oil atop Eicosane impregnated alumina samples are resumed in Figure A.2. The composite surfaces are oleophilic in nature as indicated by small SCAs of Hexadecane and Fomblin® liquids. It was also observed that, the liquid drops: water, Hexadecane and Fomblin® oil do not slide off the Eicosane impregnated alumina surfaces. The main difficulty here is to able to precisely tune the Eicosane surface fraction and the associated roughness underneath the liquid droplets.

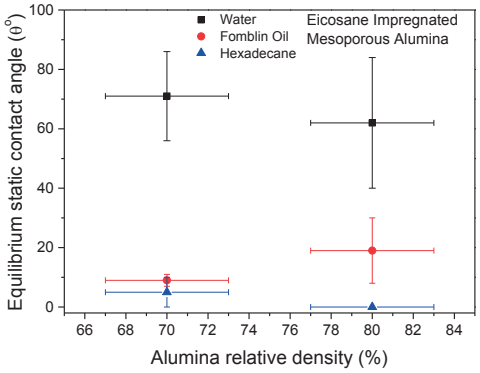

Figure A.2. Equilibrium static contact angles of water, Hexadecane, Fomblin® oil atop Eicosane impregnated 70 and 80 % dense mesoporous alumina composite surfaces

A. 2. Moldflon™ and Zonyl® impregnated composites

It was shown in the previous section that the Eicosane impregnated MPA composites exhibited oleophilic nature. Hence, it was of interest to study the wetting behaviors of fluorinated impregnated MPA composites. Moldflon™ and Zonyl® are Teflon® like materials and possess a low surface energy of ~18 mJ m^{-2}. The SCAs of water drops atop Moldflon™ and Zonyl® impregnated composites are presented in Section 4.1, Chapter 4. When a Moldflon™ impregnated 70 % dense bulk (5–6 mm in thickness) MPA composite was cut by a diamond wire, the cross–section also exhibited hydrophobic behavior. However, it is to be noted that the amount of Moldflon™, Zonyl® materials atop MPA composite surfaces could not be controlled and further, in most cases, the alumina surfaces are fully covered with the second phase materials.

A. 3. Tribological characterizations of solid impregnated MPA composites

The frictional and wear behavior of Eicosane and Moldflon™ impregnated unpolished alumina samples were evaluated. The tribological evaluation of Eicosane impregnated 80±3% MPA

against diamond was carried out with an oscillating sliding contact (refer Section 3.10, Chapter 3). The experimental parameters are: apparent normal load of 200 N (corresponds to pressure of 10.2 MPa), stroke of 4 mm, speed of 0.1 m s^{-1} for a sliding distance of 5241 m. Figure A.3.a presents the measured friction coefficient (FC/μ) as a function of sliding time. The steady state FC of above described tribological system is 0.11±0.004 with a very low wear rate of 1.57×10^{-7} mm^3 $N^{-1}.m^{-1}$. The confocal measurements revealed an increase in the roughness and S_a from 2.6±0.6 μm to 5.3±1 μm measured over 500×500 μm^2 due to wear. The wetting studies post wear reveals that the surface becomes hydrophilic as shown in the Figure A.3b–c. The 20° SCA observed in the Figure A.3c could be because Eicosane does not cover alumina completely after the wear and the increase in the roughness of alumina surfaces. However, it is also less than predicted SCA (43°) for 80 % dense Eicosane impregnated MPA.

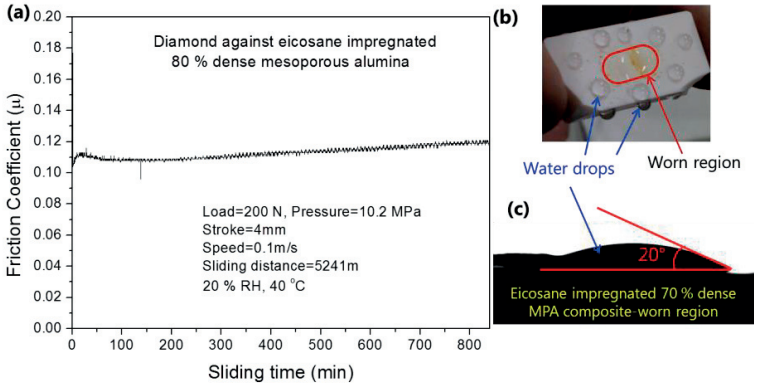

Figure A.3. (a) Friction coefficient data of solid Eicosane impregnated 80 % dense MPA composite as a function of increase in normal load and (b–c) the corresponding wetting behavior of water drop atop unworn and worn regions of the sample after wear test. In (b) the water drops do not slide or roll even when the sample is tilted upside down.

Similarly, the tribological characterization of Moldflon™ impregnated 90 % dense MPA composite revealed a FC of ~0.9 for apparent normal load of 50 N (~1 MPa) as shown in Figure A.4. The confocal measurements revealed a decrease in the roughness (R_a) from 6.8±2 μm to 3.6±0.7 μm measured over 500×500 μm^2 due to wear. The sample exhibited complete hydrophilicity (CA of <5°) post wear. Such hydrophilic behaviors post wear tests could be because the second phase solid materials could not replenish the alumina surface and presence of nano debris consisting of alumina surfaces that strongly attracted water.

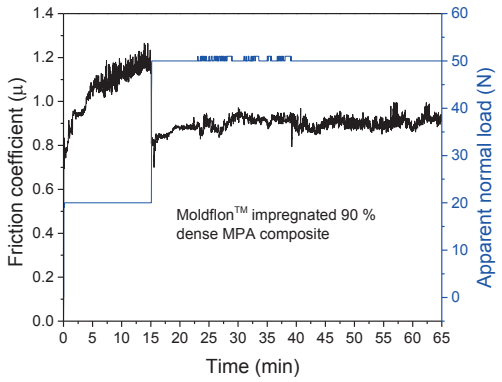

Figure A.4. Friction coefficient curve of Moldflon™ impregnated 90 % dense MPA composite for a constant normal load of 50 N (~1 MPa) and a pre load of 20 N plotted as a function of time.

Appendix B
Supporting information

Sliding Behavior and Stability of Liquid–Liquid Impregnated Alumina Composite Interfaces

Sriharitha Rowthu, Edin E. Balic, Patrik Hoffmann**

Advanced Materials Processing Laboratory, Empa, Swiss Federal Laboratories for Materials Science and Technology, Feuerwerkerstrasse 39, 3602 Thun, Switzerland

E–Mail*: haritha.iitm@gmail.com; patrik.hoffmann@empa.ch

Telephone*: +41 58 765 6225

B. 1. Equilibrium SCAs of liquids with flat sapphire with and without employing O_2 plasma treatment

Table S1. Static contact angle measurements of liquids with flat sapphire with and without employing O_2 plasma treatment

Liquid	CA (θ°) with flat sapphire	
	Employing O_2 plasma treatment	Without O_2 plasma treatment
Water	0	18
Fomblin® Y25	0	20
Dodecane	0	0
Hexadecane	0	0

B. 2. Open and closed porosity measurements

The slip cast alumina samples were sintered in air to achieve 70±3, 80±3 and 90±3 % dense samples when sintered at $0.61T_m$, $0.64T_m$ and $0.66\ T_m$ temperatures respectively (T_m, melting point of α–Al_2O_3 = 2050 °C). It is thus clear from the Figure S1 that majority of the total porosity (100–% total relative density) is open, connected porosity in each of 70, 80 and 90 % densifications. The accurate values of total density, open porosity and closed porosity for 70, 80 and 90 % dense MPA samples are also presented in Table S2.

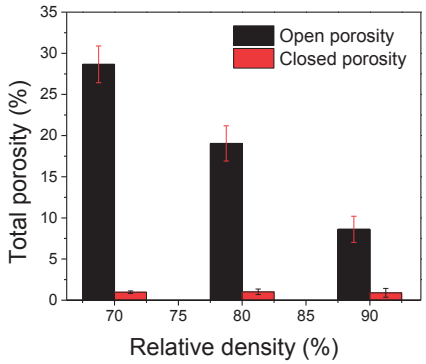

Figure S1. The fraction of open and closed porosity in 70, 80 and 90 % dense mesoporous alumina samples as measured with the Archimedes principle using water as the suspending liquid.

Table S2. Relative density, open porosity and closed porosity of alumina samples sintered with one step sintering process

Relative Density (%)	**Open Porosity (%)**	**Closed Porosity (%)**
70	28.66±2.24	0.98±0.15
80	19.05±2.14	1.02±0.34
90	8.62±1.58	0.9±0.54

B. 3. Physical properties of materials used for the study

The physical and chemical properties of materials used in the current study are listed in Table S3.

Table S3. Physical properties of liquids used for wetting studies

Liquid (Molecular formula)	Dynamic viscosity (η) at 20 °C (cSt)	BP (°C)	Density (g cm^{-3})	Surface tension at 20 ^{o}C (mN m^{-1})
Water (H_2O)	1.002	100	1	72.8
Dodecane ($C_{12}H_{26}$)	1.786	214-218	0.75	25
Hexadecane ($C_{16}H_{34}$)	3.89	271-291	0.773	27.47
Fomblin® Y25 ($CF_3O[-CF(CF_3)CF_2O-]_x(-CF_2O-)_yCF_3$)	250	>270	1.9	22
HFE-7200 3M™ Novec™ ($C_4F_9OC_2H_5$)	0.43	76	1.43	13.6

B. 4. Optimal parameters for Fomblin® oil infiltration into MPA

Table S4 presents the studied impregnation parameters to obtain complete filling of open porosity of mesoporous alumina samples. The optimized parameters are 2 h impregnation time at 150 °C temperature for complete filling of the open porosity. The fraction of open porosity filled for different impregnating temperatures and times is obtained by measuring the weight of the samples prior and after the impregnation experiments. Knowing already the amount of open porosity in the sample, it is possible to estimate the fraction of open porosity filled.

Table S4. Optimization of impregnation T and time for MPA samples for complete filling

Impregnation T (°C)	**Impregnation time (h)**	**% Open porosity filled**
20	2	40
150	1	96
150	2	99.5

B. 5. Infiltration, spreading, infiltration+spreading, No infiltration+ no spreading

The following Table S5 was obtained based on the changes in width, height and volume of the test liquid drop as a function of time, the respective conclusions can be made about the behavior of the test liquids.

Table S5. Observations of spreading, infiltration, infiltration+spreading, no spreading+no infiltration based on changes in width, height and volume of the test liquid drop

Width	Height	Vol.	Conclusions
Constant	↓	↓	Infiltration
↓	Constant	↓	Infiltration
↓	↓	↓	Infiltration
↑	↓	Constant	Spreading
↑	↓	↓	Spreading+Infiltration
↓	↓	↓	
↓	↓	↓	Spreading+Infiltration
Constant	Constant	Constant	No spreading, No infiltration

B. 6. Infiltration behavior: Change in width, height and volume of water drop atop non–infiltrated dry MPA sample

The width, height and volume of the water drop are plotted as a function of time in Figure S2. All the three parameters decrease for times greater than 270 s while for below, the volume and height decreases with width constant. As seen from Table S5, they represent infiltration conditions and hence te water drop atop non–infiltrated dry MPA samples undergo infiltration.

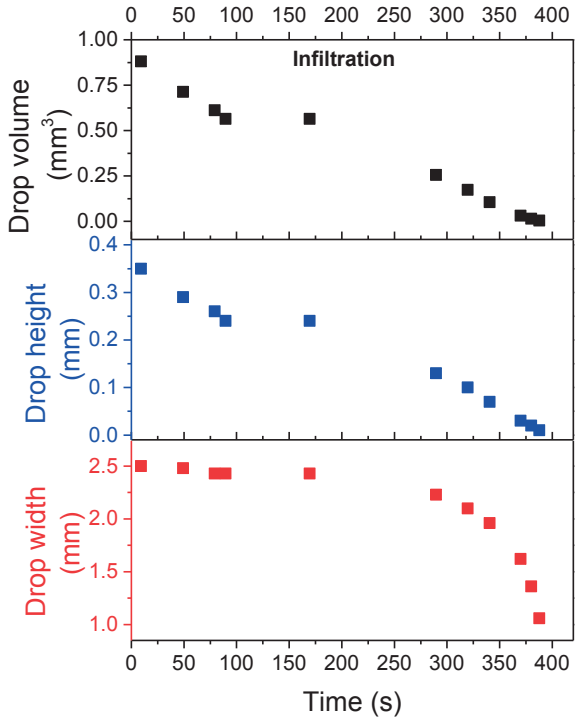

Figure S2. Plotted are the values of the water drop volume, height and width atop non–infiltrated dry 90 % dense MPA sample as a function of time. The width remained constant for the first 250 seconds with gradual decrease in the height and volume of the drop. After 250 s, width, height and volume decrease until the drop completely disappears thus exhibiting infiltration behavior into the mesoporous alumina sample.

B. 7. Wetting dynamics of water drop atop O_2 plasma treated Fomblin® impregnated MPA sample

The wetting dynamics of water drop atop O_2 plasma treated Fomblin® impregnated MPA sample are shown in Figure S3.

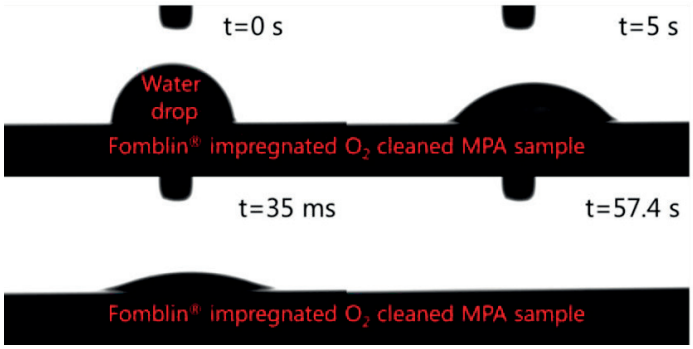

Figure S3. The continuous decrease of the SCA of water drop atop O_2 plasma treated alumina sample prior to Fomblin® oil impregnated MPA sample is presented. The Fomblin® oil does not flood the LIMPA surface and the complete infiltration and spreading of the water drop takes place by replacing the impregnating Fomblin® oil, which occurs just in 57.4 s while for untreated (without O_2 plasma) sample, it took 300 s for the same (Figure 2b, main article).

B. 8. Fomblin® oil drop atop water impregnated MPA samples

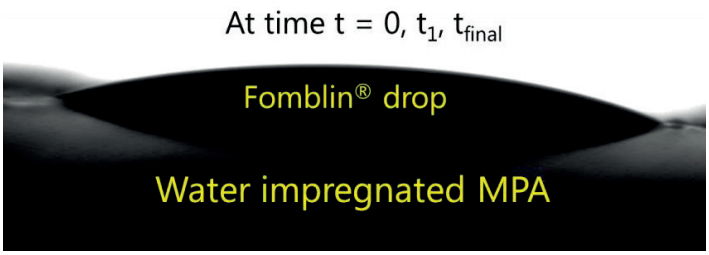

Figure S4. The Fomblin® oil drop atop water impregnated MPA sample in its equilibrium, making a static CA of 18°.

B. 9. Infiltration and Spreading behaviors: Change in width, height and volume of water drop atop Fomblin® impregnated and unflooded MPA

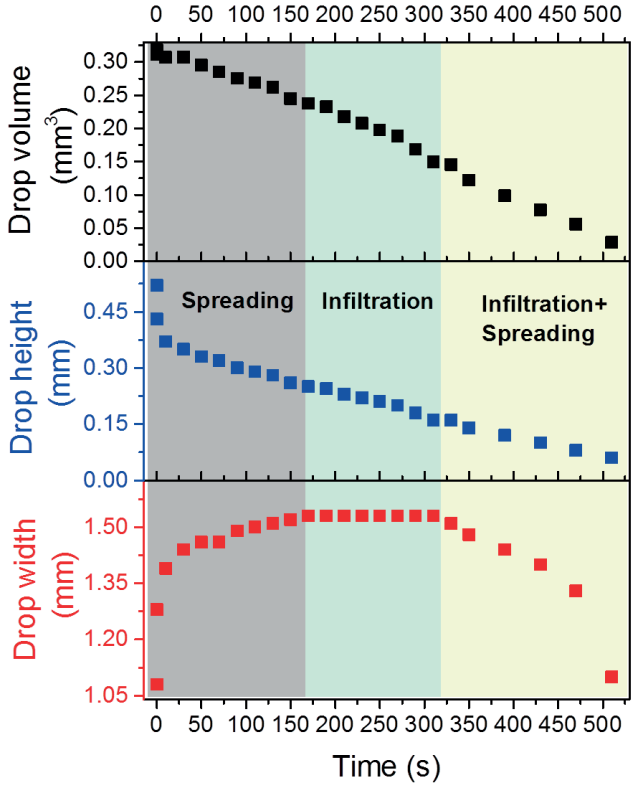

Figure S5. Plotted are the values of the water drop volume, height and width atop Fomblin® impregnated 70 % dense mesoporous alumina sample as a function of time. The drop width increased continuously for the first 170 s with gradual decrease in the height and volume of the drop, thus exhibiting the spreading behavior. From 170 s to 320 s, the width remained constant while the height and the volume decreased thus, exhibiting infiltration behavior. After 320 s, the width, height and the volume of the drop decreases until the drop completely disappears thus exhibiting a combination of infiltration and spreading behaviors into the mesoporous alumina sample.

B. 10. Effect of viscosity on impregnation dynamics

The temporal evolution of a high viscosity Fomblin® oil drop (η=475 mP.s) infiltrating for into a dry, non–infiltrated MPA sample is shown in Figure S6, where it takes 22 min for Fomblin® oil to see the impregnation behavior.

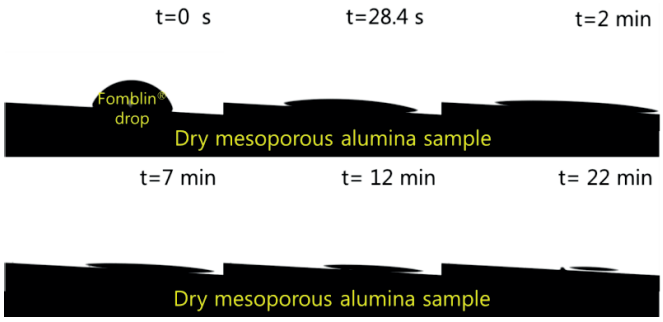

Figure S6. The temporal infiltration behavior of high viscous Fomblin® oil into a non–infiltrated dry mesoporous alumina sample at room temperature of 20 °C are shown. The static contact angle of a water drop decreased from 40° to 0° as the time increased to 300 s, indicating the completion of impregnation. While for Fomblin® oil, the static contact angle decreased from 67° to 0° as the time increased to 22 min, which indicates a higher impregnation time.

B. 11. Surface energies, surface tensions of solids and liquids respectively, and their apolar and polar components

Table S6. Surface energies/tensions and their components for materials of study [49]

Material	γ_s/γ_l **(mJ m^{-2}/mN m^{-1})**	γ^{LW} **(mJ m^{-2}/mN m^{-1})**	γ^{+} **(mJ m^{-2}/mN m^{-1})**	γ^{-} **(mJ m^{-2}/mN m^{-1})**
α–Alumina	44.8	43.7	0.004	80.5
Teflon®	17.9	17.9	0	0
Polypropylene (PP)	25.7	25.7	0	0
Corona treated PP	33	33	0	11.1
Polyethylene (PE)	33	33	0	0
Nylon 6, 6	37.7	36.4	0.02	21.6
Polymethylmethacrylate (PMMA)	40	40	0	14.6
Polystyrene (PS)	42	42	0	1.1
Cell culture PS	46.8	43.7	0.12	20
Polyvinylalcohol (PVA)	42	42	0	57
Polyvinyldinechloride (PVDC)	43.4	43.4	0	29.7
Polyvinylchloride (PVC)	43.8	43	0.04	3.5
Polyethyleneoxide (PEO)-6000	43	43	0	64
PEO	42.9	30.9	6	6
Polyamide (PA)-66	46.5	32.5	7	7
Polydimethylsiloxane (PDMS)	19.8	19	0.4	0.4
Polyethyleneterephthalate (PET)	44.6	35.6	4.5	4.5
HFE-7200 3M™	13.6	5.1025*	0.1366*	132.12*
Fomblin® Y25 oil	22	13.35*	0.13*	143.82*
Dodecane	25	25	0	0
Hexadecane	27.5	27.5	0	0
Water	72.8	21.8	25.5	25.5

*The components of surface tension values for HFE−7200 3M™ and Fomblin® are determined by measuring the contact angles of these liquids with both PE and PTFE and using van Oss theory.

Calculated interfacial surface tension between liquids

Table S7. Calculated interfacial surface tension between materials of study using van Oss−Choudary−Good equation [49]

Liquid 1	**Liquid 2**	**Interfacial surface tension–γ_{12} (mN m^{-1})**
Water	Hexadecane	51.33
Water	Dodecane	51.13
Water	3M™–HFE	-54.51
Water	Fomblin®	-64.08
Hexadecane	3M™–HFE	17.4
Hexadecane	Fomblin®	11.17
Dodecane	3M™–HFE	16.2
Dodecane	Fomblin®	10.55

Reprinted with permission from ACS Applied Materials & Interfaces 2015, 7, 24458-24469. Copyright © 2015 American Chemical Society

Appendix C
Supporting Information

Surface 3D Micro Free Forms: Multifunctional Microstructured Mesoporous α-Alumina by in Situ Slip Casting Using Excimer Laser Ablated Polycarbonate Molds

Sriharitha Rowthu[*,⊥], Karl Böhlen[⊥], Paul Bowen[#] and Patrik Hoffmann*[*,⊥]

[⊥]Advanced Materials Processing Laboratory, Empa, Swiss Federal Laboratories for Materials Science and Technology, Feuerwerkerstrasse 39, CH-3602 Thun, Switzerland

[#]Powder Technology Laboratory, Materials Science and Engineering, Ecole Polytechnique Fédérale de Lausanne, Station 12, CH-1015 Lausanne, Switzerland

E-Mail*: haritha.iitm@gmail.com; patrik.hoffmann@empa.ch

C.1. As received granulated/agglomerated alumina powder morphology

As received alumina powders are characterized with HRSEM and are agglomerated as observed in Figure S1 (a-c).

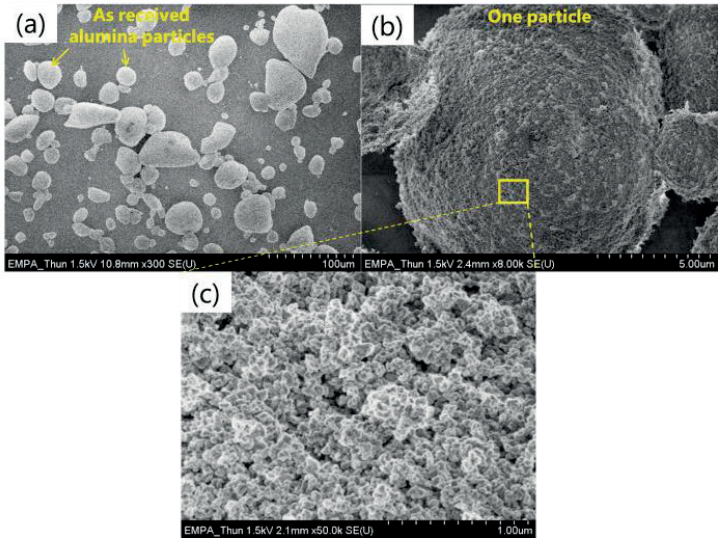

Figure S1.(a-c) HRSEM images of as-received granulated alumina powders forming big granulates as large as 100 μm in size. These particles are spherical and polygonal in shape. The magnified image c shows the presence of ultrafine grains in a single particle. These particles are de-agglomerated to obtain specific surface area, particle size distribution (which is actually grain size distribution in this case) and further rheological characteristics etc. which will be presented in later sections and are used for slip casting process.

C.2. Particle size distribution and slurry viscosity measurements

α-Al_2O_3 slurries are prepared from commercially available deagglomerated powders having particle/grain size distribution (after deagglomeration) as plotted in Figure S2 (a). The slurries are characterized to obtain rheological properties for varying solid fraction (vol. %) in the slurry. Shear stress versus shear strain data obtained for 25 vol. % solid containing ceramic slurry is plotted in the Figure S2 (b) and follows Bingham plastic behavior. A mathematical fitting of the shear stress versus shear strain rate curve has been carried out to obtain the dynamic viscosity of the slurry which is the slope of the curve. The dynamic viscosity is plotted as a function of solid volume fraction of the slurry in Figure S2 (c). If the solid content increases, viscosity increases which can cause incomplete filling of the microstructural features. However, further decrease in the solid fraction can lead to very thin green bodies and also lead to sedimentation of ceramic particles in the slurry during drying process. Hence, an optimum of 25 vol. % solid containing ceramic is used in our study to facilitate homogeneous particle size distribution in the bulk sample and complete filling of the microstructural features of structured PDMS samples.

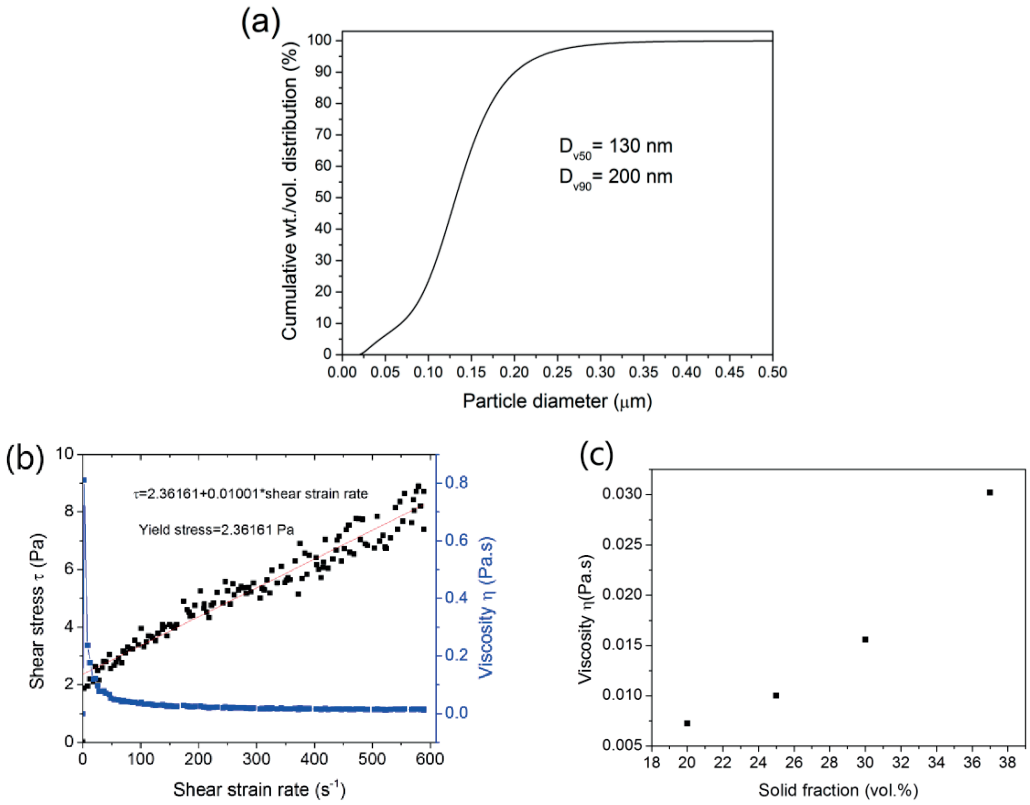

Figures S2.(a) Particle size distribution curve for α-Al2O3 powders; (b) shear stress as a function of shear strain rate for 25 vol. % solid alumina slurry; (c) calculated dynamic viscosity of Bingham plastic behavior of slurry as a function of solid volume fraction.

C.3. Pore size distribution

Hg intrusion porosimeter was used to obtain pore size distribution data for 70, 80 and 90% dense alumina samples. The samples used for the measurements have weight of ~ 3g and around 4-5 mm diameter cylinders. The technique is based on the principle of measuring the pressure required for Hg to be penetrated into a pore of the material. Knowing the contact angle (140°) that Hg makes with Alumina, Washburn Equation (S1) allows to calculate the pore radius (r) and hence the pore diameter. The measurements were obtained on minimum three samples for repeatability for every densification and the cumulative number of pores versus pore diameter is plotted in Figure S3. For 70 and 80 % dense samples, maximum number of pores have pore diameter between 45-55 nm while for 90 % dense sample, maximum number of pores have pore diameter between 28-35 nm. This is because at higher sintering temperatures of 1250 °C to achieve 90 % theoretical density, grain growth and higher necking happens to reduce the pore size.

$$P = -\frac{2\gamma_1 \cos\theta}{r} \qquad \text{(S1)}$$

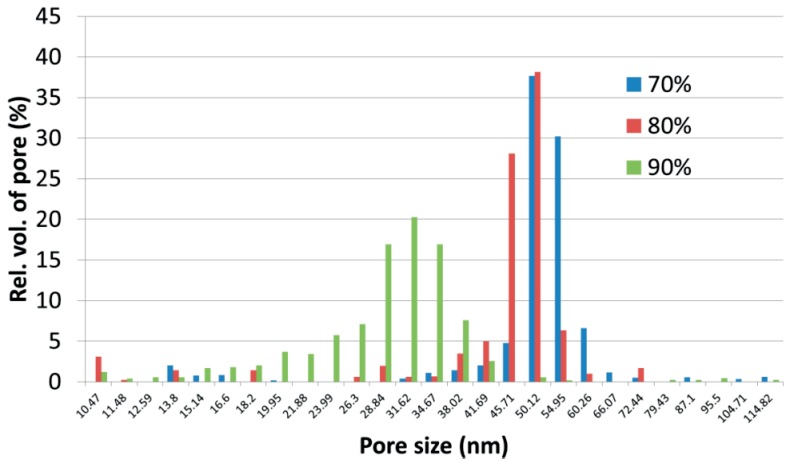

Figure S3. Porosity distribution graph for 70, 80 and 90 % relative theoretical dense α-Al_2O_3 samples measured with Hg intrusion porosimeter.

C.4. Laser ablation of polycarbonate sheet and AFM image of DOE structures

Freeform features of individual geometries with lateral dimensions typically from 1 to 1000 µm and a depth up to 150 µm are achievable on polycarbonate sheet. Direct ablation of ceramics needs one or two orders of magnitude higher laser energy densities than polymers. Hence direct excimer laser ablation of ceramics is often not economical. This ablation process is automated and allows easy workpiece handling. Polycarbonate sheet having structured areas 300×300 mm is machined in 3 h. Polycarbonate sheets having microstructured areas of 1300×800 mm has been shown in Figure S4 (a). An AFM image of diffractive optical elements has been shown in Figure S4 (b) including a line whose line profile is presented in Figure 1 (d) in the main article.

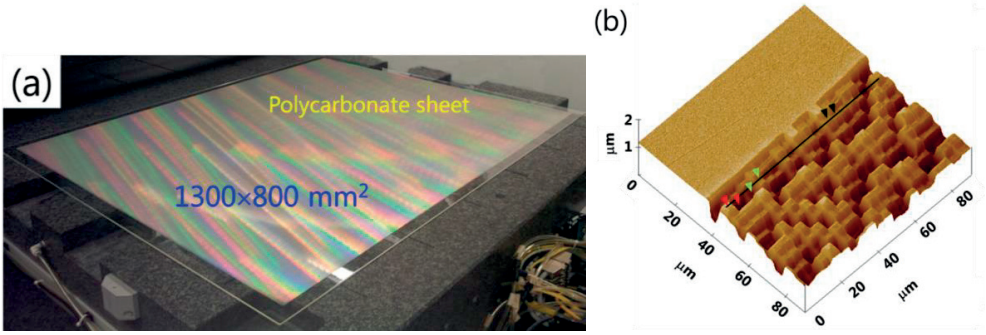

Figure S4. (a) Laser ablated PC sheet having microstructured areas of 1300×800 mm^2 and (b) AFM measurement of diffractive optical elements on PC sheet. The line profile has been taken as located by a black line.

C.5. Characterization of Sylgard PDMS showing several locations of set of concentric circles

Figure S5 (a-d) presents low magnification SEM images of set of concentric circles negatively replicated on Sylgard 184 PDMS.

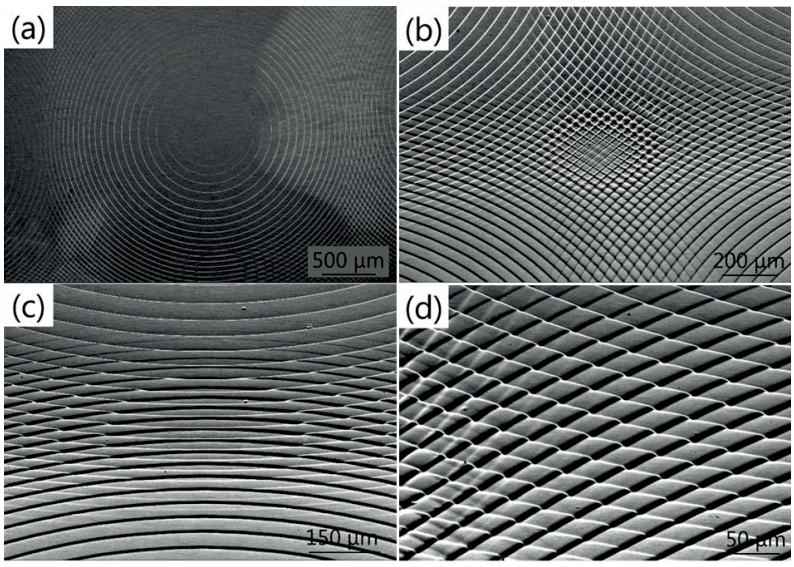

Figure S5. SEM images of set of concentric circles at (a) low magnification, (b) cross over region of 4 sets of concentric circles, (c) cross over region of 2 sets of concentric circles and (d) Zoomed in image of c at its left side.

Figure S5 (c-d) are replicated into alumina ceramic and the corresponding images are presented in Figure 5 (d) and (f) respectively in the main article.

C.6. Ceramic and Sylgard PDMS sample pictures showing macro cavity defect and defect free samples

When 1.5 mm thick structured sylgard PDMS is used in-situ slip casting process, 10 mm high ceramic slurry dried after 15 days but with a macro cavity visible as observed in Figure S6 (a) and the requisite cuboidal shape is no longer obtained due to decreased drying rate from the bottom filter paper. This inhomogeneous drying of the ceramic slurry will also lead to inhomogeneous microstructure especially significant for broad powder size distribution. Figure S6 (b) shows real pictures of Sylgard PDMS having 1.5 mm and 500 µm thickness respectively. Figure S6 (c) shows real pictures of microstructured alumina bulk samples having areas of ~300, ~1200 mm^2 and 120 cm^2 respectively each having 10 mm thickness for each sample.

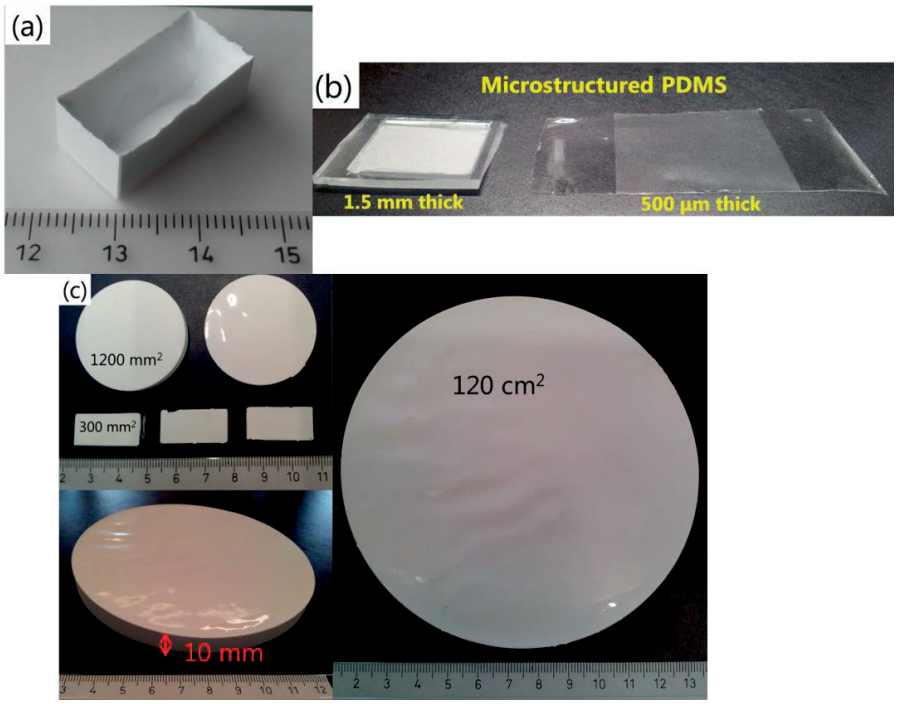

Figure S6. (a) Inhomogeneous drying of ceramic slurry due to 1.5 mm thick PDMS leading to macro cavity in the sample (scale in mm), (b) picture of 1.5 mm and 500 µm thick microstructured sylgard PDMS samples, (c) bulk alumina sample images showing microstructured areas of 300, 1200 mm^2 and 120 cm^2 each having thickness of 10 mm respectively.

C.7. Reynolds number (R_e) calculations

Reynolds number can be calculated using Equation S2.

$$R_e = \frac{V_p D_p \rho_{slurry}}{(1-\phi)\eta_{slurry}} \tag{S2}$$

Where ρ_{slurry}, η_{slurry} are respective slurry density and viscosity, the slurry density can be calculated using rule of mixture using Equation S3.

$$\rho_{slurry} = \Phi\rho_p + (1-\phi)\rho_l \tag{S3}$$

The calculated slurry density for 25 vol. % of solids is 1746.75 kg m^{-3} and has been validated with experimental measurement (1748.5 kg m^{-3}). Using Equation S2, R_e can be calculated as 1.68×10^{-11} and is <<<1. Hence, the particles in alumina slurry undergo laminar flow. Therefore, Stokes ' law can be applied in this case to obtain settling velocities for the particles in the slurry.

C.8. Low magnification image of Switzerland topography on alumina ceramic

Figure S7 shows a low magnification image of MPA surface showing Switzerland map shape on larger areas without any defects.

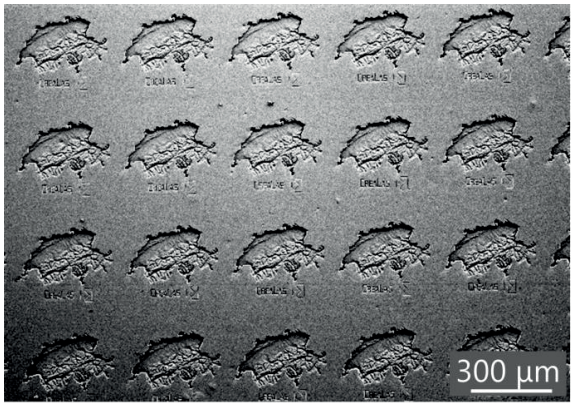

Figure S7. Low magnification image of mesoporous alumina surface showing the Switzerland map shapes

References

[1] T. Young, An essay on the cohesion of fluids, Philosophical Transactions of the Royal Society of London. 95 (1805) 65–87.

[2] W. Barthlott, C. Neinhuis, Purity of the sacred lotus, or escape from contamination in biological surfaces, Planta. 202 (1997) 1–8.

[3] C. Neinhuis, W. Barthlott, Characterization and distribution of water-repellent, self-cleaning plant surfaces, Annals of Botany. 79 (1997) 667–677.

[4] W. Barthlott, N. Ehler, Raster-Elektronenmikroskopie der Epidermis-Oberflachen von Spermatophyten, Trop. Subtrop. Pflanzenwelt, 1977.

[5] F.M. Fowkes, W.A. Zisman, et al., Contact angle, wettability, and adhesion, Advances in Chemistry Series-43, American Chemical Society, 1964.

[6] B.N. Sahoo, B. Kandasubramanian, Recent progress in fabrication and characterisation of hierarchical biomimetic superhydrophobic structures, RSC Advances. 4 (2014) 22053–22093.

[7] V. Zorba, E. Stratakis, M. Barberoglou, E. Spanakis, P. Tzanetakis, S.H. Anastasiadis, et al., Biomimetic artificial surfaces quantitatively reproduce the water repellency of a lotus leaf, Advanced Materials. 20 (2008) 4049–4054.

[8] B. Bhushan, M. Nosonovsky, The rose petal effect and the modes of superhydrophobicity, Philosophical Transactions of the Royal Society of London A: Mathematical, Physical and Engineering Sciences. 368 (2010) 4713–4728.

[9] H.E. Jeong, S.H. Lee, J.K. Kim, K.Y. Suh, Nanoengineered multiscale hierarchical structures with tailored wetting properties, Langmuir. 22 (2006) 1640–1645.

[10] E. Bormashenko, O. Gendelman, G. Whyman, Superhydrophobicity of lotus leaves versus birds wings: different physical mechanisms leading to similar phenomena, Langmuir. 28 (2012) 14992–14997.

[11] W. Ma, H. Xu, A. Takahara, Substrate-Independent Underwater Superoleophobic Surfaces Inspired by Fish-Skin and Mussel-Adhesives, Advanced Materials Interfaces. 1 (2014) 1300092.

[12] L. Barbieri, E. Wagner, P. Hoffmann, Water wetting transition parameters of perfluorinated substrates with periodically distributed flat-top microscale obstacles, Langmuir. 23 (2007) 1723–1734.

[13] W.A. Zisman, Relation of the equilibrium contact angle to liquid and solid constitution, Contact angle, Wettability and Adhesion-Advances in Chemistry Series 43, 1964.

[14] R.V. Zucker, Capillary-driven shape evolution in solid-state micro-and nano-scale systems, PhD Thesis, MIT. (2015).

[15] E. Huovinen, J. Hirvi, M. Suvanto, T.A. Pakkanen, Micro-micro hierarchy replacing micro-nano hierarchy: a precisely controlled way to produce wear-resistant superhydrophobic polymer surfaces, Langmuir. 28 (2012) 14747–14755.

[16] H.Y. Erbil, A.L. Demirel, Y. Avc\i, O. Mert, Transformation of a simple plastic into a superhydrophobic surface, Science. 299 (2003) 1377–1380.

[17] A. Marmur, Wetting on hydrophobic rough surfaces: to be heterogeneous or not to be?, Langmuir. 19 (2003) 8343–8348.

[18] T. Onda, S. Shibuichi, N. Satoh, K. Tsujii, Super-water-repellent fractal surfaces, Langmuir. 12 (1996) 2125–2127.

[19] D.M. Spori, T. Drobek, S. Zürcher, N.D. Spencer, Cassie-state wetting investigated by means of a hole-to-pillar density gradient, Langmuir. 26 (2010) 9465–9473.

[20] X.-M. Li, D. Reinhoudt, M. Crego-Calama, What do we need for a superhydrophobic surface? A review on the recent progress in the preparation of superhydrophobic surfaces, Chemical Society Reviews. 36 (2007) 1350–1368.

[21] K.K. Lau, J. Bico, K.B. Teo, M. Chhowalla, G.A. Amaratunga, W.I. Milne, et al., Superhydrophobic carbon nanotube forests, Nano Letters. 3 (2003) 1701–1705.

[22] M. Ferrari, A. Benedetti, Superhydrophobic surfaces for applications in seawater, Advances in Colloid and Interface Science. 222 (2015) 291–304.

[23] M. Krasowska, M. Ferrari, L. Liggieri, K. Malysa, Influence of n-hexanol and n-octanol on wetting properties and air entrapment at superhydrophobic surfaces, Physical Chemistry Chemical Physics. 13 (2011) 9452–9457.

[24] G. Macdougall, C. Ockrent, Surface energy relations in liquid/solid systems. I. The adhesion of liquids to solids and a new method of determining the surface tension of liquids, in: Proceedings of the Royal Society of London A: Mathematical, Physical and Engineering Sciences, 1942: pp. 151–173.

[25] R.N. Wenzel, Resistance of solid surfaces to wetting by water, Industrial \& Engineering Chemistry. 28 (1936) 988–994.

[26] A. Cassie, S. Baxter, Wettability of porous surfaces, Transactions of the Faraday Society. 40 (1944) 546–551.

[27] L. Barbieri, Wetting properties of flat-top periodically structured superhydrophobic surfaces, PhD Thesis, EPFL. (2007).

[28] V. Hejazi, M. Nosonovsky, Wetting transitions in two-, three-, and four-phase systems, Langmuir. 28 (2011) 2173–2180.

[29] S. Shibuichi, T. Onda, N. Satoh, K. Tsujii, Super water-repellent surfaces resulting from fractal structure, The Journal of Physical Chemistry. 100 (1996) 19512–19517.

[30] S. Shibuichi, T. Yamamoto, T. Onda, K. Tsujii, Super water-and oil-repellent surfaces resulting from fractal structure, Journal of Colloid and Interface Science. 208 (1998) 287–294.

[31] L. Gao, T.J. McCarthy, A perfectly hydrophobic surface (θA/θR= 180/180), Journal of the American Chemical Society. 128 (2006) 9052–9053.

[32] Y. Xiu, Fabrication of surface micro-and nanostructures for superhydrophobic surfaces in electric and electronic applications, PhD Thesis, Georgia Institute of Technology. (2008).

[33] B. Qian, Z. Shen, Fabrication of superhydrophobic surfaces by dislocation-selective chemical etching on aluminum, copper, and zinc substrates, Langmuir. 21 (2005) 9007–9009.

[34] B.T. Least, D.A. Willis, Modification of polyimide wetting properties by laser ablated conical microstructures, Applied Surface Science. 273 (2013) 1–11.

[35] L. Hao, J. Lawrence, CO2 laser modification of the wettability characteristics of a magnesia partially stabilized zirconia bioceramic, Journal of Physics D: Applied Physics. 36 (2003) 1292–1299.

[36] C.J. Wohl, M.A. Belcher, L. Chen, J.W. Connell, Laser ablative patterning of copoly (imide siloxane) s generating superhydrophobic surfaces, Langmuir. 26 (2010) 11469–11478.

[37] H.-M. Jeong, W.-Y. Lee, J.-H. Lee, D.-C. Yang, K.-S. Lim, Super-hydrophobicity of PMMA and PDMS surfaces structured by femtosecond laser pulses, in: SPIE MOEMS-MEMS, 2013: pp. 86120M–1–86120M–6.

[38] M. Röhrig, M. Thiel, M. Worgull, H. Hölscher, 3D direct laser writing of nano- and microstructured hierarchical gecko-mimicking surfaces., Small. 8 (2012) 3009–3015.

[39] S. Rowthu, K. Böhlen, P. Bowen, P. Hoffmann, Surface 3D Micro Free Forms: Multifunctional Microstructured Mesoporous α-Alumina by In-Situ Slip Casting Using Excimer Laser Ablated Polycarbonate Molds, ACS Applied Materials \& Interfaces. 7 (2015) 22458–22469.

[40] R. Blossey, Self-cleaning surfaces—virtual realities, Nature Materials. 2 (2003) 301–306.

[41] B. Bhushan, K. Koch, Y.C. Jung, Biomimetic hierarchical structure for self-cleaning, Applied Physics Letters. 93 (2008) 093101–1–093101–3.

[42] P. Ragesh, V.A. Ganesh, S.V. Nair, A.S. Nair, A review on "self-cleaning and multifunctional materials," Journal of Materials Chemistry A. 2 (2014) 14773–14797.

[43] V.A. Ganesh, H.K. Raut, A.S. Nair, S. Ramakrishna, A review on self-cleaning coatings, Journal of Materials Chemistry. 21 (2011) 16304–16322.

[44] B. Bhushan, Y.C. Jung, K. Koch, Micro-, nano-and hierarchical structures for superhydrophobicity, self-cleaning and low adhesion, Philosophical Transactions of the Royal Society A: Mathematical, Physical and Engineering Sciences. 367 (2009) 1631–1672.

[45] J.P. Youngblood, N.R. Sottos, Bioinspired materials for self-cleaning and self-healing, MRS Bulletin. 33 (2008) 732–741.

[46] X. Liu, Y. Liang, F. Zhou, W. Liu, Extreme wettability and tunable adhesion: biomimicking beyond nature?, Soft Matter. 8 (2012) 2070–2086.

[47] S. Anandan, T. Narasinga Rao, M. Sathish, D. Rangappa, I. Honma, M. Miyauchi, Superhydrophilic graphene-loaded TiO2 thin film for self-cleaning applications, ACS Applied Materials \& Interfaces. 5 (2012) 207–212.

[48] M.A.M.L. de Jesus, J.T. da Silva Neto, G. Timò, P.R.P. Paiva, M.S.S. Dantas, A. de Mello Ferreira, Superhydrophilic self-cleaning surfaces based on TiO2 and TiO2/SiO2 composite films for photovoltaic module cover glass, Applied Adhesion Science. 3 (2015) 1–9.

[49] C.J. Van Oss, Interfacial forces in aqueous media, CRC press, 2006.

[50] D.J. Preston, N. Miljkovic, J. Sack, R. Enright, J. Queeney, E.N. Wang, Effect of hydrocarbon adsorption on the wettability of rare earth oxide ceramics, Applied Physics Letters. 105 (2014) 011601–1–011601–5.

[51] R. Robinson, R. Sandberg, D. Allred, A. Jackson, J. Johnson, W. Evans, et al., Removing surface contaminants from silicon wafers to facilitate EUV optical characterization, in: Proceedings of the Annual Technical Conference-Society of Vacuum Coaters, 2004: pp. 368–376.

[52] P. Atkins, J. De Paula, Elements of physical chemistry, Oxford University Press, USA, 2013.

[53] M.H. Rausch, L. Kretschmer, S. Will, A. Leipertz, A.P. Fröba, Density, Surface Tension, and Kinematic Viscosity of Hydrofluoroethers HFE-7000, HFE-7100, HFE-7200, HFE-7300, and HFE-7500, Journal of Chemical \& Engineering Data. 60 (2015) 3759–3765.

[54] H. Abe, Y. Imai, N. Tokunaga, Y. Yamashita, Y. Sasaki, Highly Efficient Electrohydrodynamic Pumping: Molecular Isomer Effect of Dielectric Liquids, and Surface States of Electrodes, ACS Applied Materials \& Interfaces. 7 (2015) 24492–24500.

[55] R.K. Holman, M.J. Cima, S.A. Uhland, E. Sachs, Spreading and infiltration of inkjet-printed polymer solution droplets on a porous substrate., Journal of Colloid and Interface Science. 249 (2002) 432–440.

[56] S. Höhne, C. Blank, A. Mensch, M. Thieme, R. Frenzel, H. Worch, et al., Superhydrophobic Alumina Surfaces Based on Polymer-Stabilized Oxide Layers, Macromolecular Chemistry and Physics. 210 (2009) 1263–1271.

[57] Y. Xiu, Y. Liu, D.W. Hess, C. Wong, Mechanically robust superhydrophobicity on hierarchically structured Si surfaces, Nanotechnology. 21 (2010) 155705–155710.

[58] T. Yanagisawa, A. Nakajima, M. Sakai, Y. Kameshima, K. Okada, Preparation and abrasion resistance of transparent super-hydrophobic coating by combining crater-like silica films with acicular boehmite powder, Materials Science and Engineering: B. 161 (2009) 36–39.

[59] I.S. Bayer, A. Brown, A. Steele, E. Loth, Transforming anaerobic adhesives into highly durable and abrasion resistant superhydrophobic organoclay nanocomposite films: a new hybrid spray adhesive for tough superhydrophobicity, Applied Physics Express. 2 (2009) 125003–1–125003–3.

[60] Y. Li, L. Li, J. Sun, Bioinspired Self-Healing Superhydrophobic Coatings, Angewandte Chemie. 49 (2010) 6129–6133.

[61] J. Zimmermann, F.A. Reifler, G. Fortunato, L.-C. Gerhardt, S. Seeger, A Simple, One-Step Approach to Durable and Robust Superhydrophobic Textiles, Advanced Functional Materials. 18 (2008) 3662–3669.

[62] M. Xiong, J. Stein, L. Zheng, H. Lei, J. Xiao, T. Deng, et al., Superhydrophobic coating composition and coated articles obtained therefrom, US Patent, App. 11/487,004. (2006).

[63] Y.C. Jung, B. Bhushan, Mechanically durable carbon nanotube-composite hierarchical structures with superhydrophobicity, self-cleaning, and low-drag., ACS Nano. 3 (2009) 4155–4163.

[64] X. Deng, L. Mammen, Y. Zhao, P. Lellig, K. Müllen, C. Li, et al., Transparent, thermally stable and mechanically robust superhydrophobic surfaces made from porous silica capsules., Advanced Materials. 23 (2011) 2962–2965.

[65] C.-H. Xue, J.-Z. Ma, Long-lived superhydrophobic surfaces, Journal of Materials Chemistry A. 1 (2013) 4146–4161.

[66] X. Deng, L. Mammen, H.-J. Butt, D. Vollmer, Candle soot as a template for a transparent robust superamphiphobic coating, Science. 335 (2012) 67–70.

[67] Z. Cui, Q. Wang, Y. Xiao, C. Su, Q. Chen, The stability of superhydrophobic surfaces tested by high speed current scouring, Applied Surface Science. 254 (2008) 2911–2916.

[68] L. Xu, R.G. Karunakaran, J. Guo, S. Yang, Transparent, superhydrophobic surfaces from one-step spin coating of hydrophobic nanoparticles, ACS Applied Materials \& Interfaces. 4 (2012) 1118–1125.

[69] W. Hou, B. Mu, Q. Wang, Studies on wettability of polypropylene/methyl-silicone composite film and polypropylene monolithic material, Journal of Colloid and Interface Science. 327 (2008) 120–124.

[70] N.J. Shirtcliffe, G. McHale, M.I. Newton, C.C. Perry, Intrinsically superhydrophobic organosilica sol-gel foams, Langmuir. 19 (2003) 5626–5631.

[71] I.A. Larmour, G.C. Saunders, S.E. Bell, Compressed metal powders that remain superhydrophobic after abrasion, ACS Applied Materials \& Interfaces. 2 (2010) 2703–2706.

[72] C.-H. Xue, Y.-R. Li, P. Zhang, J.-Z. Ma, S.-T. Jia, Washable and Wear-Resistant Superhydrophobic Surfaces with Self-Cleaning Property by Chemical Etching of Fibers and Hydrophobization, ACS Applied Materials \& Interfaces. 6 (2014) 10153–10161.

[73] T.-S. Wong, S.H. Kang, S.K. Tang, E.J. Smythe, B.D. Hatton, A. Grinthal, et al., Bioinspired self-repairing slippery surfaces with pressure-stable omniphobicity, Nature. 477 (2011) 443–447.

[74] J.D. Smith, R. Dhiman, S. Anand, E. Reza-Garduno, R.E. Cohen, G.H. McKinley, et al., Droplet mobility on lubricant-impregnated surfaces, Soft Matter. 9 (2013) 1772–1780.

[75] Y. Tsuruki, M. Sakai, T. Isobe, S. Matsushita, A. Nakajima, Static and dynamic hydrophobicity of alumina-based porous ceramics impregnated with fluorinated oil, Journal of Materials Research. 29 (2014) 1546–1555.

[76] S. Anand, A.T. Paxson, R. Dhiman, J.D. Smith, K.K. Varanasi, Enhanced condensation on lubricant-impregnated nanotextured surfaces, Acs Nano. 6 (2012) 10122–10129.

[77] A. Eifert, D. Paulssen, S.N. Varanakkottu, T. Baier, S. Hardt, Simple Fabrication of Robust Water-Repellent Surfaces with Low Contact-Angle Hysteresis Based on Impregnation, Advanced Materials Interfaces. 1 (2014) 1300138.

[78] A. Grinthal, J. Aizenberg, Mobile interfaces: Liquids as a perfect structural material for multifunctional, antifouling surfaces, Chemistry of Materials. 26 (2013) 698–708.

[79] S. Sunny, N. Vogel, C. Howell, T.L. Vu, J. Aizenberg, Lubricant-Infused Nanoparticulate Coatings Assembled by Layer-by-Layer Deposition, Advanced Functional Materials. 24 (2014) 6658–6667.

[80] M. Nosonovsky, Materials science: Slippery when wetted, Nature. 477 (2011) 412–413.

[81] C. Urata, B. Masheder, D.F. Cheng, A. Hozumi, Unusual dynamic dewetting behavior of smooth perfluorinated hybrid films: potential advantages over conventional textured and liquid-infused perfluorinated surfaces, Langmuir. 29 (2013) 12472–12482.

[82] W. Ma, Y. Higaki, H. Otsuka, A. Takahara, Perfluoropolyether-infused nano-texture: a versatile approach to omniphobic coatings with low hysteresis and high transparency, Chemical Communications. 49 (2013) 597–599.

[83] Q. Liu, X. Wang, B. Yu, F. Zhou, Q. Xue, Self-healing surface hydrophobicity by consecutive release of hydrophobic molecules from mesoporous silica, Langmuir. 28 (2012) 5845–5849.

[84] K. Manabe, S. Nishizawa, K.-H. Kyung, S. Shiratori, Optical Phenomena and Antifrosting Property on Biomimetics Slippery Fluid-Infused Antireflective Films via Layer-by-Layer Comparison with Superhydrophobic and Antireflective Films, ACS Applied Materials \& Interfaces. 6 (2014) 13985–13993.

[85] X. Yao, Y. Hu, A. Grinthal, T.-S. Wong, L. Mahadevan, J. Aizenberg, Adaptive fluid-infused porous films with tunable transparency and wettability, Nature Materials. 12 (2013) 529–534.

[86] V.A. Ganesh, S.S. Dinachali, S. Jayaraman, R. Sridhar, H.K. Raut, A. Góra, et al., One-step fabrication of robust and optically transparent slippery coatings, RSC Advances. 4 (2014) 55263–55270.

[87] C. Urata, G.J. Dunderdale, M.W. England, A. Hozumi, Self-lubricating organogels (SLUGs) with exceptional syneresis-induced anti-sticking properties against viscous emulsions and ices, Journal of Materials Chemistry A. 3 (2015) 12626–12630.

[88] D.F. Miranda, C. Urata, B. Masheder, G.J. Dunderdale, M. Yagihashi, A. Hozumi, Physically and chemically stable ionic liquid-infused textured surfaces showing excellent dynamic omniphobicity, APL Materials. 2 (2014) 056108.

[89] J. Aizenberg, M. Aizenberg, S.H. Kang, T.S. Wong, P. KIM, Slippery surfaces with high pressure stability, optical transparency, and self-healing characteristics, US Patent, App. 14/140,391. (2014).

[90] P. Kim, T.-S. Wong, J. Alvarenga, M.J. Kreder, W.E. Adorno-Martinez, J. Aizenberg, Liquid-infused nanostructured surfaces with extreme anti-ice and anti-frost performance., ACS Nano. 6 (2012) 6569–6577.

[91] A. Lafuma, D. Quéré, Slippery pre-suffused surfaces, EPL (Europhysics Letters). 96 (2011) 56001.

[92] D.F. Cheng, B. Masheder, C. Urata, A. Hozumi, Smooth perfluorinated surfaces with different chemical and physical natures: Their unusual dynamic dewetting behavior toward polar and nonpolar liquids, Langmuir. 29 (2013) 11322–11329.

[93] A.K. Epstein, T.-S. Wong, R.A. Belisle, E.M. Boggs, J. Aizenberg, Liquid-infused structured surfaces with exceptional anti-biofouling performance, Proceedings of the National Academy of Sciences. 109 (2012) 13182–13187.

[94] J. Li, T. Kleintschek, A. Rieder, Y. Cheng, T. Baumbach, U. Obst, et al., Hydrophobic liquid-infused porous polymer surfaces for antibacterial applications, ACS Applied Materials \& Interfaces. 5 (2013) 6704–6711.

[95] L. Xiao, J. Li, S. Mieszkin, A. Di Fino, A.S. Clare, M.E. Callow, et al., Slippery liquid-infused porous surfaces showing marine antibiofouling properties, ACS Applied Materials \& Interfaces. 5 (2013) 10074–10080.

[96] A.B. Tesler, P. Kim, S. Kolle, C. Howell, O. Ahanotu, J. Aizenberg, Extremely durable biofouling-resistant metallic surfaces based on electrodeposited nanoporous tungstite films on steel, Nature Communications. 6 (2015).

[97] J. Archard, Contact and rubbing of flat surfaces, Journal of Applied Physics. 24 (1953) 981–988.

[98] J. Williams, Engineering tribology, New York Cambridge University Press, 2005.

[99] I.M. Hutchings, Tribology: friction and wear of engineering materials, London: Edward Arnold. (1992) 82–84.

[100] P.J. Blau, S.D. Henry(eds), ASM Handbook: Friction, Lubrication, and Wear Technology, ASM International, 1992.

[101] S. Sasaki, The effects of the surrounding atmosphere on the friction and wear of alumina, zirconia, silicon carbide and silicon nitride, Wear. 134 (1989) 185–200.

[102] M. Gee, The formation of aluminium hydroxide in the sliding wear of alumina, Wear. 153 (1992) 201–227.

[103] A. Blomberg, S. Hogmark, J. Lu, An electron microscopy study of worn ceramic surfaces, Tribology International. 26 (1993) 369–381.

[104] N.P. Suh, Fundamentals of Tribology, International Conference on the Fundamentals of Tribology, 19-22 June, Massachusetts, USA. 11 (1978) 77.

[105] K. Kato, K. Adachi, Wear of advanced ceramics, Wear. 253 (2002) 1097–1104.

[106] P. Andersson, A. Blomberg, Alumina in unlubricated sliding point, line and plane contacts, Wear. 170 (1993) 191–198.

[107] A. Blomberg, M. Olsson, S. Hogmark, Wear mechanisms and tribo mapping of Al 2 O 3 and SiC in dry sliding, Wear. 171 (1994) 77–89.

[108] K.-H. Zum Gahr, J. Schneider, Surface modification of ceramics for improved tribological properties, Ceramics International. 26 (2000) 363–370.

[109] S. Chaiwan, M. Hoffman, P. Munroe, U. Stiefel, Investigation of sub-surface damage during sliding wear of alumina using focused ion-beam milling, Wear. 252 (2002) 531–539.

[110] K.-H. Zum Gahr, W. Bundschuh, B. Zimmerlin, Effect of grain size on friction and sliding wear of oxide ceramics, Wear. 162-164 (1993) 269–279.

[111] D. Qin, Y. Xia, G.M. Whitesides, Soft lithography for micro- and nanoscale patterning, Nat Protoc. 5 (2010) 491–502.

[112] P. Bowen, C. Carry, D. Luxembourg, H. Hofmann, Colloidal processing and sintering of nanosized transition aluminas, Powder Technology. 157 (2005) 100–107.

[113] M.A. Golub, T. Wydeven, R.D. Cormia, ESCA study of the effect of hydrocarbon contamination on poly (tetrafluoroethylene) exposed to atomic oxygen plasma, Langmuir. 7 (1991) 1026–1028.

[114] F. Egitto, L. Matienzo, Modification of polytetrafluoroethylene and polyethylene surfaces downstream from helium microwave plasmas, Polymer Degradation and Stability. 30 (1990) 293–308.

[115] F. Yang, F. Prade, M. Griffa, I. Jerjen, C. Di Bella, J. Herzen, et al., Dark-field X-ray imaging of unsaturated water transport in porous materials, Applied Physics Letters. 105 (2014) 154105.

[116] T. Ondarçuhu, J.-P. Aimé, Nanoscale Liquid Interfaces: Wetting, Patterning and Force Microscopy at the Molecular Scale, CRC Press, 2013.

[117] S.C. Maroo, J. Chung, Negative pressure characteristics of an evaporating meniscus at nanoscale., Nanoscale Research Letters. 6 (2011) 72.

[118] M. Köber, E. Sahagún, P. García-Mochales, F. Briones, M. Luna, J.J. Sáenz, Nanogeometry matters: unexpected decrease of capillary adhesion forces with increasing relative humidity., Small. 6 (2010) 2725–2230.

[119] C. Jai, J. Aime, D. Mariolle, R. Boisgard, F. Bertin, Wetting an oscillating nanoneedle to image an air-liquid interface at the nanometer scale: Dynamical behavior of a nanomeniscus, Nano Letters. 6 (2006) 2554–2560.

[120] D. Dimitrov, A. Milchev, K. Binder, Capillary rise in nanopores: molecular dynamics evidence for the Lucas-Washburn equation, Physical Review Letters. 99 (2007) 054501.

[121] P. Schatzberg, Molecular diameter of water from solubility and diffusion measurements, The Journal of Physical Chemistry. 71 (1967) 4569–4570.

[122] S. Sazhin, Droplets and sprays, Springer, 2014.

[123] C. Taylor, L. Flamand, G. Dalmaz, D. Dowson, T. Childs, Y. Berthier, et al., Elastohydrodynamics-'96: fundamentals and applications in lubrication and traction, Elsevier, 1997.

[124] A. Jabbarzadeh, J. Atkinson, R. Tanner, Nanorheology of molecularly thin films of n-hexadecane in Couette shear flow by molecular dynamics simulation, Journal of Non-Newtonian Fluid Mechanics. 77 (1998) 53–78.

[125] M. McMahan, S. Meaney, D. Hubbard, B. Feinberg, Stripping with a Fomblin supersonic jet at 112.5 keV/nucleon, Proceedings of the 1988 Linear Accelerator Conference, Williamsburg, Virginia, USA. (1989) 88–90.

[126] R. Kusy, J.Q. Whitley, Effects of surface roughness on the coefficients of friction in model orthodontic systems, Journal of Biomechanics. 23 (1990) 913–925.

[127] A. Krell, P. Blank, The influence of shaping method on the grain size dependence of strength in dense submicrometre alumina, Journal of the European Ceramic Society. 16 (1996) 1189–1200.

[128] Z.R. Hesabi, M. Haghighatzadeh, M. Mazaheri, D. Galusek, S. Sadrnezhaad, Suppression of grain growth in sub-micrometer alumina via two-step sintering method, Journal of the European Ceramic Society. 29 (2009) 1371–1377.

[129] A. Krell, P. Blank, H. Ma, T. Hutzler, M. Nebelung, Processing of High-Density Submicrometer Al2O3 for New Applications, Journal of the American Ceramic Society. 86 (2003) 546–553.

[130] P.M. Lugt, Grease lubrication in rolling bearings, John Wiley \& Sons, 2013.

[131] C. Hooke, Minimum film thicknesses in lubricated point contacts operating in the elastic piezoviscous regime, Proceedings of the Institution of Mechanical Engineers, Part C: Journal of Mechanical Engineering Science. 202 (1988) 73–84.

[132] Y. Wang, S.M. Hsu, The effects of operating parameters and environment on the wear and wear transition of alumina, Wear. 195 (1996) 90–99.

[133] G. Stachowiak, A.W. Batchelor, Engineering Tribology, Butterworth-Heinemann, Elsevier, http://www.sciencedirect.com/science/book/9780750678360, 2013.

[134] M. Kalin, S. Novak, J. Vi\vzintin, Wear and friction behavior of alumina ceramics in aqueous solutions with different pH, Wear. 254 (2003) 1141–1146.

[135] J. Olofsson, S. Johansson, S. Jacobson, Influence from humidity on the alumina friction drive system of an ultrasonic motor, Tribology International. 42 (2009) 1467–1477.

[136] H.E. Sliney, C. DellaCorte, The friction and wear of ceramic/ceramic and ceramic/metal combinations in sliding contact, National Aeronautics and Space Administration. 106348 (1993) 1–16.

[137] J. Olofsson, U. Bexell, S. Jacobson, Tribofilm formation of lightly loaded self mated alumina contacts, Wear. 289 (2012) 39–45.

[138] J. Olofsson, S. Jacobson, The influence of grain size and surface treatment on the tribofilm formation on alumina components, Wear. 292-293 (2012) 17–24.

[139] N. Krishnamurthy, M. Prashantharedy, H. Raju, H. Manohar, A study of parameters affecting wear resistance of alumina and yttria stabilized zirconia composite coatings on Al-6061 substrate, ISRN Ceramics. 2012 (2012) 1–14.

[140] M. Munro, Evaluated Material Properties for a Sintered alpha-Alumina, Journal of the American Ceramic Society. 80 (1997) 1919–1928.

[141] A.K. Mukhopadhyay, M. Yiu-Wing, Grain size effect on abrasive wear mechanisms in alumina ceramics, Wear. 162-164 (1993) 258–268.

[142] S.-J. Cho, B.J. Hockey, B.R. Lawn, S.J. Bennison, Grain-Size and R-Curve Effects in the Abrasive Wear of Alumina, Journal of the American Ceramic Society. 72 (1989) 1249–1252.

[143] A. Krell, D. Klaffke, Effects of Grain Size and Humidity on Fretting Wear in Fine-Grained Alumina, Al2O3/TiC, and Zirconia, Journal of the American Ceramic Society. 79 (1996) 1139–1146.

[144] R.S. Roy, H. Guchhait, A. Chanda, D. Basu, M. Mitra, Improved sliding wear-resistance of alumina with sub-micron grain size: a comparison with coarser grained material, Journal of the European Ceramic Society. 27 (2007) 4737–4743.

[145] S. Gruener, P. Huber, Imbibition in mesoporous silica: rheological concepts and experiments on water and a liquid crystal, Journal of Physics: Condensed Matter. 23 (2011) 184109.

[146] J. Bear, Dynamics of fluids in porous media, American Elsevier, New York. (1972).

[147] G.K. Batchelor, An introduction to fluid dynamics, Cambridge university press, 2000.

[148] T.M. O'Connor, M.S. Jhon, C.L. Bauer, B.G. Min, D.Y. Yoon, T.E. Karis, Surface diffusion and flow activation energies of perfluoropolyalkylether, Tribology Letters. 1 (1995) 219–223.

[149] W. Sutherland, LXXV. A dynamical theory of diffusion for non-electrolytes and the molecular mass of albumin, The London, Edinburgh, and Dublin Philosophical Magazine and Journal of Science. 9 (1905) 781–785.

[150] I. Utke, P. Hoffmann, J. Melngailis, Gas-assisted focused electron beam and ion beam processing and fabrication, Journal of Vacuum Science \& Technology B. 26 (2008) 1197–1276.

[151] W.A. Glaeser, Characterization of tribological materials, Momentum Press, 2010.

[152] R.E. Cunningham, R. Williams, Diffusion in gases and porous media, Springer, DOI: 10.1007/978-1-4757-4983-0 , 1980.

[153] K. Dittmar, Nanostructured titania coatings for drug-eluting medical implants, PhD Thesis, EPFL. (2009).

[154] F. Saeidi, B. Meylan, P. Hoffmann, K. Wasmer, Effect of surface texturing on cast iron reciprocating against steel under starved lubrication conditions: A parametric study, Wear. 348-349 (2016) 17–26.

[155] S.P. Mishra, A.A. Polycarpou, Tribological studies of unpolished laser surface textures under starved lubrication conditions for use in air-conditioning and refrigeration compressors, Tribology International. 44 (2011) 1890–1901.

[156] I. Etsion, State of the art in laser surface texturing, Journal of Tribology. 127 (2005) 248–253.

[157] Y. Xia, G.M. Whitesides, Soft lithography, Annual Review of Materials Science. 28 (1998) 153–184.

[158] S.P. Harimkar, N.B. Dahotre, Rapid surface microstructuring of porous alumina ceramic using continuous wave Nd: YAG laser, Journal of Materials Processing Technology. 209 (2009) 4744–4749.

[159] J. Ihlemann, A. Scholl, H. Schmidt, B. Wolff-Rottke, Nanosecond and femtosecond excimer-laser ablation of oxide ceramics, Applied Physics A. 60 (1995) 411–417.

[160] H. Ting, K. Abou-el-Hossein, H. Chua, Review of micromachining of ceramics by etching, Transactions of Nonferrous Metals Society of China. 19 (2009) s1–s16.

[161] V. Piotter, W. Bauer, T. Benzler, A. Emde, Injection molding of components for microsystems, Microsystem Technologies. 7 (2001) 99–102.

[162] V. Piotter, T. Hanemann, R. Ruprecht, J. Hausselt, Injection molding and related techniques for fabrication of microstructures, Microsystem Technologies. 3 (1997) 129–133.

[163] R. Ruprecht, T. Gietzelt, K. Müller, V. Piotter, J. Haußelt, Injection molding of microstructured components from plastics, metals and ceramics, Microsystem Technologies. 8 (2002) 351–358.

Curriculum vitae

Sriharitha Rowthu

Masters in Materials Science & Engineering
Date of Birth: 22.08.1988 (27 years old), single, Indian
haritha.iitm@gmail.com
LinkedIn profile[1]

FIELDS OF EXPERTISE

Wetting, Tribology, Microfabrication, High Entropy Alloys

- Synthesis — Mechanical alloying, Sintering, Slip casting, Replication techniques, Hot Embossing
- Characterization — SEM, XRD, DSC, Optical Microscopy, Confocal Microscopy, Optical Profilometry
- Testing — Contact angle, SRV® oscillating tribometer, Vickers hardness, 4 point bending tests, Compression testing
- Others — Au & C sputtering machines, glove box

EDUCATION

Nov 2011–May, 2016	Graduate student, Materials Science & Engineering, EPFL (École Polytechnique Fédérale de Lausanne), Switzerland
2006–2011	Integrated Masters and Bachelors of Technology, Materials Science & Engineering, IIT (Indian Institute of Technology) Madras, India

AWARDS & ACHIEVEMENTS

Best oral presentation, 2015	E–MRS, Warsaw, Poland
Best poster presentations (for three consecutive years: 2013, 2014, 2015)	CCMX, Switzerland
Best poster presentation, 2013	EDMX research day, EPFL, Switzerland
Best poster presentation, 2010	NMD–ATM, India
Top 2 % in India (Maths, Physics, Chemisty), 2006	All India Rank 2423 out of 200,000 students in IIT-JEE (Joint Entrance Examination for Indian Institute of Technology–the toughest examination in engineering in our nation)
GATE (Graduate Aptitude Test in Engineering), 2009	All India Rank 39 out of 800 students. Test equivalent to subject GRE
XI Examination in Sciences & English, 2004	All India rank 8 out of 6, 21, 953 students
Project X, 2007, Hand–on technical event	Won 3rd prize out of 100 teams, Shaastra, the annual technical festival of IIT Madras, India.
Recipient of Merit cum Means (MCM) scholarship, 2006–2011	IIT Madras, India
Job offer, Reliance Industries Limited (RIL), 2010	As an appreciation of my internship work at RIL, India
Secured rank 4 out of 65 students, 2002	St. Ann´s convent school, Pathapatnam, India

[1] https://ch.linkedin.com/in/rowthu-sriharitha-78b90376

PROFESSIONAL EXPERIENCES

Nov 2011–present	Empa–Swiss Federal Laboratories for Materials Science & Technology, Research assistant–SEM, sputtering machines, Laboratory for Advanced Materials Processing
March–Nov, 2010	Research assistant of sophisticated Nanoindenter during my Bachelors
2012–2013	Teacher assistant, Chemistry of Surfaces course, EFPL
July–Dec, 2015	Research guide to an internship student–Elias Stutz on 4 point bending experiments of mesoporous alumina
May–July, 2009	2 months internship at Reliance OIL & GAS industry, under Y.C. YORA, India. I was offered a job as an appreciation of my work.
June–July, 2008	1 month internship at Tata Steel Plant, India

PUBLICATIONS (h-index : 2, i-10 index: 2)

1. **S. Rowthu**, K. Böhlen, P. Bowen, P. Hoffmann, "Surface 3D Micro Free Forms: Multifunctional Micro-structured Mesoporous α-Alumina by In Situ Slip Casting Using Excimer Laser Ablated Polycarbonate Molds", ACS Applied Materials & Interfaces, 2015, 7, 24458–24469. **(IF: 6.72)**
2. **R. Sriharitha**, B. S. Murty, Ravi S. Kottada "Alloying, Thermal Stability and Strengthening in Spark Plasma Sintered $Al_xCoCrCuFeNi$ High Entropy Alloys", Journal of Alloys and Compounds 2014, 583, 419-426. **(IF: 3)**
3. **R. Sriharitha**, B. S. Murty, Ravi S. Kottada "Phase formation in mechanically alloyed $Al_xCrCuCoFeNi$ (x=0.45, 1, 2.5, 5 moles) high entropy alloys", Intermetallics, 2013, 32, 119-126. **(IF: 2.13)**
4. **S. Rowthu**, E. E. Balic, P. Hoffmann, "Anti–Sticking Behavior and Stability of Liquid–Liquid Impregnated Mesoporous Alumina Composite Interfaces", *To be submitted*, 2016.
5. **S. Rowthu**, P. Hoffmann, "Retention of Anti–Sticking and Sliding Behaviors in Perfluoroether Impregnated Mesoporous Alumina Composites Post Wear", *To be submitted, 2016.*
6. **S. Rowthu**, R. Kaufmann, Y. Fei, P. Hoffmann, "Self–replenishing wettability in liquid impregnated mesoporous alumina composites", *in preparation*.
7. **S. Rowthu**, E. Balic, P. Hoffmann, "Tribological Characterizations of self-mated liquid impregnated mesoporous alumina composites for varying alumina matrix densities", *in preparation*.
8. **S. Rowthu**, P. Hoffmann, "Superhydrophobic behavior of polymeric surfaces replicated from laser ablated polycarbonate master molds", *in preparation.*

PATENT

- **Sriharitha Rowthu**, Patrik Hoffmann, "Superhydrophobic polymer surfaces", Application number EP180021.6, European Patent, filed on August 6th, 2015.

EXTRACURRICULAR ACTIVITIES

- Core member of publicity for AMALGAM 2009 (technical festival for department of Metallurgical and Materials Engineering at IIT Madras.
- Hospitality deputy coordinator for Shaastra 2007 (annual technical festival of IIT Madras), hospitality coordinator of AMALGAM 2008.
- Part of the 6 member women's team, which represented IIT Madras in SPORTS–FEST2008 (sports event for inter–colleges in Chennai) and won silver medal in chess.
- Secured district (in Orissa) level 3rd prize in AIDS awareness essay competition in 2000.

OTHERS

Software skills	C, X Pert HighScore Plus, Image J, Photoshop, Origin, Microsoft Excel
Certificates	HF safety training course, 2014, Empa, Switzerland
Languages	English (fluent), Telugu (native), Hindi (basic)
Interests	Classical Indian dance, Chess, Cooking